DTU Library

Synthesis and application of carbon materials in heterogeneous catalysis

Christensen, David Benjamin

Publication date:
2020

Document Version
Publisher's PDF, also known as Version of record

[Link back to DTU Orbit](#)

Citation (APA):
Christensen, D. B. (2020). *Synthesis and application of carbon materials in heterogeneous catalysis*. Technical University of Denmark.
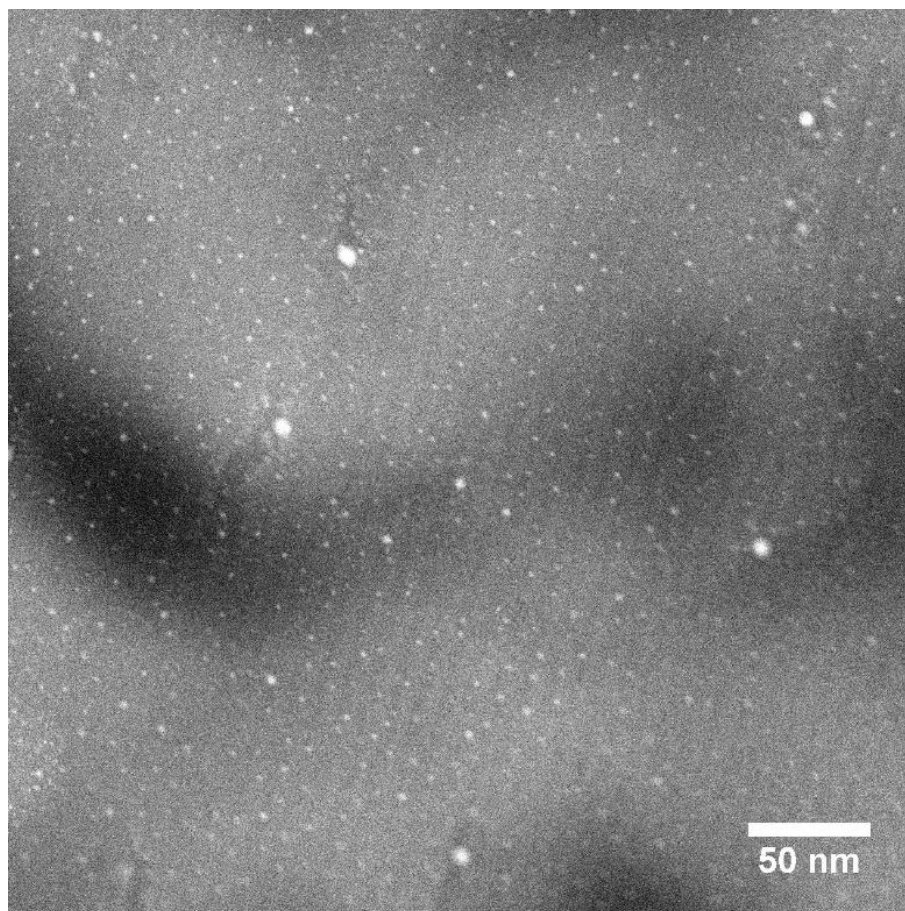
Synthesis and application of carbon materials in heterogeneous catalysis

Ph.D. dissertation by David B. Christensen, M.Sc.

August 2020

DTU Chemistry

David Benjamin Christensen
Synthesis and application of carbon materials in heterogeneous catalysis
Ph.D. dissertation, August 2020
Technical University of Denmark
E-mail address: dachr@kemi.dtu.dk

Front-page image:
STEM image of Pt nanoparticles dispersed on
nitrogen-doped ordered mesoporous carbon.

Preface

This dissertation is culmination of the work carried out at the Center of Catalysis and Sustainable Chemistry (CSC), Department of Chemistry at the Technical University of Denmark (DTU). The work presented was conducted from the 1st of May 2017 to the 1st of June 2020 under the supervision of Prof. Søren Kegnæs. The project was funded by the Villum Foundation (Project number 13158) for the research of catalysts for the replacement of fossil resources with sustainable resources.

As part of the dissertation, research was conducted at Dr. Ryan Wang's group, Department of Chemical Engineering at University College London (UCL). The research stay consisted of four trips of 2-4 days at Diamond Light Source, doing high-resolution analysis of catalysts, and a stay at UCL from the 2nd of September to the 4th of October 2019.

The dissertation is broken down into six chapters, starting with a brief introduction to catalysis and green chemistry, including key concepts and descriptors used for evaluating and comparing the produced catalysts. Chapter 2 introduces the relevant kinds of carbon support materials used for the research, as well as some of the general advantages of carbon supports. Chapter 3 gives insight into the key techniques used for analyzing the materials, their nanostructure, porosity and the dispersion of the active phase. These methods are important for understanding the functionality of the catalysts and comparing their relative activity and stability. Chapter 4 focuses on the research conducted on the dehydrogenation of formic acid to produce pure hydrogen and carbon dioxide. The reaction is carried out in the vapor-phase using mainly ordered mesoporous carbon materials. Chapter 5 is about porous organic polymers and research into their usefulness in the production of formic acid from hydrogen and carbon dioxide (Paper 5). This would allow hydrogen to be stored as a liquid chemical, which can be converted back to hydrogen, creating a cyclic system with the dehydrogenation reaction from the previous chapter. Chapter 6 concerns the use of base metal catalysts for hydrosilylation of ketones, as part of the effort to replace traditional catalysts containing expensive and limited precious metals for important organic reactions (Paper 3).

David Benjamin Christensen

Denmark, May 2020

List of publications

1. *Stabilization of Metal Nanoparticle Catalysts via Encapsulation in Mesoporous Zeolites by Steam-Assisted Recrystallization*. Rasmussen, K. H., Goodarzi, F., Christensen, D. B., Mielby, J. J., & Kegnæs, S. (2019). ACS Applied Nano Materials, 2(12), 8083-8091. https://doi.org/10.1021/acsanm.9b02205
   A paper on improving encapsulation in zeolites via a steam-assisted recrystallization. My contribution consist of characterization of the synthesized and post-reaction catalysts (TEM, STEM and XPS).

2. *The effect of active site distribution in bi-functional Pt-zeolite catalysts for ethane dehydroaromatization.* Goodarzi, F., Christensen, D. B., Joensen, F., Kegnæs, S., & Mielby, J. J. (2020). Applied Catalysis A: General, 592, 117383. https://doi.org/10.1016/j.apcata.2019.117383
   An investigation of the influence of morphology of ZSM-5 and the dispersion of Pt nanoparticles on reactivity. The catalysts BTX selectivity and activity for the dehydroaromatization of ethane was investigated. My contribution consist of characterization of the synthesized and post-reaction catalysts (TEM, STEM and EDX).

3. *Study of CoCu Alloy Nanoparticles Supported on MOF-Derived Carbon for Hydrosilylation of Ketones.* Christensen, D. B., Mortensen, R. L., Kramer, S., & Kegnæs, S. (2020). Catalysis Letters, 150, 1537–1545. https://doi.org/10.1007/s10562-019-03065-2
   A method of producing bimetallic (CoCu) MOF-derived catalysts. The resulting carbon catalysts were tested for the hydrosilylation of ketones. Personal contribution was the writing, synthesis, testing and characterization, as a continuation of a project started by Rasmus L. Mortensen and William Gundtorp.

4. *Selective formic acid dehydrogenation at low temperature over a RuO2/COF pre-catalyst synthesized on the gram scale.* Gonçalves, L. P. L., Christensen, D. B., Meledina, M., Salonen, L. M., Petrovykh, D. Y., Carbó-Argibay, E., Sousa, J. P. S., Soares, O. S. G. P., Pereira, M. F. R., Kegnæs, S., & Kolen'ko, Y. V. (2020). Catalysis Science and Technology, 10, 1991-1995. https://doi.org/10.1039/d0cy00145g
   A paper on the synthesis and application of ruthenium on a TpBD-Me2 COF for the vapour-phase dehydrogenation of formic acid. My personal contribution was the catalytic testing of the catalyst and data treatment.

5. *Heterogeneous production of formic acid by hydrogenation of CO2 using Ir-bpy embedded in polyphenylene POPs.* Bennedsen, N. R, Christensen, D. B., Mortensen, R. L., Wang, R., Kramer, S., Kegnæs, S, (Submitted 2020).
   A project on the production of formic acid from CO_2 using POPs with embedded organic ligands to bridge the gap between heterogeneous and homogeneous catalysts. My contribution consist of the testing and characterization of the catalysts.

6. *Dehydrogenation of bioethanol using Cu nanoparticles supported on N-doped ordered mesoporous carbon.* Thumbayil, R. P, Christensen, D. B., Mielby, J., Kegnæs, S, (Submitted 2020).
   Investigation into the role of nitrogen content on dehydrogenation of bioethanol. Personal contribution consist of developing the synthesis method and supporting with characterization and DRIFTS analysis.

7. *A Synergic Activity of Urea/Butyl Imidazolium Ionic Liquid Supported on UiO-66-NH2 Metal–Organic Framework for Synthesis of Oximes.* Askari, S., Jafarzadeh, M., Christensen, D. B. & Kegnæs, S. (2020). Catalysis letters, https://doi.org/10.1007/s10562-020-03203-1.
   Acquired TEM images of the samples and assisted Mohammed during his stay at DTU.

Acknowledgements

First of all, I would like to thank my supervisor Søren Kegnæs for these past three years. Under his supervision, there was always ideas to be explored and he always helped me whenever I felt stuck. It has proven to be both a fun and challenging task to work here, and has been the best years of my life. I have enjoyed both a good working atmosphere and teamwork throughout my project.

I also want to sincerely thank Jerrik Mielby, who has been a fountain of ideas and different approaches to solving problems. Thank you for including me whenever new equipment arrived or when changes had to be made to existing setups. The hours of discussion, to make heads and tails of results have also proved invaluable throughout each of the projects. I want to thank Søren Kramer for being an invaluable help with organic chemistry and his input for both the hydrosilylation project and the use of POPs for CO_2 hydrogenation.

Furthermore, I would like to thank every one of my colleagues, who I have worked with and shared office with. I would like to thank Kristoffer Rasmussen and Simone Zacho, who I have studied with since I started at DTU. Thanks for always making working at DTU enjoyable and for always being available whenever I had something to discuss. To Niklas Bennedsen, I am grateful for our work on the POPs for formic acid production. I have enjoyed working together and was always inspired by your hard work.

I am grateful to Ryan Wang for letting me stay with his group during the autumn of 2019 and for the joint research grant at Diamond Light Institute to use their high-resolution electron microscopes, I am also grateful for Yury Kolen'ko and Lillian Gonçalves for letting me be part of their project on Ru/COFs.

I also want to thank my family, who have been a never-ending source of support and patience during my work and during writing my thesis. Especially, during these last two month before handing in.

Finally, I would like to thank all of CSC and DTU chemistry and all of the students from the courses I have taught and the projects I have helped supervise. I only encountered kind and helpful people during my time here and I do not have the words to describe, how much that means to me.

Abstract

Catalysts play a key role in the chemical industry owing to their ability to increase the yield and purity of the product of a given process. Concerns of long turn sustainability and impact on the climate have seen an increased desire to move toward green chemistry. By developing new catalysts, processes may be performed under milder conditions, produce less waste or use abundant rather than scarce resources.

This thesis covers several examples of projects aiming to improve upon the durability, sustainability or activity of carbon-based catalysts for important chemical reactions. This includes the formation of formic acid, which has potential as a liquid organic hydrogen carrier. Formic acid could be produced using low concentrations of an Ir precursor (0.00001 M $IrCl_3$) on a porous organic polymer (bpy-PP-POP). The catalysts even showed some promise in catalyzing the reverse reaction, dehydrogenation to hydrogen and CO_2, in a continuous setup to produce pure hydrogen.

The dehydrogenation of formic acid was examined in more detail using a series of nitrogen-doped ordered mesoporous catalysts. Nitrogen was shown to improve the reactivity and selectivity of the catalysts in the vapor phase system, but did not directly affect dispersion of the active metal or reaction mechanism according to analysis using ME-PSD-DRIFTS. Pt on nitrogen-doped ordered mesoporous carbon (Pt@NOMC) proved to be the best among the tested catalysts with a TOF of 870 h^{-1} at 120 °C with no production of CO.

Finally, a method for synthesizing bimetallic MOF-derived carbon catalysts was tested in the hydrosilylation of ketones. CoCu containing catalysts were produced by carbonizing ZIF-67 impregnated with Cu-solutions to achieve bimetallic materials with tunable metal ratios. The carbonization introduced mesoporosity into the structure and at lower Cu-loadings; the overall dodecahedral structure of ZIF-67 could be retained. The Co_9Cu_1@NC catalyst was investigated in detail, showing an overall first order reaction and the formation of a radical intermediate. Reactivity of the Co_9Cu_1@NC was stable after having been recycled once, and it showed good activity for the hydrosilylation of cyclohexanone and acetophenone.

Resumé

Katalysatorer spiller en vigtig rolle i den kemiske industri takket være deres evne til at øge udbyttet og renheden af produkter fra en given kemisk proces. Bekymringer med hensyn til bæredygtighed og klimapåvirkninger har skabt et øget ønske om at bevæge sig mod en grønnere kemisk industri. Ved at udvikle nye katalysatorer er det muligt at anvende mildere reaktionsbetingelser, producere færre affaldsprodukter og anvende ressourcer, som vi har rigeligt af i verden.

Denne tese gennemgår eksempler på projekter, hvor målet har været at forbedre holdbarheden, bæredygtigheden og aktiviteten af karbon-baseret katalysatorer, som kan anvendes i vigtige reaktioner. Det inkluderer dannelsen af myresyre, som kan anvendes som en flydende organisk hydrogen bærer. Myresyre kunne produceres ved brug af lave koncentrationer af en Ir kilde (0.00001 M $IrCl_3$) sammen med en porøs organisk polymer (bpy-PP-POP). Katalysatoren kunne også anvendes til at katalysere den modsatte reaktion, dehydrogenering af myresyre til hydrogen og CO_2, i et kontinuert setup, hvor den kunne producere ren hydrogen.

Dehydrogeringen af myresyre blev undersøgt i mere detaljeret grad ved brug af en serie nitrogen-dopede ordnede mesoporøse karbon katalysatorer. Nitrogen viste sig at kunne forbedre aktiviteten og selektiviteten af katalysatorerne i det vapor-baseret system, men nitrogen påvirkede ikke fordelingen af det aktive metal eller reaktionsmekanismen ifølge analyser udført med ME-PSD-DRIFTS. Pt på nitrogen-dopede ordnede mesoporøs karbon (Pt@NOMC) viste sig at være den bedste katalysator med en TOF på 870 h^{-1} og ingen produktion af CO.

I det sidste kapitel gennemgås et projekt om syntetisering af bimetalliske MOF-afledte karbon katalysatorer, som blev anvendt til hydrosilylering af ketoner. Katalysatorer med CoCu blev produceret ved at karbonisere ZIF-67 imprægneret med Cu-opløsninger for at skabe bimetalliske materialer med justerbare metal forhold. Karboniseringen introducerede mesoporer i strukturen og i materialerne med lavere Cu indhold kunne den oprindelige dodekaeder struktur fra ZIF-67 bevares. Co_9Cu_1@NC katalysatoren blev undersøgt i nærmere detaljer, og viste sig at følge en overordnede første ordens mekanisme under dannelse af et radikal intermediat. Reaktiviteten af Co_9Cu_1@NC var stabil efter at være blevet genanvendt en gang, og viste god aktivitet i hydrosilyleringen af cyklohexanon og acetophenon.

List of abbreviations

ADF	Annular dark field
BET	Brunauer-Emmett-Teller
BF	Bright field
bpy	bipyridine
CCS	Carbon capture and storage
CCU	Carbon capture and utilization
COF	Covalent organic framework
DRIFTS	Diffuse Reflectance Infrared Fourier Transform Spectroscopy
EDS	Energy dispersive x-ray spectroscopy
EDTA	Ethylenediaminetetraacetic acid
EELS	Electron energy loss spectroscopy
GC	Gas chromatography
GC-MS	Gas chromatography – mass spectroscopy
HAADF	High angle annular dark field
HCP	Hyper cross-linked polymer
ICDD	International center for diffraction data
ICP-OES	Inductively coupled plasma – optical emission spectroscopy
IUPAC	International Union of Pure and Applied Chemistry
LOHC	Liquid organic hydrogen carrier
ME-PSD-DRIFTS	Modular Excitation - Phase Sensitive Detection - DRIFTS
MOF	Metal organic framework
NMR	Nuclear magnetic resonance
NOMC	Nitrogen-doped ordered mesoporous carbon
OMC	Ordered mesoporous carbon
PAF	Porous aromatic framework
Phen	Phenanthroline
POP	Porous organic polymer
PP	Polyphenoline
SAXS	Small angle x-ray scattering
SEM	Scanning electron microscopy
STEM	Scanning transmission electron spectroscopy
TEM	Transmission electron microscopy
TEMPO	2,2,6,6-Tetramethyl-1-piperidinyloxy
TGA	Thermogravimetric analysis
TOF	Turn-over frequency
TON	Turn-over number
XPS	X-ray photoelectron spectroscopy
XRD	X-ray diffraction
XRF	X-ray flourescence
ZIF	Zeolitic imidazolate framework

Table of Contents

Chapter 1.   Importance of catalysts for industry and climate change

The purpose of this chapter is to give a brief introduction to the field of catalysis and its use in the chemical industry. The concept of green chemistry is introduced as it plays an important role in the development of future catalysts. The basic functionality of catalysts along with some key concepts and descriptors will be introduced, as these will be the key parameters in the later chapters. Catalysts can be separated into several groups, each with their own advantages and disadvantages, which will be covered briefly.

A catalyst is defined as any substance that participates in a chemical reaction and increases the reaction rate without being consumed in the process. More than 80% of all syntheses of industrial chemicals make use of a catalyst at some point in their production [1]. In addition, catalysts are immensely important for the cleaning of exhaust gases from factories and in the transport sector. The exhaust from the combustion of gasoline or diesel typically contain a significant amount of CO, NO_x and unburned hydrocarbons (C_nH_n). In a so-called three-way catalytic converter, the CO and hydrocarbons are oxidized to the far less environmentally harmful CO_2, while NO_x is reduced to N_2 to prevent the formation of acid rain [2].

Besides the obvious benefit of increasing the product formation rate, catalysts also have the potential to improve the selectivity of the reaction towards one of several possible products. In many cases, this allows industrial processes to produce less waste and run under milder conditions, limiting their strain on the climate. With the increasing concerns regarding climate change, the development of new catalysts for new greener alternatives to the burning of fossil fuels and the sustainable production of chemicals are in high demand. The transition is helped by the economic benefits to the industry, due to the decrease in operating costs whenever a decrease in energy demand, waste production or byproducts is possible.

The term "green chemistry" is often used to describe this trend towards more benign conditions for humans and the environment. The 12 principles of green chemistry as defined by Paul Anastas and John Warner in 1998, gives a quick overview of the challenges that should be taken into account during the development of sustainable production of green chemicals and energy [3]. A brief summary of green chemistry is to limit waste production, optimize energy and atom usage, while also moving towards using more benign reactants and reaction conditions. Considering the potential

12 Principles of green chemistry

1. Prevention
2. Atom economy
3. Less hazardous synthesis
4. Design benign chemicals
5. Benign solvent and auxiliaries
6. Design for energy efficiency
7. Use of renewable feedstocks
8. Reduce derivatives
9. Catalysis
10. Design for degradation
11. Real-time analysis for pollution prevention
12. Inherently benign chemistry for accident prevention

of catalysts, it is no surprise that it makes up one of those principles. Specifically, development of any process should attempt to replace stoichiometric reagents, which are consumed during the reaction and generate waste, with catalysts.

Utilization of hydrogen as an alternative fuel source is a classic example of green chemistry. Combustion of hydrogen comes with the benefit of producing harmless water rather than CO_2. Despite this, hydrogen faces the same issue as other upcoming technologies in having to deliver similar performance and reliability as current solutions. A great amount of research has gone into systems like hydrogen fuel cells, but current cost of materials and insufficient efficiency limit their widespread commercial use [4]–[6]. Additional considerations like transportation and storage remain challenging issues. Hydrogen itself is an explosive gas and requires high-pressurized or cryogenic containers, leading to safety concerns that also have to be addressed [7].

Another concept that has attracted the attention of researchers working with green and sustainable chemistry is the idea of closing the carbon cycle. By utilizing the carbon end products, mainly CO_2, rather than releasing it into the atmosphere, it removes the negative impact upon the climate. CO_2 utilization is made difficult by the high stability of the molecule, making it inactive for most reactions unless combined with a high-energy reagent (like hydrogen). Current CO_2 usage includes disposal (CCS), which mainly consist of enhanced oil recovery by injecting CO_2 into the reservoir to reduce the interfacial tension between oil and water, and to displace the oil. Secondly, there is carbon capture and utilization (CCU), which includes its use in beverages, food packaging, as additives to fuels and in chemical production [8]. Catalysts play an essential role in expanding the utilization of CO_2. They are needed to activate the inactive CO_2 and co-reactants to enable the production of higher-value chemicals. Ideally, the entire process should be balanced, so that the consumption of CO_2 exceeds its production. Potential products include formic acid, methanol, ethane, propene etc.

Due to the potential for catalysts of increasing product yield, lowering energy requirements and limiting byproducts, the development of catalysts holds tremendous potential. It is a key component of green and sustainable chemistry [9].

The focus of this project is to develop catalysts based on carbon materials for use in green processes. Utilizing the inherent advantages of carbon-based materials; the projects included in this thesis illustrate a number of challenges in the design of new catalysts and strategies for solving them. This includes the replacement of precious metals for abundant earth metals, increasing stability and activity by nanostructuring and doping of supports as well as the usage of single-atom catalysts to optimize metal usage. The targeted reactions include the production of complex chemical molecules (silyl ketones), selective decomposition to make hydrogen and the utilization of CO_2 to produce formic acid.

1.1.   Introduction to catalysis

A catalyst increases the rate of a chemical reaction without being consumed. Ideally, this means that an effective catalyst will produce more product in less time with no additional costs aside from the initial cost of the catalyst. Of course, in reality, catalysts have limitations and will eventually deactivate, providing less of an increase in reaction rate and potentially give more impure products. These advantages and limitation create a need for development of new catalysts or improving upon the design of catalysts currently in use.

The working principle behind a catalytic material is that it provides an alternative reaction pathway, which allows the reaction to occur more easily by requiring less energy. This can be illustrated by looking at the change to the activation energy of the reaction. For any reaction to occur, it is not enough for the right molecules to meet; it also requires them to have enough energy to undergo the reaction. This energy barrier is called the "activation energy" (E_a). A catalyst effectively lowers the activation energy of a reaction, allowing it to happen more easily thus increasing the rate of the reaction as illustrated in Figure 1.1.
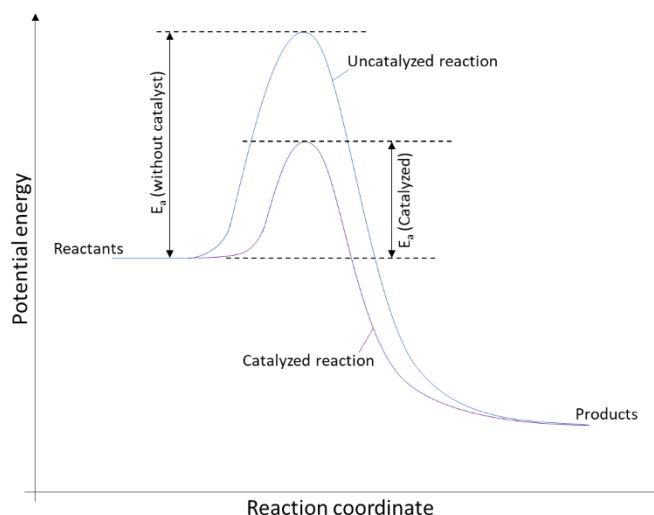
Figure 1.1: Schematic representation of an energy diagram with a catalyzed vs. an uncatalyzed reaction.

Typically, the alternative pathway consists of breaking down the reaction into several less energy demanding steps. In Figure 1.1 the catalyzed reaction is illustrated with a single reaction step. However, it could also have been several steps, each with a lower activation energy barrier than the uncatalyzed reaction.

A model reaction by Langmuir-Hinshelwood describes a typical example of a catalytic mechanism. The basic mechanism is illustrated in Figure 1.2. First, a reactant binds to the reactive site on a catalytic surface. The reactant can undergo reaction either with itself or with another reactant bonded to the surface. After the reaction, the product molecule desorbs and diffuses back into the reaction medium. Having the molecules on the same surface increases the likelihood that they can interact and undergo reaction. Being bonded to the surface can also weaken chemical bonds within the reactant molecules, making it easier for them to break the bonds and form new ones.
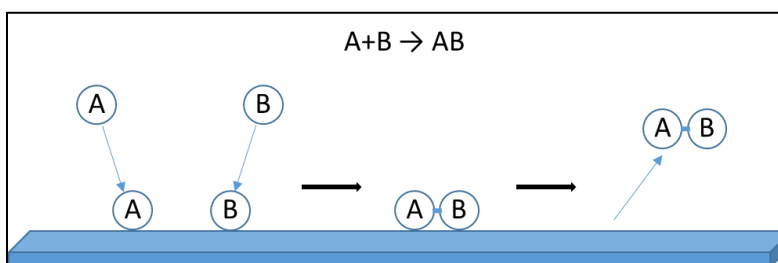
Figure 1.2: Surface reaction by the Langmuir-Hinshelwood mechanism.

It is not necessarily the whole surface, which is capable of binding reactants, allowing the reaction to occur. The reaction takes place the *active site*. Optimization of catalysts consists of maximizing the number of active sites, the number of reactions per time per site and their stability towards deactivation. If possible, the active site should also be designed to improving selectivity toward the desired product and optimizing the usage of the entire material, to create a more cost-effective catalyst.

It is important to note that the lowered activation energy does not affect thermodynamics or the equilibrium of the reaction. As illustrated back in Figure 1.1, the energy level of the starting reactant and the final products do not change in the presence of a catalyst. A classic example is the Haber-Bosch process that converts hydrogen and nitrogen into ammonia. Ammonia is a vital bulk chemical used for the production of fertilizers. From a thermodynamic viewpoint, the reaction is favorable even at room temperature. However, the reaction is extremely slow due to the high activation energy of the reaction, caused by the strong bonds found in N_2.

$$N_2 + 3H_2 \longrightarrow 2NH_3$$

The addition of an iron catalyst, high pressure and increased temperature are needed for this reaction to be industrially viable. The equilibrium is actually limited by the increased temperature, but without the addition of heat, the reaction still proceeds to slowly. This illustrates the contradiction sometimes found in catalytic processes. Lower temperature favors the formation of NH_3, but the reaction takes more time to occur, so the temperature is increased instead.

To get around the issues with the equilibrium, the resulting product, ammonia, is continuously removed. This allows for a new equilibrium to set in, generating more product. This method makes use of what is called Le Chatelier's principle, which states that any system will try to minimize changes made to it. As an example, consider a reaction of A and B react to make C and D.

$$A + B \longrightarrow C + D$$
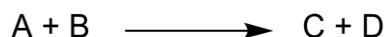
If more A is added, the system will convert more of it to C and D to minimize changes. Similarly, if C or D is removed from the system, more A and B will react to yield more product. A relevant example of this principle is the formation of formic acid from H_2 and CO_2. The reaction is conducted at high pressure (and temperature) to push the equilibrium towards formic acid. To minimize the impact of the increased pressure, it is preferable to convert two molecules into a single molecule [10].

1.2. Heterogeneous, Homogeneous and Biocatalysts

Catalysts can assume many forms, but are typically classified as heterogeneous, homogeneous or biocatalysts. Homogenous catalysts are in the same phase as the reactants, meaning that if the reacting molecules are liquids, the catalyst is a liquid as well. Heterogeneous catalysts are in a different phase from the reactants. In many cases, the catalyst is a solid material with reactants being in the liquid or gas phase. Finally, there are biocatalysts, which include enzymes or entire cells.

Homogeneous catalysts commonly consist of soluble molecular metal complexes, where the challenge is to find a combination of ligands and metals, which can selectively create the desired product while offering high stability and activity. Due to the limited amount of atoms present in the catalytic complex, it is possible to do computer modeling of the reaction. A combination of calculations based on

approximated solutions to the Schrödinger equation with supporting experimental results gives insight into the reaction mechanism. By understanding how the reaction occurs, it becomes possible to optimize the conditions and achieve higher activity and selectivity. This is often much harder to do for heterogeneous and biocatalysts, as they consist of significantly more atoms, making them difficult to model without a number of simplifying assumptions. Due to the tunable nature of the homogeneous complexes and better understanding of the reaction mechanisms, homogeneous catalysts tend to offer higher activity and selectivity than their heterogeneous counterparts. This is to be expected, as all the molecules of a homogenous catalyst are available for reaction, whereas only the surface atoms of heterogeneous catalysts can participate in a reaction.

Despite this, there is significant research towards replacing homogeneous with heterogeneous catalysts. This is due to the increased stability and ease of separation afforded by heterogeneous catalysts. It is far easier to isolate a solid material from a gas or liquid, compared to a catalyst in the same phase. This allows them to be more easily isolated and reused, limiting the cost of replacement. Biocatalysts have their own strengths, offering high selectivity towards transforming only specific groups or making only specific stereoisomers. They function under mild reaction conditions and are often considered green, since they usually function in aqueous media. However, their organic nature makes them very sensitive to higher temperatures and the pH value of the liquid. In addition, due to their complexity their use is usually limited to a few reactions and requires a long time to develop.

Heterogeneous catalysts are structured on many different scales to optimize their efficiency. At the cm scale, the catalyst takes the shape of pellets. The pellets are structured to allow for ease of transportation of large volumes to prevent diffusion limitations in the reactor. When going down to the μm scale, individual particles can be found. Many heterogeneous catalysts consist of a support material like silica or carbon, and an active material, typically a transition metal acting as the active sites. The role of the supporting material is to function as a stabilizing platform for the active component, typically metal atoms or particles. This includes chemical and thermal stability, making it more resistant to the reaction mixture and to higher temperatures, both of which can reduce the effectiveness and lifetime of a catalyst. To maximize the surface area available for the active material, the support is porous with the surface area predominantly inside the pores of the material. The pores and the active sites are on the nm scale, invisible to the human eye, but crucial to the activity of the total catalyst. In many industrial catalysts, the active sites are situated on small metal nanoparticles that ranges in size from less than one nm to tens of nanometers. It is possible to acquire images of the materials at this scale using high-resolution techniques as shown in Figure 1.3.

Pellets (cm)   Particles (µm)   Metal Nanoparticles (nm)
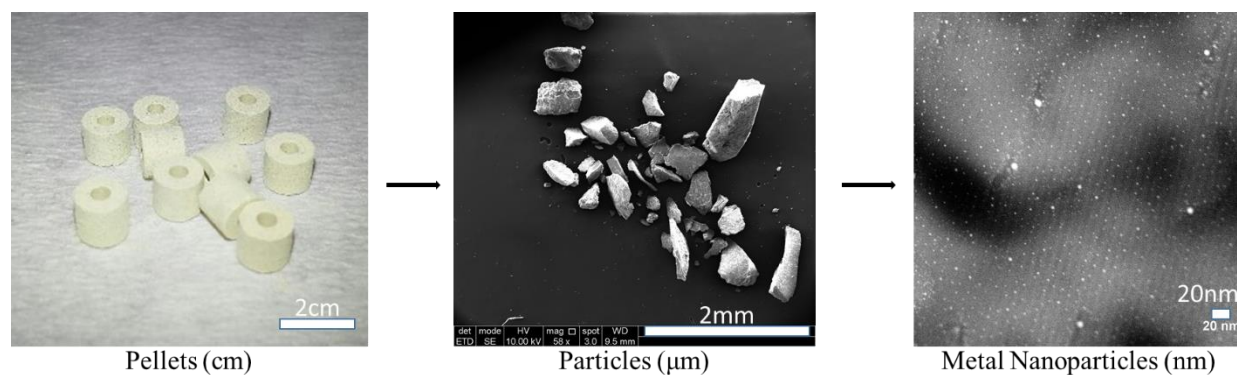
Figure 1.3: Example of a catalyst at different scales ranging from whole pellets (left) to porous particles (SEM image in the middle) and individual metal particles (STEM image to the right).

1.3.   Active sites and nanoparticles

The active site is the place where the reaction occurs; thus, it makes sense to design a catalyst to have as many as possible. In the case of nanoparticles, this can be done by decreasing their size. Smaller particles have a higher ratio of surface atoms, providing a larger number of active sites, compared to large particles where the majority are encased by other metal atoms. At the edge of the scale is single-atom catalyst, where each active site consists of only one atom per site. Creating and stabilizing single metal atoms is one of the goals of the bpy-POP catalysts, which will be covered in Chapter 5. For expensive and scarce metals like Pt, Pd, Ru and Ir, creating single-atom catalysts is an effective way to reduce costs and maximize metal utilization. Having low coordination can also provide some unique catalytic abilities, such as is the case for edge and corner atoms, which are directly bonded to fewer atoms than those found on the surface [11]. Compared to single-atoms, nanoparticles are easier to synthesize and stabilize.

Figure 1.4: Volcano plot illustrating Sabatier's principle, requiring a catalyst having an optimal binding strength to the reactant.

According to the Sabatier principle, the interaction between the active site and the reactant has to be neither too strong nor too weak. A weak interaction will mean that the reactant is likely to bind and undergo reaction, thus limiting the rate of reaction. If the interaction is too strong, the resulting product will be more difficult to remove from the active site, blocking access for the next reactant molecule. The principle 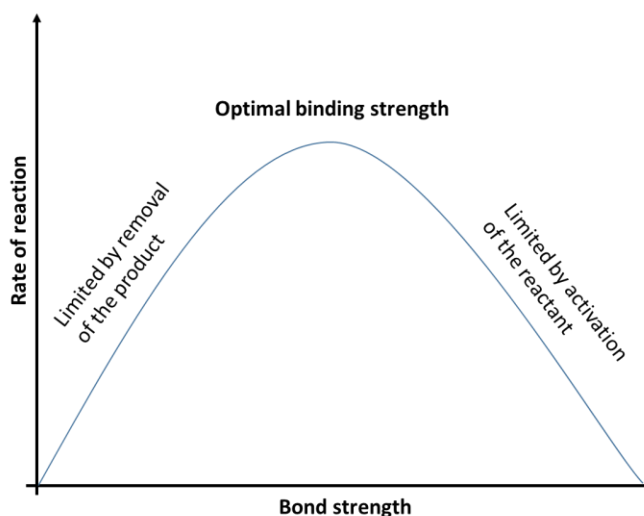is illustrated by a volcano plot seen in Figure 1.4. A useful property of the volcano plot is the ability to estimate the binding strength of an alloy between two metals. The alloy will have a binding strength in between that of its components [12], [13].

The surface of nanoparticles also presents a variety of different active sites, depending on the structure of the surface. Corners, edges and defects all provide different catalytic pockets for reactant molecules to bind. In some cases, the majority of the catalytic activity stems from only one kind of site [14], [15]. Figure 1.5 shows the variety of different surface sites found on any given particle. Since they are bonded to different amounts of atoms and have different degrees of spatial freedom, each of these active sites can be expected to have different activities in a given reaction [16].
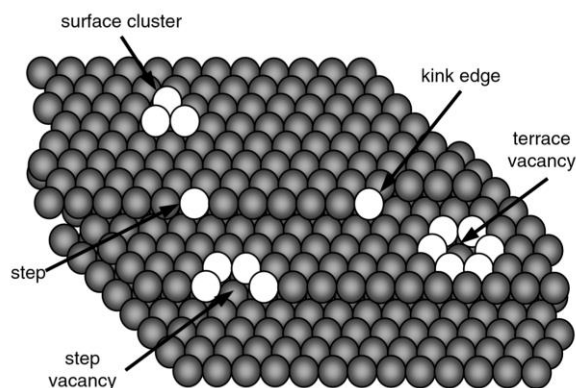
Figure 1.5: Illustration of different types of surface sites found on nanoparticles. Adapted from [16].

The atom binding to the reactant is not the only factor determining the reactivity of a catalyst. Through interaction with nearby atoms, internal molecular bonds may be weakened, making it easier for the reaction to occur. The immediate surroundings can also be designed to improve selectivity, either by only making space for certain reactants or by limiting the space for forming certain products [17]–[19]. Homogeneous catalysts are more well-defined and typically only have one kind of active site, making it easier to model, predict and investigate reaction mechanisms. Such is not the case for heterogeneous catalysts, where every defect and inconsistency in particle size and porosity can affect the nature of each active site. The observed reactivity of the heterogeneous catalyst is a combination of all the various active sites, with their different catalytic activities contributing to the overall reaction rate. This makes it much more difficult to model and predict reaction mechanisms of heterogeneous catalysts.

Activity can be quantified in a number of ways at any given reaction conditions. The most common way of comparing two catalysts in terms of reactivity is by their turnover frequency (TOF). TOF describes the number of reactions occurring at each active site per unit of time. It is common for a number of simplifying assumptions to be made, for the sake of calculating the TOF values. Typically, the TOF value is the average activity of each site, regardless of whether they are edge, corner or defect sites. The amount of active sites for nanoparticle containing catalysts are calculated either by assuming all metal atoms function as active sites (even if they are unreachable) or by calculating the number of surface

metal atoms based on the average particle size. The turnover number (TON) is another common metric used when evaluating the efficiency of a catalyst. TON is used in catalysis to denote the number of reactions an active site can catalyze before deactivation. It is also commonly used to denote the number of reactions per active site during a reaction under a defined set of parameters, even if the catalyst is not confirmed to be deactivated [20]. There will be significant differences between TON and TOF values, depending on how they are defined and calculated, and the method applied should always be specified for a given project.

1.4. Deactivation

Although catalysts are not consumed in the catalytic reaction, they do not have an infinite lifetime. Over time, the catalyst will lose efficiency due to deactivation of the active sites. This introduces additional cost and waste, as the catalyst has to either be replaced or reactivated. Deactivation can happen in several ways. These include poisoning, fouling, thermal degradation, vapor formation or attrition.

One of the most common deactivation mechanisms is the irreversible binding of an inactive specie. These are referred to as catalyst poisons and include common molecules like CO, H_2S, CN and phosphite. CO forms strong bonds to metals like Pd, thus blocking access to the atom and reducing the overall activity. The reduction in activity can be multifold as strong bonding of an atom may also change the geometry or electronic properties of the neighboring atoms [21]. This demonstrates the importance of using a feedstock similar to those found in the industry, when evaluating the performance of potential catalysts. Often the real feedstock will contain trace or substantial amounts of other components unrelated to the targeted reaction. This may include a catalytic poison, which the active material needs to be designed to resist. In some cases, industrial catalysts are deliberately poisoned to improve their selectivity. In steam-reforming S and Cu are added to the Ni catalysts to minimize formation of carbon. Initial activity is sacrificed for higher selectivity and increased long term stability [22].

Both single atoms and nanoparticles can also undergo deactivation by sintering. Sintering is an example of thermal deactivation and involves having smaller particles combine to form large ones. In a reaction medium or at elevated temperatures, the particles can migrate across the surface of the catalysts. The particles may coalesce upon coming into contact with other particles. The driving energy behind this process is the lowering of surface energy. Small nanoparticles are inherently unstable due to having a high ratio between surface and corner atoms, both of which are under-coordinated. By combining into large particles, the ratio of surface and corner atoms is lowered, thus making them more stable. Having less exposed atoms means less active sites, and a lowering of the overall activity. In addition, there are some cases where reactivity is lost upon an increase in particle size. This is the case for Au nanoparticles, where high activity and selectivity are seen for particles below 5 nm in size, but are almost completely inactive upon agglomerating [23]. Sintering can be limited by working at lower temperatures, to minimize the mobility of the particles on the support. Strengthening interaction with the supporting surface or encapsulating the particle can also be effective strategies.

Chapter 2.   Carbon-based support materials

Heterogeneous catalysis makes use of a large variety of solid materials as supports for the active component of the catalyst. The support plays a key role in stabilizing the active component to increase its lifespan. It can even increase the activity of the catalyst depending on its interaction with the active sites. Carbon is a highly versatile element, capable of forming a many useful supporting materials. The types of carbon materials covered here, only make up a small fraction of carbon-based support materials.

Carbon is the 6th chemical in the periodic table, the 15th most abundant chemical in the earth crusts and capable of forming four covalent bonds. The huge variety of functionalities and structural possibilities that arises from this simple property is evident from its role as the primary building block in all organic matter. Its structural properties allow it to form soft materials like graphite, two-dimensional materials like graphene and hard materials like diamond. Because of its versatility and availability, carbon has been used for a number of catalytic applications. This includes both hydrocarbon and polymeric materials.

Carbon materials has a number of distinct advantages that make them excellent for specific purposes. Pure carbon materials are relatively inert, limiting them from doing unwanted side reactions. Carbon inertness can be beneficial when an active phase requires reduction before use, which can sometimes prove problematic for conventional alumina supports [24]. Other useful properties include high thermal stability, mechanical resistance and high specific surface area. The physical and chemical properties of polymer supports can be modified by changing the identity of the monomers to include different functional groups during polymerization or through post-synthesis modification. It is easy to synthesize polymers with a wide variety of functional groups, such as carboxylic acids (-COOH), hydroxides (-COH), amines (-NH$_2$) and so on. These functional groups can affect the catalytic activity themselves or provide binding sites for metal atoms.

In this thesis, examples of carbon-based materials with designed porosity and nanostructure are covered and utilized for the projects in the later chapters (chapter 4-6). These include nitrogen-doped carbon structures, polymer based catalysts and MOF-derived materials.

2.1. Graphitic carbon support materials

Among the graphitic materials, the most widely used is called "activated carbon", a highly porous material that can be obtained by carbonizing organic material such as wood, coconut shells, coal ect. [25]. Carbonization involves heating the organic matter to 600-900 °C in an inert gas, typically N$_2$ or Ar [26]. The resulting structure consist of the well-known sp^2-hybridized carbon sheets from graphite illustrated in Figure 2.1. The specific surface area of activated carbon often exceed 1000 m^2/g [27].
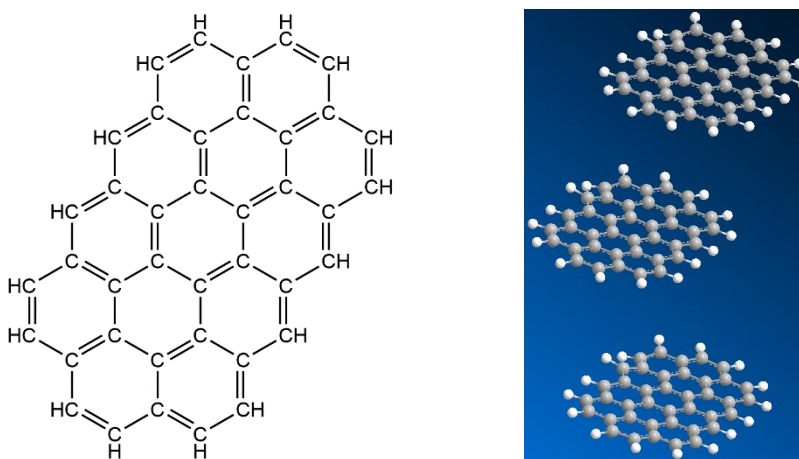
Figure 2.1: (Left) Single sheet of graphite (graphene). (Right) Several layers stacked to make graphite.

It is common to use commercially available catalysts of activated carbon with metal nanoparticles, often precious metals like Ru, Pd and Pt, for comparison in articles about catalytic materials [28], [29]. Applications include reduction of N_2O and NO [30], [31], hydrogen evolution reaction [32], [33] and oxygen reduction reaction [34]. Activated carbon is also used for adsorption of gasses. The material has a large quantity of micropores (less than 2 nm), which are ideal for gas adsorption and as a support for metal nanoparticles. Larger pores are also present and these help transport gasses and liquids through the materials to the micropores. As a catalytic support, activated carbon also benefits from its stability toward medium temperatures of about 500 °C and pressure [26]. Another important property is its ability to transfer electrons. The sheets of carbon are excellent at transferring electrons across the π-bonding system created by the many double bonds in the structure. These electrons can be transferred from the edges to metal nanoparticles deposited on the sheets or to a reactant in order to facilitate or increase the rate of reaction [35].

Metal-free carbon can be used as a catalyst. This includes materials like graphene and carbon nanotubes. Graphene consists of a single or few layers of graphite as shown in Figure 2.1. Graphene has been a subject of great interest since it was discovered by peeling off layers of graphite with tape. Graphene has higher mechanical strength than its graphite counterpart and increased electronic properties, making it useful for electrochemistry and as a heterogeneous catalyst [36]–[38]. Carbon nanotubes are a different kind of material made from layers of graphite rolled into hollow tubes. Both graphene and carbon nanotubes are flexible materials and can also be modified post-synthesis for fine-tuning of the electronic properties [39], [40].

2.1.1. Nitrogen-doped carbon

One of the methods for fine-tuning carbon materials is by replacing carbon with other atoms, heteroatoms, like nitrogen, boron, phosphor and sulfur. Nitrogen has one more electron than carbon and boron has one less, so adding them to the carbon network changes the electron density of the material. The resulting carbon materials are referred to as being "doped" with these atoms and have been shown to improve both activity and selectivity of both metal-free and metal-containing carbon catalysts [41]–[44].
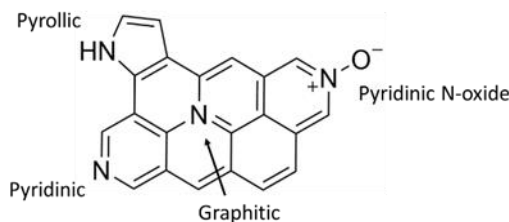
Figure 2.2: Four types of nitrogen-doping in carbon materials.

Nitrogen is a particularly common dopant in carbon-based heterogeneous catalysts. Four different types of nitrogen can be incorporated into the carbon network (shown in Figure 2.2). Graphitic nitrogen binds to three carbon atoms and becomes part of the carbon network, which maintains its planar structure. Pyridinic and Pyrrolic nitrogen both bind to two carbon atoms as part of a six- or five-membered rings respectively. They are located either at the edges of the sheets or by defects in the carbon network. Finally, there are pyridinic nitrogen-oxide species, which are an oxidized form of the pyridinic species. Using x-ray photoelectron spectroscopy (XPS), which will be covered in the next chapter, it is possible to distinguish between these species [40], [45]. All of the materials covered in the following chapters will be nitrogen containing hydrocarbon or polymeric materials.

2.1.2 Ordered Mesoporous Carbon

A study by Dongyuan Zhao et al. described a family of carbon materials with highly ordered mesopores synthesized via organic-organic self-assembly [46]. This group of materials were referred to as Ordered Mesoporous Carbon (OMC) as they share common methods of synthesis and some useful properties as support materials for heterogeneous catalysts. The most common way of synthesizing OMCs involve creating a polymeric structure in solution containing a surfactant. The surfactant can form micelles, which are imbedded into the generated polymer with regular spacing. Upon carbonization by heating the polymer in an inert atmosphere, the micelles are decomposed leaving a highly porous carbon framework. An example of the resulting structure is illustrated in Figure 2.3.
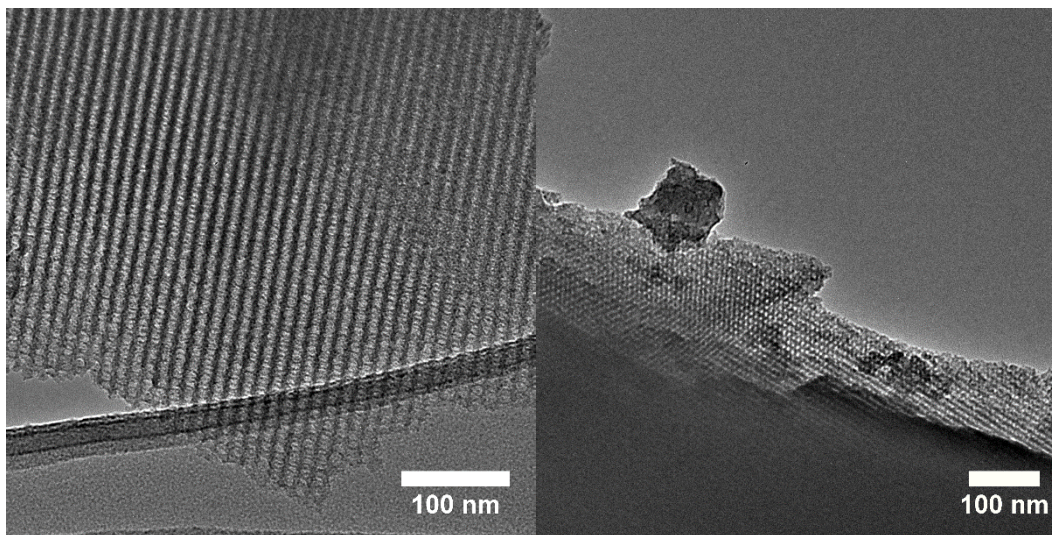

Figure 2.3: Ordered Mesoporous Carbon (OMC) synthesized from resorcinol and formaldehyde with F-127 as a surfactant. The resulting polymer was carbonized at 600 °C. The TEM images show the ordered pores from two different angles.

OMC materials can also be formed using a hard template approach. A porous carbon material is achieved by polymerizing around a porous inorganic framework such as a zeolite followed by carbonization [47]. Afterwards, the inorganic template can be dissolved leaving the carbon structure.

By using reactants containing heteroatoms such as sulfur, phosphor, boron or nitrogen it is possible to generate highly doped variants of OMC often named according to the heteroatom (e.g. NOMC being nitrogen-doped ordered mesoporous carbon). OMC materials without heteroatoms and boron variants have shown promise as supercapacitors [48], [49]. P and N containing OMCs have proved useful in the important oxygen reduction reaction [50], [51] and as support materials in heterogeneous catalysis [52]–[55]. The advantage of OMCs is their high surface area combined with the ease of creating varied structures by changing the polymerization reactants. A different way of changing the pore structure involves using a different surfactant or use a different carbonization temperature.

2.2.   Metal-Organic frameworks

Metal-organic frameworks (MOF) are a group of materials that, in the last two decades, have attracted a lot of attention for catalytic purposes [56], [57]. MOFs consist of networks of metal cations and organic linkers, making up three-dimensional organic structures with a high metal content. The organic linker has to be capable of binding two or more metal atoms. Since each metal ion can be coupled to several linkers, they build up a network of metal ions and organic linkers (Figure 2.4). MOFs tend to form three-dimensional structures, but various methods for preparing two-dimensional MOFs have also been developed [58].
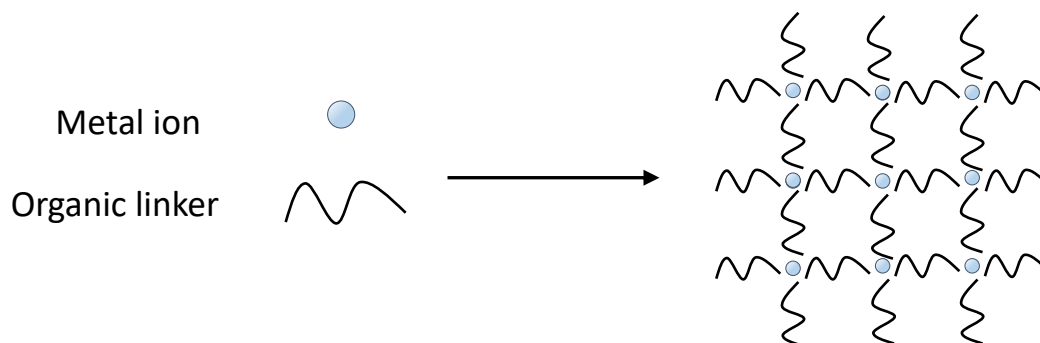
Figure 2.4: Simple illustration of a metal-organic framework made from one kind of metal ions and an organic linker with two binding sites.

Different kinds of MOFs have been discovered for almost all di-, tri- and tetravalent metal ions in the periodic table. MOFs have a micro-/mesoporous structure, a desirable trait for catalytic materials, and may have binding sites available at the metal ions not occupied by the organic linker. These sites allow MOFs to act as Lewis acid catalysts, but can also be used as anchor points for modification. For example, amino groups can be anchored on the organic ligand to make basic catalytic sites [59]. MOFs can also be used for support materials for metal nanoparticles, which can be encapsulated in the micropores or as part of the network structure. This may prevent them from leaching into the solution or from agglomerating into larger particles, limiting the amount of active sites.

The crystalline nature and microporous structure of MOFs are often compared to that of zeolites. Zeolites are a class of microporous crystalline minerals made from aluminosilicate used for a variety of catalytic processes in the industry [60]. Just like zeolites, MOFs have uniform micropores and high

internal surface areas. The advantage of MOFs is the ability to easily make changes to the framework structure and chemical functionality by changing the groups on the organic linker. MOFs have been demonstrated as being useful for several processes including gas separation, sensors and as heterogeneous catalysts [61].

Despite the potential of MOFs, their use is impaired by a limited chemical and thermal stability compared to other catalytic materials such as zeolites and carbon. There are a few examples of MOFs being thermally stable up to 500 °C, but this is still less compared to most carbon and zeolite materials. Another issue is the MOF structure often breaking down upon the removal of the solvent, making them more difficult to isolate and store [57]. A series of MOF-based catalysts will be used in Chapter 6, based on the cobalt containing ZIF-67, which is illustrated in Figure 2.5.

2.2.1. MOF derived carbon materials

A method of improving the thermal and chemical stability of catalysts based on MOFs is to carbonize them i.e. heating them to 600-900 °C in an inert atmosphere. When MOFs are subjected to carbonization, they retain much of their porous characteristics, while increasing their stability. The organic linkers will become more graphitic in nature and lose their functional groups. The resulting material is often termed as MOF-derived carbon [62]. The metal ions that helped make up the network structure will aggregate to metal nanoparticles, effectively encapsulating them in the newly formed material. This approach has demonstrated to be capable of forming nanoporous catalysts with well-dispersed nanoparticles [63]. It can also be used to form bi-metallic nanoparticles [64] and to introduce a controllable amount of nitrogen content [65].
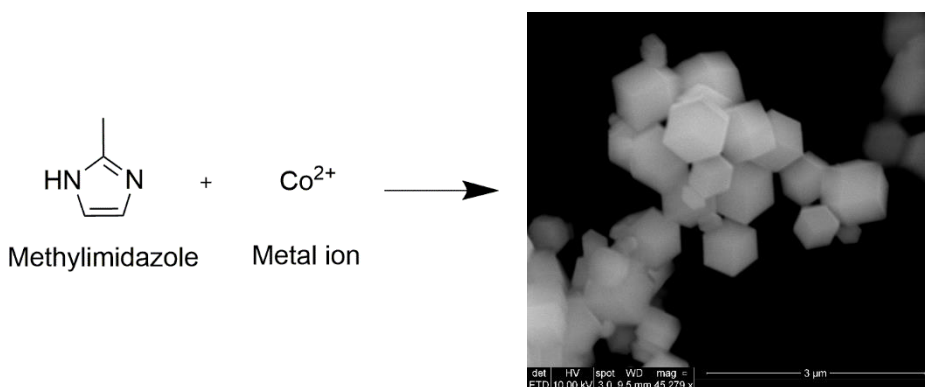
Figure 2.5: Example of a ZIF material made from methylimidazole and Co. The resulting crystals are termed ZIF-67.

A sub-group of MOFs known as zeolitic imidazolate frameworks (ZIFs) is a commonly used starting material for making MOF-derived carbon materials [65]–[67]. This is due to the nitrogen groups of imidazole giving the resulting catalyst a high-nitrogen content. As the name suggests, ZIFs have structures very similar to that of zeolites. This is due to the angle between the nitrogen atoms of imidazole being close to 145°, which is the same as the Si-O-Si angle found in zeolites [68].

2.3. Polymers

Polymers are defined by IUPAC as materials composed of macromolecules ranging in size from a few hundred thousand to millions grams/mole [69]. Polymers are large molecules build up from repeated units connected by a chain reaction. Their utility includes usage as packaging, semiconductors, construction materials, membranes and, more importantly in this case, as catalytic materials. Because of the seemingly endless variety of possible polymer structures, it is possible to tailor a polymer to fit the desired reaction conditions. Pure polymer materials have found use in reactions like ester hydrolysis, and reactions requiring acidic or basic groups. Examples of the active groups include pyridine (basic) and sulfonate (acidic) groups [70].
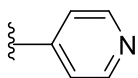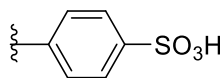
Pyridine group   Sulfonate group

The more common strategy for using polymers in catalysis, is to use the build in functional groups as binding sites for active metals or ligands, acting more as support materials rather than active materials. Cross-linked polymers are often used as support materials in catalysis, due to having lower solubility making them easier to isolate and reuse [71]. Linear polymers can also be utilized, but are more easily soluble, and usually require a precipitation step to collect the polymer before being reused. Due to the ease of modification of these materials, it is also possible to design the catalytic pocket, the site and surroundings where the reaction takes place. Doing so makes it possible to mimic the ability of enzymes, which often owe their high reactivity and selectivity to their catalytic pockets having been subjected to optimization throughout the evolutionary process.

2.3.1. Heterogenizing homogeneous catalysts

The incorporation of ligands into a polymer structure represent an exciting opportunity for combining the high activity and selectivity of homogeneous catalysts with the stability and ease of separation of heterogeneous catalysts. In principle, it would be possible to preserve the nature of the active site, provided that the surrounding polymer does not block access or affect the binding energies of the reaction through electron donation or withdrawal.

Aside from the benefit of mimicking the reactivity of homogeneous catalysts, heterogenized homogeneous catalysts generally only need one metal atom per active site. Strong binding to the ligands helps to prevent the common deactivation mechanisms of particle agglomeration and leaching into solution. The aim is to combine the high activity and selectivity of homogeneous catalyst, with the stability and ease of separation of heterogeneous catalysts.

This concept holds significant promise in the field of asymmetric synthesis, where the goal is to obtain only one out of potentially several stereoisomeric products. Stereoisomers are compounds that possess the same bonds, but have different three-dimensional structures. The most common example is two compounds that are each other's mirror image (also known as enantiomers). Creating catalysts capable of selectively catalyzing only one of several compounds is difficult to do with heterogeneous catalysts, and often requires homogeneous catalysts with chiral ligands to perform [72]. By immobilizing the chiral ligands on a polymer backbone, it is possible to make highly selective heterogeneous catalysts [73].

2.3.2. Porous Organic Polymers (POPs)

Porous organic polymers (POP) is a broad term used to describe materials containing a network of covalently bonded organic building blocks [74], [75]. POPs can be either crystalline or amorphous depending on the degree of order in their structure. Examples of amorphous POPs include hyper-cross linked polymers (HCPs) and porous aromatic frameworks (PAFs). Common features for POPs are large pore sizes, high surface area and good stability in various solvents.

By using ligands from homogeneous catalysts as building blocks for the POPs, the binding sites become an intrinsic part of the structure. An example is shown in Figure 2.6, the central structure made from four five-membered rings is called porphyrin and is a ligand capable of binding a metal-ion in the central cavity [76]. POPs may also be built using more than one building block to change pore-size or increase cross-linking.
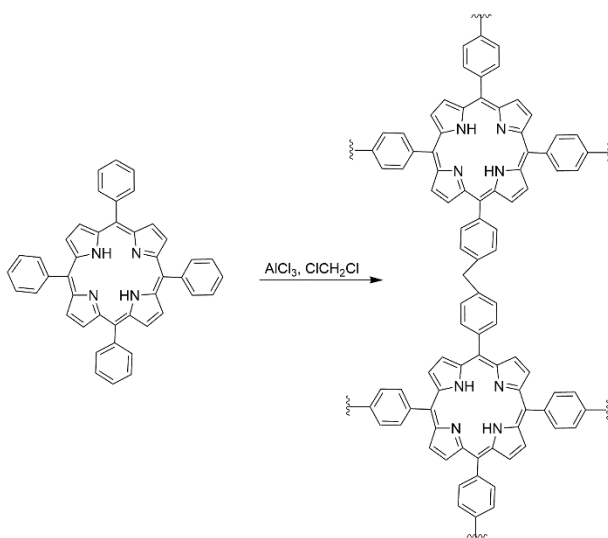
Figure 2.6: Example of a POP made from polymerization of a ligand [74].

Despite the simplicity of the concept, there are still differences in activity and catalytic species between the heterogeneous POPs and their homogeneous analogous. Homogeneous catalysts may go into a resting state, where the metal ion has additional ligands bonded to it. This is not possible in POPs due to the limited mobility of the ligands. POPs are still a relatively new class of materials for heterogeneous catalysis, and the reaction/deactivation mechanisms are still in need of further study. A POP based on polyphenylene will be used in Chapter 5 for the hydrogenation of CO_2. A bipyridine ligand is built into the structure to act as a binding site for Ir.

2.3.3 Covalent Organic Frameworks

Covalent organic frameworks (COFs) are a type of crystalline POPs with highly ordered structures. Both micro- and mesoporous structures of COFs can be synthesized. This combination of structural regularity, tunable pores size combined with a high surface area have made COFs an interesting candidate as a support material for heterogeneous catalysts [77]–[79]. An example of a simple COF (COF-1) is obtained upon condensation of benzene-1,4-diboronic acid at 120 °C for 72 hours forming a 2D hexagonal structure as shown in figure 2.7.
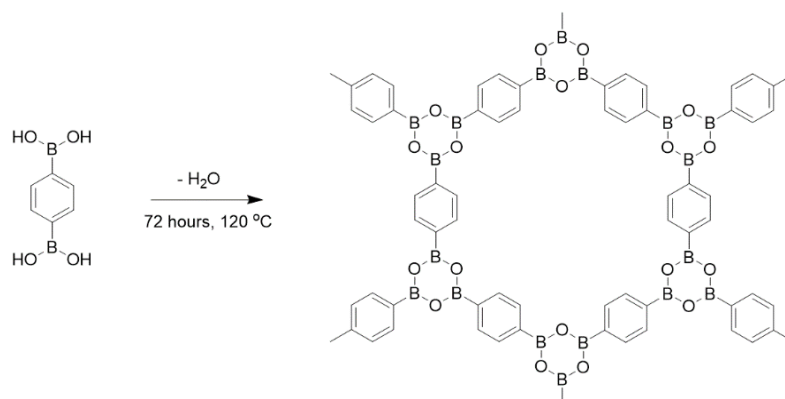
Figure 2.7: Synthesis scheme for COF-1 made from condensation of benzene-1,4-diboronic acid. Recreated from [77].

COF materials have shown potential as photo-catalysts and electro-catalysts owing to their resistance to harsh reaction conditions, which allows them to be used in green applications such as Li-ion batteries and solar cells [80]. In a study by M. Makee et al., a COF structure was created, which contained nitrogen ligands able to stabilize single-site Ni species. The Ni-COF showed activity comparable to a homogeneous reference catalyst in the oligomerization of ethylene [81], [82]. These examples highlight the potential of COF materials, which are still a relatively new addition to the catalogue of polymer support materials.

Chapter 3.   Methods of Characterization

Catalysts are often structured at the nanoscale making it impossible to see with the naked eye or even through an optical microscope. In order to know the structure and properties of the synthesized catalysts, a series of highly advanced techniques are utilized. These include techniques specifically designed for characterizing the surface of materials, some for visualization of nanoparticles, atoms and nanostructures, some for physical properties and some for compositional information. This chapter is meant to introduce the main methods used for all the covered projects, responsible for key information needed draw conclusions. It is by no means a comprehensive list of techniques utilized in the field of catalysis and does not cover all the techniques used as part of this thesis.

3.1.   X-ray photoelectron spectroscopy

Reactions in Heterogeneous catalysis using solid materials occur on the surface. Therefore, several analytical techniques exist, which specifically give information about surface properties [83]. X-ray Photoelectron Spectroscopy (XPS) is among the most widely used techniques. The techniques makes use of the electrons limited ability to penetrate materials depending on their kinetic energy. A sample is exposed to a beam of X-rays typically generated from an Al Kα (1486.6 eV) or Mg Kα (1253.6 eV) source. If the X-ray is adsorbed by an atom or molecule, an electron can be ejected. The kinetic energy of the electron depends on the energy of the adsorbed photon and the binding energy of the electron (1).

$$E_K = h\nu - E_B \qquad\qquad (1)$$

The ejected electrons, known as photoelectrons, can be generated throughout the entire sample, as X-rays can easily penetrate thick samples. However, the photoelectrons can only escape from the surface layers of the sample (<10 nm) without colliding with other atoms or molecules thereby losing their information about the sample. This distance is called the inelastic mean free path and can be illustrated as a function of the kinetic energy (**Error! Reference source not found.**)
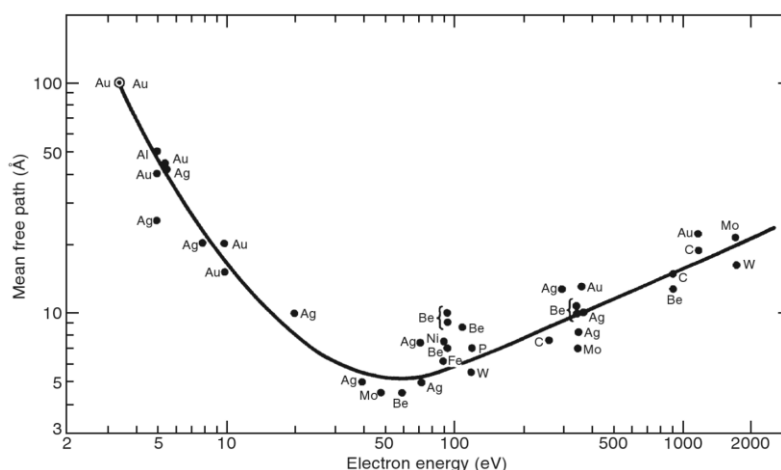

Figure 3.1: The universal curve showing the relationship between the kinetic energy of an electron and its mean free path. It is important to notice that the depth of penetration can be limited to a few layers, if the electrons have between 20-1000 eV [84].

The detector measures the kinetic energy of the ejected photoelectrons, which allows for the binding energy to be calculated. Due to the binding energies of electrons being well-defined, it is possible to identify the element and the orbital to which the electron belongs. It is even possible to get information on the oxidation state and nearby atoms based on the number of peaks and their specific binding energies. The magnitude of these *chemical shifts* is only a few electron volts. In addition, the signal intensity will depend on the concentration (and sensitivity factor) of each elements, allowing XPS to be used to determine the composition of the surface.

3.2.   X-ray diffraction

X-ray diffraction (XRD) is one of the most common techniques for material characterization. A sample is exposed to a beam of x-rays, which will be diffracted at specific angles upon interacting with lattice planes in the sample. The diffracted x-rays will undergo constructive interference at specific angles, depending on the spacing of the atoms within the planes. These can be used as a fingerprint of crystalline materials, allowing for easy identification when compared to a database. The carbon materials used for the projects included in this thesis are typically amorphous, thus not giving rise to characteristic peaks in XRD. The method can however still be used for the metal nanoparticles supported on these materials. It should be noted that due to their small size, surface effects and changes in electronic properties are known to have some interesting effects called quantum size effects [85].

3.3.   Nitrogen physisorption

Nitrogen physisorption is the most common method for determining the surface area of heterogeneous catalysts. This includes both the external surface area of the particles, together with the exposed surface found within the porous structure of most materials. In a typical procedure, a known amount of solid material is put under vacuum. Then an inert gas (usually N_2, Ar or Kr) is added in small quantities and the relative pressure is measured. On this basis, the amount of inert gas adsorbed on the surface is known and based on the surface area occupied by each adsorbed molecule or atom, the total surface area of the material can be calculated when a single monolayer of adsorbents has been formed. In reality, the process is more complex, as the gas tends to form multilayers (gas molecules stacked on top of one another) as more gas is added. To account for this, researchers typically use the Brunauer-Emmett-Teller (BET) equation to calculate the specific surface area, sometimes termed the BET area.

$$\frac{p}{n^a \cdot (p^O - p)} = \frac{1}{n_m^a} + \frac{(C-1)}{n_m^a \cdot C} \cdot \frac{p}{p^O}$$

The data is presented as an adsorption isotherm showing the amount of gas adsorbed as a function of the relative pressure. The shape of the isotherm has characteristic features, depending on the pore structure and the strength of interaction with the inert gas. In 1985, IUPAC classified the types of isotherms into 6 categories shown below in Figure 3. [86].
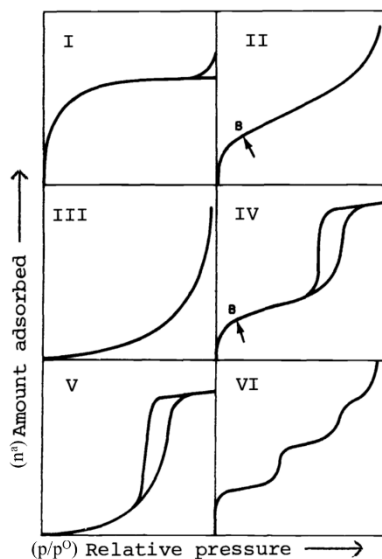
Figure 3.2: Different types of isotherms according to IUPACs definition. Adapted from [86].

Type I is found for microporous materials with relatively small external surface area, such as activated carbon. Pore size ranges from less than 2.5 nm to less than 1 nm. Type II is seen for nonporous or macro-porous materials. Its shape stems from the unrestricted adsorption of mono- and multilayers. Type III materials have no clear point of monolayer coverage, as the weak interactions between gases and surface causes the gas molecules to form clusters around the most favorable sites. Type IV is common for mesoporous structures and consists of formation of a monolayer on the external surface and mesopores, followed by pore condensation in the mesopores. The pore condensation gives rise to a hysteresis loop, due to the multilayers in the pores forming metastable structures. The hysteresis loop can also be classified into six different types, depending on the shape and uniformity of the pores. Type V is similar to type III, due to low interaction between surface and gas molecules, followed by pore filling. It is commonly observed for water adsorption on hydrophobic materials with micro- and mesopores. Type VI is observed for highly uniform surfaces. The step-by-step increase in adsorption represents the formation of individual layers of gas molecules.

3.4.   Infrared spectroscopy

Light in the infrared region is used in several analytical techniques used in chemistry. It includes all photons with wavenumbers between 10-14000 cm^{-1} (700 nm to 1 millimeter). In the range of a few hundred cm^{-1} to about 4000 cm^{-1}, the energy of the photons matches the energy needed to excite chemical bonds. The bonds are only capable of absorbing photons with the correct amount of energy to bring it to a specific excited state, due to the quantized nature of the energy levels at this scale. By irradiating a sample with a range of infrared light and detecting the reflected light, a spectrum is obtained, where light absorbed by the sample is missing, thus giving information as to what kind of chemical bonds the sample contains. Diffuse-Reflectance Infrared Fourier Transformed Spectroscopy (DRIFTS) is a technique for analyzing powdered samples. The infrared light scattered in all direction from the powdered sample is collected and focused by either an ellipsoidal or parabolic mirror. A more specialized IR technique called Modular Excitation Phase Sensitive Detection Diffuse-Reflectance Infrared Fourier Transformed Spectroscopy (ME-PSD-DRIFTS) is utilized in chapter 5.

3.4.1 ME-PSD-DRIFTS

Contributions to the infrared spectrum include background, baseline shift, noise and surface signals. The intermediate species generated during a reaction give low signals, which makes them difficult to isolate and detect. ME-PSD-DRIFTS uses a periodic change in the concentration of reactant over the catalyst. The system switches between an On/Off state, with either an inert gas or a mixture of the inert gas with vaporized reactant being passed over the catalyst (Modulation Excitation). The concentration of reactant, product and intermediate species in the system can be expressed using sinusoidal curves matching the modulation frequency. Using Fourier transformation to convert the data into the phase domain allows for these sinusoidal responses (Phase Sensitive Detection). When converted back into the time domain, the resulting data has been cleared of the transient changes, and is expected to enhance the signals of reaction intermediates. The concentration of the reactant added to the system has to be kept low in order to ensure that the system reaches a quasi-steady state. The change is illustrated in Figure 3.3.
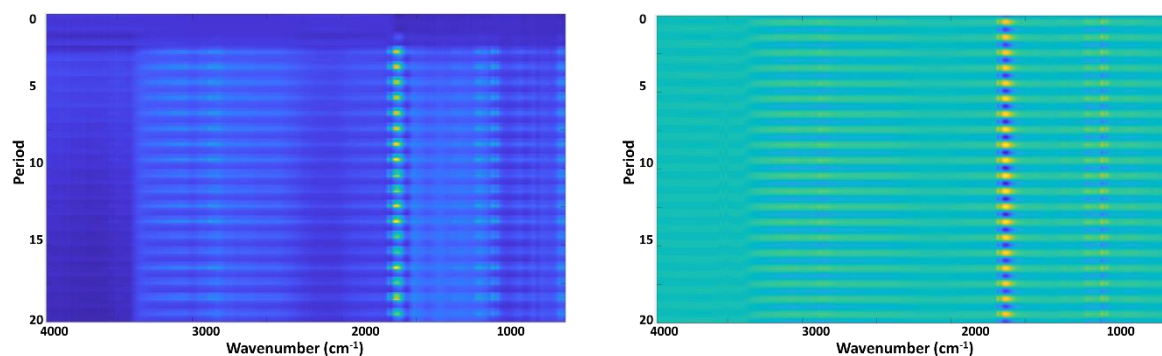
Figure 3.3: (Left) 20 periods from a ME-PSD-DRIFTS experiment before Fourier transformation. (Right) After removal of signals which do not match the periodic frequency.

3.5. Electron microscopy

Modern catalysis design involves nanoscale structures invisible to the naked eye, below the resolution of visible light. It is possible to visualize samples at this scale using electrons instead. Due to the particle/wave dual behavior of electrons, it is theoretically possible to achieve a resolution down to about 2 pm ($1 \cdot 10^{-9}$mm). The resolution is defined as the minimum distance that can be separated as two distinguishable points. In practice however, the resolution of electron microscopes are limited by the lenses used to shape the beam, making the actual resolution of a modern instrument about 0.1 nm. With this kind of resolution, it is still possible to observe individual atoms. A schematic representation of an electron microscope can be seen in 3.4. Two different modes of operation are illustrated here, Scanning Transmission Electron Microscopy (STEM) and Transmission Electron Microscopy (TEM). The electron source is either a thermionic source (LaB_6, CeB_6 or tungsten), which generates electrons by heating the source like a lightbulb. An anode is used to focus the electrons into the column. Alternatively, a field emission gun is used, where a strong electrostatic field is used to extract electrons from a tungsten tip. These have higher resolution and current, but are also more costly. In order to have an electron beam, the system has to be under high or ultra-high vacuum, otherwise the electrons would be scattered or absorbed by any gas present. The microscope column itself consist of a system of

electromagnetic lenses used to shape and focus the beam before and after interacting with the sample. After each lens is an aperture used to absorb electron scattered at too high angles.
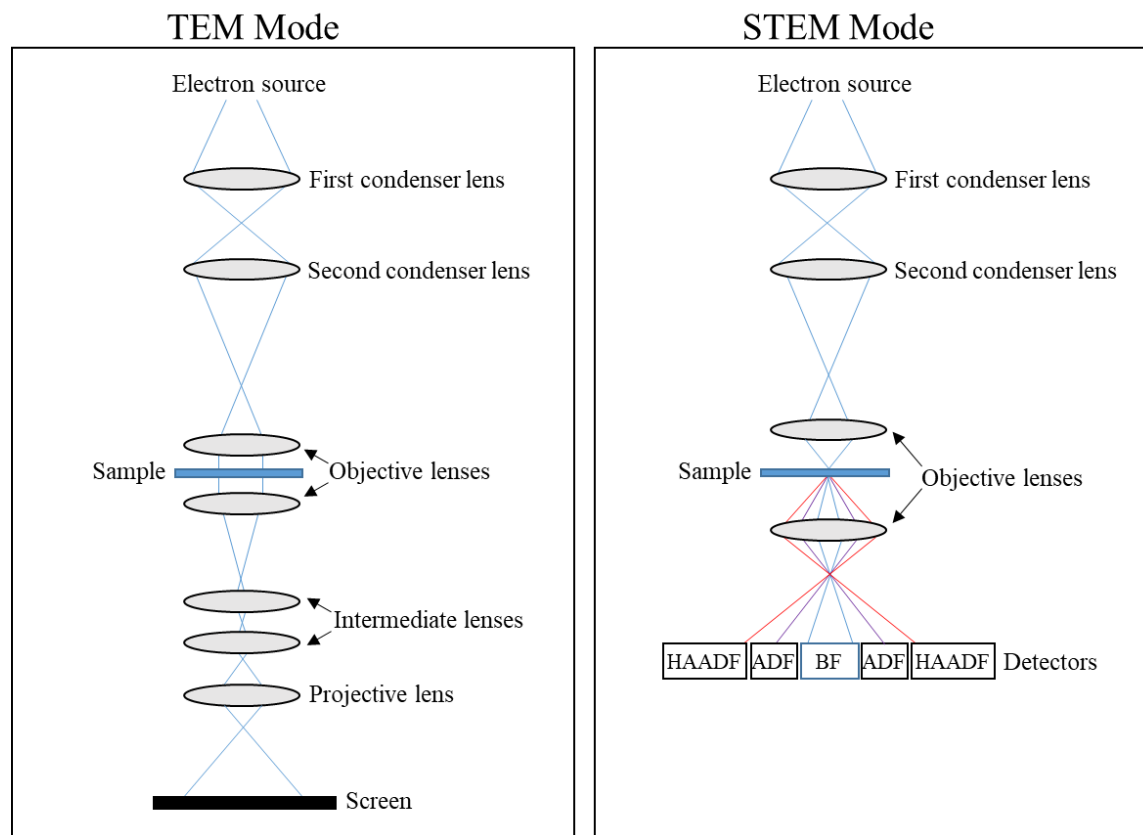
Figure 3.4: Schematic illustration of an electron microscope in TEM mode (Left) and STEM mode (Right). TEM forms the image using transmitted electron from a planar beam hitting the sample. STEM uses a focused beam on the sample and form the image using scattered (ADF/HAADF) or unscattered electrons (BF).

Both methods use transmitted electrons for generating an image. Transmitted electrons pertains to all electrons, which have passed through the sample. In order to have enough electron for an image, the sample has to be thin (preferably less than 100 nm). The images themselves are two-dimensional representation of the sample, where contrast is achieved by a difference in thickness and density. Thicker samples allow less electrons to pass through, while heavy elements are denser and thus scatter electrons more easily.

3.5.1. Transmission electron microscope

In TEM, the electron beam is shaped to form a parallel beam illuminating an area of the sample depending on the magnification. An example can be seen in Figure 3.. The image shows a carbon support with Pd nanoparticles dispersed on it. The carbon is a light element and appear as shades of grey, depending on the thickness, whereas the Pd nanoparticles are far heavier and scatters the electron beam easier, giving them a black color. It is worth noting, that the images from the electron microscope gives a 2D image if the sample. This can make it difficult to evaluate the position of each individual particle. It is possible to tilt the sample, and even record a series of images at varying tilt to generate a 3D structure of the object in focus.

Figure 3.5: (Left) TEM image of Pd on a carbon support. (Right) STEM image of Pt on a carbon support. Notice that heavier elements appear dark in TEM and bright in the HAADF image from STEM.

3.5.2. Scanning transmission electron microscope
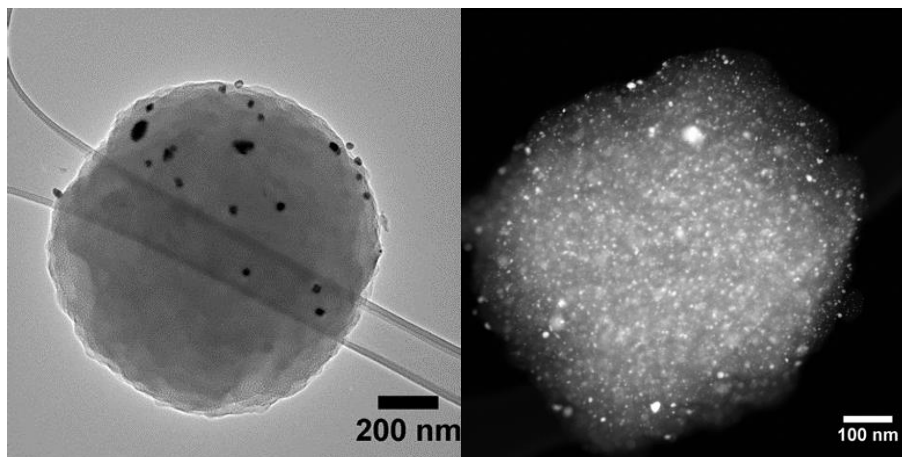
In STEM, the beam is focused into a probe, which scans across an area of the sample. Unlike TEM, which generates the whole image at once, STEM generates the image point by point. The electrons are sorted depending on how much they are scattered at each point in the sample. A Bright-Field (BF) detector uses low angle and unscattered electrons for the image, creating contrast in the same manner as in TEM. Annular Dark Field (ADF) and High Angle Annular (HAADF) use the electrons scattered at high angles, which primarily includes those that have interacted with heavy elements. In ADF and HAADF images, the contrast is inverse, with the denser and heavier part of the sample appearing bright as seen in Figure 3.. STEM offers higher resolution than TEM, due to a lack of chromatic aberration and not needing additional lenses for forming the image. The resolution of a STEM is instead linked to the probe size on the sample. Probe alignment of the setup is required in order to achieve atomic resolution.

3.5.3. Additional methods for characterization

The electron beam creates more than just a beam of transmitted electrons when hitting the sample. A brief overview of some of the signals created by the illumination by the electron beam is shown in Figure 3.6. The high-energy electrons from the beam can knock out core electrons from atoms (secondary electrons). The excited atoms may relax either by emitting a so-called Auger electron or by emitting an x-ray. The energy of both of these carry information as to what atom they originate. Energy Dispersive X-ray Spectroscopy (EDS) targets the x-rays and use them to analyze the composition of the illuminated sample. In TEM mode the methods gives the composition of an area, while in STEM it is possible to map out the distribution of elements on the targeted area. The method works best for heavier elements and requires the sample to be stable in the beam for an extended period of time.
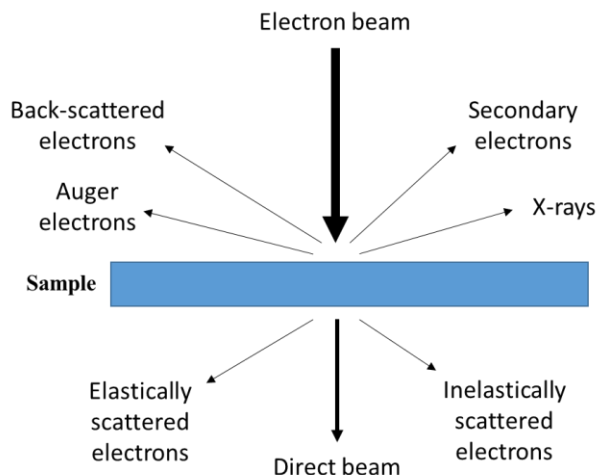
Figure 3.6: Upon hitting the sample, the electron beam generates many different sources of information. The scattered electrons and the direct beam are used for imaging.

Secondary electrons and back-scattered electron can be used for imaging just like the transmitted electron. These images can reveal information about the topography of the sample and can be used even if the sample is not electron transparent. This includes bulk or particularly dense materials. Electron Energy Loss Spectroscopy (EELS) separates the electrons depending on their loss of energy during their interaction with the sample (inelastically scattered electrons). The resulting spectrum can be used to identify the source of these losses, whether it is from plasmon excitation, phonon excitation or core-loss peak, similar to those seen in EDS. The technique requires very thin samples, but can provide information about all elements of the periodic table (except hydrogen) unlike EDS, where many of the elements have overlapping peaks. Since electrons also exhibit wave-like behavior, they can be used for diffraction. Upon interaction with crystal planes, electrons that fulfill Bragg's law will be diffracted like in XRD. All electrons reflected by the same set of planes will end up at same points in what is known as the diffraction plane. Examining the diffraction pattern can give information on the crystal structure and used for identification. The observed pattern will depend the orientation between each crystal plan relative to the electron source. An example of such a pattern is shown in Figure 3.7.

Figure 3.7: Diffraction pattern of a zeolite. Each spot corresponds to a series of parallel planes.

3.6.   Scanning electron microscopy

Scanning electron microscopy (SEM) is very similar to TEM and STEM. The instrument uses an electron beam with a lower accelerating voltage, around 1-30 kV, to generate secondary and backscattered electrons. Secondary 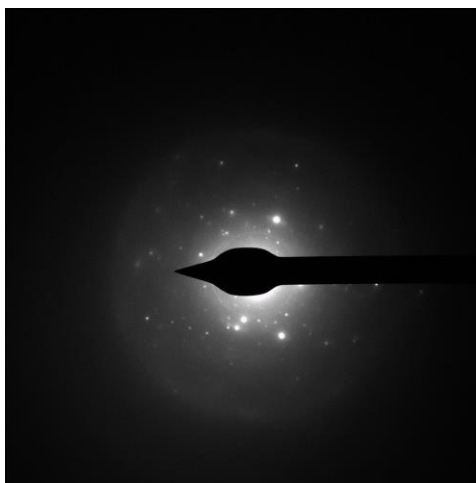electrons have low energy and come from the surface of the sample. Secondary electrons generated deeper into the sample are quickly absorbed by the sample again. They can be used to obtain topographical images of a sample, as brightness depends on the angle of which the electrons are hitting the sample. The resolution is lower compared to that of TEM and STEM, but it is still possible to reach resolution at the nanometer level. The backscattered electrons generated by the electron beam also contains information. Backscattered electrons have higher energy and can thus escape from the deeper regions of the sample. Heavier elements can scatter electrons more easily, generating more backscattered electrons and thus a higher signal. This can be used to get information on compositional differences within a sample.

3.7.   Inductively coupled plasma optical emission spectroscopy

Inductively Coupled Plasma Optical Emission Spectroscopy (ICP-OES) is a useful technique for detecting trace amounts of metals both qualitatively and quantitatively. It can be used to detect elements from most of the periodic table, and can quantify amounts from milligrams to nanograms. It uses an inductively heated gas (Argon) to form a high-temperature plasma. When the sample of interest is passed through the plasma, it is atomized and ionized. The high temperature causes the atomized sample to give off radiation. The light emitted is characteristic for each element and based on their intensity, the relative concentration of each element can be determined. XPS introduced in the beginning of this chapter only gave the composition of the surface, whereas ICP-OES can be used for compositional analysis of the bulk sample. In the presented projects, the technique is used for determining the metal loading of catalytic samples and to examine reaction mixtures for trace amounts of metals, which might have leached out of the catalysts during reaction.

Chapter 4.   Formic Acid Dehydrogenation

The use of formic acid as a Liquid Organic Hydrogen Carrier (LOHC) requires a highly selective catalyst to release pure H_2 under mild reaction conditions. In this project, I mainly focused on the use of Ordered Mesoporous Carbon materials (OMCs) with different metals, metal loadings and reaction conditions. The reaction was done on a continuous flow setup to provide a steady formation of H_2. The role of the nitrogen content was examined in details and compared with a nitrogen-free carbon support. Its influence on dispersion, activity and mechanism was analyzed using electron microscopy, XPS, and diffuse reflectance infrared Fourier transformed spectroscopy (DRIFTS).

As mentioned previously, hydrogen is a promising alternative to fossil fuels and continued work into making it commercially viable has been ongoing for over a decade now. It has a high energy density, almost three times that of gasoline and is considered a clean and renewable source of energy. However, one of the challenges yet to be resolved concerning its widespread use is the ability to transport and store large quantities safely. Hydrogen is an explosive gas, making it potentially dangerous to handle as well as requiring either high pressurized or cryo-containers [7], [87]. The process of pressurizing or liquefying hydrogen demands large quantities of energy, representing a significant loss of efficiency as an energy source. To circumvent this, methods of storing hydrogen by absorbing it on high surface area materials such as zeolites [88], [89] and metal organic frameworks [56], [90] have been explored. However, to avoid the release of hydrogen from these materials during storage requires them to be stored at low temperature. Alternatively, hydrogen can be chemisorbed in materials such as complex hydrides [91] or liquid organic hydrogen carriers (LOHC) [92]–[94]. These methods allow hydrogen storage at ambient temperatures by converting it into more stable liquid or solid chemicals.
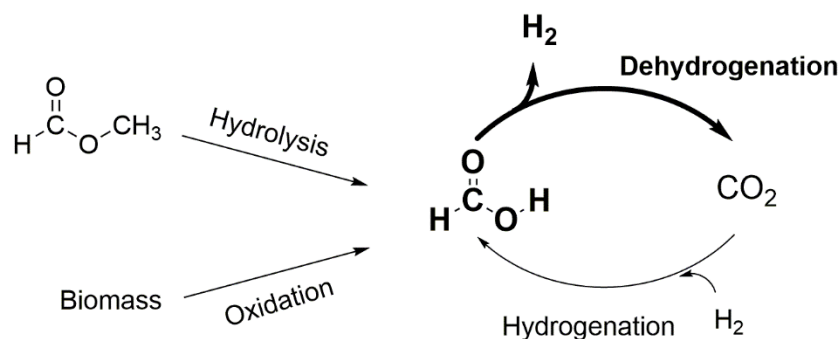
Figure 4.1: Scheme for utilizing formic acid as a liquid-organic hydrogen carrier (LOHC).

Formic acid is considered one of the most promising candidates for a liquid organic hydrogen carrier. It has a hydrogen content of 4.4 wt% and a volumetric hydrogen content of 52 g/L, but more importantly, the hydrogen can be released at low temperatures using a catalyst. The release of hydrogen occurs through dehydrogenation of formic acid, forming H_2 and CO_2 in equal amounts. Ideally, the use of formic acid would allow for a circular system as illustrated in Figure 4.1, since CO_2 can react with hydrogen to reform formic acid (see Chapter 5). The process is somewhat complicated by the dehydration of formic acid. This alternate reaction causes formic acid to decompose into CO and H_2O, a highly undesirable

reaction. CO is a well-known catalyst poison due to its ability to form strong bonds with precious metals like Pd and Pt used for fuel cells.
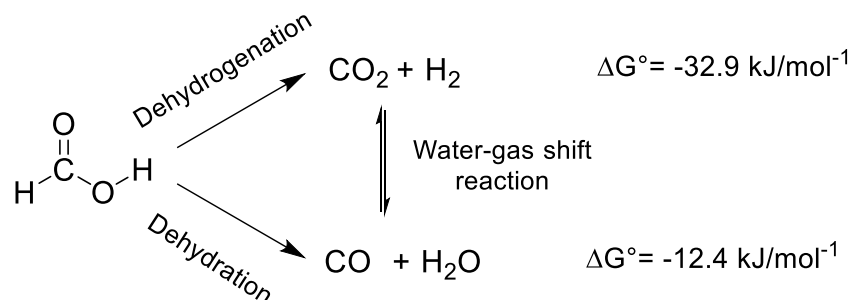
Figure 4.2: Decomposition pathways for formic acid. Dehydrogenation is the desired reaction, but is connected via the water-shift reaction to the formation of undesirable CO and H_2O.

The products from both decomposition reactions are connected by the water-gas shift reaction. This means that interconversion between the products is another thing to consider, when deciding upon the reaction conditions. Conversion to CO and water is possible at relatively low temperatures in the gas phase (less than 200 °C), and can even be converted back to hydrogen at room temperature in the liquid phase [95].

Current research and catalysts

If formic acid is to be used as a storage medium for H_2, the decomposition back to H_2 has to be possible with a minimum amount of energy required. This can be achieved using a well-designed catalyst, as the reaction is thermodynamically favored even at room temperature as shown by the negative Gibbs free energy in Figure 4.. It is also important that any catalysts for the process is highly selective, being able to exclusively make H_2 and CO_2 to avoid deactivation of the catalyst by CO. Even if the catalyst itself is resistant to CO poisoning, a standard fuel cell using a Pt/C electrode deactivates at concentrations as low as 25 ppm at 80 °C [96].

Several studies have previously investigated the use of heterogeneous catalysts for the dehydrogenation of formic acid both in the liquid [97]–[100] and in the vapor phase[42], [101]–[105]. Dehydrogenation in the liquid phase using homogeneous catalysts show incredibly high TOF-values (up to 228.000 h^{-1})[100], but suffer from limited reusability of the catalysts and the need for a base. Furthermore, the homogeneous catalysts are typically used in batch reactors [106]–[108]. Heterogeneous catalysts have also displayed good selectivity in the liquid phase using nitrogen-doped carbon catalysts at room temperature [109], [110]. In the vapor phase, the reaction runs continuously and with no additives, however it does require higher temperatures (100-200 °C) for the reaction to occur [101], [103], [111].

Carbon materials have already been shown to work for the dehydrogenation of formic acid in the vapor-phase. A common way of improving the activity of the carbon-based catalysts is to dope them with nitrogen. As an example, Bulushev *et al.* studied Pd on different carbon frameworks with and without nitrogen doping on the dehydrogenation in the vapor phase for biomass-derived formic acid. They found that factors such as the metal precursor, nitrogen content, nitrogen species, support structure and foreign atoms all contribute in some ways to the activity of the catalysts [112]. Nitrogen was important

for the selectivity towards hydrogen and CO_2, while potentially playing a role in the dispersion of metal on the carbon support. However, it is still a subject in need of further analysis.

4.1. Catalyst synthesis

The carbon materials used for this project were mainly Ordered Mesoporous Carbon materials (OMC). The basic synthesis scheme is illustrated in Figure 4.3. By synthesizing a polymer in a solution of micelles, a highly ordered carbon nanostructure is constructed. The micelles used for forming the pores are prepared by dissolving a surfactant in the reaction medium. The surfactant may form spherical or rod-shaped micelles depending on the choice of surfactant. During carbonization, the micelles are decomposed, while the polymer is carbonized. The pores in the structure left by decomposing the micelles are in the mesoporous range, which are considered ideal for dispersing an active metal phase and allow for reactants to reach the resulting active sites without diffusion limitations. A variety of ordered mesoporous polymers and carbon materials have been reported in the literature as a support for active metals or as capacitors [46], [113]–[115]. The ordered mesoporous carbon materials are typically referred to as NOMC and OMC depending on whether or not they contain nitrogen.
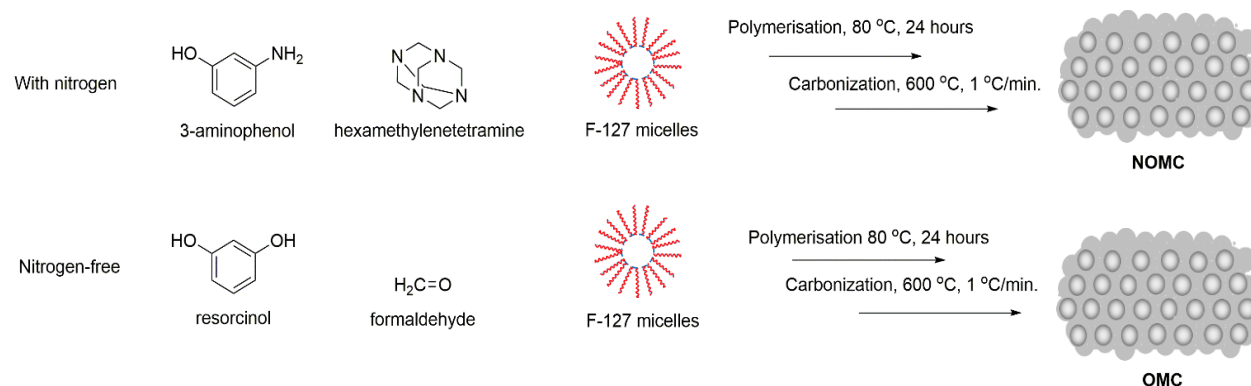
Figure 4.3: Synthesis scheme for NOMC and OMC via polymerization of 3-aminophenol and hexamethylenetetramine or resorcinol and formaldehyde. The F-127 micelles included in the reaction mixture forms the ordered porous structure upon carbonization.

The mesoporous network, high porosity and high nitrogen content of NOMC was expected to help create highly selective catalysts for the dehydrogenation of formic acid. The nitrogen-free counterpart (OMC) was synthesized by exchanging the building blocks of the polymer with similar nitrogen-free building blocks. 3-aminophenol was exchanged with resorcinol, thereby replacing the amine group in the meta position with another phenol group. Hexamethylenetetramine breaks down into formaldehyde and ammonia, which react with the 3-aminophenol to form the polymer. For the nitrogen-free OMC material, the hexamethylenetetramine is replaced with an equal amount of formaldehyde. $NaHCO_3$ was added to the reaction mixture, instead of NH_4OH, to create the basic conditions needed for the polymerization. Metals were dispersed on the carbon materials either by incipient-wetness impregnation or by metalation. A list of the ordered mesoporous materials covered in this chapter can be found in Table 4.1.

Nitrogen-doped Ordered Mesoporous Carbon (NOMC): This procedure was inspired by the work of Yu et al. [115]. 8.80 g of F-127, 4.40 g of 3-Aminophenol and 2.80 g of Hexamethylenetetramine were mixed in a 1L flask containing 208 mL H_2O. The mixture was heated to 80 °C while stirring. Once all the reactants had dissolved, 8 mL of 30 wt% NH_4OH was added. The polymerization was allowed to run for 24 hours at 80 °C before the polymer was collected by centrifugation and washed with H_2O. After drying at 60 °C, the polymer was carbonized in a tubular oven under N_2 atmosphere at 600 °C, 1 °C/min. for 2 hours. The resulting black powder was finely grinded and labelled NOMC.

Nitrogen-free Ordered Mesoporous Carbon (OMC): 4.40 g of F-127, 2.22 g of resorcinol and 8.85 mL of formaldehyde were mixed in a 250 mL flask containing 104 mL of H_2O. The reactants were dissolved by heating to 80 °C while stirring. 41 mg of $NaHCO_3$ was added to the mixture and the polymerization was allowed to occur at 80 °C for 24 hours. The polymer was collected by centrifugation and washed using H_2O. After drying at 60 °C, the polymer was carbonized in a tubular oven under Ar atmosphere at 600 °C, 1 °C/min. for 2 hours. The resulting black powder was finely grinded and labelled OMC.

Incipient-wetness impregnation of carbon materials: The OMC/NOMC materials were dried in a vacuum oven overnight before impregnation. An aqueous solution of the desired metal precursor ($H_2PtCl_6 \cdot xH_2O$, $Co(NO_3)_2 \cdot 6H_2O$, $Cu(NO_3)_2 \cdot 2.5H_2O$, AgCl, $Pd(NO_3)_2 \cdot 2H_2O$, $RuCl_3 \cdot 6NH_3$, $IrCl_3 \cdot xH_2O$ or $HAuCl_4 \cdot xH_2O$(was added to 200 mg of dry OMC/NOMC material. The impregnated powder was rapidly stirred for 10 min. before being dried in an oven at 60°C. The material was reduced using formier gas at 300°C for 2 hours using a heating rate of 5°C/min.

Metalation of carbon materials: 95 mg of NOMC or OMC support was added to a solution of 15 mL absolute ethanol containing 5 mg of either Pt, Pd or a 2.5 mg mixture of Au and Pd. The dispersion was left under magnetic stirring for 24 h before being filtered and washed with absolute ethanol. The powder was allowed to dry on the filter before being reduced in formier gas at 300 °C for 2 h.

Experimental procedure: 30 mg of catalysts was mix with 270 mg of fractionated quartz (355-700 nm) to prevent plugging up the reactor. The powder was transferred to a quartz reactor tube heated by an aluminum block. A 50 ml/min. flow of N_2 was bubbled through a flask of 100 mL of formic acid (98-100%). The formic acid was heated to 40 °C to saturate the flow with excess formic acid. The gas was then passed over two condensers kept at 20 °C to remove excess formic acid. This setup provided a uniform saturation of the gas flow. The saturated gas was passed through the reactor containing the catalyst and quartz, followed by a cold trap to capture unreacted formic acid before reaching the detector. The detector is a Rosemount Binos 100 IR gas analyzer, which measures the percentage of CO and CO_2 in the product flow. Hydrogen yield is based on the amount of CO_2 measured as they are produced in equal amounts from the reaction. The detector was calibrated using pure nitrogen and a gas mixture of 1% CO, 20.69 % O_2 and nitrogen. The CO_2 signal was calibrated by adding 200 mg of a gold on silicalite-1 catalyst in the reactor and passing the 1% CO mixture through. The Au catalyst easily converts the 1% CO to 1% CO_2 for the calibration. The flow was checked before and after each experiment, using a flowmeter to ensure that no leaks or blockage were present.

Table 4.1: List of NOMC/OMC materials covered in this chapter.

Impregnation method	Catalyst	Metal precursor
Incipient-wetness	1 wt% Pt@NOMC	$H_2PtCl_6 \cdot xH_2O$
	1 wt% Pd@NOMC	$PdNO_3 \cdot 2H_2O$
	1 wt% AuPd@NOMC	$HAuCl_4 \cdot 3H_2O$ / $PdNO_3 \cdot 2H_2O$
	1 wt% Ru@NOMC	$RuCl_3 \cdot 3NH_3$
	1 wt% Au@NOMC	$HAuCl_4 \cdot 3H_2O$
	1 wt% Ag@NOMC	$AgNO_3$
	1 wt% Ir@NOMC	$IrCl_3 \cdot xH_2O$
Metalation	Pt@NOMC	$H_2PtCl_6 \cdot xH_2O$
	Pt@OMC	$H_2PtCl_6 \cdot xH_2O$
	Pd@NOMC	$PdNO_3 \cdot 2H_2O$
	Pd@OMC	$PdNO_3 \cdot 2H_2O$
	AuPd@NOMC	$HAuCl_4 \cdot 3H_2O$ / $PdNO_3 \cdot 2H_2O$
	AuPd@OMC	$HAuCl_4 \cdot 3H_2O$ / $PdNO_3 \cdot 2H_2O$

4.2. Characterization of carbon catalysts

The ordered mesoporous carbon materials gave fine black powders. XRD showed no peaks other than a broad band below 30 °, indicating an amorphous structure (Figure 4.4). SEM showed large agglomerates of amorphous carbon particles about 1-3 µm in size.
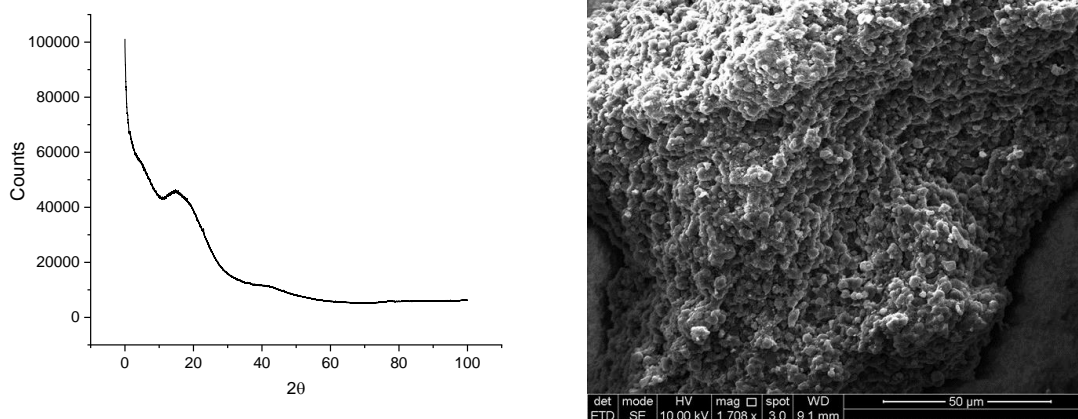
Figure 4.4: Left) XRD of NOMC, which shows no clear peaks other than a broad peak below 30 °.
Right) SEM image of NOMC. The sample consists of large agglomerates of smaller carbon particles about 1-3 µm in size.

Images from TEM shows that the OMC/NOMC materials have ordered pores across the material. The pores are homogeneous in size (about 9 nm diameter) and the overall carbon material has a varied structure, but has a tendency to make hexagonal particles of carbon (Figure 4.5).
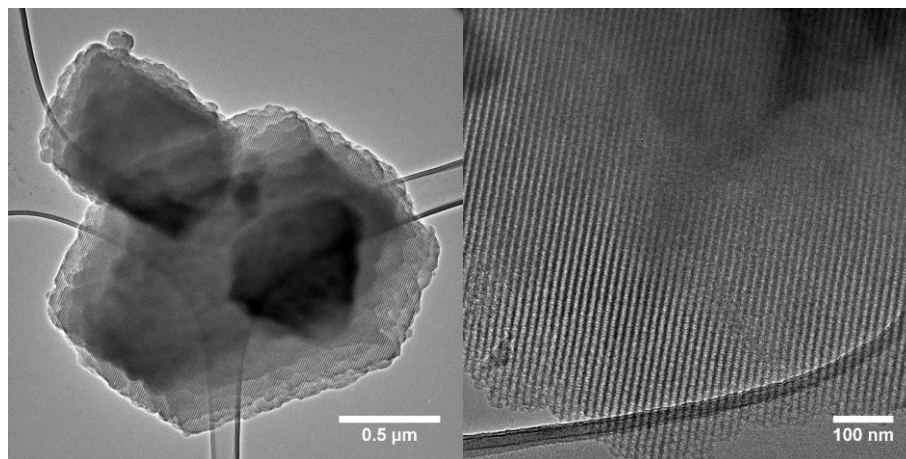
Figure 4.5: TEM images of OMC (Left) and NOMC (Right) before impregnation. A series of ordered pores are observed across the entire material.

After impregnation, metal nanoparticles are dispersed across the materials. As an example, Figure 4.6 shows STEM images of the sample containing 1 wt% Pt. Nanoparticles of about 2 nm in size are observed in the pores of the carbon material. Appendix A1 and A2 holds images and particle size distributions from the remaining materials.
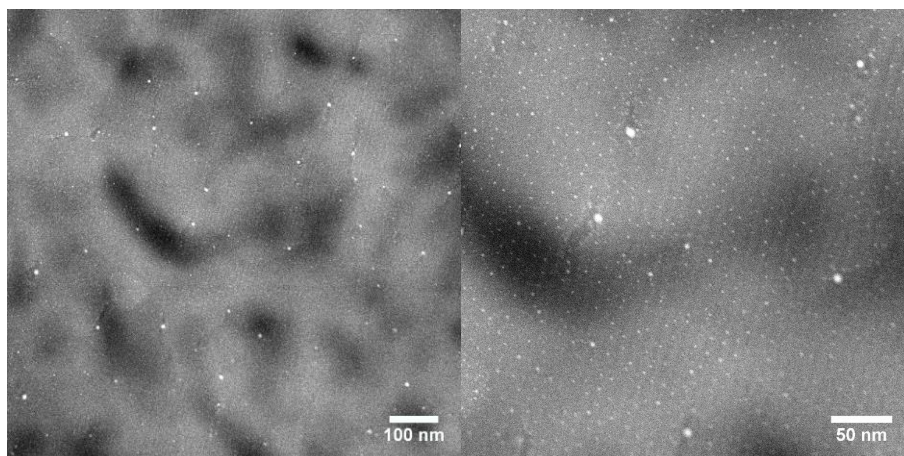
Figure 4.6: STEM images of 1 wt% Pt dispersed on NOMC. Each bright dot stems from a Pt nanoparticle ranging in size from about 2 nm to 6 nm.

Nitrogen physisorption isotherms from OMC/NOMC can be seen in Figure 4.7. Both materials have a typical Type IV shape, indicating a mesoporous material. The BET surface area of NOMC and OMC were measured to be 494 cm^3/g and 580 cm^3/g, respectively. BJH analysis of OMC and NOMC are found in Appendix A.4.
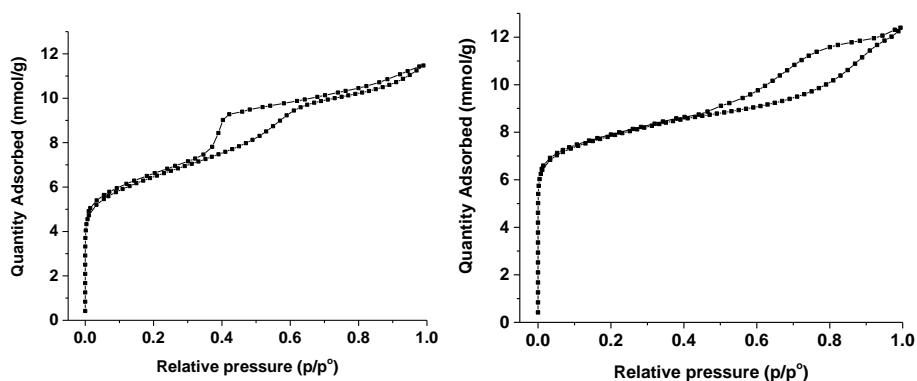
Figure 4.7: Nitrogen physisorption isotherms of the NOMC (Left) and OMC (Right) carbon supports. Both have the typical form of a mesoporous material. The surface area and pore volume of NOMC is 494 m^2/g and 0.38 cm^3/g, respectively, while for OMC it is 580 m^2/g and 0.41 cm^3/g.

The surface composition of the materials was determined by XPS. The nitrogen content of NOMC was measured to be about 6.8% (Table 4.2). The nitrogen peak was deconvoluted to distinguish between the various nitrogen species in the NOMC sample. The nitrogen incorporated in the structure is mainly graphitic and pyridinic nitrogen with a small amount of pyridinic-oxide. An example of the deconvolution is displayed in Figure 4.8. Elemental analysis of the samples measured the total nitrogen content of NOMC measured to be about 8.5%. No clear peaks were seen in XRD, only a broad band below 30 °. SAXS analysis was also conducted and gave similar signals for both OMC and NOMC (Appendix A.5).

Table 4.2: Composition of the OMC materials based on measurements from XPS. The relative amount of different nitrogen species of NOMC is listed along with the position.

Support	Carbon C1s (285 eV)	Oxygen O1s (532 eV)	Nitrogen N1s(400 eV)	Graphitic N 400.1 eV	Pyridinic N 398.9 eV	Pyridinic-oxide 403.3 eV
NOMC	87.9%	5.3%	6.8%	49%	39%	12%
OMC	83%	17%	-	-	-	-
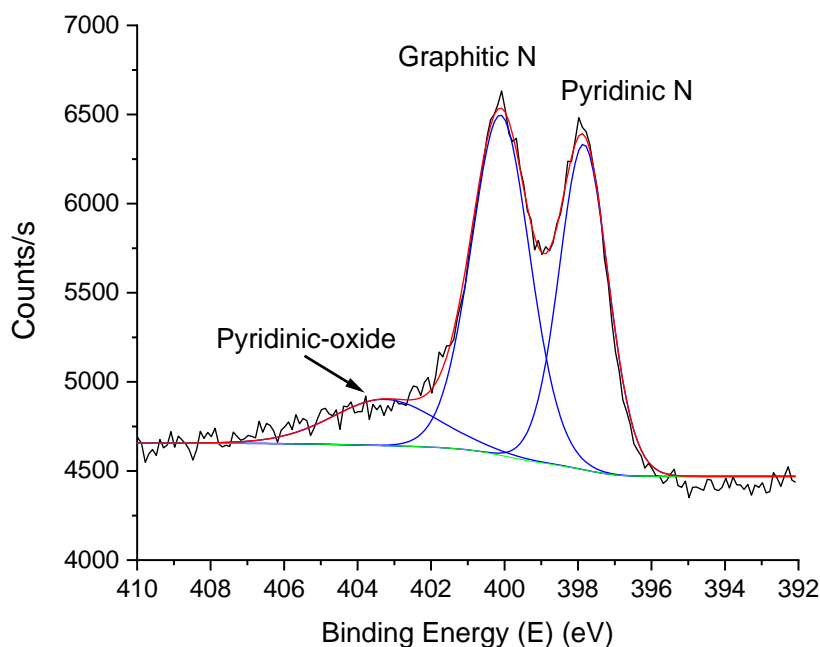
Figure 4.8: Deconvolution of the nitrogen peak of NOMC from XPS. Pyridinic N is located at 397.88 eV, graphitic N is located at 400.08 eV and pyridinic-oxide is seen at 403.28 eV.

4.3.   Dehydrogenation using various metals on ordered mesoporous carbon

Our initial work focused on finding the metals offering the highest yield and selectivity when deposited on nitrogen-doped ordered mesoporous carbon. Afterward, the best three metal catalysts were selected for further research into the influence of nitrogen on the dispersion of the metal nanoparticles, particle size, yield and selectivity toward dehydrogenation. ME-PSD-DRIFTS was conducted on the samples to investigate differences in the reactant species found on the surface or the catalysts.

4.3.1. Screening using 1 wt% of various metals on NOMC

An initial screening using different platinum group metals (Pd, Pt, Ru, Au and Ir), alongside more abundant metals (Co, Cu and Ag). All catalysts were synthesized with 1 wt% of metal. An alloy of Au/Pd was also tested as it is known in the literature to be highly reactive for this reaction [109], [116]. All of these catalysts were prepared by incipient-wetness impregnation. The temperature of the reactor was increased in steps of 20 °C starting from 120 °C up to 200 °C. The temperature was kept steady at each interval for one hour to ensure that the conversion was stable. The resulting CO_2 yield are shown in Figure 4.9.
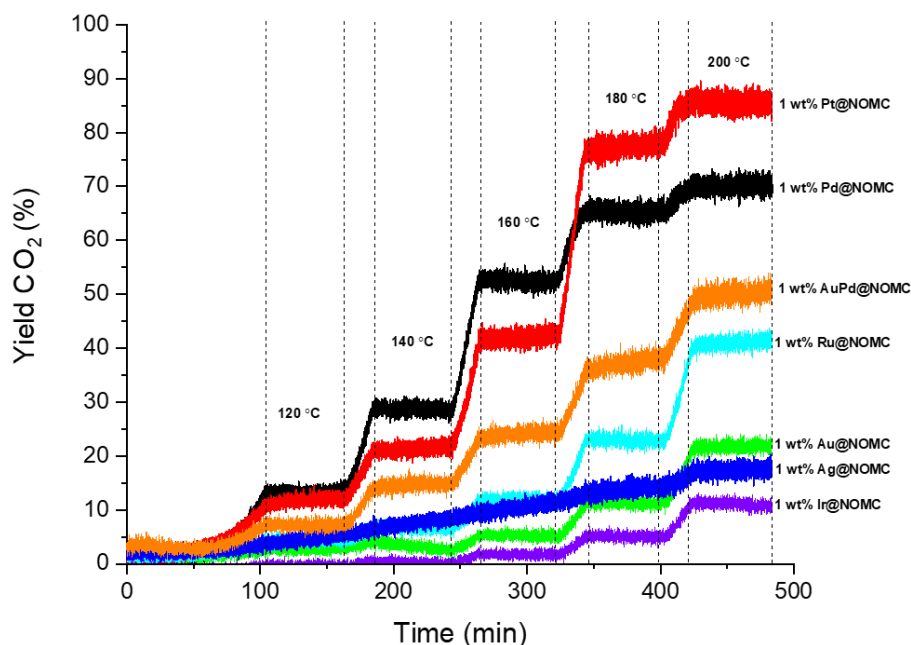
Figure 4.9: Yield using different metals on NOMC for the dehydrogenation of formic acid. An experiment using a 1 wt% CoCu alloyed material was also conducted, but gave no detectable yield. All catalysts consisted of 1 wt% metal.

At higher temperatures (>160 °C) Pt@NOMC proved to be the best catalyst, while Pd@NOMC performed better between 140-160 °C. The two catalysts performed equally well at low temperature (≤120 °C). AuPd@NOMC and Ru@NOMC resulted in medium yields, while Au@NOMC, Ag@NOMC and Ir@NOMC gave low yields even at 200 °C. The yield of CO_2 below 120 °C was minimal for all catalysts. Selectivity toward dehydrogenation ($CO_2 + H_2$) was evaluated by measuring the amount of CO produced by dehydration ($CO + H_2O$). The average concentration of CO measured at various temperatures can be seen in Table 4.3.

Table 4.3: CO concentrations measured in the gas flow at various temperature. The detection limit of the detector is between 0-200 ppm for CO.

	100 °C	120 °C	140 °C	160 °C	180 °C	200 °C
Sample	ppm CO measured in product flow					
1 wt% Pt@NOMC	-	-	<100	200	390	370
1 wt% Pd@NOMC	-	-	100	340	450	470
1 wt% AuPd@NOMC	-	<100	<100	160	170	270
1 wt% Ru@NOMC	220	610	1230	2240	4610	7630
1 wt% Au@NOMC	-	-	<100	<100	<100	200
1 wt% Ag@NOMC	-	-	-	<100	120	260
1 wt% Ir@NOMC	-	-	-	<100	110	280

At lower temperatures (≤140 °C), the concentration of CO was insignificant for all catalysts, except Ru@NOMC. Ru@NOMC produced far higher concentrations of CO compared to the remaining catalysts. The TOFs of the catalysts are calculated using the total number of metal atoms and the average size of the metal nanoparticles are shown in Table 4.4.

Table 4.4: Average metal nanoparticle size based on TEM images and TOF values calculated using the total number of metal atoms.

Catalyst	Average particle size[1]	TOF[2]
1 wt% Pt@NOMC	4.3 nm	752 h^{-1}
1 wt% Pd@NOMC	4.1 nm	485 h^{-1}
1 wt% AuPd@NOMC	4.8 nm	339 h^{-1}
1 wt% Ru@NOMC	3.3 nm	142 h^{-1}
1 wt% Au@NOMC	126 nm	207 h^{-1}
1 wt% Ag@NOMC	2.7 nm	151 h^{-1}
1 wt% Ir@NOMC	6.7 nm	-

[1]Based on measurements of at least 200 particles in TEM images
[2]TOF value calculated based on yield at 120 °C

Pt@NOMC, Pd@NOMC and AuPd@NOMC were selected for further studies, due to having a combination of good yield and low tendency toward the formation of CO.

4.3.2. Influence of nitrogen on dehydrogenation yield

Nitrogen is suspected to influence the activity of carbon catalysts for dehydrogenation of formic acid by improving the dispersion of active metals on the carbon surface and/or improving the activity of the catalysts by donating electrons to the active metals [29], [44], [104], [117]. Nitrogen has previously been shown to improve the activity of carbon catalysts for the dehydrogenation of formic acid in the liquid phase [118]. To investigate this, a series of ordered mesoporous carbon catalysts were synthesized with Pt, Pd and an AuPd alloy on nitrogen-containing NOMC and nitrogen-free OMC. Rather than using wetness-impregnation for dispersing the metals on the carbon support, a solution of the metal precursors in pure ethanol were prepared. 200 mg of the carbon supports were stirred in the solution for 24 hours. If interaction with nitrogen in the carbon structure plays a role in dispersing the metal, the metal content should be higher and particle sizes should be smaller for the nitrogen-containing NOMC. A comparison of the different catalysts can be found in Figure 4.10. The yield of CO_2 has been normalized, due to the disparity in metal loading.
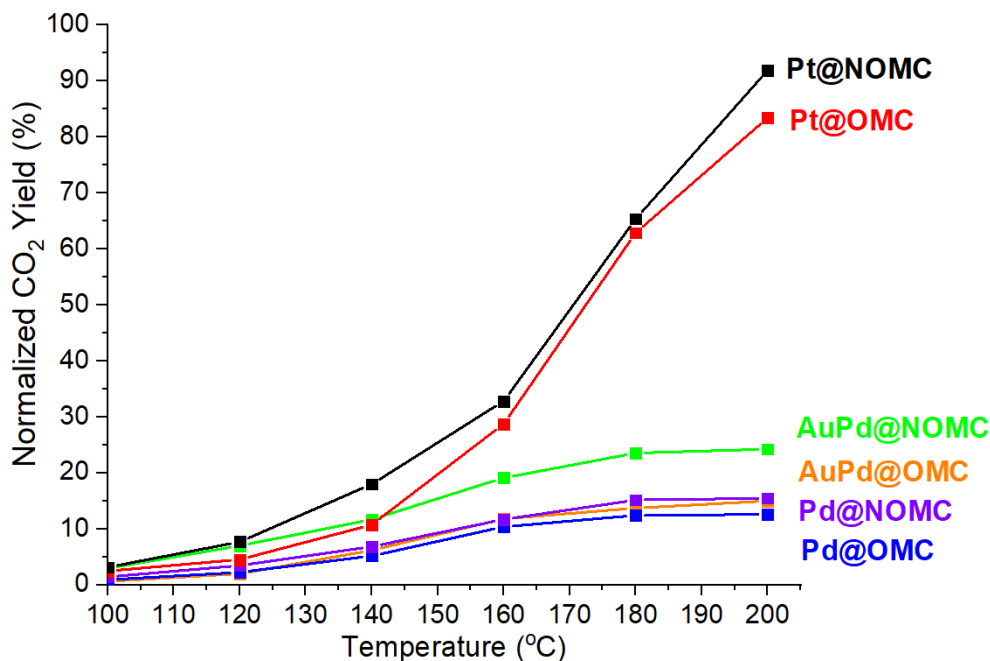
Figure 4.10: Comparison of the carbon catalysts with nitrogen (NOMC) and without nitrogen (OMC). Yields have been normalized to account for the difference in metal loading.

Each of the NOMC catalysts have slightly higher activity, compared to their OMC counterpart. The CO concentration of each of the catalysts is found in Table 4.5. The concentration of CO is higher for each of the OMC catalysts despite their lower activity.

Table 4.5: CO measurements for each of the catalysts at various temperatures.

	100 °C	120 °C	140 °C	160 °C	180 °C	200 °C
Sample	ppm CO measured in product flow					
Pt@NOMC	-	-	<100	120	260	320
Pt@OMC	-	-	160	520	1030	1250
Pd@NOMC	-	<100	280	650	1180	1290
Pd@OMC	-	<100	590	1470	1690	1610
AuPd@NOMC	<100	<100	150	160	230	270
AuPd@OMC	-	<100	430	680	780	790

The metal loading of the catalysts was determined using ICP-OES. To prepare the samples for ICP-OES, 50 mg of each of the samples was treated with 10 mL of boiling aqua regia for one hours to dissolve the metal content, followed by filtration and diluted using 2% HNO_3. The metal content, average particle size and TOFs of the catalysts are shown in Table 4.6.

Table 4.6: Metal content, average particle size and TOF values of the OMC/NOMC materials produced using metalation. TOFs are calculated based on the total amount of metal.

Catalyst	Metal loading[1]	Average particle size[2]	TOF[3]
Pt@OMC	0.65 wt%	2.3 nm	631 h^{-1}
Pt@NOMC	0.55 wt%	4.6 nm	870 h^{-1}
AuPd@OMC	2.16 wt%	2.7 nm	291 h^{-1}
AuPd@NOMC	1.78 wt%	5.2 nm	819 h^{-1}
Pd@OMC	2.30 wt%	12.6 nm	276 h^{-1}
Pd@NOMC	1.90 wt%	3.9 nm	412 h^{-1}

[1]Measured using ICP-OES
[2]Average size calculated based on measurements of at least 200 particles from TEM images
[3]TOF value calculated based on yield at 120 °C

The OMC catalysts have slightly higher metal loadings compared to the NOMC materials. There is no clear trend in the average sizes of the metal nanoparticles present. For each of the catalysts a clear improvement in the TOFs is seen for the NOMC materials. Using the carbon supports without any metal deposited did not show any catalytic activity at 200 °C.

4.3.3. DRIFTS study of surface species

DRIFTS analysis was used to investigate formate species generated on the catalyst surface under reaction conditions. *Modular Excitation-Phase Sensitive Detection Diffuse Reflectance Infrared Fourier Transform Spectroscopy* (ME-PSD-DRIFTS), as described in detail by Bravo-Suárez et al.[119], was utilized to minimize the background noise and eliminate peaks from surface species that did not participate in the reaction. All of the measurements were carried out in-situ.

DRIFTS analysis procedure:

DRIFTS analysis was carried out on a Praying Mantis accessory from Harrick Scientific Products mounted on a Thermo Scientific Nicolet iS50 FT-IR Spectrometer. The reaction chamber was a High-temperature Reaction Chamber designed for the Praying Mantis.

15 mg of the sample was diluted with 135 mg of dried KBr, before being mixed and ground to a fine powder. A flow of 100 mL/min nitrogen was passed through the reaction chamber from the bottom, through the sample mixture. The gas line was fitted with a VICHI switching valve from Valco Instruments, which switches between a pure nitrogen flow and one with nitrogen mixed with 60 µL/h 99% formic acid. The FTIR-setup uses an MCT detector cooled with liquid nitrogen.

The catalysts were investigated at 100 °C to limit the reaction rate and increase the lifespan of the active species on the catalyst surface. The detector takes 40 spectra, each requiring 4 scans, before switching between pure nitrogen and formic acid. Each individual scan from 600-4000 cm^{-1} takes 2 seconds to complete. A period is defined as 40 spectra of formic acid flow in addition to 40 spectra of pure nitrogen flow, making a full period 80 spectra. A total of 20 periods are run per experiment, to ensure that the system has stabilized. All values are displayed on a Log(1/R) axis. According to a study by Oliger and Griffiths the concentration of adsorbents can be assumed to be linearly related to log(1/R) for strongly absorbing matrices [120], [121].

Comparison of NOMC/OMC with and without metals:

DRIFTS analysis was performed on Pt@NOMC, Pt@OMC, Pd@NOMC and the metal-free carbon supports. A complete period for each of the samples are displayed in Figure 4.11-14. The data has been normalized based on the intensity of the most intensive peak (1750 cm^{-1}). The shift in colour from blue to red indicates an increase in species that absorb at those frequencies. The high intensity of the peaks seen at 1100-1250 cm^{-1}, 1750 cm^{-1} and 2950-3300 cm^{-1} fits with the IR spectrum recorded for formic acid on KBr, which is used for diluting the solid samples. KBr does not absorb infrared light between 600-4000 cm^{-1}, and is also used for the windows of the cell.
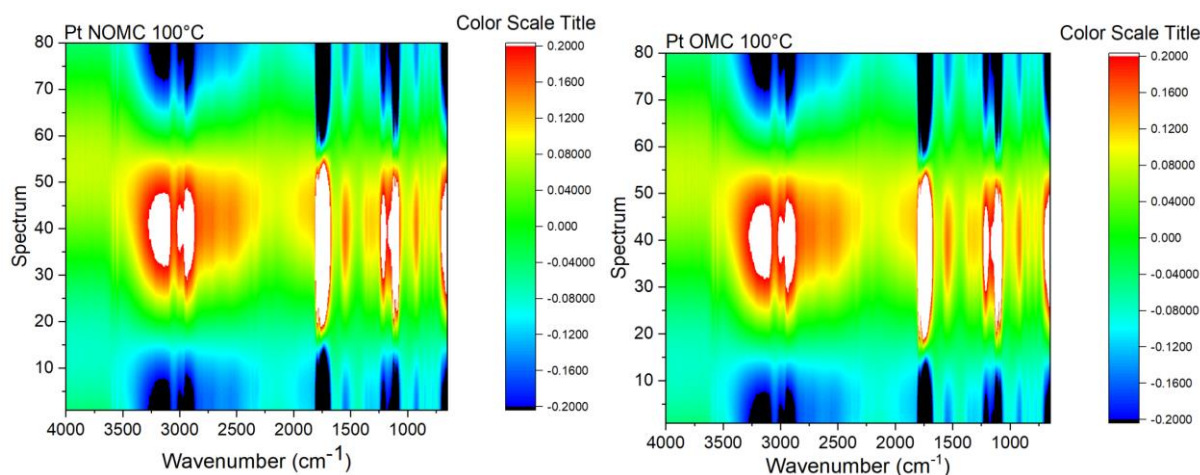
Figure 4.11: DRIFTS analysis of Pt@NOMC and Pt@OMC catalysts at 100 °C. A complete period (80 scans) is displayed for each of them after a steady-state has been reached.

The peaks at 1543 cm^{-1} (strong), 2316 cm^{-1} and 776 cm^{-1} (medium) and at 2216 cm^{-1} (weak) do not show up on the spectrum from formic acid on KBr or in the list of fundamental frequencies of formic acid (Figure 4.12). These peaks appear in the spectrum from both Pt@NOMC and Pt@OMC.
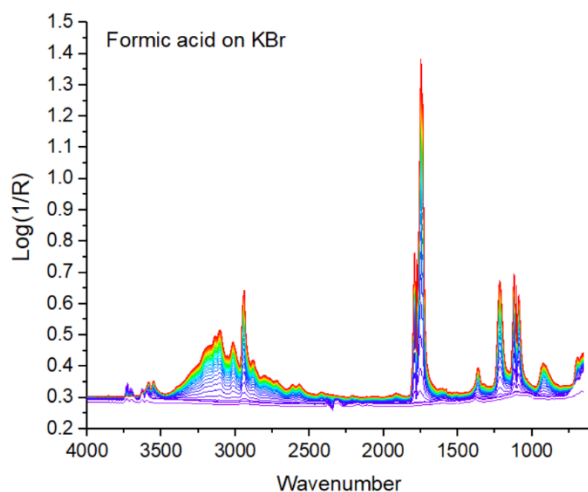
Formic acid peaks	Wavenumber, cm^{-1}
OH stretch	3570
CH stretch	2943
C=O stretch	1770
CH bend	1387
OH bend	1229
C-O stretch	1105
CH bend	1033

Fundamental frequencies from NIST Chemistry Webbook

Figure 4.12: (Left) IR spectrum from formic acid on KBr at 120 °C. (Right) List of fundamental frequencies of formic acid.

The DRIFTS analysis of Pd@NOMC shows the same peaks as for the Pt@NOMC and Pt@OMC samples, but the peaks at 2950-3300 cm^{-1} belonging to the C-H stretch have a lower relative intensity compared to the C=O stretch of those samples.
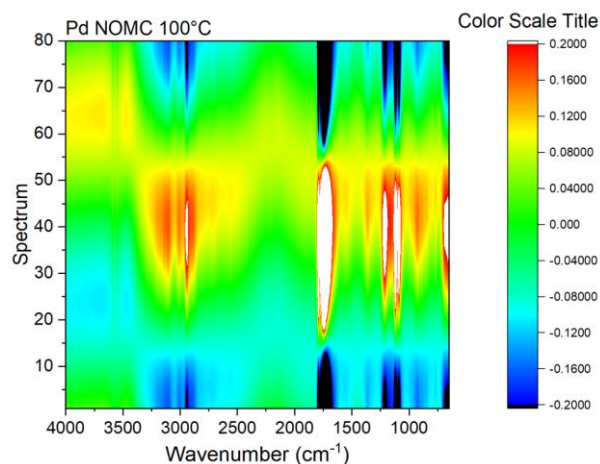
Figure 4.13: A single complete period from the DRIFTS analysis of Pd@NOMC at 100 °C.

DRIFTS analysis of the supporting materials themselves shows a much lower intensity of all peaks. The unidentified peak at 1543 cm^{-1} is still barely visible, while the remaining signals correlate well with the peaks expected from adsorbed formic acid.
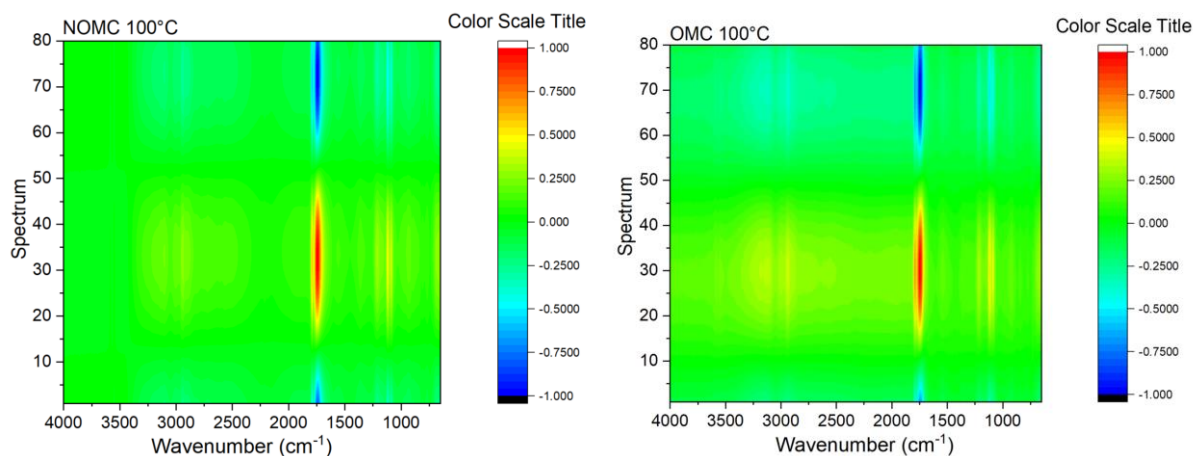
Figure 4.14: DRIFTS analysis of NOMC and OMC catalysts at 100 °C.

4.3.4. Dehydrogenation of formic acid using Ru/COF

In a separate project, published together with Yury V. Kolen'ko and Liliana P. L. Gonçalves [122], the catalytic activity of RuO$_2$ on a covalent organic framework (COF) was investigated. The COF support shares many similarities with the OMC materials, but the polymerization does not use micelles to create pores in the structure. The COF is synthesized by reacting hexamethylenetetramine and phloroglucinol at 100 °C under acidic conditions to make triformylphloroglucinol (Tp), which has proven to make robust and stable COFs [123]. The COF is produced by reacting the Tp with o-tolidine at 120 °C over 3 days. The resulting COF was impregnated with Ru by stirring it in an aqueous solution with RuCl$_x$ for 15 min. followed by the addition of NaOH to produce RuO$_2$ nanoparticles. The catalysts had a fine dispersion of

nanoparticles (<2 nm) with some agglomerates of about 10 nm in size. When used for the dehydrogenation of formic acid, the Ru/COF catalyst showed good activity at higher temperatures. It reached complete conversion at 200 °C with a selectivity toward H_2 of 98%. The Ru/COF catalyst was compared to a commercial 5 wt% Ru/C catalyst, and showed better activity and stability despite having a lower metal loading (Figure 4.15).

Figure 4.15: (Left) Formic acid dehydrogenation using Ru/COF and Ru/C at temperatures from 80-200 °C. (Middle) Comparison of Ru/COF and Ru/C at 120 °C. (Right) STEM image of Ru/COF showing Ru clusters and particles dispersed on the COF support.

4.4.   Discussion

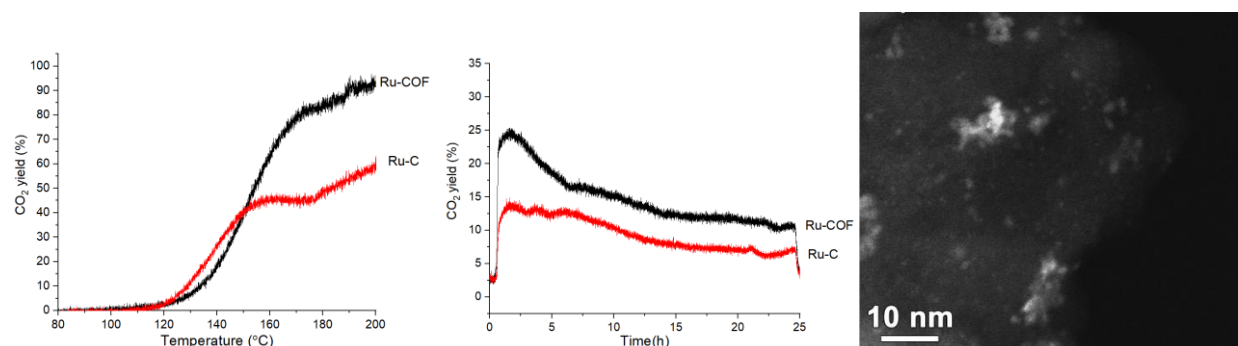The two kind of carbon supports produced with and without nitrogen have the desired mesoporous structure as indicated by TEM and nitrogen physisorption. Both of them have high degree of ordered pores (9-10 nm in diameter) and a high BET surface area (494-580 cm^3/g). The difference in BET surface area, pore volume and shape of the isotherm indicates that some differences in the overall structure exists.

The synthesized carbon materials generally show good activity and selectivity toward the dehydrogenation of formic acid. Pt@NOMC, Pd@NOMC and AuPd@NOMC gave the highest yield, along with high purity of H_2 and CO_2 in the product flow, especially at low temperatures. Ru@NOMC was the only catalyst to produce a fair amount of CO. In order to be used for commercial fuel cells the CO concentration should be below 10 ppm [96], which is at the limit of what the detector in our setup can measure (0-200 ppm).

The comparison between the OMC and NOMC materials indicated that the presence of nitrogen improves the activity of all the catalysts. There was no pattern in the size of the metal nanoparticles and the metal loadings were higher for the OMC materials. Stability of the nanoparticles found on the OMC and NOMC materials also seem similar. Images of the catalysts was recorded for each of the catalysts after having been used for the dehydrogenation reaction up to 200 °C (Appendix A.3). A slight trend toward larger particles, indicate some sintering during the reaction, however these changes remain small. The resulting increase in activity is likely due to the effect of nitrogen donating electrons to the active site. The apparent activation energy of the Pt@NOMC catalysts, which had the highest TOF and selectivity, was estimated to be 50 kJ/mol based on an Arrhenius plot of the TOFs at 120 °C (Figure 4.16). The activation energy of Pt@OMC is calculated to be 56 kJ/mol. The TOFs of the Pt@NOMC and Pd@NOMC are comparable to those found in previous studies of supported platinum group metals for vapor phase decomposition of formic acid at 120 °C [112], [118]. A list of results from literature can be found in Table 4.7.

Table 4.7: Metal content, average particle size and TOF values of the OMC/NOMC materials produced using metalation. TOFs are calculated based on the total amount of metal.

Sample	Phase	Temperature	TOF	Reference
Pt@NOMC	Vapor phase	120 °C	870 h^{-1}	This work
Ru/COF	Vapor phase	120 °C	321 h^{-1}	This work
Pd/N-C	Aqueous (1M HCOONa)	45 °C	645 h^{-1}	[97]
Pd/C	Aqueous (1M HCOONa)	45 °C	361 h^{-1}	[97]
0.2 wt% Ir-CTF	3M Formic Acid	80 °C	27000[a] h^{-1}	[99]
Cp*Ir thbpym	Aqueous (1M HCOONa)	90 °C	228000[a] h^{-1}	[100]
Ru-P MOF	Vapor phase	145 °C	2000 h^{-1}	[101]
1wt% Au/SiO$_2$	Vapor phase	200 °C	7000 h^{-1}	[103]
AuPd n-CNS-T$_h$-160	Aqueous (5M HCOONa/HCOOH)	25 °C	459[a] h^{-1}	[109]
Pd/CN$_{0.23}$	Aqueous (1M HCOOH)	25 °C	3625[a] h^{-1}	[110]
1wt% Pd/N-PCN	Vapor phase	125 °C	1000 h^{-1}	[112]
1wt% Pd/PCN	Vapor phase	125 °C	400 h^{-1}	[112]
1wt% Pt/N-CNF	Vapor phase	125 °C	900 h^{-1}	[118]

[a] Initial activity

The experiments with the Ru/COF showed similar activity and reactivity to the Ru@NOMC catalysts. At 200 °C the yield of each of the catalysts is linearly proportional to their respective loading, with Ru/COF having a loading of 2.4 wt% and a yield of 95%, while Ru@NOMC had a loading of 1 wt% and 40% yield. The Ru particles dispersed on the COF material was determined to be RuO_2 by XPS, but during the initial stages of the catalytic reaction, the RuO2 is reduced to metallic Ru, which functions as the active phase. The higher nitrogen content of the COF (9.9 vs. 6.8 wt%) is expected to be the reason for the better dispersion of the Ru nanoparticles. Both of the catalysts had a similar selectivity of 98% toward CO_2, indicating that the reduced particle size and higher nitrogen content did not affect the equilibrium of the reaction.
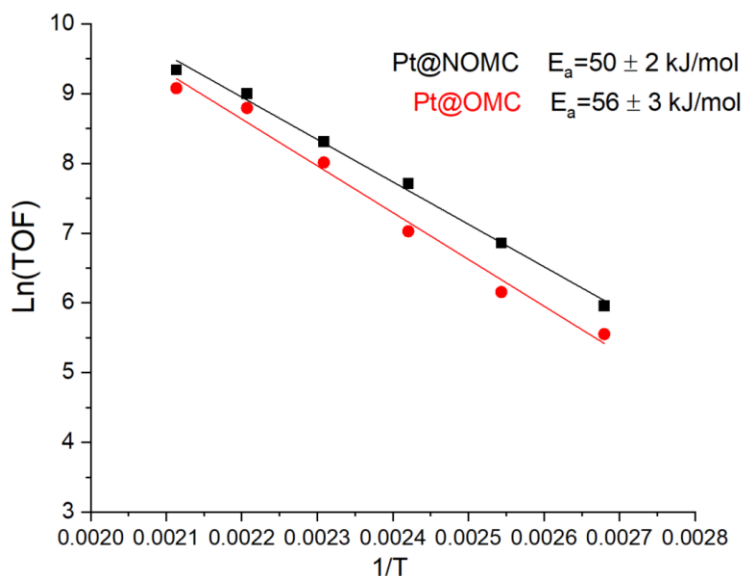
Figure 4.16: Arrhenius plot of Pt@NOMC and Pt@OMC for the dehydrogenation of formic acid at 120 °C.

An experiment to compare the relative stability of Pt@NOMC and Pt@OMC was conducted. Each of the catalysts were run for 18 hours at 200 °C (Figure 4.17). Both of the catalysts saw a slight improvement in yield over the 8 hours. The Pt@NOMC catalyst had a slight decrease in activity over the following 10 hours, while the Pt@OMC catalyst remained stable. This is contrary to the expectation that the nitrogen content of NOMC could help stabilize the particles. The average size of the Pt nanoparticles found on Pt@OMC is also slightly lower than Pt@NOMC and would be expected to have a higher tendency towards agglomeration, leading to a lower number of available active sites.
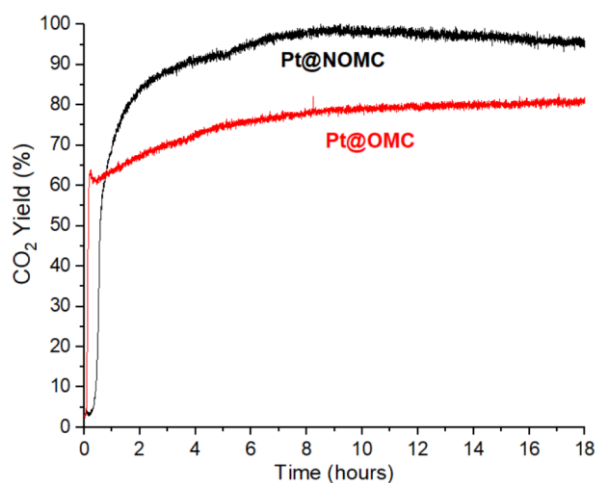
Figure 4.17: Stability test of Pt@NOMC and Pt@OMC at 200 °C for the dehydrogenation of formic acid.

Since there are no clear differences in the ME-PSD-DRIFTS data for Pt@NOMC and Pt@OMC, the reaction is expected to occur via the same mechanism. The mechanism for the dehydrogenation reaction has previously been modelled as occurring by having either one (monodentate) or both oxygen

atoms of formate (bidentate) coordinating to the surface of the catalyst [124]. Both of these mechanisms are several orders of magnitude more likely to undergo dehydrogenation to CO_2 and H_2 as opposed to the dehydration to CO and H_2O. The band 1543 cm^{-1} is assigned to the asymmetric vibration of formate species on the surface [125], [126]. The O-C-O symmetric vibrations of formate are expected to overlap with those of formic acid around 1290-1366 cm^{-1}. The symmetric vibration peaks at the lower wavenumbers belong to monodentate formate, while the peak at higher wavenumber belongs to bidentate formate [126]. Formate is expected to be able to switch between being coordinated via one or both oxygen atoms [124]. The peak at 776 cm^{-1} is assigned to the O-C-O bend of formate. If any CO had been generated by dehydration of formic acid, the C=O adsorbed on the Pt surface would give vibrational peaks at either 1831 cm^{-1} (bridged) or 2074 cm^{-1} (linear) [127]. The peak at 2316 cm^{-1} is assigned to the asymmetric vibration of CO_2 [128], [129].

The increased activity of the NOMC materials is expected to be due to the nitrogen content. Doping carbon materials with nitrogen increases the electron density in the material. When used for electrochemical purposes (capacitors, semi-conductors) doping with nitrogen can be used for modifying the band gap [41], [130]. The increased electron density caused by the nitrogen doping has also been proposed to lead to higher activities in heterogeneous catalysts consisting of metal nanoparticles dispersed on carbon. Nitrogen close to the active metal particles can donate electrons to the active site, which can contribute to the activation of the reactant [131]–[133]. This would lead to a lower activation energy, thus increasing the rate of reaction. The difference in activation energy between the Pt@NOMC and Pt@OMC catalysts could be an indication that nitrogen has donated electrons to the active site.

4.5.   Summary

A series of carbon-based catalysts with ordered pores were tested for the vapor phase dehydrogenation of formic acid to produce H_2 and CO_2. The ordered porous structure was synthesized by polymerizing in a solution containing micelles, which were decomposed afterward giving high content of pores of 9-10 nm in diameter. Nitrogen content was not shown to have an effect on loading or metal nanoparticle size when the catalysts were prepared by metalation. Catalysts containing Pt, Pd and AuPd gave the highest yield with high selectivity (CO < 100 ppm up to 140 °C). Comparison between nitrogen-containing (NOMC) versus nitrogen-free (OMC) carbon supports, showed that the NOMC gave higher yields compared to their OMC counterparts. Pt@NOMC proved to be the best catalyst with a TOF of 870 h^{-1} at 120 °C with no detectable amount of CO produced. Analysis of the surface species found on the Pt@NOMC and Pt@OMC catalysts by ME-PSD-DRIFTS did not show any differences in the detectable peaks, indicating a similar reaction mechanism. The improved activity of the nitrogen containing catalysts is attributed to the ability of nitrogen to donate electrons to the active metals.

Chapter 5. CO_2 hydrogenation using porous organic polymers

Using formic acid as a chemical storage compound for hydrogen requires effective catalysts, which can synthesize formic acid. Traditional means of formic acid synthesis relies on fossil fuels. A more desirable means of producing formic acid is through the hydrogenation of carbon dioxide. This not only stores hydrogen as a liquid compound (formic acid), but also utilizes the undesirable greenhouse gas, CO_2, for sustainable purposes. Porous organic polymers are a class of carbon-based catalysts, which have shown tremendous potential for bridging the gap between the highly active homogenous catalysts and the more stable heterogeneous catalysts. Our goal is to uses these materials to create a new kind of active, stable and easy to separate catalysts for this challenging reaction.

CO_2 utilization is a matter of great interest to both the industrial and scientific communities. CO_2 is a cheap waste product from many processes and an important greenhouse gas contributing to climate change. If CO_2 could be captured and utilized, it would not only be beneficial for the global climate, but also present new opportunities for the industry. The process of hydrogenating CO_2 to more valuable chemicals already exist in the industry, and is being utilized to form methanol using a mixture of CO, H_2 and CO_2 [134].
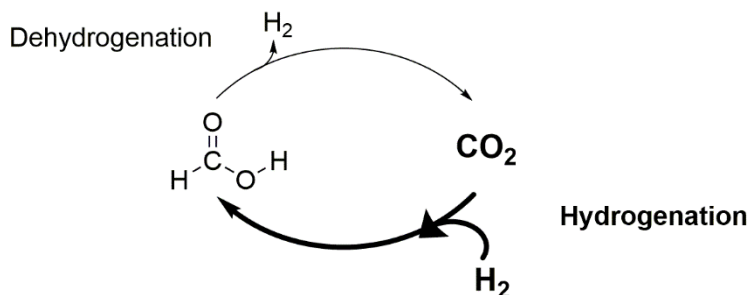
Figure 5.1: Formic acid as a liquid-organic hydrogen carrier.

For these reasons, CO_2 hydrogenation to formic acid has been studied in some detail. The reaction allows for the storage of hydrogen in formic acid, and completes the cycle of formic acid as a liquid-organic hydrogen carrier. Currently the industrial production of formic acid is accomplished through hydrolysis of methyl formate or formamide [8], [135] and back in 2015 the yearly production was about 600 kt/year. This is commonly done using CO from coal or methane reforming. It is also possible to produce formic acid from renewable sources by oxidation of biomass as has been shown by Wasserscheid *et al.* [136]. The advantage of doing CO_2 hydrogenation is two-fold; it utilizes the otherwise undesirable, environmentally harmful CO_2 and stores hydrogen in liquid form.

The hydrogenation of CO_2 involves two gaseous compounds reacting to form a liquid product. The change in entropy of this reaction makes this pathway highly disfavored. To make the formation of formic acid more favorable, a solvent needs to be present. In the aqueous phase, the reaction is slightly exergonic.

$$CO_2(g) + H_2(g) \rightleftharpoons HCOOH(l) \qquad \Delta G°_{(298K)} = 32.9 \text{ kJ/mol}$$

$$CO_2(aq) + H_2(aq) \rightleftharpoons HCOOH(aq) \qquad \Delta G°_{(298K)} = -4 \text{ kJ/mol}$$

In order to obtain acceptable yields in practice, the reaction is conducted in the presence of secondary reactions or molecule interactions. Common strategies involve esterification of the produced formate/formic acid with methanol, reactions with amines to form formamides, or neutralization with a weak base to shift the equilibrium towards formate.

Current research and catalysts

Compared to the dehydrogenation into CO_2 and H_2 covered in the last chapter, the hydrogenation of CO_2 is far less optimized and often requires harsh reaction conditions. This includes high temperature and high pressure of both H_2 and CO_2. In addition, the system requires the presence of a base in order to achieve any significant yield [137]. Optimization of the reaction and comparison with the literature is complicated by the number of parameters affecting the activity. Parameters to optimize include the choice of base, pressure, temperature, reaction medium, H_2/CO_2 ratio, pH and additives [138]. The base is usually a carbonate ($NaHCO_3$, $KHCO_3$, Na_2CO_3 and K_2CO_3) or an organic base like Et_3N.

CO_2 hydrogenation has already been examined for a large variety of homogeneous complexes. Among the most successful are the ones containing Ir, Rh or Ru as the active metal center [139]–[141]. With proper choice of solvent and additives, the reaction may even be run at room temperature and medium pressure (50-100 bar)[142]. Filonenko *et al.* [143] reported the seemingly highest activity using a Ru PNP-pincer catalysts achieving an initial TOF of over 1.000.000 h^{-1}. However, activity quickly declined during the first hour of reaction.

Due to the challenges of isolating the catalyst after use and the limited stability, a great deal of continued work on developing heterogeneous alternatives is currently being carried out. Among the more promising methods is the heterogenization of known homogeneous catalysts. By using the ligands found in homogeneous catalysts as building blocks in polymers, similar active sites can be created while having the ease of separation and increased stability of a heterogeneous catalyst.

Best case would be to have a catalyst capable of both producing and releasing H_2, depending on the reaction conditions. This would allow for a complete system with a single catalyst to be integrated into systems used for the transporting H_2. A few groups have reported making catalysts capable of catalyzing both the hydrogenation of CO_2 and the dehydrogenation of formic acid [143]–[145]. As an example, Yoon et al. [144] used a mesoporous graphitic carbon nitride with 9.5wt% Pd to catalyze the hydrogenation of CO_2 at 40 bar and 150 °C over 24 hours, while also being capable of selectively decomposing formic acid to hydrogen in the liquid-phase (initial TOF = 144h^{-1}). However, the high loading of Pd, limited durability and low TOF value for hydrogenation of CO_2 (TOF = 4.2 h^{-1}) indicates that significant improvement is still necessary.

A porous organic polymer (POP) catalyst made from polyphenylene (PP) with bipyridine ligands (bpy) was prepared using readily available reactants. Homogeneous bpy-Ir^{3+} hydride complexes have shown good activity toward CO_2, but due to the homogeneous nature of the catalyst, recovery required adjustment of pH to precipitate the catalyst [146]. Our heterogeneous bpy-POP catalyst was mixed with IrCl$_3$ in the reaction mixture to produce the catalyst *in situ*. Single atoms of Ir^{3+} were expected to bind to

the bipyridinic sites of the polymer and produce the active site. A separate sample containing phenanthroline (Phen) ligands instead of bipyridine was also prepared. POPs with phenanthroline have previously proved capable of immobilizing iridium ions, achieving a TON of 14400 over 2 hours when used for the hydrogenation of CO_2 [147]. The synthesis of the POP materials was developed in cooperation with Dr. Ryan Wang's group from University College London (UCL). The catalysts were tested for both the hydrogenation of CO_2 and the decomposition of formic acid.

5.1.   Catalyst synthesis

In a typical synthesis for 1 g of bpy-PP-POP without metal, 1.53 g (3.38 mmol) of 1,2,4,5-tetrabromobenzene, 0.342 g (7.78 mmol) of 5,5′-dibromo-2,2′-bipyridine and 1.28 g (1.09 mmol) of benzene-1,4-diboronic acid are mixed in a 250 mL two-neck round bottomed flask fitted with a condenser. 120 mL of DMF solvent is added and the components are stirred until everything is dissolved. 15 mL of 2M K_2CO_3 is added during stirring to neutralize the acid formed. The resulting salt has low solubility in DMF making it easy to see. Polymerization is initiated by the addition of 0.3 g of [Pd(PPh$_3$)$_4$]. The Pd complex catalyzes the Suzuki-Miyaura reaction between the boronic acid and the bromine groups of the reactants to form the polymeric structure. The Pd complex is sensitive to air, so it is added last and the atmosphere in the flask is changed to an inert nitrogen atmosphere over a Schlenk line. The reaction is allowed to run at 150 °C for 20 hours.
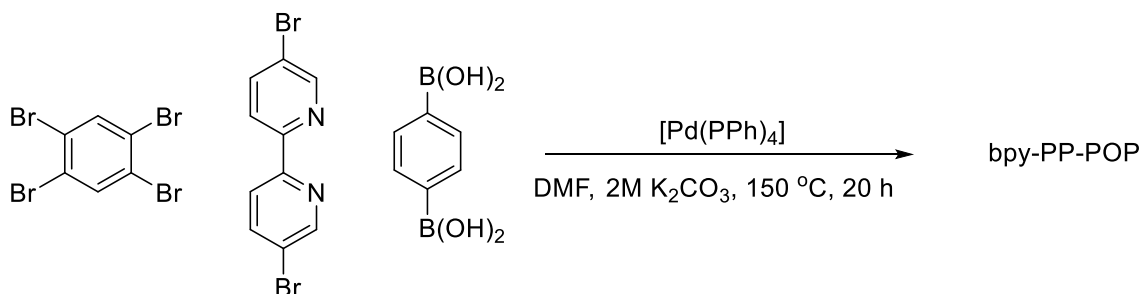
The resulting mixture is cooled down and transferred to a glass beaker containing 600 mL of water. The solid polymer material is collected on a glass filter, where it is washed three times with water and three times with methanol before being dried overnight in a vacuum oven.

Removal of palladium

The removal of any deposited palladium during the polymerization is done in a two-step process; Oxidation in acid and mixing with a solution of EDTA ligands. In the acid treatment, the dried polymer is added to a round-bottom flask fitted with a reflux condenser and a stir bar. A solution of 100 mL of ethanol, 50 mL H_2O, 50 mL HCl 32% and 10 mL H_2O_2 30% is added and the mixture is left to react overnight at room temperature. The reaction is continued the next day for 4 hours at 60 °C. Collection and washing of the polymer is done in the same manner as after polymerization.

To remove coordinated Pd in the polymer structure a solution of 150 mL ethanol, 75 mL H_2O, 5 mL NH_3 30% and 7.5 g of Na$_2$EDTA·H_2O are prepared. The polymer and solution is added to a round-bottom flask with a stir bar and connected to a condenser. The mixture is stirred for 24 hours at 70 °C, before the solids are filtered and washed in the same manner as earlier. The obtained yellow powder is labelled as bpy-PP-POP. Additional materials containing double and quadruple amounts of bpy ligands are

produced as well. A separate sample containing phenanthroline ligands, rather than bipyridine ligands, is also produced for comparison. The reactant amount used can be found in Table 5.1 below.

Table 5.1: Reactant amount used for synthesizing POP-materials

Sample	1,2,4,5-tetrabromobenzene	1,4-diboronic acid benzene	4,4'-dibromo-2,2'-bipyridine or 3,8-dibromo-1,10-phenanthroline
PP-POP	3.38 mmol	7.78 mmol	-
bpy-PP-POP	3.34 mmol	7.78 mmol	1.09 mmol
2bpy-PP-POP	2.80 mmol	7.78 mmol	2.19 mmol
4bpy-PP-POP	1.70 mmol	7.78 mmol	4.36 mmol
Phen-PP-POP	3.34 mmol	7.78 mmol	1.09 mmol

5.2. Material characterization

Composition data obtained from elemental analysis and XPS indicates that the polymers consist of about 85-88 atom% carbon, 4-8 atom% nitrogen and a small percentage of oxygen (Table 5.). Elemental analysis (CHN analysis) indicates similar levels of nitrogen content in the bulk of the polymeric structures, but shows that the Phen-PP-POP has a notably lower carbon content. The nitrogen content for the three bpy-PP-POP catalysts does not match the expected ratio of 1:2:4, but instead they have a ratio of 1:1.5:2.5. Regardless, they will be referred to as 2bpy-PP-POP and 4bpy-PP-POP.

Table 5.2: Compositional analysis of the polymeric materials.

Sample	Composition from XPS (atom%)			Composition from Elemental Analysis (wt%)		
	C	N	O	C	N	H
PP-POP	-	-	-	79.2%	0.46%	4.43%
bpy-PP-POP	87%	4%	6%	75.2%	3.28%	4.32%
2bpy-PP-POP	84%	5%	6%	72.2%	4.90%	4.11%
4bpy-PP-POP	88%	8%	3%	78.8%	8.22%	4.33%
Phen-PP-POP	-	-	-	53.0%	3.81%	3.20%

The XPS survey also indicates a small amount of Cl on the surface of the materials, which is likely a remnant from the acid treatment used for removing Pd. The signal for Pd can be found at 335 eV, but the survey scan show than all but trace amounts of Pd have successfully been removed, as seen in Figure 5.2: Survey scan of bpy-PP-POP. Trace amounts of Si are likely due to tiny pieces from the glass filters used during the several washing steps. This would explain the nanosize pieces of silica sometimes seen in TEM, which were identified using EDS.
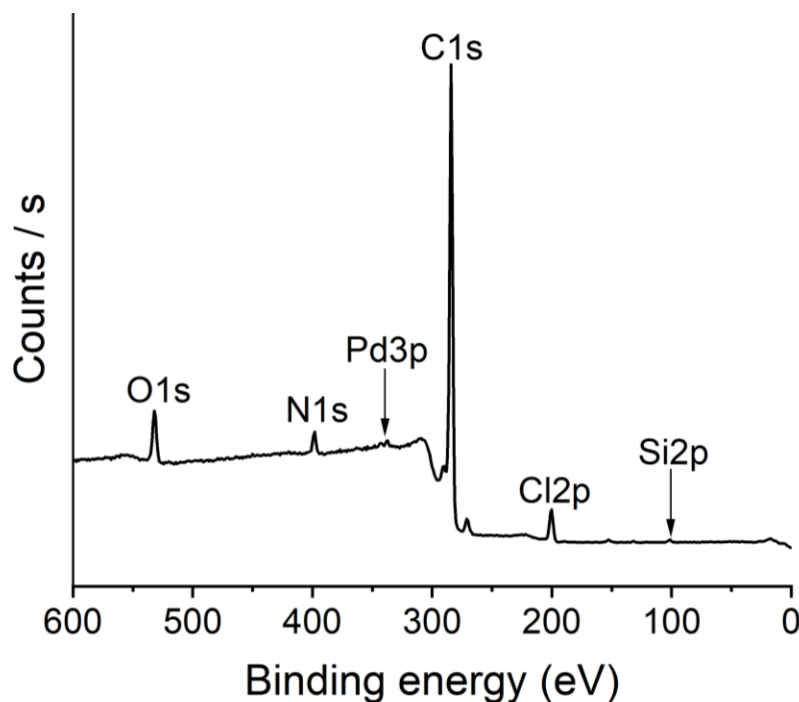
Figure 5.2: Survey scan of bpy-PP-POP. Samples were fastened on carbon tabs for analysis. Survey scans from the remaining materials show the same peaks.

Close analysis of the C1s and N1s peaks shows only one peak for each (Appendix B.1). The C1s peak (284 eV) is from C-C bonds with no peaks from oxidized carbon (~286 eV or ~289 eV). The N1s peak is found at 398.3 eV, which belongs to the pyridinic-N found in the bipyridine group [50]. Data from Ryan Wang's group finds that the material contains 0.00045 mmol bpy/mg polymer. Isotherms from nitrogen-physisorption show that only the PP-POP has any measurable porosity (Figure 5., Left). The unusual behavior of the POPs in nitrogen physisorption has been documented in the past, and despite having low absorption values for nitrogen, the materials may still absorb other gasses in its micropores[74], [148]. Thermogravimetric (TGA) measurements indicate that the polymer is stable in air up to 400 °C before experiencing rapid loss of mass (Figure 5., Right).
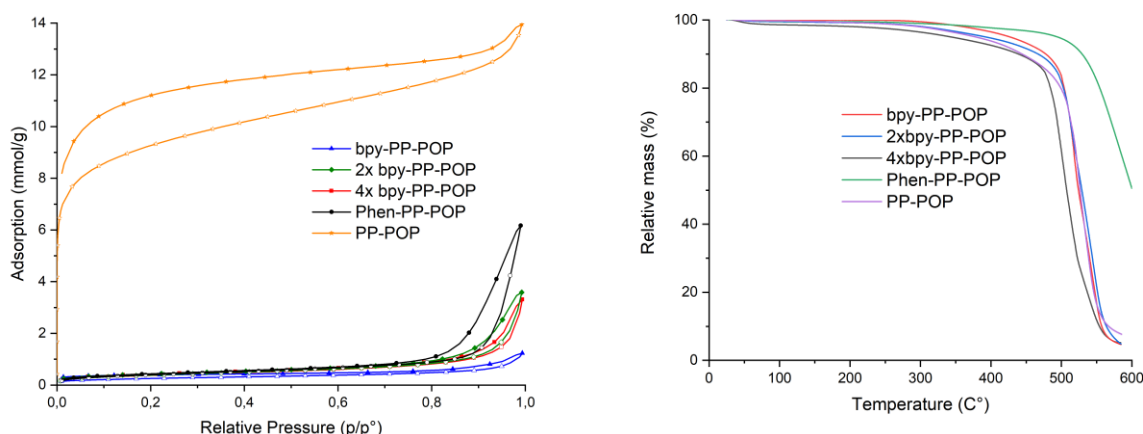
Figure 5.3: (Left) Isotherms from nitrogen-physisorption. (Right) TGA analysis of POP materials showing significant loss above 500 °C.

The pore volume is determined to be 0.39 cm^3/g with a BET surface area of 670 m^2/g. The isotherms of the ligand containing polymers indicate limited porosity compared to the stating material. The BET surface and porevolume of the materials are listed in Table 5.3.

Table 5.3: Nitrogen physisorption data for the POP materials.

Sample	BET Surface area	Porevolume (Adsorption)
PP-POP	670 m^2/g	0.39 cm^3/g
bpy-PP-POP	20 m^2/g	0.03 cm^3/g
2bpy-PP-POP	31 m^2/g	0.06 cm^3/g
4bpy-PP-POP	30 m^2/g	0.05 cm^3/g
Phen-PP-POP	33 m^2/g	0.10 cm^3/g

SEM and TEM images of the bpy-PP-POP show an amorphous material (Figure 5.). The overall morphology of the sample is seemingly homogeneous. This is supported by XRD analysis of the sample, which only shows a broad peak around 2θ = 19° (Appendix B.2). There are no Pd nanoparticles visible on the SEM images or crystalline peaks corresponding to Pd in the XRD spectrum, indicating that the post-polymerization treatment of the polymers with peroxide and EDTA successfully removed Pd.
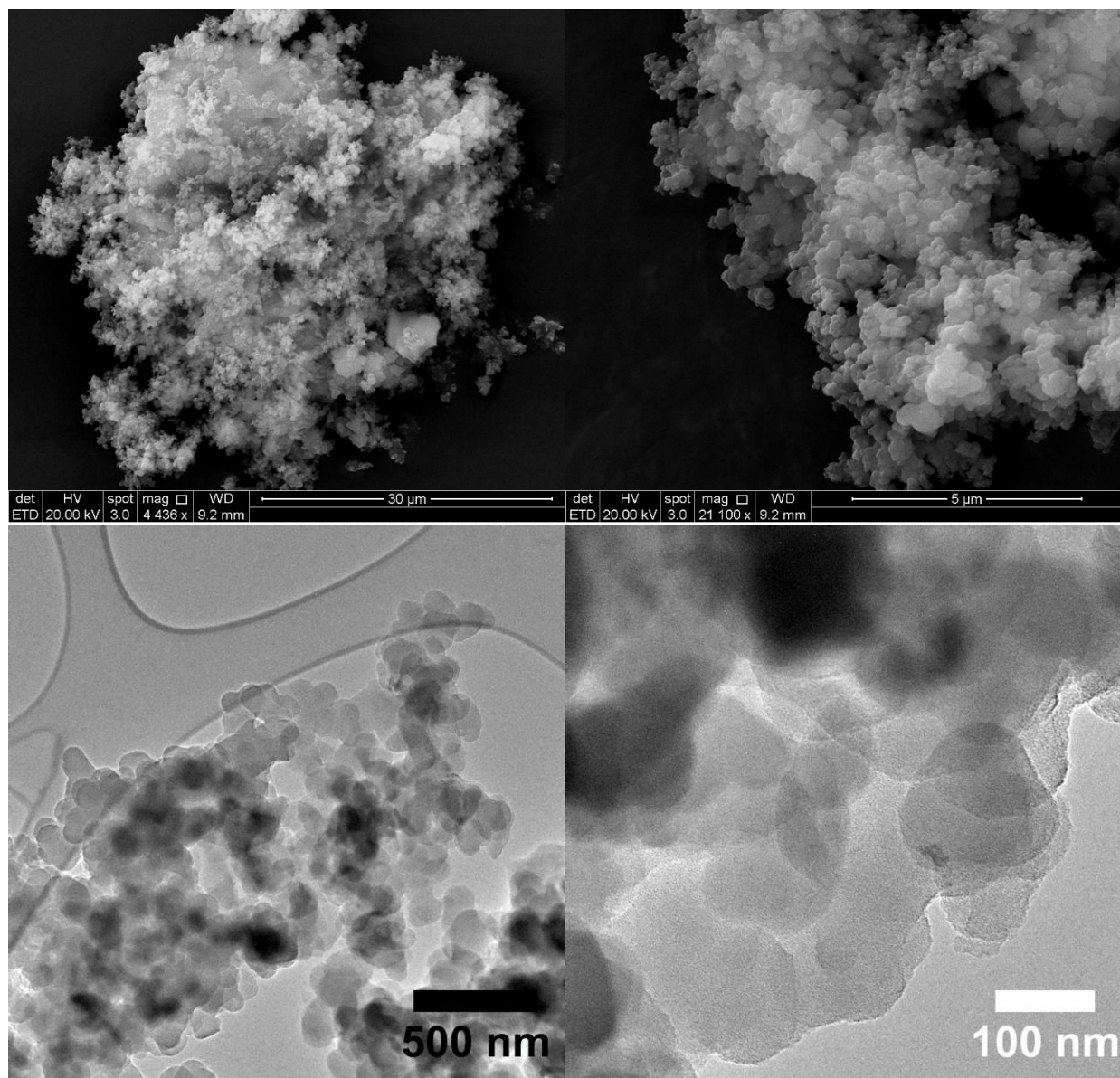
Figure 5.4: SEM (top) and TEM images (bottom) of bpy-PP-POP showing an amorphous material.

5.3. Hydrogenation of CO_2

A standard reaction consisted of 5 mL of an aqueous solution of 1 M Et_3N mixed with $IrCl_3$ and the desired amount of polymer. Exact amounts of polymer and Ir precursor are indicated for each experiment. The mixture is added to a 70 mL stainless steel autoclave with a Teflon lining, which is flushed three times with nitrogen to remove air, before being filled with 28 bar of CO_2 and 28 bar of H_2. The autoclave is mounted on a magnetic stirrer fitted with a heating mantel and the reaction is heated to 140 °C over 1 hour and left to run for an additional 24 hours. Upon completion, the autoclave is rapidly cooled down in ice. 0.5 mL of the resulting mixture is filtered using 0.22 μm syringe filters, and combined with 0.2 mL of D_2O before the formate concentration is determined by NMR. The yield is calculated based on the ratio of Et_3N to formate, since the product formation is expected to require a

corresponding amount of base. The pressures listed in the following tables correspond to the pressure at ambient temperature.

5.3.1. Initial optimization

Initially each of the polymers were tested with 0.01 M of $IrCl_3$. The amount of polymer added was adjusted to theoretically have one ligand for each atom of Ir^{3+} in the solution. The bpy-PP-POP and Phen-PP-POP both gave good yields (32% and 34%) providing a starting point for further analysis. Interestingly, having a higher amount of bipyridine (bpy) ligand in the polyphenylene (PP) structure had a negative effect, while using the same amount of $IrCl_3$.

Table 5.4: Results from the hydrogenation of CO_2 utilizing the different polymers with equal amount of Ir and ligands.

POP	Ir conc.	P (CO_2)	P (H_2)	P (Total)	Yield[a]	TON[b]
bpy-PP-POP (111 mg)	0.01 M	28	25.3	53.3	32%	36
2xbpy-PP-POP (56 mg)	0.01 M	25	22.5	47.5	24%	27
4xbpy-PP-POP (28 mg)	0.01 M	25	21.3	46.3	7%	8
Phen-PP-POP (111 mg)	0.01 M	30	26.3	56.3	34%	38

[a] Yield quantified by ^{1}H-NMR using D_2O as solvent and Et_3N as a standard.
[b] TON calculated by the following equation: the $n_{(formate)}/n_{(Ir)}$ where $n_{(formate)}$ is given by yield*$n_{(Et3N)}$ and the total amount of iridium is estimated based on a iridium content of 52% for the $IrCl_3$*xH_2O salt.

The turnover numbers for the reactions are low due to the relatively high concentration of Ir^{3+}. To test the limits of the catalysts, both bpy-PP-POP and Phen-PP-POP were investigated using lower concentrations of $IrCl_3$. These results can be found in table 5.5. Phen-PP-POP showed a significant loss in activity with the yield decreasing from 34% to 12%, while bpy-PP-POP showed an increase in yield from 32% to 42% under the same conditions. Lowering the concentration even further down to 0.00001 M of Ir did not give a corresponding loss in activity leading to a higher TON of 20041.

Table 5.5: Results from reducing the concentration of Ir precursor.

POP	Ir conc.	P (Total)	Yield[a]	TON[b]
Phen-PP-POP (111 mg)	0.0001 M	54	12%	1336
bpy-PP-POP (111 mg)	0.0001 M	54	42%	4676
bpy-PP-POP (111 mg)	0.00001 M	56	18%	20041
bpy-PP-POP (222 mg)	0.00001 M	54	16%	17814
2xbpy-PP-POP (56 mg)	0.00001 M	58	5%	5567
4xbpy-PP-POP (28 mg)	0.00001 M	55	5%	5567

[a] Yield quantified by ^{1}H-NMR using D_2O as solvent and Et_3N as a standard.
[b] TON calculated by the following equation: the $n_{(formate)}/n_{(Ir)}$ where $n_{(formate)}$ is given by yield*$n_{(Et3N)}$ and the total amount of iridium is estimated based on a iridium content of 52% for the $IrCl_3$*xH_2O salt.

Doubling the amount of polymer added from 111 mg to 222 mg for the same concentration of Ir lead to a small loss of activity from 18% to 16%. The polymers with double and quadruple concentration of ligands embedded in the polymer did not perform better than bpy-PP-POP, with both of them giving 5% yield. Lowering the concentration of Ir further did not lead to an improvement in the TON of bpy-PP-POP. bpy-pp-POP was chosen for continued study, due to it having the highest yield and TON. The concentration of Ir was kept at 0.00001 M in the following experiments in order to minimize the risk of forming nanoparticles and to achieve the highest TON. Running the reaction for 24 hours at 140 °C and 56 bar are considered to be the standard reaction parameters moving forward unless otherwise specified.

5.3.2. Activity and reusability of bpy-PP-POP

A number of control experiments and stability tests were conducted, to examine the stability, reusability and heterogeneous nature of the catalysts. These are summarized in Table 5.6.

Table 5.6: List of experiments including different precursors, commercial counterparts, reusability and control experiments. The K[IrbpyCl$_4$] salt used for Entry 7 was synthesized according to reported literature [149].

$$CO_2 + H_2 \xrightarrow[\substack{1 \text{ M Et}_3\text{N (aq) (5mL)}, \\ \text{time, temp}}]{\text{[Ir], ligand}} \quad H\text{-}C(=O)\text{-}O^-$$

Entry	Ligand	[Ir] (conc.)	time	temp	P (Total)	Yield[a]	TON[b]
1	bpy-PP-POP	IrCl$_3$ (0.00001 M)	48 h	140 °C	56	15%	16701
2	bpy-PP-POP	[IrCp*Cl]$_2$ (0.00001 M)	24 h	140 °C	57	12%	13360
3	bpy-PP-POP	[Ir(cod)MeO]$_2$ (0.00001 M)	24 h	140 °C	57	10%	11134
4	bpy-PP-POP	IrCl$_3$ (0.00001 M)	24 h	120 °C	54	2%	2227
5	2,2'-bipyridine (0.01 M)	IrCl$_3$ (0.00001 M)	24 h	140 °C	57	<1%	-
6	bpy-PP-POP + 2,2'-bipyridine[1]	IrCl$_3$ (0.00001 M)	24 h	140 °C	55	6%	6080
7	-	K[IrbpyCl$_4$] (0.00001 M)	24 h	140 °C	57	2%	2227
8	-	Ir/C 0.0001 M[2]	24 h	140 °C	56	3%¨	3340
9	bpy-PP-POP (used)	-	24 h	140 °C	54	12%	13361
10	bpy-PP-POP (used)	IrCl$_3$ (0.00001 M)	24 h	140 °C	55	17%	18928
11	-	-	24 h	140 °C	56	<1%	-
12	bpy-PP-POP	-	24 h	140 °C	55	6%	6680
13	-	IrCl$_3$ (0.00001 M)	24 h	140 °C	55	<1%	-

[a] Yield quantified by ^{1}H-NMR using D$_2$O as solvent and Et$_3$N as a standard.
[b] TON calculated by the following equation: the $n_{(formate)}/n_{(Ir)}$ where $n_{(formate)}$ is given by yield*$n_{(Et3N)}$ and the total amount of iridium is estimated based on a iridium content of 52% for the IrCl$_3$*xH$_2$O salt.
[1] The amount of added 2,2'-bipyridine is 1 equivalent of the added iridium.
[2] Commercially available Ir/C was bought from VWR (Product number: 38330.06 - Iridium on activated carbon 1% wetted with ca. 50% water, pulver, reduced)

Extending the reaction time to 48 hours gave the same yield as 24 hours (Entry 1). Using other Ir precursors instead of IrCl$_3$, like [IrCp*Cl]$_2$ (Entry 2) and [Ir(COD)MeO]$_2$ (Entry 3), still resulted in the formation of formate, yielding 12% and 10% respectively. Lowering the temperature to 120 °C resulted in a dramatic drop in activity, lowering the yield from 16% at 140 °C to 2% at 120 °C (Entry 4).

The reaction was also conducted with the homogeneous ligand, 2,2'-bipyridine (bpy) to see whether its incorporation into the polymeric structure affects its reactivity. bpy was added in excess (0.01 M compared to 10 µM of IrCl$_3$), but the amount of formate in the product mixture was barely detectable (Entry 5). Running the reaction with both the polymer and homogeneous ligand present (Entry 6), resulted in a yield of 6%, which is significantly lower compared to having no homogeneous ligand added.

If the reaction is run with an Ir-bipyridine salt to ensure a 1:1 ratio between Ir and bipyridine (Entry 7), the yield is slightly higher (2%) compared to having an excess amount of bpy. A commercial Ir catalyst on activated carbon (Ir/C) was tested for comparison. Despite having 10 times the amount of Ir in the reaction mixture (0.0001 M), the yield of formate was only 3% (Entry 8).

Reusability of the bpy-PP-POP was examined by isolating the polymer after a standard reaction using filtration followed by washing it three times with water. Running the reaction with the recycled polymer under the same conditions, without the addition of new $IrCl_3$, caused the yield to drop from 16% down to 12% (Entry 9). If new $IrCl_3$ was added in addition to the recycled polymer, the yield went back up to 17% (Entry 10). The remaining three experiments listed here (Entry 11-13) show that no measurable amount of formate is formed when using no catalysts or just the $IrCl_3$ precursor (Entry 11 and 13). Running the reaction with the bpy-PP-POP alone yields 6% of formate (Entry 12).

5.4.   Decomposition of formic acid

The ideal scenario would be to have a catalyst capable of catalyzing both the synthesis and decomposition of formic acid depending on the reaction conditions. This would allow for a single system to be used for the storage and release of hydrogen. For this reason, we also tested the ability of our bpy-PP-POPs in the gas phase to perform the dehydrogenation of formic acid. The bpy-PP-POP materials were tested in the same setup as described in Chapter 4. Since the reaction takes place over a solid material, the polymer has to be combined with the $IrCl_3$ beforehand rather than *in situ*. This was accomplished via both incipient-wetness impregnation and by metalation. Incipient-wetness impregnation affords better control over the Ir loading, while the deposition in solution should minimize the risk of particle formation and increase the saturation of available bipyridine sites. Three samples with different Ir loadings were prepared for the dehydrogenation of formic acid. One sample was prepared by incipient-wetness to obtain a loading equal to the best hydrogenation catalyst. The other two samples were prepared by metalation, by stirring the polymer in solutions containing one and three equivalents of $IrCl_3$ compared to the number of ligand sites available.

5.4.1. Impregnation of bpy-PP-POP

The two metalation samples were prepared by adding $IrCl_3$ to a vial containing 2 mL of a 3:1 mixture of CH_3CN and water. The mixture was stirred until the salt was completely dissolved yielding an orange solution. 50 mg of bpy-PP-POP was added and stirred overnight at room temperature. The impregnated sample was isolated by filtration on a glass filter and washed with water, CH_3CN and diethyl ether. The amount of $IrCl_3$ depends on the sample. One was made with three equivalents of Ir^{3+} per ligand site available (0.0225 mmol) and is termed Ir3-bpy-PP-POP. The other is made with only one equivalent of Ir^{3+} (0.0075 mmol) and named Ir1-bpy-PP-POP.

A third sample was prepared using incipient-wetness using the same amount of Ir as for the standard experiment during the hydrogenation of CO_2. 42 µL of an $IrCl_3$ solution (0.5 mg/mL) was added to 100 mg of bpy-PP-POP under intense stirring. The sample was dried in a vacuum oven overnight to yield the final product termed Ir0.001-bpy-PP-POP.

5.4.2. Experimental procedure

30 mg of the impregnated polymer was mixed with 270 mg of fractionated quartz (355-700 nm) to prevent plugging of the flow. A nitrogen flow of 50 mL/min saturated with formic acid was passed over the catalyst. The sample was heated from 20 to 200 °C at a rate of 1 °C/ min. The remaining experimental conditions are identical to those described in Section 4.1.

5.4.3. Results

Results from the decomposition of formic acid using the three bpy-PP-POPs are displayed in Figure 5.5. Only Ir3-bpy-PP-POP showed any notable activity toward decomposition of formic acid to yield hydrogen. No yield is observed below 140 °C making it significantly less active than the materials covered in Chapter 4. Fortunately, the conversion toward hydrogen and CO_2 is selective with only a barely registrable signal from CO appearing above 190 °C.
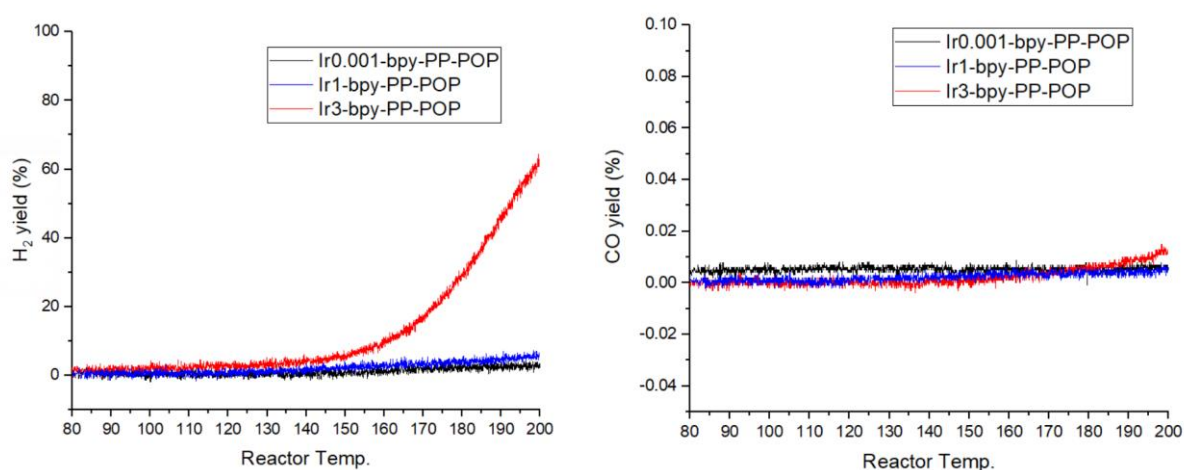

Figure 5.5: Results from decomposition of formic acid. (Left) Hydrogen yield as a function of reactor temperature. (Right) Yield of unwanted CO as a function of reactor temperature.

The activity is significantly lower compared to the nitrogen-doped ordered mesoporous carbon materials (NOMCs) described in chapter 4, but the high selectivity towards dehydrogenation is a desirable trait.

5.5.   Additional CO_2 hydrogenations using NOMC

The samples created as part of the project on decomposition of formic acid were also tested for the hydrogenation of CO_2. Previous studies of carbon materials like mesoporous graphitic carbon nitride (mpg-C_3N_4) and graphene carbon nanotubes have shown some catalytic activity towards CO_2 hydrogenation when using Pd or Pd alloys [144], [150]. The experiments were conducted at pressures of 10-50 bar and temperatures between 40-150 °C, but their carbon catalysts had a high content of Pd (5-10 wt%) and low TON after 24 hours (<100).

Several of the synthesized NOMC materials containing precious metals were tested and the results are summarized in Table 5.7. Pd@NOMC proved to have TON comparable to those found in the previous studies even at a total pressure of 30 bar and a temperature of 80 °C. The TON values are lower than those of homogeneous catalysts and heterogenized homogeneous catalyst, which is expected, as these use single atoms per active site, compared to the nanoparticles found in most heterogeneous catalysts.

The NOMC support showed no measurable yield by itself. The best result was achieved by raising both temperature and pressure to 150 °C and 50 bar respectively. The ratio of H_2 to CO_2 was adjusted to 1:2 as this was shown to have a positive effect on the yield (Entry 5 and 7).

Table 5.7: Results from the hydrogenation of CO_2 using NOMC materials.

$$CO_2 + H_2 \xrightarrow[\substack{\text{1 M Et}_3\text{N (aq) (5mL),}\\ \text{time, temp}}]{\text{catalysts}} \quad H-CO_2^-$$

Entry	Catalyst	Amount	Time	Temperature	Pressure H_2:CO_2 bar	Yield[a]	TON[b]
1	NOMC	53.4 mg	24 h	80 °C	15:15	<0.1%	<1
2	1wt% PtNOMC	97.9 mg	24 h	80 °C	15:15	0.3%	3
3	1 wt% RuNOMC	50.5 mg	24 h	80 °C	15:15	0.6%	6
4	1 wt% AuPdNOMC	50.3 mg	24 h	80 °C	15:15	4.6%	47
5	1 wt% PdNOMC	53.4 mg	24 h	80 °C	15:15	2.2%	22
6	1 wt% PdNOMC	53.4 mg	20 h	150 °C	15:15	7.1%	72
7	1 wt% PdNOMC	50.3 mg	20 h	80 °C	16:33	2.6%	27
8	1 wt% PdNOMC	50.9 mg	20 h	80 °C	25:25	2.2%¨	22
9	1 wt% PdNOMC	53.0 mg	20 h	150 °C	16:33	18%	187
10	1 wt% PdOMC	53.1 mg	20 h	150 °C	16:33	0.1%	<1
11	**1 wt% IrNOMC**	**2.6 mg**	**24 h**	**140 °C**	**28:28**	**43%**	**15895**

[a] Yield quantified by ^{1}H-NMR using D_2O as solvent and Et_3N as a standard.
[b] TON calculated by the following equation: the $n_{(formate)}/n_{(Ir)}$ where $n_{(formate)}$ is given by yield*$n_{(Et3N)}$.

For comparison with the bpy-PP-POP materials, a NOMC catalyst containing 1 wt% of Ir was also tested under the same reaction conditions (Entry 11). The catalyst showed excellent activity and TON compared to the remaining catalysts at a temperature of 140 °C and 56 bar of pressure. This result needs to be verified and is a promising starting point for a future project.

5.6.   Discussion

Our highest TON of 20.041 for the hydrogenation of CO_2 using bpy-PP-POP compares well to that of a similar study by Yoon et al. using an iridium POP based on phenanthroline [147]. At similar pressure and temperature (140 °C and 60 bar), their IrCl$_3$-Phen-POP reached a TON of 11.650. This is expected to be due to the reaction times being different (2 hours compared to 24 hours).

IrCl$_3$ proved to be the best of the tested precursors and the control experiments confirm the need for both the Ir source and the polymer to be present in order to obtain good yields of formate. Considering how increasing the reaction time from 24 to 48 hours did not show a change in yield, it is likely that either the catalyst is deactivated or the reaction has reached an equilibrium. Since higher yields were obtained during the initial tests (42% using bpy-PP-POP and 0.0001 M IrCl$_3$), deactivation is likely the explanation. The recycling experiments indicate that the catalyst is indeed being deactivated during the reaction, as it did lose 25% of its activity during recycling (yield went from 16% to 12%). The addition of new Ir could restore the activity, which suggests that the Ir is either lost or has become inactive over time. This could be due to the Ir sintering into nanoparticles, which are less active compared to

individual atoms of Ir bonded to the bipyridine ligands in the polymer structure. This is supported by the low activity of the commercial catalyst, Ir/C, which consists entirely of Ir nanoparticles with a size of a few nanometers. STEM images of the bpy-PP-POP after reaction can be seen below in Figure 5.6.
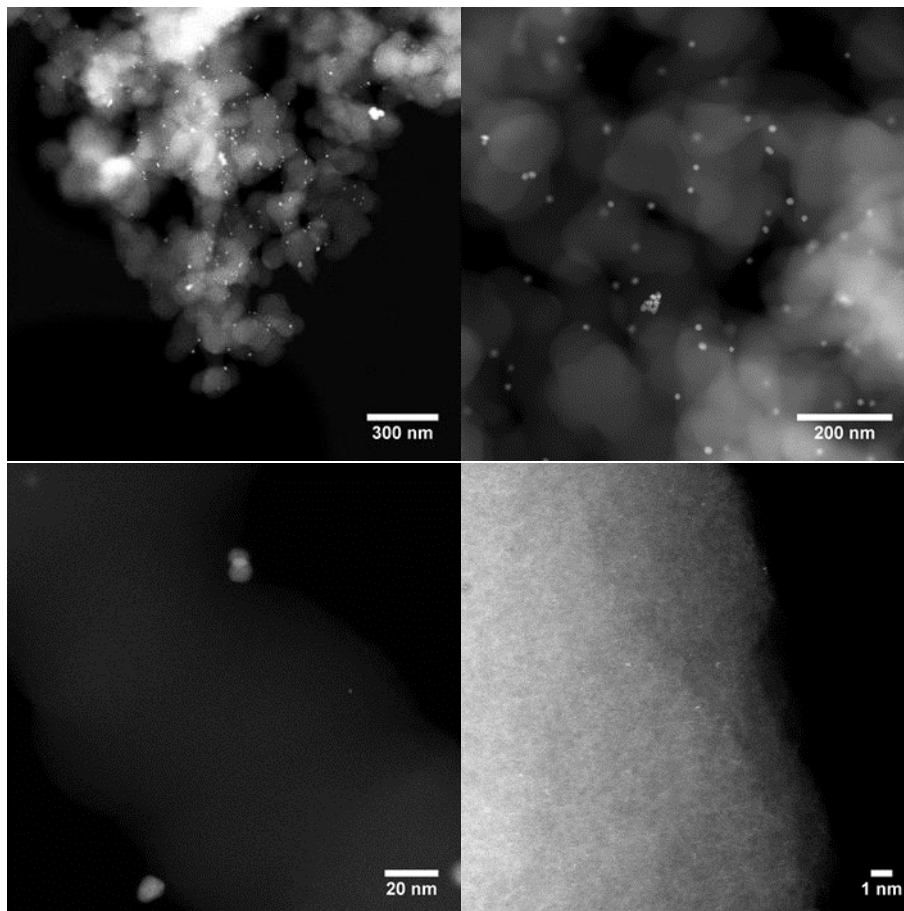

Figure 5.6: STEM of bpy-PP-POP after use in CO_2-hydrogenation. Enlarged version of bottom right image can be found in Appendix B.3.

It is clear from the images that several Ir nanoparticles have formed on the polymer structure. They seem to be predominantly positioned at the surface and are about 10 nm in size. Looking closer (bottom right) also reveals the presence of single atoms. They are hard to detect even in high-resolution STEM, due to being embedded within the polymer structure, but can still be visualized near the edges of the polymer. The limited porosity measured by nitrogen physisorption may be due to inaccuracies resulting from the use of nitrogen as the adsorbent [151]. In order to get around these limitations, it might be beneficial to conduct the physisorption analysis with CO_2 at 273K, which would help prevent inaccuracies due to kinetic restrictions.

A common source of deactivation, which might also play a role in the loss of activity, is loss of metal due to leaching. The filtration process used for collecting the polymer after reaction includes washing it three times with water. This is to remove any unreacted reagents, bound product and Et_3N solvent

trapped in the polymer. There is a risk of Ir being washed out during this process, leaving the catalyst with less active sites. The recovery of activity by addition of more $IrCl_3$ could support this assumption (Table 5.6 Entry 10). This could be confirmed by doing ICP on the product mixture after filtering off the catalyst.

The experiments using $IrCl_3$ and the bpy-PP-POP by themselves having low activity indicates the needs for both an active metal and a support being present for the reaction to work. The heterogeneous catalyst shows higher activity than its homogeneous counterpart as shown by the experiments containing equal and excess amount of the free homogeneous ligands. This might be due to the bpy ligand binding too strongly to the Ir^{+3} ions. Each individual Ir^{3+} can accommodate three bpy ligands, which might saturate them completely. In the heterogeneous structure, it is unlikely that several bpy ligands bind to the same Ir^{+3} ion due to their incorporation in the polymer structure. This is supported by the experiment containing both the bpy-PP-POP with $IrCl_3$ and the addition of homogeneous bpy ligand, which had lower yield compared to the same experiment without the homogeneous ligand. This might also explain the decrease in activity when more ligands are present in the polymer structure, as both 2bpy-PP-POP and 4bpy-PP-POP showed much lower activity.

The idea of using embedded ligands to limit the amount of chelating ligands around an active site has been shown previously by Sawamura et al. [152]. Their experiments with biphosphine embedded in polystyrene allowed first row transition metals to catalyze reactions, which were not possible using their homogeneous counterpart. They attribute this to the limited mobility of the biphosphine, allowing only for the formation of monochelating species. However, even when using a prepared salt of $K[IrbpyCl_4]$ with a single bpy ligand per Ir^{3+} ion, the yield is still only about 2%. This suggests that the heterogeneous bpy-PP-POP itself may play a role in the increase of the activity. The reusability experiments with Ir-bpy-PP-POP show that the POP support can be easily isolated and reused, but requires the addition of new Ir likely due to the agglomeration of Ir. Sintering and leaching remain the key challenges for the use of heterogenized homogenous catalysts for hydrogenation of CO_2 [138], [153].

5.7.   Summary
The synthesized bpy-PP-POP materials showed the potential for single atom catalysts in the hydrogenation of CO_2 to form formate. A combination of bpy-PP-POP with a ligand loading of 0.00045 mmol/mg with 0.00001 M of $IrCl_3$ provided the best result at 140 °C and 56 bar of pressure. This achieved a maximum yield of 18% H_2 corresponding to a TON of 20.041 after 24 hours. High selectivity toward dehydrogenation of formic acid indicates that with further optimizations the POP materials can catalyze the reversible storage of hydrogen, allowing formic acid to be used as a liquid organic hydrogen carrier. Further experiments are still needed to investigate the deactivation mechanism and the special influence of embedding the ligand in the polymeric backbone. In addition, iridium deposited on a NOMC support showed promise during the initial testing under the same conditions.

Chapter 6.   Hydrosilylation of ketones

This chapter concerns our work on a simple synthesis method of bimetallic carbon catalysts, through the carbonization of ZIF-67 doped with copper. The resulting CoCu materials were tested for the hydrosilylation of ketones. Mechanistic studies as well as a scope are included to illustrate the potential of this preparation method. The magnetic properties of the synthesized catalysts are expected to help ease the isolation of the used catalysts, making it a simple matter to recycle the catalysts. The results and figures presented here have been published in Catalysis Letters back in 2019 [154].

Synthesizing complex molecules is normally a multi-step process involving a myriad of different reaction conditions. Careful considerations have to be made for each step to ensure that only the desired changes are made. If for example oxidizing conditions are used to oxidize an alcohol to a carboxylic acid, other functional groups may also undergo oxidization. This can be avoided by adding protective groups to the functionalities that should remain. Hydrosilylation is a reaction, which involves the addition of silyl groups (Si-H) to unsaturated bonds of carbon, nitrogen and oxygen.
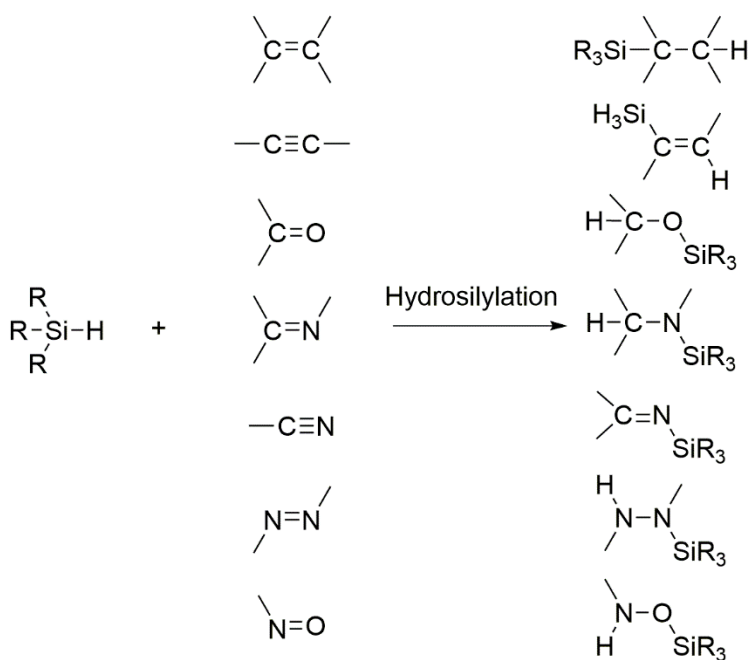

Figure 6.1: Hydrosilylation reactions involving a silyl group (R_3Si-H) and different unsaturated bonds. The unspecified R-groups may be different and are typically alkyls.

The hydrosilylation reaction adds the silyl group across the unsaturated bond, providing an easy way of forming organosilanes. The added silyl group can act as a protective group, which may be removed using acids or flourides. In this project, we will be focusing on the hydrosilylation of ketones to form silyl enol ethers. The reaction achieves a double functionalization of the ketone, by reducing it to an alcohol group and adding a protective group. This process is used for the formation of intermediates in a range of

industrial applications. Notable examples of its use include the pharmaceutical and agricultural industry, where it is used for the production of fine chemicals [155], [156]. Removal of the silyl group is simple, and can often be done through an acid treatment.
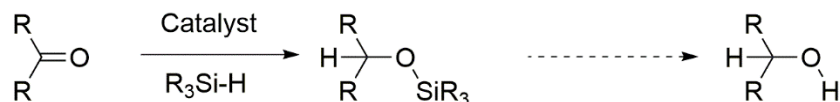

Figure 6.2: Reaction scheme for the formation of silyl enol ethers and the subsequent removal of the protective group.

Current research and catalysts

Hydrosilylation is traditionally accomplished using homogeneous complexes with precious metals like Ru, Pd or Pt [156], [157]. For industrial scale hydrosilylation, the majority of reactions are performed using Pt catalysts like Speier's and Karstedt's catalysts. Hydrosilylation of ketones dates back to the 1970's, where it was originally conducted using Wilkinson's catalyst, a homogenous rhodium catalyst with triphenylphosphine ligands [158], [159]. In the past two decades, various groups have managed to perform hydrosilylation of ketones using heterogeneous catalysts containing precious metals [155], [160], [161] and even some containing base metals like Co, Fe, Ni and Cu [162]–[165].

The reaction mechanism depends on the catalyst and over the years, several pathways have been detailed. The Chalk-Harrod and modified Chalk-Harrod are the most prevalent reaction mechanisms found in literature [155], [166], [167]. A scheme outlining the mechanisms for ketones can be seen below in Figure 6.3, however the same mechanism is observed for various unsaturated carbon bonds. Both of the regular and modified mechanism start with the oxidative addition of silane to the active metal. This increases the oxidation state of the metal by +2 and is a common reaction step in various catalytic reactions. Next, the carbonyl is coordinated to the metal. Depending on the mechanism, the carbonyl is then inserted into either the [M]-Si or [M]-H bond. Finally, the product is released via reductive elimination, which forms the final bond to either -SiR$_3$ or –H and lower the oxidation state of the metal back to its initial state.
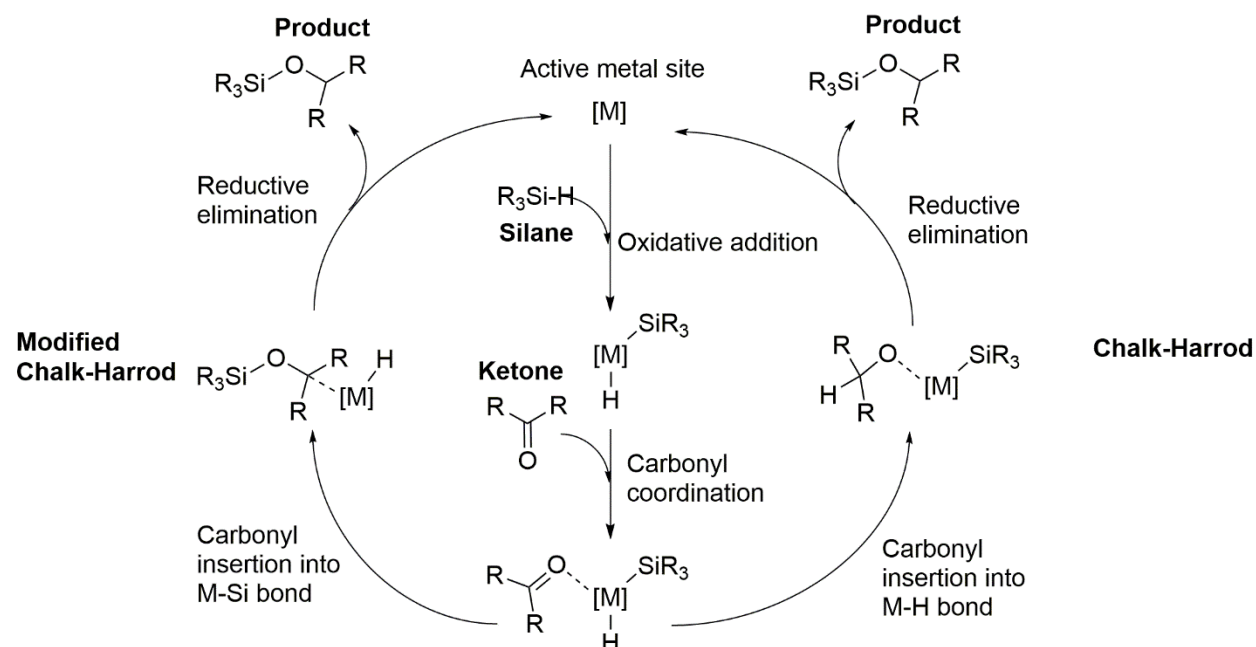
Figure 6.3: Hydrosilylation of ketones by the Chalk-Harrod and modified Chalk-Harrod mechanism.

In the case of a cobalt catalyst, a different mechanism has also been reported. Thomas *et al.* used a Co/Zr bimetallic complex for the hydrosilylation of ketones [164]. They proposed the formation of ketyl radicals instead of the carbonyl coordination in the second step of the Chalk-Harrod mechanisms. The reaction may also be initiated by the formation of silyl radicals, where the Si-H bond is broken and the resulting free radical can attack the unsaturated carbon bond [168].

When using base metals for hydrosilylation, the catalyst generally has to be bimetallic in order to obtain good yields, which can require long and complicated synthesis processes with limited control. Finding new simple ways to make bimetallic catalysts would make the transition from expensive and limited precious metals to readily available base metals easier. ZIF-67 is a cobalt MOF that belong to the family of Zeolitic Imidazolate Frameworks (ZIFs) [68], [169]. The organic linker in ZIF-67 is 2-methylimidazole, and together with Co^{2+}, it forms a cubic crystal structure with microporosity similar to that of zeolites. The two nitrogen atoms in the five-membered ring function as the binding sites for the metal ions.

Our idea was to dope the Co and N containing ZIF-67 with a solution of Cu. Previous work by our research group proved that it was possible to obtain bimetallic CoNi carbon materials using this approach [162]. Preparation of the material is done using simple incipient-wetness impregnation followed by carbonization. During the carbonization, the Cu and Co is expected to aggregate to form metal nanoparticles consisting of a CoCu alloy. The carbonized ligands of the MOF form a carbon framework for housing the nanoparticles. This is illustrated in Figure 6.4. Both Co and Cu are base metals, which are much cheaper, compared to precious metals like Au, Pt and Pd. This would provide a simple way to make nitrogen-doped carbon materials with bimetallic nanoparticles.
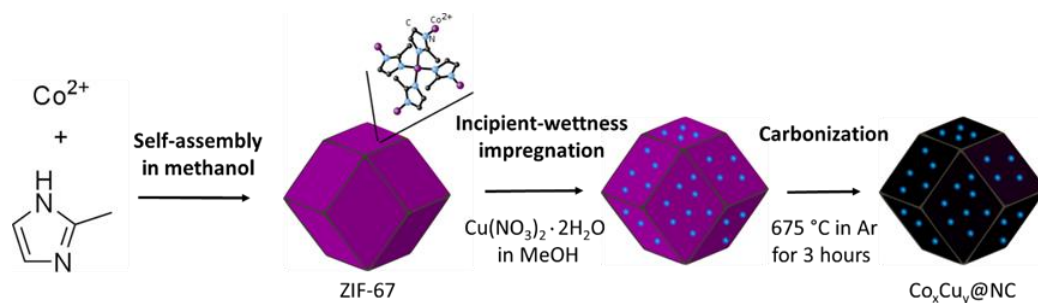
Figure 6.4: Schematic illustrating the basic process for synthesizing the MOF-derived bi-metallic catalysts. The ratio x:y between Co and Cu can be adjusted by changing the concentration of the Cu solution.

6.1. Catalyst synthesis

The first step was the synthesis of ZIF-67, which was accomplished by self-assembly in water. The process was inspired by previous work from Lou *et al.* [170]. A typical synthesis yields 0.5 g of ZIF-67. A solution of 3.284 g of 2-methylimidazole in 250 mL of methanol was prepared and mixed with a solution of 2.91 g of $Co(NO_3)_2 \cdot 6\,H_2O$ in 250 of methanol at ambient temperature. The mixture was stirred for 5 min. before being allowed to age for 24 hours. The resulting purple solution was centrifuged to collect the resulting ZIF-67 and washed with water three times.

ZIF-67 was dried in a vacuum oven overnight before impregnation. The desired amount of $Cu(NO_3)_2 \cdot 2.5\,H_2O$ was dissolve in 85 μL of methanol. The Cu solution was added dropwise to 100 mg of ZIF-67 during continuous stirring. Afterwards, the impregnated powder was heated in a tubular oven to 675 °C in an Ar atmosphere to carbonize it. The setup used a heating rate of 5 °C/min. and rested at 675 °C for 3 hours. The resulting catalysts were labelled as $Co_xCu_y@NC$, where x and y denote the intended relative amounts of Co and Cu in terms of atom%.

A separate sample containing only Cu was prepared by synthesizing the copper containing ZIF-8, using the same procedure as for ZIF-67. Instead of $Co(NO_3)_2 \cdot 6\,H_2O$, the ZIF-8 structure was synthesized using 22.7 mg of $Cu(NO_3)_2 \cdot 2.5\,H_2O$. The final sample is denoted as Cu@NC.

6.2. Material characterization

XRF and ICP-OES were used to examine the resulting Co/Cu ratios of the resulting $Co_xCu_y@NC$ materials. XRF was conducted directly on the powdered samples with no prior treatment. The results are summarized in Table 6.1 together with the $Cu(NO_3)_2 \cdot 2.5\,H_2O$ amounts added during the synthesis of each catalyst.

Table 6.1: Metal loadings in the catalytic materials determined by XRF.

Entry	Catalyst	$Cu(NO_3)_2 \cdot 2.5H_2O$ added/ 100 mg ZIF-67	Cu/Co ratio[a]
1	Co@NC	-	-
2	$Co_{99}Cu_1$@NC	1.05 mg	1/66
3	$Co_{19}Cu_1$@NC	5.55 mg	1/15.7
4	Co_9Cu_1@NC	11.7 mg	1/7.9
5	Co_3Cu_1@NC	35.1 mg	1/2.6
6	Co_1Cu_1@NC	105.2 mg	1/0.9

[a] Atomic ratios calculated from XRF

ICP-OES on all the carbon materials was conducted by heating 20 mg of each of them in aqua regia for one hour, followed by filtration to remove undissolved carbon. Each of the filtered solutions were diluted to 2% HNO_3 before measuring. The cobalt loading of the initial ZIF-67 before carbonization was 26%, which fits with the empirical formula for the crystalline structure ($C_8H_{10}N_4Co$). The cobalt loading after carbonization increases slightly, and reached about 30 wt% for all samples.

Table 6.2: ICP results from all carbon materials.

Entry	Catalyst	Weight% Co	Weight% Cu	Co/Cu ratio[a]
1	ZIF-67	26%	-	-
2	Co@NC	30%	-	-
3	$Co_{99}Cu_1$@NC	34%	0,32%	114/1
4	$Co_{19}Cu_1$@NC	31%	2,0%	17/1
5	Co_9Cu_1@NC	27%	4,0%	7/1

[a] Atomic ratios calculated from ICP

Nitrogen physisorption shows the change in porosity after carbonization, as seen in Figure 6.5, using Co_1Cu_9@NC for comparison. ZIF-67 has the isotherm of a typical microporous material (Type I), but after carbonization to Co_xCu_y@NC the isotherm has changed to a type IV, indicating a mesoporous material. The surface area of ZIF-67 is 1364 cm^2/g and the total pore volume is 0.762 cm^3/g, which fits well with previous studies by other groups [171], [172]. The porosity measured was used for estimating the amount of Cu-solution needed for the incipient-wetness impregnation. After carbonization, the surface area and pore volume drops significantly. Co_1Cu_9@NC has a surface area of 244 cm^2/g and a total pore volume of 0.079 cm^3/g. BJH adsorption and isotherms at different copper loadings can be found in the Appendix C.1 and C.2.
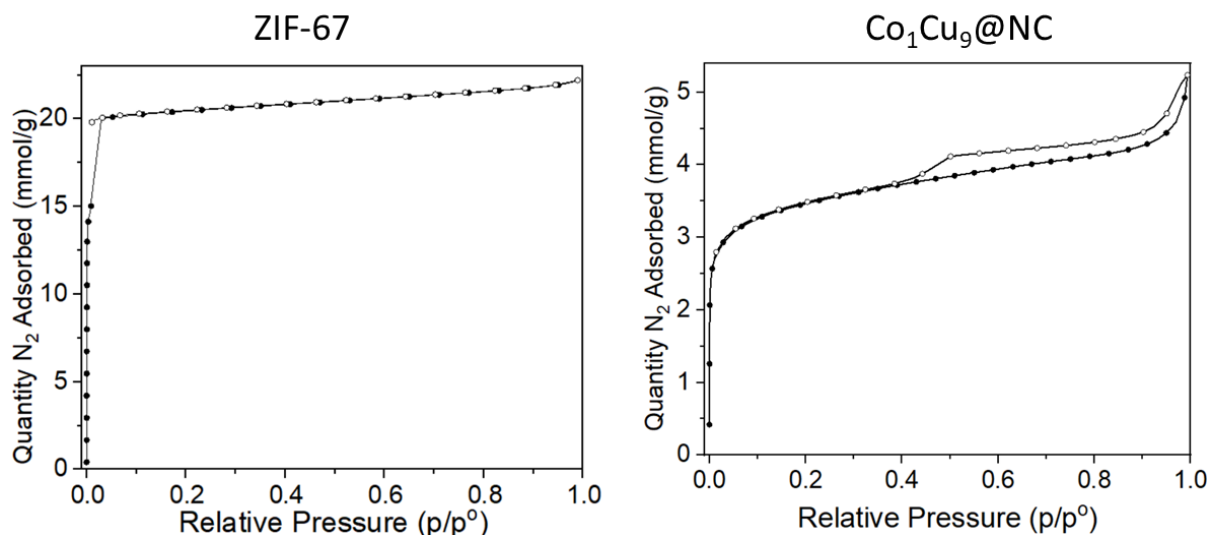
Figure 6.5: Nitrogen physisorption of ZIF-67 (Left) and Co_1Cu_9@NC (Right). ZIF-67 has an isotherm typical for microporous materials, while Co_1Cu_9@NC has a hysteresis loop indicating a mesoporous material.

SEM images of ZIF-67 (Figure 6.6 Left) shows the characteristic dodecahedron structure of the material. The crystals vary in size from about 0.5 μm to about 1 μm. After carbonization to form the Co_xCu_y@NC materials, the particles have a more distorted shape, which is still reminiscent of the original dodecahedral structure (Figure 6.6 Right).
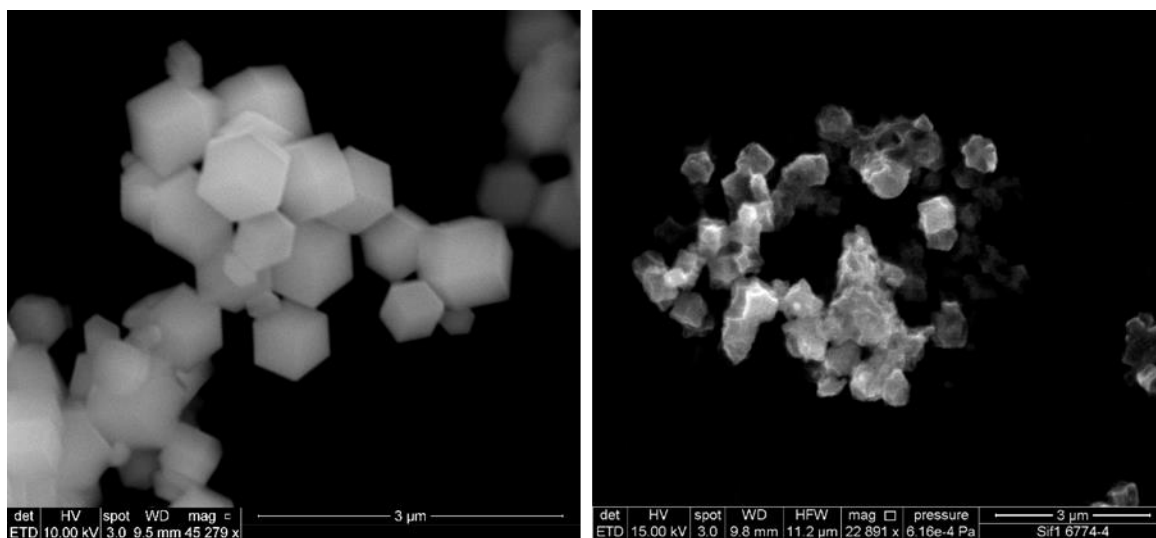

Figure 6.6: SEM images of ZIF-67 (Left) and Co_1Cu_9@NC (Right).

XRD was used to confirm the crystallinity of the samples along with an indication of the degree of alloy formation. A comparison of the materials can be seen in Figure 6.7. The graphitization of the ZIF-67 structure is indicated by the lack of peaks from the ZIF-67 structure, which features several intense peaks between 5° and 40°. An XRD spectrum of the ZIF-67 precursor can be found in Appendix C.3. The peaks were identified using data from the ICDD. Cobalt and copper each have a characteristic peak at

about 44° and 52°. A close-up of the peaks at 44° (Figure 6.7 Right) shows, that the cobalt (111) peak (44.32°) shifts slightly towards the copper (111) peak (43.31°). In the case of Co_1Cu_1@NC, which had the largest amount of copper added during synthesis, the cobalt peak has shifted to 44.20°. According to Vegard's law for alloyed materials [173], there is a linear correlation between the location of the peak from alloys and its composition. Based on the location of the Co (111) peak, the cobalt nanoparticles are estimated to contain roughly 10% copper. The Cu (111) peak is not shifted noticeably from its expected location. This suggests that the samples contain a fair amount of pure copper particles as well.
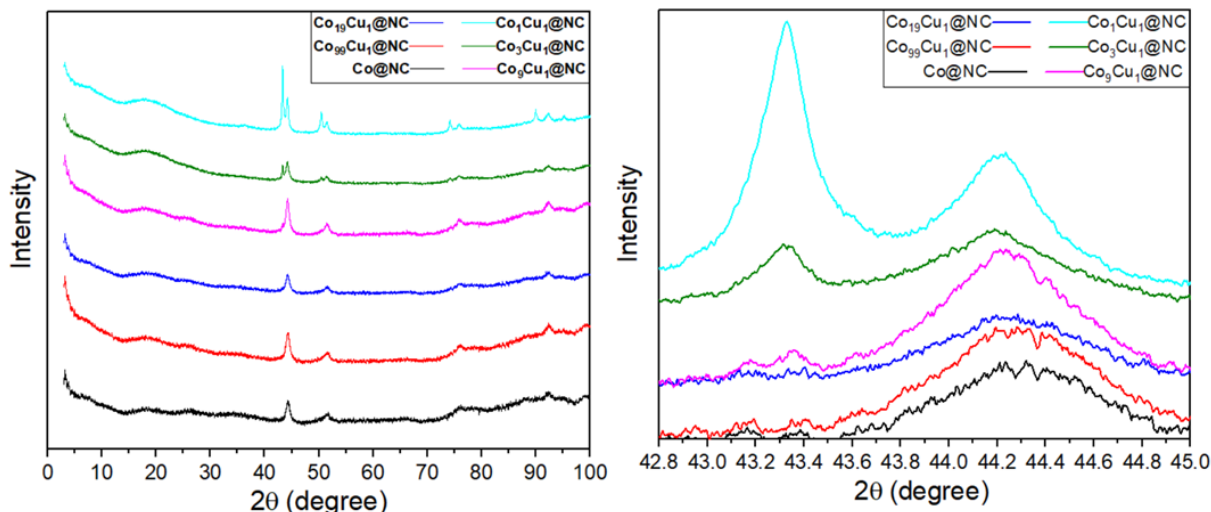

Figure 6.7: XRD measurements from all the Co_xCu_y@NC materials. The full spectrum is displayed on the left, while a close-up of the Co (~44.3 °) and Cu (~43.3 °) peaks is displayed on the right.

TEM images of the samples show the presence of metal nanoparticles after carbonization. Selected images for each sample can be seen in Figure 6.8. The metal nanoparticles mainly range in size from 5-30 nm. The two samples with the highest amount of copper doped into their structure (Co_1Cu_3@NC and Co_1Cu_1@NC) also had several large metal particles reaching sizes of up to 100 nm. Histograms of the particle size distributions have been included in Appendix C.4 with additional TEM images. The carbon structure of the materials is reminiscent of the starting material, ZIF-67, with the dodecahedron structure being clearly visibly for the samples containing CoCu ratios up to 9:1 (Co_9Cu_1@NC). For the samples made with CoCu ratios of 1:1 (Co_1Cu_1@NC) and 3:1 (Co_3Cu_1@NC), the shape of the carbon has become distorted and they start to agglomerate and fall apart. This is also reflected in the size of the dodecahedron structure. For the remaining samples the dodecahedrons range in size from about 500 nm to 1 μm, similar to that of ZIF-67, while Co_1Cu_1@NC and Co_3Cu_1@NC have dodecahedral structures up to a few μm in size. TEM-EDS images of Co_9Cu_1@NC show a homogeneous distribution of both cobalt and copper across the catalyst. TEM-EDS of Co_1Cu_1@NC illustrates that the large nanoparticles dispersed across the sample consist of pure copper, while copper and cobalt is still strewn across the remainder of the catalytic material. These images along with elemental maps can be found in Appendix C.5 and C.6.
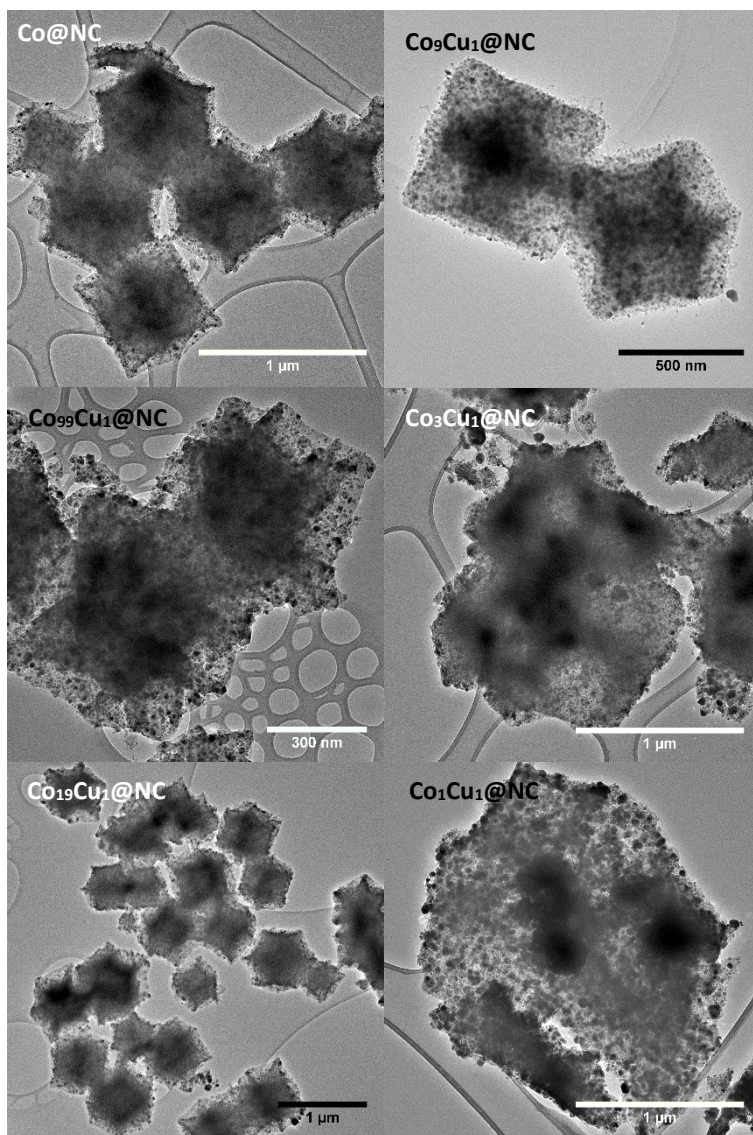
Figure 6.8: TEM images of the various $Co_xCu_y@NC$ materials.

The Cu@NC sample based on the copper containing ZIF-8 instead of ZIF-67 is seen in Figure 6.9. The carbonized MOF has lost most of its crystalline structure and has agglomerated to form an amorphous structure reaching sizes of a few micrometers. The copper from the ZIF-8 precursor has agglomerated to form nanoparticles of varying size. Small nanoparticles less than 10 nm in size can be seen strewn about the material, while larger agglomerates more than 100 nm in size can be found at the surface.
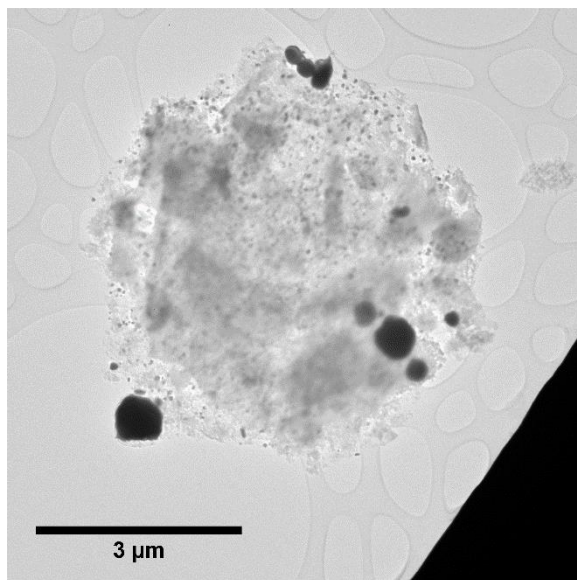
Figure 6.9: TEM image of Cu@NC. Several large metal nanoparticles several hundred nanometers in size can be seen at the surface.

XPS measurements of the catalysts show a relatively high nitrogen content from 4-11 atom% and a very low concentration of metals in the top layers of the materials. The copper containing materials exhibit a higher nitrogen content, ranging from 7-11 atom%, while the Co@NC sample has a much lower nitrogen content of only 4 atom%. The results have been compiled in Table 6.3.

Table 6.3: Composition of the Co_xCu_y@NC catalytic materials determined from XPS survey scans. All percentages presented refer to atom%.

Sample	% Nitrogen	% Carbon	% Oxygen	%Copper	% Cobalt
Co@NC	3.8	78.6	16.4	-	1.3
Co99Cu1@NC	7.8	74.7	13.5	0.1	3.8
Co19Cu1@NC	11.0	78.1	7.8	<0.1	3.1
Co9Cu1@NC	8.7	81.1	5.4	0.7	4.0
Co3Cu1@NC	9.6	75.8	10.4	1.8	2.5
Co1Cu1@NC	8.0	64.5	11.2	2.4	2.4
Cu@NC	8.4	80.6	8.6	0.8	-

The relative amount of the different nitrogen species found in the Co_xCu_y@NC materials were determined by deconvolution of scans performed in the nitrogen region (390-410 eV). An example of the peak fitting can be found in Appendix C.7. The results from the deconvolution have been summarized in Table 6.4 below. The samples have a roughly equal amount of pyridinic and graphitic nitrogen with the exception of Co@NC, which has about 32% pyrrolic nitrogen and about 13% graphitic nitrogen.

Table 6.4: Nitrogen species in found in the $Co_xCu_y@NC$ samples as determined by deconvolution of the nitrogen peak from XPS.

Sample	% Nitrogen total	% Graphitic	% Pyrolic	% Pyridinic
Co@NC	3.8	12.5	31.9	55.6
Co99Cu1@NC	7.8	51.6	-	48.4
Co19Cu1@NC	11.0	45.4	-	54.6
Co9Cu1@NC	8.7	48.6	-	51.4
Co3Cu1@NC	9.6	44.8	55.2	55.2
Co1Cu1@NC	8.0	33.2	-	66.8
Cu@NC	8.4	50.8	-	49.2

6.3.   Hydrosilylation of ketones

Hydrosilylation of cyclohexanone was used as the standard reaction for comparison of all the catalytic materials. The reaction is sensitive to air; therefore, the mixing was carried out in a glovebox. For a standard reaction, 8 mol% of catalyst (roughly 10 mg depending on the loading) was added to 0.5 mL of toluene containing 0.5 mmol of cyclohexanone and 0.6 mmol of dimethylphenylsilane. The reaction mixtures were sealed in 4 mL vial using Teflon caps. The stirring and heating of the reaction mixtures were carried out outside the glovebox on a magnetic stirrer, fitted with a heating mantel. A typical reaction was allowed to run for 24 hours at 90 °C.

Dibenzylether was added as an external standard after reaction, for measuring the amount of product using NMR. 1 mmol of dibenzylether was mixed with 3.3 mL of ethyl acetate. 1 mL of this solution was added to the hydrosilylation reaction mixture after the reaction was completed. The carbon catalyst was removed by filtering the mixture using a 0.22 μm syringe filter. The ethyl acetate was evaporated by connecting the container to a Schlenk line and applying vacuum for about 1 min. A typical NMR spectrum can be seen in Appendix C.8.

6.3.1. Comparison of different CoCu ratios

Results from the hydrosilylation of cyclohexanone (1a) to form the corresponding silane (2a) can be found in Table 6.5. The carbonized ZIF-67 with no copper added, Co@NC, had the lowest yield of 21 %. A CoCu ratio of 99 to 1 increased the yield to 35%. Addition of more copper gave a continuous increase in yield, until complete conversion was achieved from a CoCu ratio of 3 to 1 and onwards. The Cu@NC sample made from carbonization of ZIF-8 gave a much lower yield of 9%.

Table 6.5: Conversion and yield for each of the Co_xCu_y@NC materials. All yields were determined by NMR, using dibenzylether as an external standard.

Entry	Catalyst	Yield	Conversion
1	Co@NC	21%	38%
2	$Co_{99}Cu_1$@NC	35%	41%
3	$Co_{19}Cu_1$@NC	38%	45%
4	Co_9Cu_1@NC	72%	72%
5	Co_3Cu_1@NC	100%	100%
6	Co_1Cu_1@NC	100%	100%
7	Cu@NC	9%	29%

Yield based on NMR.

Co_9Cu_1@NC was selected for continued studying, including the reaction mechanism and scope of additional hydrosilylation reactions. It was selected for having high yield under the standard conditions, while also maintaining the dodecahedron structure of the original ZIF-67 as indicated by the TEM images in Figure 6.8.

6.3.2. Mechanistic studies of Co_1Cu_9@NC for hydrosilylation of cyclohexanone

As mentioned in the beginning of the chapter, several mechanisms for the hydrosilylation reaction have been documented. If the reaction takes place via formation of a silyl or ketyl radical mechanism, similar to that of Thomas *et al.* [164], it should be possible to trap radical intermediates. An experiment with cyclohexanone and triethylsilane, but with the addition of TEMPO, was conducted to test this. TEMPO (2,2,6,6-Tetramethyl-1-piperidinyloxy) is a stable radical, which reacts with any other radicals produced in a reaction medium.
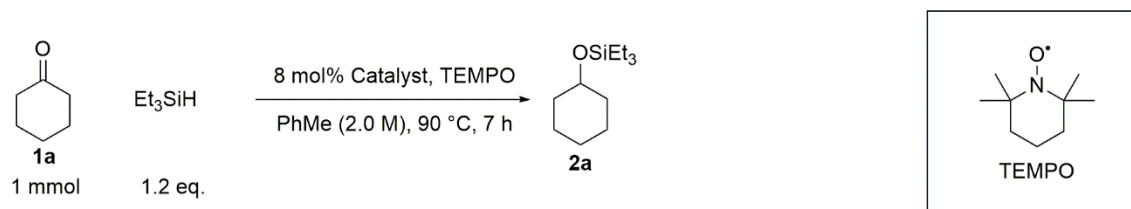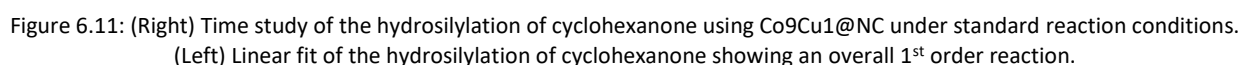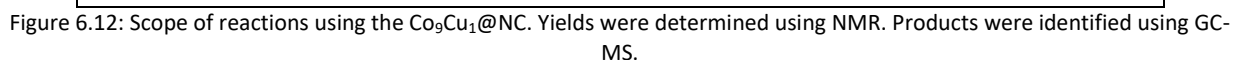

Figure 6.10: Reaction scheme for the experiment with TEMPO.

GC and GC-MS of the product mixture showed 73% yield from a reaction between triethylsilane and TEMPO, which indicate that the reaction proceeds via the formation of silyl radicals. A time study was conducted using Co_9Cu_1@NC under the standard reaction conditions. The trend in yield over 24 hours is shown in Figure 6.11. No induction period was observed and the results fit with an overall 1st order reaction, as shown by the linear plot of ln(1-yield) vs. time.

Figure 6.11: (Right) Time study of the hydrosilylation of cyclohexanone using Co9Cu1@NC under standard reaction conditions. (Left) Linear fit of the hydrosilylation of cyclohexanone showing an overall 1st order reaction.

6.3.3. Reaction scope using Co_1Cu_9@NC for hydrosilylation

Co_9Cu_1@NC was used for a variety of hydrosilylation reactions, using the standard reaction conditions aside from the ketone. Cyclohexanone was exchanged for different aryl and alkyl ketones with electron withdrawing, electron donating or bulky groups to examine their effect on the overall yield.

Figure 6.12: Scope of reactions using the Co_9Cu_1@NC. Yields were determined using NMR. Products were identified using GC-MS.

Adding a bulky tert-butyl group to cyclohexanone (**1b**) gave limited yield. Good yields were obtained from the hydrosilylation of acetophenone (**1d**) and several of its derivatives (**1e-h**). Some yield was also observed for a linear alkyl ketone (**1j**).

6.3.4. Recyclability of Co_9Cu_1@NC

The recyclability of our heterogeneous catalysts, Co_9Cu_1@NC, was evaluated using the standard reaction conditions for several cycles. After each reaction cycle, the product mixture was removed with a syringe, leaving behind the solid catalyst. Afterwards, new reaction mixture could be added for the next cycle. The separation was easy to perform due to the magnetic properties of the catalyst. The catalyst was kept in place by holding a magnet against the bottom of the reaction vial as the product mixture was removed. The yield for each cycle is presented in Figure 6.13 in comparison to the initial cycle.
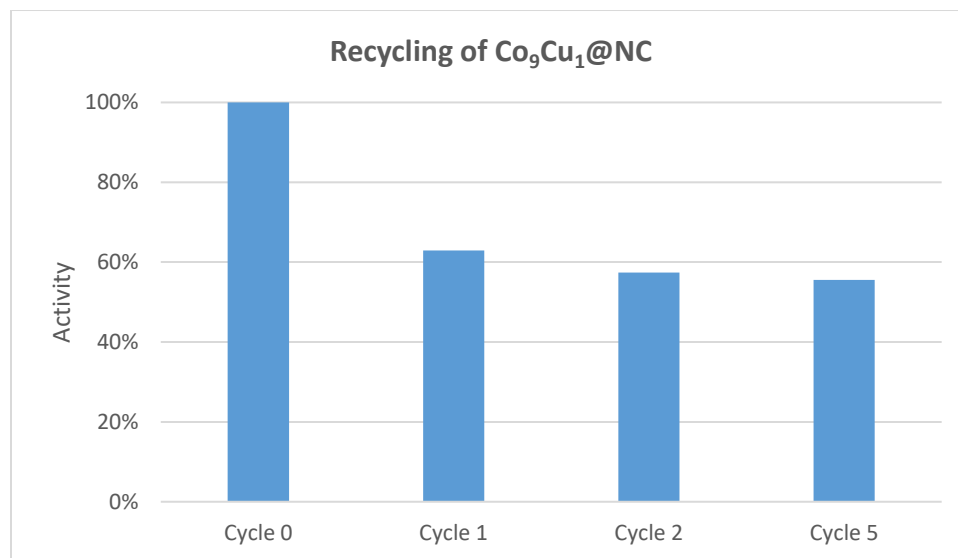

Recycling of Co_9Cu_1@NC

Figure 6.13: Recycling of Co_9Cu_1@NC for the hydrosilylation of cyclohexanone.

After having been reused once, the catalyst drops to 64% of its original activity. Afterwards, the activity of the catalyst only sees a slight decline for up to 5 cycles. A hot filtration experiment was conducted, where a standard reaction was allowed to run for 24 hours, followed by the filtration of the catalyst. The filtered solution was reheated and stirred under the same conditions for another 24 hours. No change in yield was observed.

6.4.   Discussion

The method of doping the cobalt-containing MOF (ZIF-67) before carbonization has proven to be an easy way of making bimetallic carbon catalysts. Simple incipient-wetness impregnation followed by reduction of the metals during carbonization bypasses the need for complicated methods of dispersion and additional reduction steps commonly found during the preparation of similar materials in literature [174], [175]. A different approach found in literature involve the carbonization of bimetallic MOFs, but is limited to metals capable of forming structures using the same ligands [176], [177].

The copper concentration and CoCu ratio can be adjusted easily by changing the concentration of the doping solution, but the actual concentration in the final material is slightly lower than expected, as shown by XRF and ICP. At lower copper loadings, the MOF-derived material retains much of its original

structure, but at higher loadings (Co_3Cu_1@NC and Co_1Cu_1@NC) the copper agglomerates as large nanoparticles as illustrated by the TEM-EDS found in Appendix C.6. It seems that the material reaches a level of saturation at loadings between Co_9Cu_1@NC and Co_3Cu_1@NC. The nitrogen-physisorption isotherm also confirms that the carbonization introduces mesopores, an attractive property for heterogeneous catalyst, since it provides easier access to the active sites and prevent diffusion limitation of reactants. The hydrosilylation of cyclohexanone shows that higher copper loadings gave better results, with Co_3Cu_1@NC and Co_1Cu_1@NC giving 100% yield under the standard reaction conditions. Due to the broader size distribution, degradation of the original ZIF structure and agglomeration of copper as illustrated by TEM-EDS, it was decided early on to focus on Co_9Cu_1@NC. It has the highest copper loading among the samples, which still retain the dodecahedral structure across the sample. The analysis of the cobalt and copper peaks from XRD also indicate that Co_9Cu_1@NC, Co_3Cu_1@NC and Co_1Cu_1@NC form CoCu alloy nanoparticles with about 10% Cu. This can be seen from the location of the Co peak, which is nearly identical for all of these samples.

With regards to the scope of reactions conducted using Co_9Cu_1@NC, it is known that aryl ketones are generally easier to transform into silyl ethers, as exemplified by the high yield obtained from acetophenone (**1d**). The addition of bulky groups hampers the yields significantly, as illustrated by the addition of a tert-butyl group to cyclohexanone (**1b**). The same goes for substituents at the para position of acetophenone. Methyl is a small electron donating group and lowers the yield to 75% (**1e**), while electron withdrawing groups like fluoride and chloride give significantly lower yield (**1h** and **1i**). For comparison, the standard reaction was also conducted with two commercially available products, 3 wt% Cu/C and 10 wt% Pt/C. Both of them were purchased from Sigma-Aldrich, and neither of them showed any significant activity toward hydrosilylation of cyclohexanone with Pt/C only giving 2% yield and Cu/C giving no measurable amount.

The Co_9Cu_1@NC catalyst is recyclable after experiencing an initial drop in activity. The hot filtration experiment showed no change in yield after the catalyst was removed, indicating that the catalyst does not leach active species, or that the leached species have been rendered inactive during the leaching. The initial drop in activity is expected to be caused by the initial agglomeration of metal nanoparticles under reaction conditions. TEM images of the catalyst before and after a standard reaction can be seen below in Figure 6.14. There are no clear indication that the nanoparticles have agglomerated, so the loss of activity might also be due to leeching of inactive species. Additional images of the Co_9Cu_1@NC catalyst after reaction can be found in Appendix C.9.
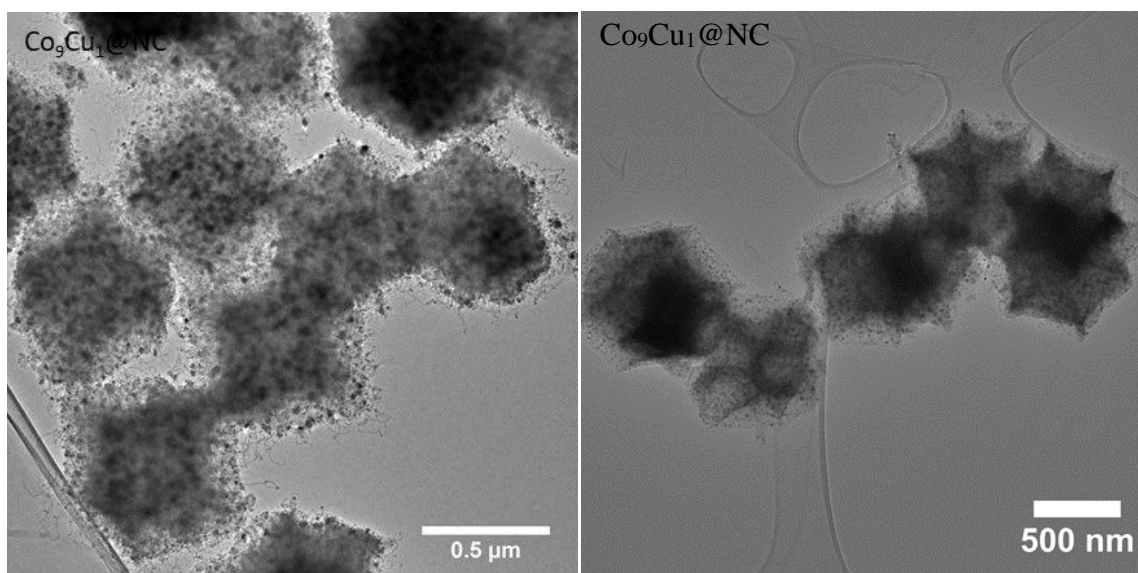
Figure 6.14: Co$_9$Cu$_1$@NC before (Left) and after (Right) hydrosilylation of cyclohexanone under standard reaction conditions.

6.5. Summary

Our method of producing bimetallic nitrogen-doped carbon by impregnating ZIF-67 before carbonization allows for the synthesis of a complex material using a simple, common approach. The resulting catalysts have a high loading of Co (30 wt%) and can introduce mesopores into the carbon material. It even maintains its dodecahedral shape for copper loading of at least 4 wt%. When used for the hydrosilylation of ketones, the catalysts exhibit good activity toward cyclohexanone, acetophenone and several acetophenone derivatives. This allow for the reduction of the ketone group along with the addition of a silyl protection group in one step, without having to use homogeneous catalysts, which are harder to collect and reuse. Due to the magnetic properties and heterogeneous nature of the catalyst, it can easily be collected by filtration or decantation using a magnet. In the case of Co$_9$Cu$_1$@NC, the catalyst proved to retain its catalytic activity after having been recycled once. The catalyst showed only a slight decrease in activity after at least five subsequent reaction cycles. No active species were observed in the product mixture after removal of the catalyst and only slight differences in the particle size distribution were observed after one reaction cycle.

Chapter 7.   Conclusion

Heterogeneous catalysts hold tremendous potential for the chemical industry, and its transition toward more green and sustainable production of chemicals. Considering the continued expansion in global needs, the gradual change towards long-term stability and renewable resources is only getting more relevant. This project focused on the application and understanding of carbon-based support materials and their myriad of advantages as heterogeneous catalysts.

In Chapter 1, an introduction to some of the important facets of catalysts were covered. When designing new catalysts, the aim should always be to consider the principles of green chemistry and sustainability. High selectivity, mild reaction conditions and usage of abundant raw materials are examples of some of the aspects, which need to be considered. The carbon materials used for each of the covered projects share a number of characteristic properties and inherent advantages, which were discussed in Chapter 2. The many possible porous structures allow for improved dispersion of the active phase, while the introduction of heteroatoms provides a myriad of ways to fine-tune electron density and composition near the active site. Nitrogen is a common dopant used in carbon materials, and is suspected of improving both activity, stability and dispersion of nanoparticles. Chapter 3 covered the main techniques used for characterization of the materials. Important aspects of their structure and their composition require high-resolution methods of detection.

Chapter 4 introduced the use of ordered mesoporous carbon materials for the dehydrogenation of formic acid. Nitrogen-doping is a common method for improving upon the activity of such catalysts, however its impact on the vapor phase decomposition is still not fully explored. An initial screening showed that catalysts based on Pt, Pd and an AuPd alloy provided the best reactivity with high selectivity (>99%). Comparison with a nitrogen-free carbon support showed that the nitrogen-containing counterpart provided higher activity and slightly higher selectivity. No pattern in particle size or overall metal loading was observed, and analysis using ME-PSD-DRIFTS indicated no difference in intermediates present during the reaction. The difference in reactivity was attributed to electrons donated from nearby nitrogen atoms to the active site, resulting in a lowering of the activation energy. Nitrogen-doped carbon materials are still important support materials in a variety of reaction, however the influence of nitrogen and optimization of nanostructure remain key components for improving their catalytic properties. The ME-PSD-DRIFTS method is believed to hold potential for identifying intermediate species on active surfaces. Optimizing the approach to increase the lifetime of intermediates and increasing the amount of active sites could help enhance the signal of individual species, which hopefully would allow the method to see use for study of reactions with many intermediates.

Chapter 5 focused on the inverse reaction, the hydrogenation of CO_2 to formic acid. This reaction is far more challenging. When combined with the dehydrogenation described in Chapter 4, it would help create a closed cycled system for the storage of H_2 and utilization of CO_2. A polyphenylene POP was synthesized with homogeneous ligands (bpy, Phen) built into its structure to stabilize active Ir under the high pressure and moderate temperature needed to run the reaction. Using 0.00001 M of $IrCl_3$ a maximum yield of 18% H_2 was achieved after 24 hours, corresponding to a high TON of 20.041. Single-atoms of Ir were visible in STEM, but agglomeration of Ir into nanoparticles is believed to be a key reason for deactivation. Activity can be regained upon addition of more Ir precursor, but it is more desirable to improve the stability of generated active sites could potentially be achieved with stronger binding ligands.

Chapter 6 used carbonized MOFs with earth-abundant metals for the important hydrosilylation reaction of ketones, which reduced the ketone group to an alcohol, while adding a protective group. MOFs are notorious for their low chemical and thermal stability, but upon carbonization, their structure can not only be preserved with decent activity, but their long-term stability was also significantly improved as illustrated with the hydrosilylation of ketones. After having been recycled once, the activity of the Co_9Cu_1@NC was stable for subsequent cycles. These MOF-derived catalysts come with the added benefit of granting control of the ratio between Co and Cu in this bimetallic catalyst, a prospect that has the potential to be utilized for other alloys and reactions. The Co_9Cu_1@NC catalyst in particular had a high loading of Co and Cu, while retaining the dodecahedral shape of the MOF after carbonization. It showed high activity toward hydrosilylation of cyclohexanone and several acetophenone derivatives. The work is one of several projects showing the potential of decomposition of MOF to create well-dispersed nanoparticles in porous carbon structures. Using the doping approach covered herein allows for the creation of a myriad of alloyed nanoparticles, which could potentially rival conventional precious metal catalysts.

Bibliography

[1]   V. V. Ranade and S. S. Joshi, "Catalysis and Catalytic Processes," in *Industrial Catalytic Processes for Fine and Specialty Chemicals*, Elsevier Inc., 2016, pp. 1–14.

[2]   D. Astruc, "Transition-metal Nanoparticles in Catalysis: From Historical Background to the State-of-the Art," in *Nanoparticles and Catalysis*, Wiley-VCH Verlag, 2008.

[3]   P. T. Anastas and J. C. Warner, "Green Chemistry: Theory and Practice," *Oxford Univ. Press New York*, p. 30, 1998.

[4]   T. Sinigaglia, F. Lewiski, M. E. Santos Martins, and J. C. Mairesse Siluk, "Production, storage, fuel stations of hydrogen and its utilization in automotive applications-a review," *Int. J. Hydrogen Energy*, vol. 42, no. 39, pp. 24597–24611, 2017.

[5]   P. Kurzweil and J. Garche, "Overview of batteries for future automobiles," in *Lead-Acid Batteries for Future Automobiles*, Elsevier B.V., 2017, pp. 27–96.

[6]   Z. Chen, D. Higgins, A. Yu, L. Zhang, and J. Zhang, "A review on non-precious metal electrocatalysts for PEM fuel cells," *Energy Environ. Sci.*, no. 4, pp. 3167–3192, 2011.

[7]   K. Müller, K. Brooks, and T. Autrey, "Hydrogen Storage in Formic Acid: A Comparison of Process Options," *Energy and Fuels*, vol. 31, no. 11, pp. 12603–12611, 2017.

[8]   M. Aresta, F. Nocito, and A. Dibenedetto, "What Catalysis Can Do for Boosting CO2 Utilization," in *Advances in Catalysis*, 1st ed., vol. 62, Elsevier Inc., 2018, pp. 49–111.

[9]   P. T. Anastas, M. M. Kirchhoff, and T. C. Williamson, "Catalysis as a foundational pillar of green chemistry," *Appl. Catal. A Gen.*, vol. 221, no. 1–2, pp. 3–13, 2001.

[10]   W. Xu, L. Ma, B. Huang, X. Cui, X. Niu, and H. Zhang, "Thermodynamic analysis of formic acid synthesis from CO2 hydrogenation," *2011 Int. Conf. Mater. Renew. Energy Environ. Shanghai*, vol. 2, pp. 1473–1477, 2011.

[11]   N. Cheng, L. Zhang, K. Doyle-Davis, and X. Sun, "Single-Atom Catalysts: From Design to Application," *Electrochem. Energy Rev.*, vol. 2, no. 4, pp. 539–573, 2019.

[12]   A. J. Medford *et al.*, "From the Sabatier principle to a predictive theory of transition-metal heterogeneous catalysis," *J. Catal.*, vol. 328, pp. 36–42, 2015.

[13]   Y. Tang, C. A. Roberts, R. T. Perkins, and I. E. Wachs, "Revisiting formic acid decomposition on metallic powder catalysts: Exploding the HCOOH decomposition volcano curve," *Surf. Sci.*, vol. 650, pp. 103–110, 2016.

[14]   S. Back, M. S. Yeom, and Y. Jung, "Active Sites of Au and Ag Nanoparticle Catalysts for CO2 Electroreduction to CO," *ACS Catal.*, vol. 5, pp. 5089–5096, 2015.

[15]   G. Li *et al.*, "All The Catalytic Active Sites of MoS2 for Hydrogen Evolution," *J. Am. Chem. Soc.*, vol. 138, no.

51, pp. 16632–16638, 2016.

[16] G. Rothenberg, "Heterogeneous Catalysis," in *Catalysis: Concepts and Green Applications*, WILEY-VCH Verlag, 2008, pp. 127–187.

[17] Z. Zhang, X. Zhang, B. Liu, and J. Liu, "Molecular Imprinting on Inorganic Nanozymes for Hundred-fold Enzyme Specificity," *J. Am. Chem. Soc.*, vol. 139, no. 15, pp. 5412–5419, 2017.

[18] E. T. Kaiser and C. Radziejewski, "The Design of New Enzyme Active Sites for the Catalysis of Specific Chemical Reactions," in *Enzymes in Organic Synthesis*, 2008, pp. 219–237.

[19] K. Haupt and K. Mosbach, "Molecularly imprinted polymers and their use in biomimetic sensors," *Chem. Rev.*, vol. 100, no. 7, pp. 2495–2504, 2000.

[20] M. Boudart, "Turnover Rates in Heterogeneous Catalysis," *Chem. Rev.*, vol. 95, no. 3, pp. 661–666, 1995.

[21] C. H. Bartholomew, "Mechanisms of catalyst deactivation," *Appl. Catal. A Gen.*, vol. 212, no. 1–2, pp. 17–60, 2001.

[22] C. H. Bartholomew, "Carbon Deposition in Steam Reforming and Methanation," *Catal. Rev.*, vol. 24, no. 1, pp. 67–112, 1982.

[23] M. Haruta, "Size- and support-dependency in the catalysis of gold," *Catal. Today*, vol. 36, no. 1, pp. 153–166, 1997.

[24] F. Rodriguez-reinoso, "The role of carbon materials in heterogeneous catalysis," *Carbon N. Y.*, vol. 36, no. 3, pp. 159–175, 1998.

[25] A. Yehaskel, *Activated Carbon, Manufacture and Regeneration*. Noyes Data Corporation, 1978.

[26] H. Jiintgen, "Activated carbon as catalyst support," *Fuel*, vol. 65, no. 10, pp. 1436–1446, 1986.

[27] F. Rodríguez-Reinoso, "Activated Carbon and Adsorption," in *Encyclopedia of Materials: Science and Technology*, Elsevier Ltd, 2001, pp. 22–34.

[28] X. Zou *et al.*, "Cobalt-embedded nitrogen-rich carbon nanotubes efficiently catalyze hydrogen evolution reaction at all pH values," *Angew. Chemie - Int. Ed.*, vol. 53, no. 17, pp. 4372–4376, 2014.

[29] S. Ren, F. Huang, J. Zheng, S. Chen, and H. Zhang, "Ruthenium supported on nitrogen-doped ordered mesoporous carbon as highly active catalyst for NH3 decomposition to H2," *Int. J. Hydrogen Energy*, vol. 42, no. 8, pp. 5105–5113, 2017.

[30] Z. H. Zhu, L. R. Radovic, and G. Q. Lu, "Effects of acid treatments of carbon on N2O and NO reduction by carbon-supported copper catalysts," *Carbon N. Y.*, vol. 38, no. 3, pp. 451–464, 2000.

[31] Z. H. Zhu and G. Q. Lu, "Catalytic Conversion of N2O to N2 over Potassium Catalyst Supported on Activated Carbon," *J. Catal.*, vol. 187, pp. 262–274, 1999.

[32] X. Yan *et al.*, "Activated carbon becomes active for oxygen reduction and hydrogen evolution reactions," *Chem. Commun.*, vol. 52, pp. 8156–8159, 2016.

[33] V. A. Online, W. Cui, Q. Liu, N. Cheng, A. M. Asiri, and X. Sun, "Activated carbon nanotubes: a highly-active metal-free electrocatalyst for hydrogen evolution reaction," *Chem. Commun.*, vol. 60, pp. 9340–9342, 2014.

[34] X. Yao and S. Xiangdong, "Defects on carbons for electrocatalytic oxygen reduction," *Chem. Soc. Rev.*, vol. 47, pp. 7628–7658, 2018.

[35] O. Salomé and G. Soares, "Development of carbon materials as metal catalyst supports and metal-free catalysts for catalytic reduction of ions and advanced oxidation processes," *Boletín del Grup. Español del Carbón*, no. 40, pp. 36–41, 2016.

[36] X. Liu, L. Zhu, H. Wang, G. He, and Z. Bian, "Catalysis performance comparison for electrochemical reduction of CO 2 on Pd–Cu/graphene catalyst," *RSC Adv.*, vol. 6, no. 44, pp. 38380–38387, 2016.

[37] Z. Luo *et al.*, "Pyridinic N doped graphene: synthesis, electronic structure, and electrocatalytic property," *J. Mater. Chem.*, vol. 21, p. 8038, 2011.

[38] P. K. Aneesh, S. R. Nambiar, T. P. Rao, and A. Ajayaghosh, "Electrochemically synthesized partially reduced graphene oxide modified glassy carbon electrode for individual and simultaneous voltammetric determination of ascorbic acid, dopamine and uric acid," *Anal. Methods*, vol. 6, no. 14, pp. 5322–5330, 2014.

[39]   U. N. Maiti *et al.*, "25th anniversary article: Chemically modified/doped carbon nanotubes & graphene for optimized nanostructures & nanodevices," *Adv. Mater.*, vol. 26, no. 1, pp. 40–67, 2014.

[40]   L. F. Mabena, S. Sinha Ray, S. D. Mhlanga, and N. J. Coville, "Nitrogen-doped carbon nanotubes as a metal catalyst support," *Appl. Nanosci.*, vol. 1, no. 2, pp. 67–77, 2011.

[41]   C. N. R. Rao, K. Gopalakrishnan, and A. Govindaraj, "Synthesis, properties and applications of graphene doped with boron, nitrogen and other elements," *Nano Today*, vol. 9, no. 3, pp. 324–343, 2014.

[42]   M. Zacharska *et al.*, "Ruthenium Clusters on Carbon Nanofibers for Formic Acid Decomposition: Effect of Doping the Support with Nitrogen," *ChemCatChem*, vol. 7, no. 18, pp. 2910–2917, 2015.

[43]   F. Liu, K. Huang, Q. Wu, and S. Dai, "Solvent-Free Self-Assembly to the Synthesis of Nitrogen-Doped Ordered Mesoporous Polymers for Highly Selective Capture and Conversion of CO2," *Adv. Mater.*, vol. 29, no. 27, pp. 1–8, 2017.

[44]   Y. Cao, S. Mao, M. Li, Y. Chen, and Y. Wang, "Metal/Porous Carbon Composites for Heterogeneous Catalysis: Old Catalysts with Improved Performance Promoted by N-Doping," *ACS Catal.*, vol. 7, no. 12, pp. 8090–8112, 2017.

[45]   W. W. Wang, J. S. Dang, X. Zhao, and S. Nagase, "Formation Mechanisms of Graphitic-N: Oxygen Reduction and Nitrogen Doping of Graphene Oxides," *J. Phys. Chem. C*, vol. 120, no. 10, pp. 5673–5681, 2016.

[46]   Y. Meng *et al.*, "A family of highly ordered mesoporous polymer resin and carbon structures from organic-organic self-assembly," *Chem. Mater.*, vol. 18, no. 18, pp. 4447–4464, 2006.

[47]   M. R. Benzigar *et al.*, "Recent advances in functionalized micro and mesoporous carbon materials: Synthesis and applications," *Chem. Soc. Rev.*, vol. 47, no. 8, pp. 2680–2721, 2018.

[48]   Z. Ling *et al.*, "Sustainable Synthesis and Assembly of Biomass-Derived B/N Co-Doped Carbon Nanosheets with Ultrahigh Aspect Ratio for High-Performance Supercapacitors," *Adv. Funct. Mater.*, vol. 26, no. 1, pp. 111–119, 2016.

[49]   J. Li *et al.*, "Formation of graphitic tubules from ordered mesoporous carbon and their effect on supercapacitive energy storage," *J. Mater. Chem.*, vol. 22, no. 40, pp. 21472–21480, 2012.

[50]   W. Niu *et al.*, "Mesoporous N-doped carbons prepared with thermally removable nanoparticle templates: An efficient electrocatalyst for oxygen reduction reaction," *J. Am. Chem. Soc.*, vol. 137, no. 16, pp. 5555–5562, 2015.

[51]   D. S. Yang, D. Bhattacharjya, S. Inamdar, J. Park, and J. S. Yu, "Phosphorus-doped ordered mesoporous carbons with different lengths as efficient metal-free electrocatalysts for oxygen reduction reaction in alkaline media," *J. Am. Chem. Soc.*, vol. 134, no. 39, pp. 16127–16130, 2012.

[52]   P. Song, L. Zhu, X. Bo, A. Wang, G. Wang, and L. Guo, "Pt nanoparticles incorporated into phosphorus-doped ordered mesoporous carbons: Enhanced catalytic activity for methanol electrooxidation," *Electrochim. Acta*, vol. 127, pp. 307–314, 2014.

[53]   Y. Tan *et al.*, "Versatile nanoporous bimetallic phosphides towards electrochemical water splitting," *Energy Environ. Sci.*, vol. 9, no. 7, pp. 2257–2261, 2016.

[54]   H. Tan *et al.*, "Perfectly ordered mesoporous iron-nitrogen doped carbon as highly efficient catalyst for oxygen reduction reaction in both alkaline and acidic electrolytes," *Nano Energy*, vol. 36, no. February, pp. 286–294, 2017.

[55]   Z. Li, J. Liu, C. Xia, and F. Li, "Nitrogen-functionalized ordered mesoporous carbons as multifunctional supports of ultrasmall Pd nanoparticles for hydrogenation of phenol," *ACS Catal.*, vol. 3, no. 11, pp. 2440–2448, 2013.

[56]   U. Mueller, M. Schubert, F. Teich, H. Puetter, K. Schierle-Arndt, and J. Pastré, "Metal-organic frameworks - Prospective industrial applications," *J. Mater. Chem.*, vol. 16, no. 7, pp. 626–636, 2006.

[57]   J. Lee, O. K. Farha, J. Roberts, K. A. Scheidt, S. T. Nguyen, and J. T. Hupp, "Metal-organic framework materials as catalysts," *Chem. Soc. Rev.*, vol. 38, no. 5, pp. 1450–1459, 2009.

[58]   A. Dhakshinamoorthy, A. M. Asiri, and H. Garcia, "2D Metal–Organic Frameworks as Multifunctional Materials in Heterogeneous Catalysis and Electro/Photocatalysis," *Adv. Mater.*, vol. 31, pp. 1–40, 2019.

[59] A. Dhakshinamoorthy, Z. Li, and H. Garcia, "Catalysis and photocatalysis by metal organic frameworks," *Chem. Soc. Rev.*, vol. 47, pp. 8134–8172, 2018.

[60] M. E. Davis, "Zeolites and Molecular Sieves: Not Just Ordinary Catalysts," *Ind. Eng. Chem. Res.*, vol. 30, no. 8, pp. 1675–1683, 1991.

[61] C. H. Hendon, A. J. Rieth, M. D. Korzyński, and M. Dincă, "Grand Challenges and Future Opportunities for Metal-Organic Frameworks," *ACS Cent. Sci.*, vol. 3, no. 6, pp. 554–563, 2017.

[62] N. L. Torad *et al.*, "Direct synthesis of MOF-derived nanoporous carbon with magnetic Co nanoparticles toward efficient water treatment," *Small*, vol. 10, no. 10, pp. 2096–2107, 2014.

[63] X. Wang and Y. Li, "Chemoselective hydrogenation of functionalized nitroarenes using MOF-derived co-based catalysts," *J. Mol. Catal. A Chem.*, vol. 420, pp. 56–65, 2016.

[64] J. Tang *et al.*, "Bimetallic metal-organic frameworks for controlled catalytic graphitization of nanoporous carbons," *Sci. Rep.*, vol. 6, no. April, pp. 3–4, 2016.

[65] S. Gadipelli and Z. X. Guo, "Tuning of ZIF-Derived Carbon with High Activity, Nitrogen Functionality, and Yield - A Case for Superior CO2 Capture," *ChemSusChem*, vol. 8, no. 12, pp. 2123–2132, 2015.

[66] Y. Yusran, D. Xu, Q. Fang, D. Zhang, and S. Qiu, "MOF-derived Co@N-C nanocatalyst for catalytic reduction of 4-nitrophenol to 4-aminophenol," *Microporous Mesoporous Mater.*, vol. 241, pp. 346–354, 2017.

[67] W. Zhang *et al.*, "Spontaneous Weaving of Graphitic Carbon Networks Synthesized by Pyrolysis of ZIF-67 Crystals," *Angew. Chemie - Int. Ed.*, vol. 56, no. 29, pp. 8435–8440, 2017.

[68] J. Y. Choi *et al.*, "Exceptional chemical and thermal stability of zeolitic imidazolate frameworks," *Proc. Natl. Acad. Sci.*, vol. 103, no. 27, pp. 10186–10191, 2006.

[69] A. Jenkins, P. Kratochvil, R. Stepto, and U. Suter, "Glossary of Basic Terms in Polymer," *Pure Appl. Chem.*, vol. 68, no. 12, pp. 2287–2311, 1996.

[70] E. A. Bekturov, "Catalytic Properties of Polymers in Solutions," in *Catalysis by Polymers*, WILEY-VCH Verlag, 2002, pp. 1–49.

[71] S. Itsuno, "Polymer Catalysts," in *Encyclopedia of Polymeric Nanomaterials*, Springer Berlin Heidelberg, 2013, pp. 1–9.

[72] A. Pfaltz and W. J. Drury III, "Design of chiral ligands for asymmetric catalysis: From C2-symmetric P,P- and N,N-ligands to sterically and electronically nonsymmetrical P,N-ligands," *Procedings Natl. Acad. Sci. United States Am.*, vol. 101, no. 16, pp. 5723–5726, 2004.

[73] Z. Wang, K. Ding, and Y. Uozumi, "An Overview of Heterogeneous Asymmetric Catalysis," in *Handbook of Heterogeneous Asymmetric Phase-Transfer New Frontiers in Asymmetric*, WILEY-VCH Verlag, 2008, pp. 1–24.

[74] S. Kramer, N. R. Bennedsen, and S. Kegnæs, "Porous Organic Polymers Containing Active Metal Centers as Catalysts for Synthetic Organic Chemistry," *ACS Catal.*, vol. 8, no. 8, pp. 6961–6982, 2018.

[75] T. Zhang, G. Xing, W. Chen, and L. Chen, "Porous organic polymers: A promising platform for efficient photocatalysis," *Mater. Chem. Front.*, vol. 4, no. 2, pp. 332–353, 2020.

[76] S. Wang, K. Song, C. Zhang, Y. Shu, T. Li, and B. Tan, "A novel metalporphyrin-based microporous organic polymer with high CO2 uptake and efficient chemical conversion of CO2 under ambient conditions," *J. Mater. Chem. A*, vol. 5, no. 4, pp. 1509–1515, 2017.

[77] N. W. Ockwig, A. P. Cote, M. O'Keeffe, A. J. Matzger, and O. M. Yaghi, "Porous , Crystalline , Covalent Organic Frameworks," vol. 310, no. November, pp. 1166–1171, 2005.

[78] S. Y. Ding *et al.*, "Construction of covalent organic framework for catalysis: Pd/COF-LZU1 in Suzuki-Miyaura coupling reaction," *J. Am. Chem. Soc.*, vol. 133, no. 49, pp. 19816–19822, 2011.

[79] S. Clair, M. Abel, and L. Porte, "Growth of boronic acid based two-dimensional covalent networks on a metal surface under ultrahigh vacuum," *Chem. Commun.*, vol. 50, no. 68, pp. 9627–9635, 2014.

[80] S. Cao, B. Li, R. Zhu, and H. Pang, "Design and synthesis of covalent organic frameworks towards energy and environment fields," *Chem. Eng. J.*, vol. 355, no. July 2018, pp. 602–623, 2019.

[81]   E. Rozhko, A. Bavykina, D. Osadchii, M. Makkee, and J. Gascon, "Covalent organic frameworks as supports for a molecular Ni based ethylene oligomerization catalyst for the synthesis of long chain olefins," *J. Catal.*, vol. 345, pp. 270–280, 2017.

[82]   L. Liu and A. Corma, "Metal Catalysts for Heterogeneous Catalysis: From Single Atoms to Nanoclusters and Nanoparticles," *Chem. Rev.*, vol. 118, no. 10, pp. 4981–5079, 2018.

[83]   J. B. Hudson, "Photon–Surface Interactions," in *Surface Science*, Architectural Press, 1992, pp. 275–286.

[84]   J. W. Niemantsverdriet, "Photoemission and Auger Spectroscopy," in *Spectroscopy in Catalysis*, WILEY-VCH Verlag, 2007, pp. 39–83.

[85]   A. V. Vorontsov and S. V. Tsybulya, "Influence of Nanoparticles Size on XRD Patterns for Small Monodisperse Nanoparticles of Cu0 and TiO2 Anatase," *Ind. Eng. Chem. Res.*, vol. 57, no. 7, pp. 2526–2536, 2018.

[86]   M. Thommes *et al.*, "Physisorption of gases, with special reference to the evaluation of surface area and pore size distribution (IUPAC Technical Report)," *Pure Appl. Chem.*, vol. 87, no. 9–10, pp. 1051–1069, 2015.

[87]   J. O. Abe, A. P. I. Popoola, E. Ajenifuja, and O. M. Popoola, "Hydrogen energy, economy and storage: Review and recommendation," *Int. J. Hydrogen Energy*, vol. 44, no. 29, pp. 15072–15086, 2019.

[88]   J. A. Villajos, G. Orcajo, G. Calleja, J. A. Botas, and C. Martos, "Beneficial cooperative effect between Pd nanoparticles and ZIF-8 material for hydrogen storage," *Int. J. Hydrogen Energy*, vol. 41, no. 42, pp. 19439–19446, 2016.

[89]   X. Yu, Z. Tang, D. Sun, L. Ouyang, and M. Zhu, "Recent advances and remaining challenges of nanostructured materials for hydrogen storage applications," *Prog. Mater. Sci.*, vol. 88, pp. 1–48, 2017.

[90]   H.-L. L. Jiang *et al.*, "From Metal–Organic Framework to Nanoporous Carbon: Toward a Very High Surface Area and Hydrogen Uptake," *J. Am. Chem. Soc.*, vol. 133, no. 31, pp. 11854–11857, 2011.

[91]   S. Orimo, Y. Nakamori, J. R. Eliseo, A. Züttel, and C. M. Jensen, "Complex Hydrides for Hydrogen Storage," *Chem. Rev.*, vol. 107, pp. 4111–4132, 2007.

[92]   P. T. Aakko-Saksa, C. Cook, J. Kiviaho, and T. Repo, "Liquid organic hydrogen carriers for transportation and storing of renewable energy – Review and discussion," *J. Power Sources*, vol. 396, no. July, pp. 803–823, 2018.

[93]   P. Preuster, C. Papp, and P. Wasserscheid, "Liquid organic hydrogen carriers (LOHCs): Toward a hydrogen-free hydrogen economy," *Acc. Chem. Res.*, vol. 50, no. 1, pp. 74–85, 2017.

[94]   M. Yadav and Q. Xu, "Liquid-phase chemical hydrogen storage materials," *Energy Environ. Sci.*, vol. 5, no. 12, pp. 9698–9725, 2012.

[95]   Y. A. Daza and J. N. Kuhn, "CO2 conversion by reverse water gas shift catalysis: Comparison of catalysts, mechanisms and their consequences for CO2 conversion to liquid fuels," *RSC Adv.*, vol. 6, no. 55, pp. 49675–49691, 2016.

[96]   Q. Li, R. He, J.-A. Gao, J. O. Jensen, and N. J. Bjerrum, "The CO Poisoning Effect in PEMFCs Operational at Temperatures up to 200°C," *J. Electrochem. Soc.*, vol. 150, no. 12, p. A1599, 2003.

[97]   M. Jeon *et al.*, "Electronically modified Pd catalysts supported on N-doped carbon for the dehydrogenation of formic acid," *Int. J. Hydrogen Energy*, vol. 41, no. 34, pp. 15453–15461, 2016.

[98]   M. Iguchi, Y. Himeda, Y. Manaka, and H. Kawanami, "Development of an Iridium-Based Catalyst for High-Pressure Evolution of Hydrogen from Formic Acid," *ChemSusChem*, pp. 2749–2753, 2016.

[99]   A. V. Bavykina, M. G. Goesten, F. Kapteijn, M. Makkee, and J. Gascon, "Efficient production of hydrogen from formic acid using a Covalent Triazine Framework supported molecular catalyst," *ChemSusChem*, vol. 8, no. 5, pp. 809–812, 2015.

[100]   J. F. Hull *et al.*, "Reversible hydrogen storage using CO2 and a proton-switchable iridium catalyst in aqueous media under mild temperatures and pressures," *Nat. Chem.*, vol. 4, pp. 383–388, 2012.

[101]   A. Beloqui Redondo, F. L. Morel, M. Ranocchiari, and J. A. Van Bokhoven, "Functionalized Ruthenium-Phosphine Metal-Organic Framework for Continuous Vapor-Phase Dehydrogenation of Formic Acid," *ACS Catal.*, vol. 5, no. 12, pp. 7099–7103, 2015.

[102]   A. Gallas-Hulin, J. Mielby, and S. Kegnæs, "Efficient Production of Hydrogen from Decomposition of Formic Acid over Zeolite Incorporated Gold Nanoparticles," *ChemistrySelect*, vol. 1, no. 13, pp. 3942–3945, 2016.

[103]   A. Gazsi, T. Bánsági, and F. Solymosi, "Decomposition and reforming of formic acid on supported Au catalysts: Production of CO-free H2," *J. Phys. Chem. C*, vol. 115, no. 31, pp. 15459–15466, 2011.

[104]   J. Wang *et al.*, "Non-precious molybdenum-based catalyst derived from biomass: CO-free hydrogen production from formic acid at low temperature," *Energy Convers. Manag.*, vol. 164, no. December 2017, pp. 122–131, 2018.

[105]   M. Ojeda and E. Iglesia, "Formic acid dehydrogenation on Au-based catalysts at near-ambient temperatures," *Angew. Chemie - Int. Ed.*, vol. 48, no. 26, pp. 4800–4803, 2009.

[106]   D. Mellmann, P. Sponholz, H. Junge, and M. Beller, "Formic acid as a hydrogen storage material-development of homogeneous catalysts for selective hydrogen release," *Chem. Soc. Rev.*, vol. 45, no. 14, pp. 3954–3988, 2016.

[107]   C. Prichatz *et al.*, "Highly Efficient Base-Free Dehydrogenation of Formic Acid at Low Temperature," *ChemSusChem*, vol. 11, no. 18, pp. 3092–3095, 2018.

[108]   C. Chauvier, A. Tlili, C. Das Neves Gomes, P. Thuéry, and T. Cantat, "Metal-free dehydrogenation of formic acid to H2 and CO2 using boron-based catalysts," *Chem. Sci.*, vol. 6, no. 5, pp. 2938–2942, 2015.

[109]   Y. Jiang *et al.*, "AuPd Nanoparticles Anchored on Nitrogen-Decorated Carbon Nanosheets with Highly Efficient and Selective Catalysis for the Dehydrogenation of Formic Acid," *J. Phys. Chem. C*, vol. 122, no. 9, pp. 4792–4801, 2018.

[110]   Q. Y. Bi, J. D. Lin, Y. M. Liu, H. Y. He, F. Q. Huang, and Y. Cao, "Dehydrogenation of Formic Acid at Room Temperature: Boosting Palladium Nanoparticle Efficiency by Coupling with Pyridinic-Nitrogen-Doped Carbon," *Angew. Chemie - Int. Ed.*, vol. 55, no. 39, pp. 11849–11853, 2016.

[111]   F. Solymosi, Á. Koós, N. Liliom, and I. Ugrai, "Production of CO-free H2 from formic acid. A comparative study of the catalytic behavior of Pt metals on a carbon support," *J. Catal.*, vol. 279, no. 1, pp. 213–219, 2011.

[112]   M. Zacharska *et al.*, "Factors Influencing the Performance of Pd/C Catalysts in the Green Production of Hydrogen from Formic Acid," *ChemSusChem*, vol. 10, no. 4, pp. 720–730, Feb. 2017.

[113]   G. Wang, Z. Cao, D. Gu, N. Pfänder, and A. Swertz, "Nitrogen-Doped Ordered Mesoporous Carbon Supported Bimetallic PtCo Nanoparticles for Upgrading of Biophenolics," *Angew. Chemie - Int. Ed.*, vol. 55, no. 31, pp. 8850–8855, 2016.

[114]   Y. Liu *et al.*, "Well-ordered mesoporous polymers and carbons based on imide-incorporated soft materials," *Polym. Chem.*, vol. 5, no. 22, pp. 6452–6460, 2014.

[115]   G. Shen *et al.*, "Nitrogen-doped ordered mesoporous carbon single crystals: Aqueous organic-organic self-assembly and superior supercapacitor performance," *J. Mater. Chem. A*, vol. 3, no. 47, pp. 24041–24048, 2015.

[116]   Z. Wang *et al.*, "PdAu bimetallic nanoparticles anchored on amine-modified mesoporous ZrSBA-15 for dehydrogenation of formic acid under ambient conditions," *Catal. Sci. Technol.*, vol. 7, no. 11, pp. 2213–2220, 2017.

[117]   L. He, F. Weniger, H. Neumann, and M. Beller, "Synthesis, Characterization, and Application of Metal Nanoparticles Supported on Nitrogen-Doped Carbon: Catalysis beyond Electrochemistry," *Angew. Chemie - Int. Ed.*, vol. 55, no. 41, pp. 12582–12594, 2016.

[118]   D. A. Bulushev *et al.*, "Single Atoms of Pt-Group Metals Stabilized by N-Doped Carbon Nanofibers for Efficient Hydrogen Production from Formic Acid," *ACS Catal.*, vol. 6, no. 6, pp. 3442–3451, 2016.

[119]   P. D. Srinivasan, B. S. Patil, H. Zhu, and J. J. Bravo-Suárez, "Application of modulation excitation-phase sensitive detection-DRIFTS for: In situ /operando characterization of heterogeneous catalysts," *React. Chem. Eng.*, vol. 4, no. 5, pp. 862–883, 2019.

[120]   J. M. Olinger and P. R. Griffiths, "Quantitative effects of an absorbing matrix on near-infrared diffuse reflectance spectra," *Anal. Chem.*, vol. 60, no. 21, pp. 2427–2435, 1988.

[121]   J. Sirita, S. Phanichphant, and F. C. Meunier, "Quantitative analysis of adsorbate concentrations by diffuse

reflectance FT-IR," *Anal. Chem.*, vol. 79, no. 10, pp. 3912–3918, 2007.

[122]   L. P. L. Gonçalves *et al.*, "Selective formic acid dehydrogenation at low temperature over a RuO2/COF pre-catalyst synthesized on the gram scale," *Catal. Sci. Technol.*, vol. 10, no. 7, pp. 1991–1995, 2020.

[123]   X. Han *et al.*, "Chiral induction in covalent organic frameworks," *Nat. Commun.*, vol. 9, no. 1, pp. 1–10, 2018.

[124]   J. S. Yoo, F. Abild-Pedersen, J. K. Nørskov, and F. Studt, "Theoretical analysis of transition-metal catalysts for formic acid decomposition," *ACS Catal.*, vol. 4, no. 4, pp. 1226–1233, 2014.

[125]   M. D. Marcinkowski *et al.*, "Selective Formic Acid Dehydrogenation on Pt-Cu Single-Atom Alloys," *ACS Catal.*, vol. 7, no. 1, pp. 413–420, 2017.

[126]   N. R. Avery, "Reaction of HCOOH with a Pt(lll)-O surface; identification of adsorbed monodentate formate," *Appl. Surf. Sci.*, vol. 14, no. lll, pp. 149–156, 1983.

[127]   Y. Katayama *et al.*, "An in Situ Surface-Enhanced Infrared Absorption Spectroscopy Study of Electrochemical CO2 Reduction: Selectivity Dependence on Surface C-Bound and O-Bound Reaction Intermediates," *J. Phys. Chem. C*, vol. 123, no. 10, pp. 5951–5963, 2019.

[128]   L. H. Little and C. H. Amberg, "Infrared spectra of carbon monoxide and carbon dioxide adsorbed on chromia-alumina and on alumina," *Can. J. Chem.*, vol. 40, no. 1962, pp. 1997–2006, 1997.

[129]   M. G. Sensoy, H. Ustunel, and D. Toffoli, "First-principles investigation of CO and CO2 adsorption on γ-Al2O3 supported monoatomic and diatomic Pt clusters," *Appl. Surf. Sci.*, vol. 499, no. July 2019, p. 143968, 2020.

[130]   H. Gao *et al.*, "A simple method to synthesize continuous large area nitrogen-doped graphene," *Carbon N. Y.*, vol. 50, no. 12, pp. 4476–4482, 2012.

[131]   R. Goyal *et al.*, "Studies of synergy between metal-support interfaces and selective hydrogenation of HMF to DMF in water," *J. Catal.*, vol. 340, pp. 248–260, 2016.

[132]   X. Ning, H. Yu, F. Peng, and H. Wang, "Pt nanoparticles interacting with graphitic nitrogen of N-doped carbon nanotubes: Effect of electronic properties on activity for aerobic oxidation of glycerol and electro-oxidation of CO," *J. Catal.*, vol. 325, pp. 136–144, 2015.

[133]   B. Zhang and D. S. Su, "Probing the Metal-Support Interaction in Carbon-Supported Catalysts by using Electron Microscopy," *ChemCatChem*, vol. 7, no. 22, pp. 3639–3645, 2015.

[134]   I. Ganesh, "Conversion of carbon dioxide into methanol - A potential liquid fuel: Fundamental challenges and opportunities (a review)," *Renew. Sustain. Energy Rev.*, vol. 31, pp. 221–257, 2014.

[135]   R. Christoph, B. Schmidt, U. Steinberner, W. Dilla, and R. Karinen, *Formic acid*, vol. 16. 1998.

[136]   J. Albert and P. Wasserscheid, "Expanding the scope of biogenic substrates for the selective production of formic acid from water-insoluble and wet waste biomass," *Green Chem.*, vol. 17, no. 12, pp. 5164–5171, 2015.

[137]   C. Jia, J. Gao, Y. Dai, J. Zhang, and Y. Yang, "The thermodynamics analysis and experimental validation for complicated systems in CO2 hydrogenation process," *J. Energy Chem.*, vol. 25, no. 6, pp. 1027–1037, 2016.

[138]   G. H. Gunasekar, K. Park, K. D. Jung, and S. Yoon, "Recent developments in the catalytic hydrogenation of CO2 to formic acid/formate using heterogeneous catalysts," *Inorg. Chem. Front.*, vol. 3, no. 7, pp. 882–895, 2016.

[139]   W. H. Wang, Y. Himeda, J. T. Muckerman, and E. Fujita, "Interconversion of CO2/H2 and Formic Acid Under Mild Conditions in Water: Ligand Design for Effective Catalysis," in *Advances in Inorganic Chemistry*, 1st ed., vol. 66, Elsevier Inc., 2014, pp. 189–222.

[140]   A. Azua, S. Sanz, and E. Peris, "Water-soluble IrIII N-heterocyclic carbene based catalysts for the reduction of CO2 to formate by transfer hydrogenation and the deuteration of aryl amines in water," *Chem. - A Eur. J.*, vol. 17, no. 14, pp. 3963–3967, 2011.

[141]   G. Laurenczy, F. Joo, and L. Nadasdi, "Formation and characterization of water-soluble hydrido-ruthenium(II) complexes of 1,3,5-triaza-7-phosphaadamantane and their catalytic activity in hydrogenation of CO2 and HCO3- in aqueous solution," *Inorg. Chem.*, vol. 39, no. 22, pp. 5083–5088, 2000.

[142]   W. Wang, S. Wang, X. Ma, and J. Gong, "Recent advances in catalytic hydrogenation of carbon dioxide,"

Chem. Soc. Rev., vol. 40, no. 7, pp. 3703–3727, 2011.

[143] G. A. Filonenko, R. Van Putten, E. N. Schulpen, E. J. M. Hensen, and E. A. Pidko, "Highly efficient reversible hydrogenation of carbon dioxide to formates using a ruthenium PNP-pincer catalyst," *ChemCatChem*, vol. 6, no. 6, pp. 1526–1530, 2014.

[144] J. H. Lee *et al.*, "Carbon dioxide mediated, reversible chemical hydrogen storage using a Pd nanocatalyst supported on mesoporous graphitic carbon nitride," *J. Mater. Chem. A*, vol. 2, no. 25, pp. 9490–9495, 2014.

[145] J. F. Hull *et al.*, "Reversible hydrogen storage using CO2 and a proton-switchable iridium catalyst in aqueous media under mild temperatures and pressures," *Nat. Chem.*, vol. 4, no. 5, pp. 383–388, 2012.

[146] Y. Himeda, N. Onozawa-Komatsuzaki, H. Sugihara, and K. Kasuga, "Simultaneous tuning of activity and water solubility of complex catalysts by acid-base equilibrium of ligands for conversion of carbon dioxide," *Organometallics*, vol. 26, no. 3, pp. 702–712, 2007.

[147] G. H. Gunasekar and S. Yoon, "A phenanthroline-based porous organic polymer for the iridium-catalyzed hydrogenation of carbon dioxide to formate," *J. Mater. Chem. A*, vol. 7, no. 23, pp. 14019–14026, 2019.

[148] J. Weber, M. Antonietti, and A. Thomas, "Microporous networks of high-performance polymers: Elastic deformations and gas sorption properties," *Macromolecules*, vol. 41, no. 8, pp. 2880–2885, 2008.

[149] J. R. Lee, Y. R. Liou, and W. L. Huang, "Emission studies of hetero-bischelated iridium(III)-diimine complexes," *Inorganica Chim. Acta*, vol. 319, no. 1–2, pp. 83–89, 2001.

[150] L. T. M. Nguyen *et al.*, "Catalytic CO2 hydrogenation to formic acid over carbon nanotube-graphene supported PdNi alloy catalysts," *RSC Adv.*, vol. 5, no. 128, pp. 105560–105566, 2015.

[151] K. A. Cychosz and M. Thommes, "Progress in the Physisorption Characterization of Nanoporous Gas Storage Materials," *Engineering*, vol. 4, no. 4, pp. 559–566, 2018.

[152] T. Iwai, T. Harada, H. Shimada, K. Asano, and M. Sawamura, "A Polystyrene-Cross-Linking Bisphosphine: Controlled Metal Monochelation and Ligand-Enabled First-Row Transition Metal Catalysis," *ACS Catal.*, vol. 7, no. 3, pp. 1681–1692, 2017.

[153] K. Park, G. H. Gunasekar, N. Prakash, K. D. Jung, and S. Yoon, "A Highly Efficient Heterogenized Iridium Complex for the Catalytic Hydrogenation of Carbon Dioxide to Formate," *ChemSusChem*, vol. 8, no. 20, pp. 3410–3413, 2015.

[154] D. B. Christensen, R. L. Mortensen, S. Kramer, and S. Kegnæs, "Study of CoCu Alloy Nanoparticles Supported on MOF-Derived Carbon for Hydrosilylation of Ketones," *Catal. Letters*, 2019.

[155] B. Marciniec, H. Maciejewski, C. Pietraszuk, and P. Pawluc, "Hydrosilylation of Unsaturated Carbon—Heteroatom Bonds," in *Hydrosilylation - A Comprehensive Review on Recent Advances*, Springer, 2009, pp. 289–398.

[156] K. Riener, M. P. Högerl, P. Gigler, and F. E. Kühn, "Rhodium-catalyzed hydrosilylation of ketones: Catalyst development and mechanistic insights," *ACS Catal.*, vol. 2, no. 4, pp. 613–621, 2012.

[157] L. N. Lewis, J. Stein, Y. Gao, R. E. Colborn, and G. Hutchins, "Platinum catalysts used in the silicone industry," *Platin. Matals Rev.*, vol. 41, no. 2, pp. 66–75, 1997.

[158] I. Ojima, T. Kogure, M. Kumagai, S. Horiuchi, and T. Sato, "Asymmetric reduction of ketones via hydrosilylation catalyzed by a rhodium(I) complex with chiral phosphine ligands," *J. Organomet. Chem.*, vol. 122, no. 1, pp. 83–97, 1976.

[159] I. Ojima, T. Kogure, M. Nihonyanagi, and Y. Nagai, "Reduction of Carbonyl Compounds with Various Hydrosilane Rhodium(I) Complex Combinations," *Bull. Chem. Soc. Jpn.*, vol. 45, no. 11, p. 3506, 1972.

[160] H. Miura, K. Endo, R. Ogawa, and T. Shishido, "Supported Palladium-Gold Alloy Catalysts for Efficient and Selective Hydrosilylation under Mild Conditions with Isolated Single Palladium Atoms in Alloy Nanoparticles as the Main Active Site," *ACS Catal.*, vol. 7, no. 3, pp. 1543–1553, 2017.

[161] M. Benohoud, S. Tuokko, and P. M. Pihko, "Stereoselective hydrosilylation of enals and enones catalysed by palladium nanoparticles," *Chem. - A Eur. J.*, vol. 17, no. 30, pp. 8404–8413, 2011.

[162] N. R. Bennedsen, S. Kramer, J. J. Mielby, and S. Kegnæs, "Cobalt-nickel alloy catalysts for hydrosilylation of ketones synthesized by utilizing metal-organic framework as template," *Catal. Sci. Technol.*, vol. 8, no. 9, pp.

2434–2440, 2018.

[163]   M. Li, B. Li, H. F. Xia, D. Ye, J. Wu, and Y. Shi, "Mesoporous silica KIT-6 supported superparamagnetic CuFe2O4 nanoparticles for catalytic asymmetric hydrosilylation of ketones in air," *Green Chem.*, vol. 16, no. 5, pp. 2680–2688, 2014.

[164]   W. Zhou, S. L. Marquard, M. W. Bezpalko, B. M. Foxman, and C. M. Thomas, "Catalytic hydrosilylation of ketones using a Co/Zr heterobimetallic complex: Evidence for an unusual mechanism involving ketyl radicals," *Organometallics*, vol. 32, no. 6, pp. 1766–1772, 2013.

[165]   K. Garcés, F. J. Fernández-Alvarez, P. García-Orduña, F. J. Lahoz, J. J. Pérez-Torrente, and L. A. Oro, "Grafting of Copper(I)-NHC Species on MCM-41: Homogeneous versus Heterogeneous Catalysis," *ChemCatChem*, vol. 7, no. 16, pp. 2501–2507, 2015.

[166]   I. L. Zhao, N. Nakatani, and J. Hasegawa, "Theoretical Study of Rhodium-Catalyzed Hydrosilylation of Ketones : Chalk-Harrod vs . Modified Chalk-Harrod Mechanism," pp. 2–3.

[167]   A. J. Chalk and J. F. Harrod, "Homogeneous Catalysis. II. The Mechanism of the Hydrosilation of Olefins Catalyzed by Group VIII Metal Complexes," *J. Am. Chem. Soc.*, vol. 87, no. 1, pp. 16–21, 1965.

[168]   B. Marciniec, H. Maciejewski, C. Pietraszuk, and P. Pawluc, "Hydrosilylation of alkenes and their derivatives," in *Hydrosilylation - A Comprehensive Review on Recent Advances*, 2009, pp. 3–44.

[169]   B. Chen, Z. Yang, Y. Zhu, and Y. Xia, "Zeolitic imidazolate framework materials: Recent progress in synthesis and applications," *J. Mater. Chem. A*, vol. 2, no. 40, pp. 16811–16831, 2014.

[170]   H. Hu, B. Guan, B. Xia, and X. W. Lou, "Designed formation of Co3O4/NiCo2O4 double-shelled nanocages with enhanced pseudocapacitive and electrocatalytic properties," *J. Am. Chem. Soc.*, vol. 137, no. 16, pp. 5590–5595, 2015.

[171]   G. Zhong, D. Liu, and J. Zhang, "The application of ZIF-67 and its derivatives: Adsorption, separation, electrochemistry and catalysts," *J. Mater. Chem. A*, vol. 6, no. 5, pp. 1887–1899, 2018.

[172]   H. Yang, X. W. He, F. Wang, Y. Kang, and J. Zhang, "Doping copper into ZIF-67 for enhancing gas uptake capacity and visible-light-driven photocatalytic degradation of organic dye," *J. Mater. Chem.*, vol. 22, no. 41, pp. 21849–21851, 2012.

[173]   A. R. Denton and N. W. Ashcroft, "Vegards law," *Phys. Rev. A*, vol. 43, no. 6, pp. 3161–3164, 1991.

[174]   X. X. Wang *et al.*, "Ordered Pt3Co Intermetallic Nanoparticles Derived from Metal-Organic Frameworks for Oxygen Reduction," *Nano Lett.*, vol. 18, no. 7, pp. 4163–4171, 2018.

[175]   Q. Yang, Y. Liu, M. Yan, Y. Lei, and W. Shi, "MOF-derived hierarchical nanosheet arrays constructed by interconnected NiCo-alloy@NiCo-sulfide core-shell nanoparticles for high-performance asymmetric supercapacitors," *Chem. Eng. J.*, vol. 370, no. January, pp. 666–676, 2019.

[176]   H. Wang, X. Li, X. Lan, and T. Wang, "Supported Ultrafine NiCo Bimetallic Alloy Nanoparticles Derived from Bimetal-Organic Frameworks: A Highly Active Catalyst for Furfuryl Alcohol Hydrogenation," *ACS Catal.*, vol. 8, no. 3, pp. 2121–2128, 2018.

[177]   J. Long, K. Shen, L. Chen, and Y. Li, "Multimetal-MOF-derived transition metal alloy NPs embedded in an N-doped carbon matrix: Highly active catalysts for hydrogenation reactions," *J. Mater. Chem. A*, vol. 4, no. 26, pp. 10254–10262, 2016.

Appendix A, supporting information for Chapter 4

All histograms are based on measurements from 200-500 particles from at least 10 images.

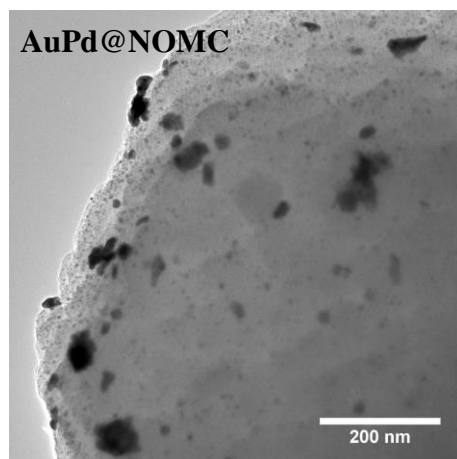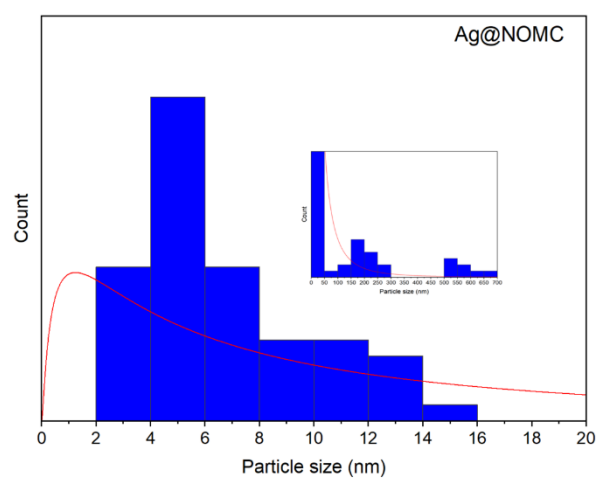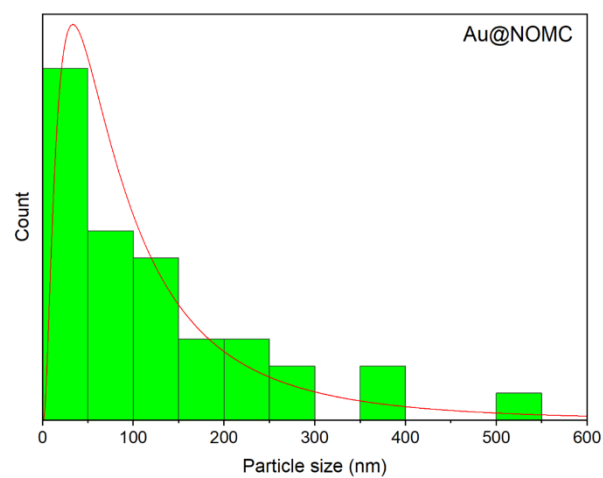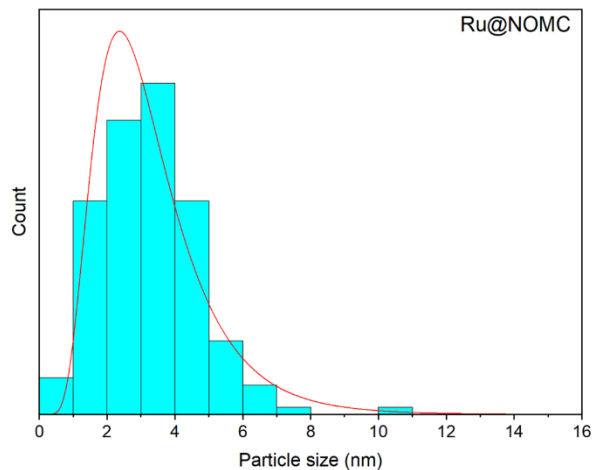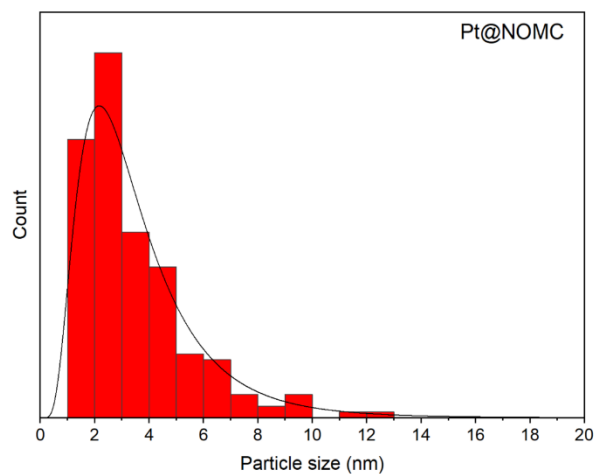## A.1 Examples of TEM images of all NOMC samples produced by incipient-wetness
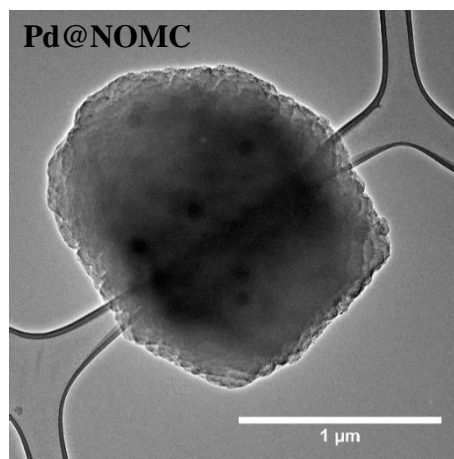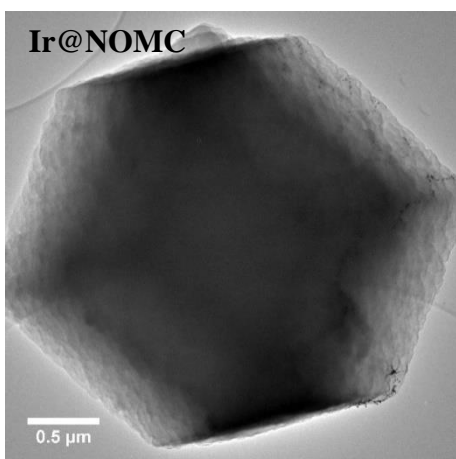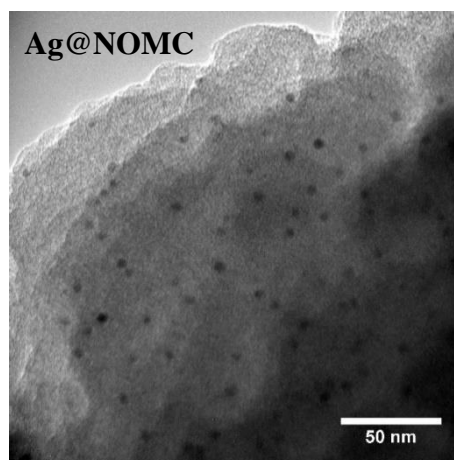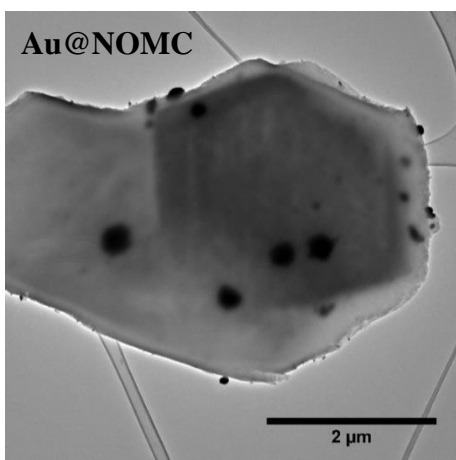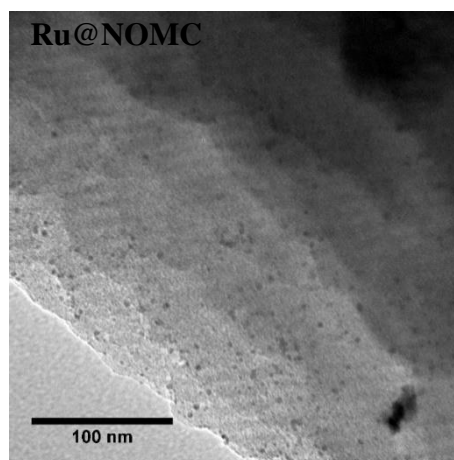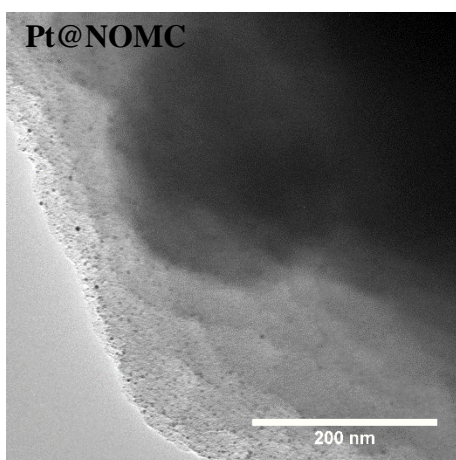
Figure A.1.1: TEM images of all NOMC samples prepared by incipient-wetness for the dehydrogenation of formic acid. Each samples has a loading of 1 wt. Depending on the angle of the image, ordered pores in the structure are visible ranging in size from about 7-9 nm in diameter.
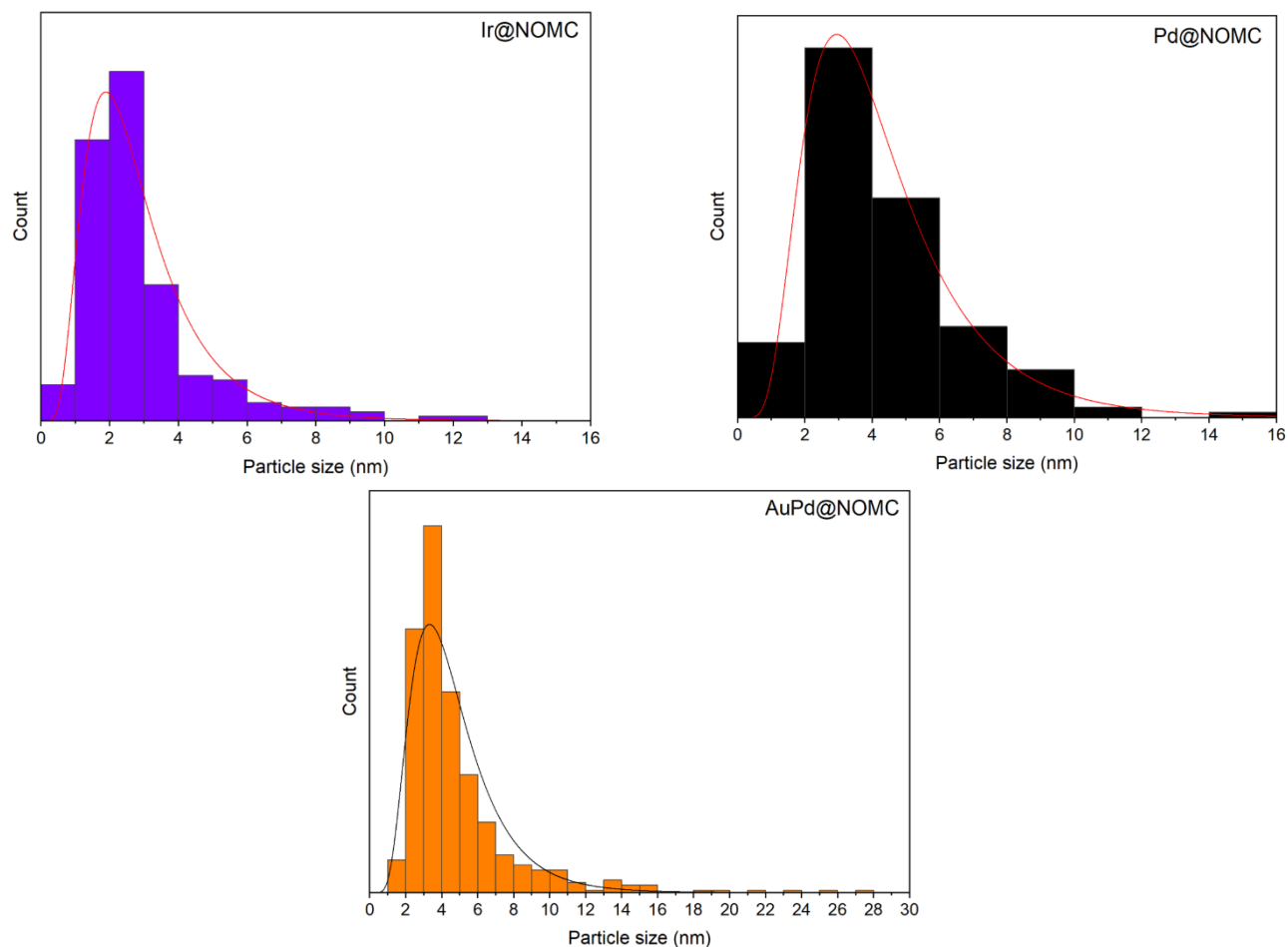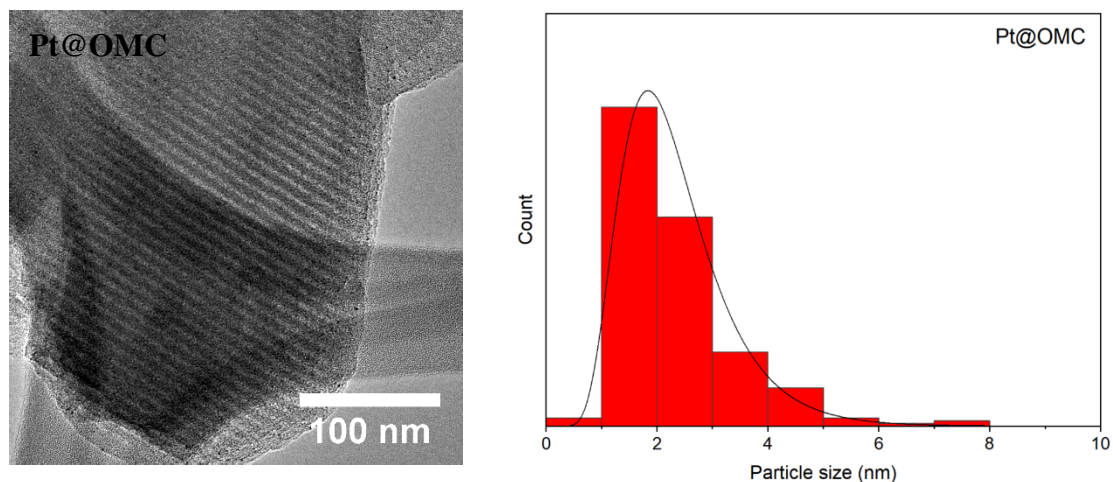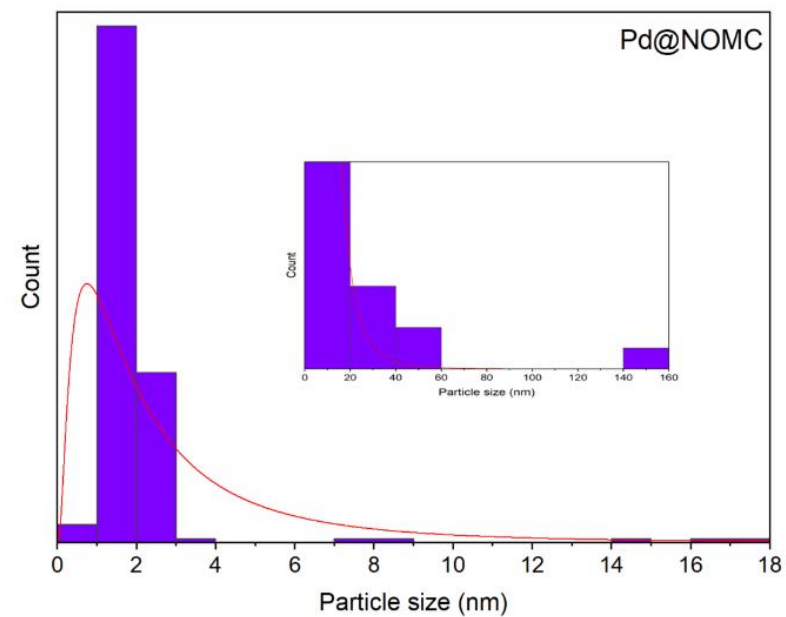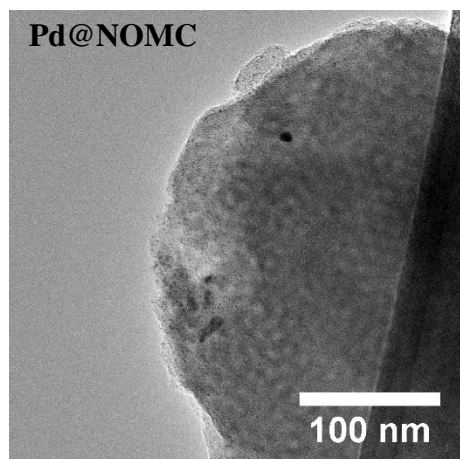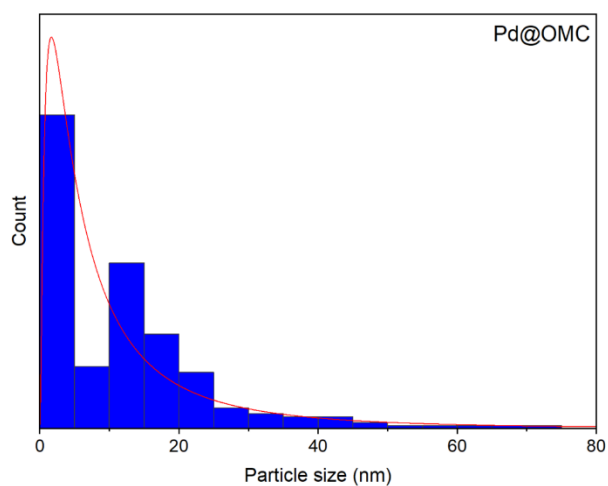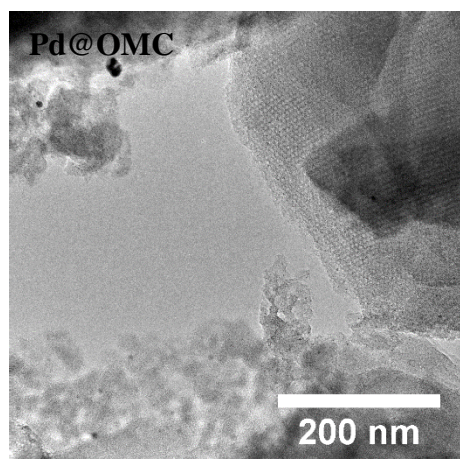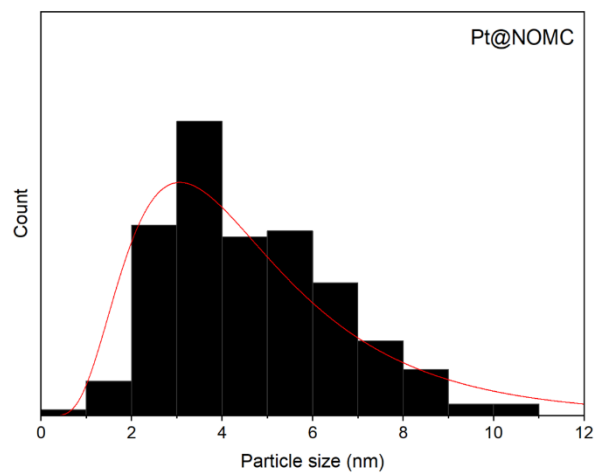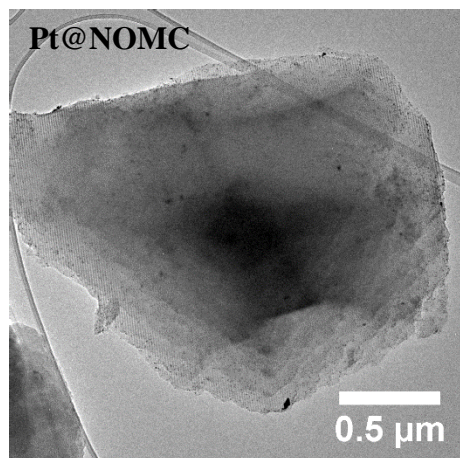
Figure A.1.2: Histograms from each of the NOMC samples used in section 4.3.1. Histograms are based on the measurements of at least 200 particles from at least ten images at different sites. Normal distribution has been included in the form of a line.

A.2 Examples of TEM images of all samples produced by metalation
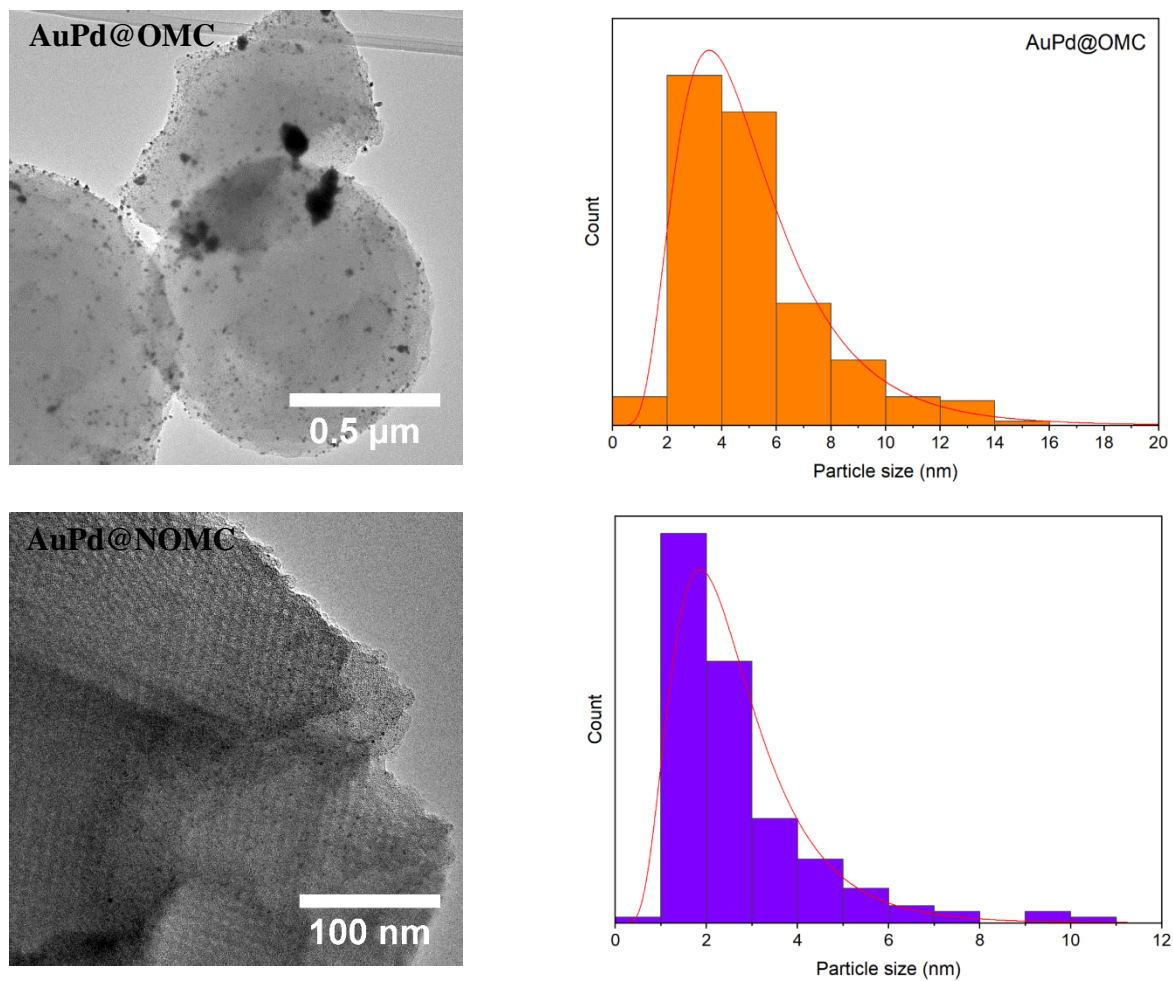
Figure A.2.1: Example of TEM images and histograms from each of the OMC and NOMC samples used in section 4.3.2. An expanded view of Pd@NOMC has been included, due to the presence of some large agglomerates.

A.3 Examples of TEM images of metalation samples after reaction
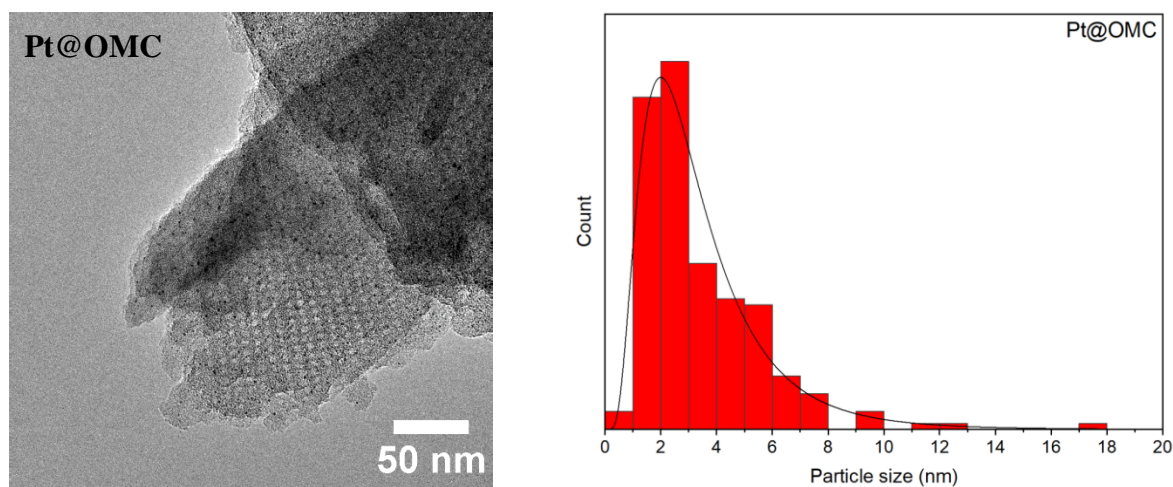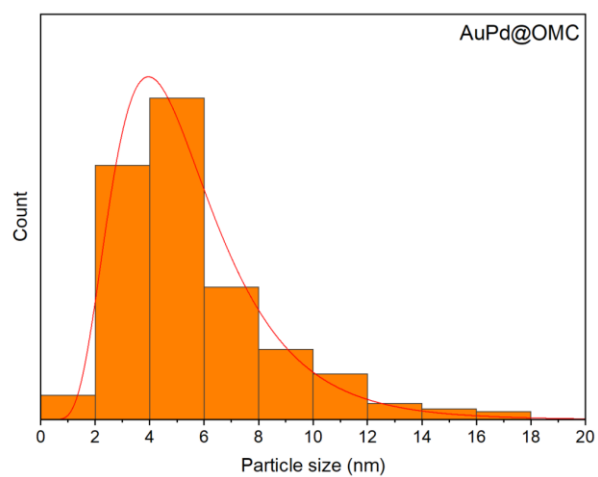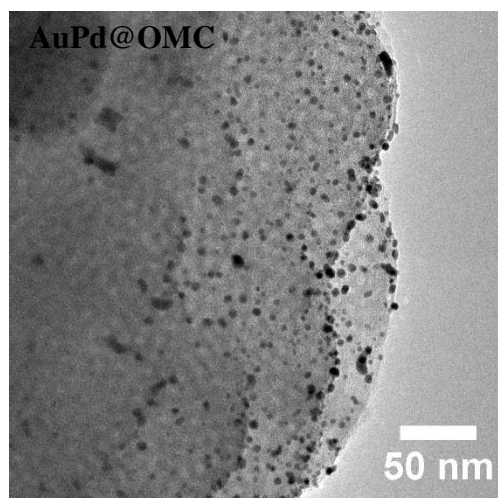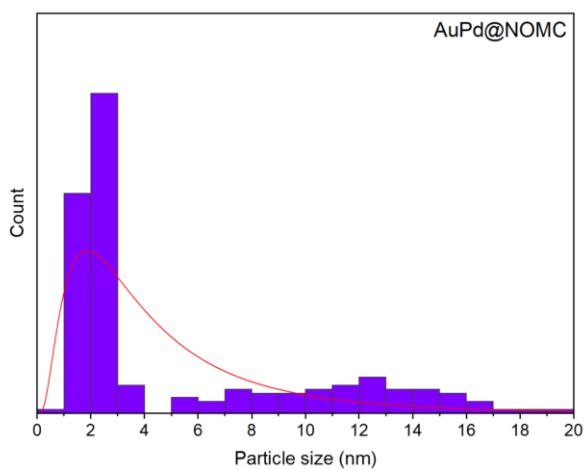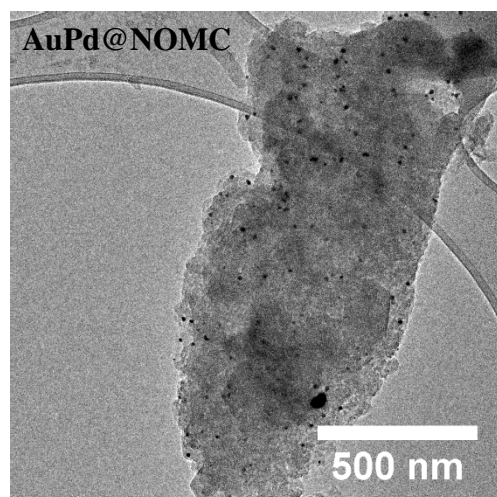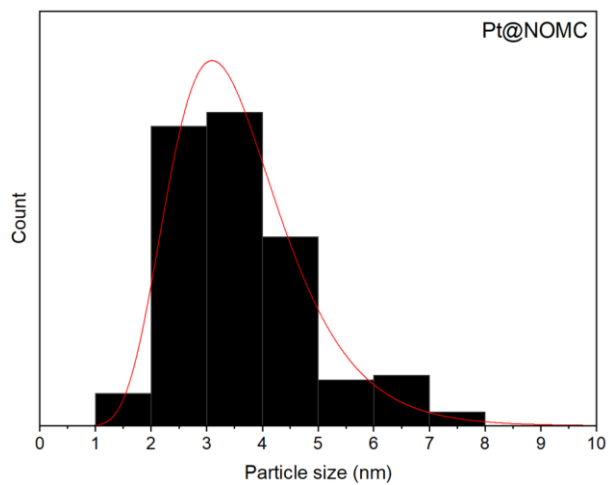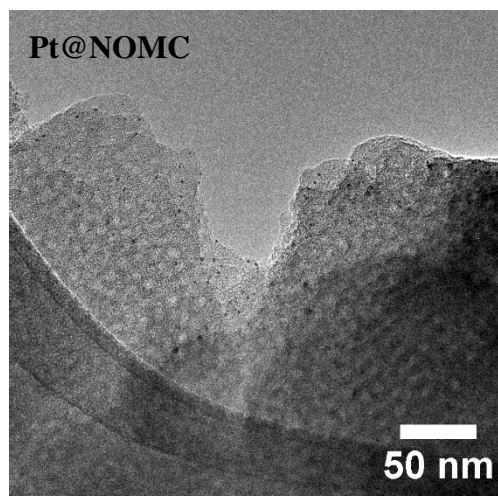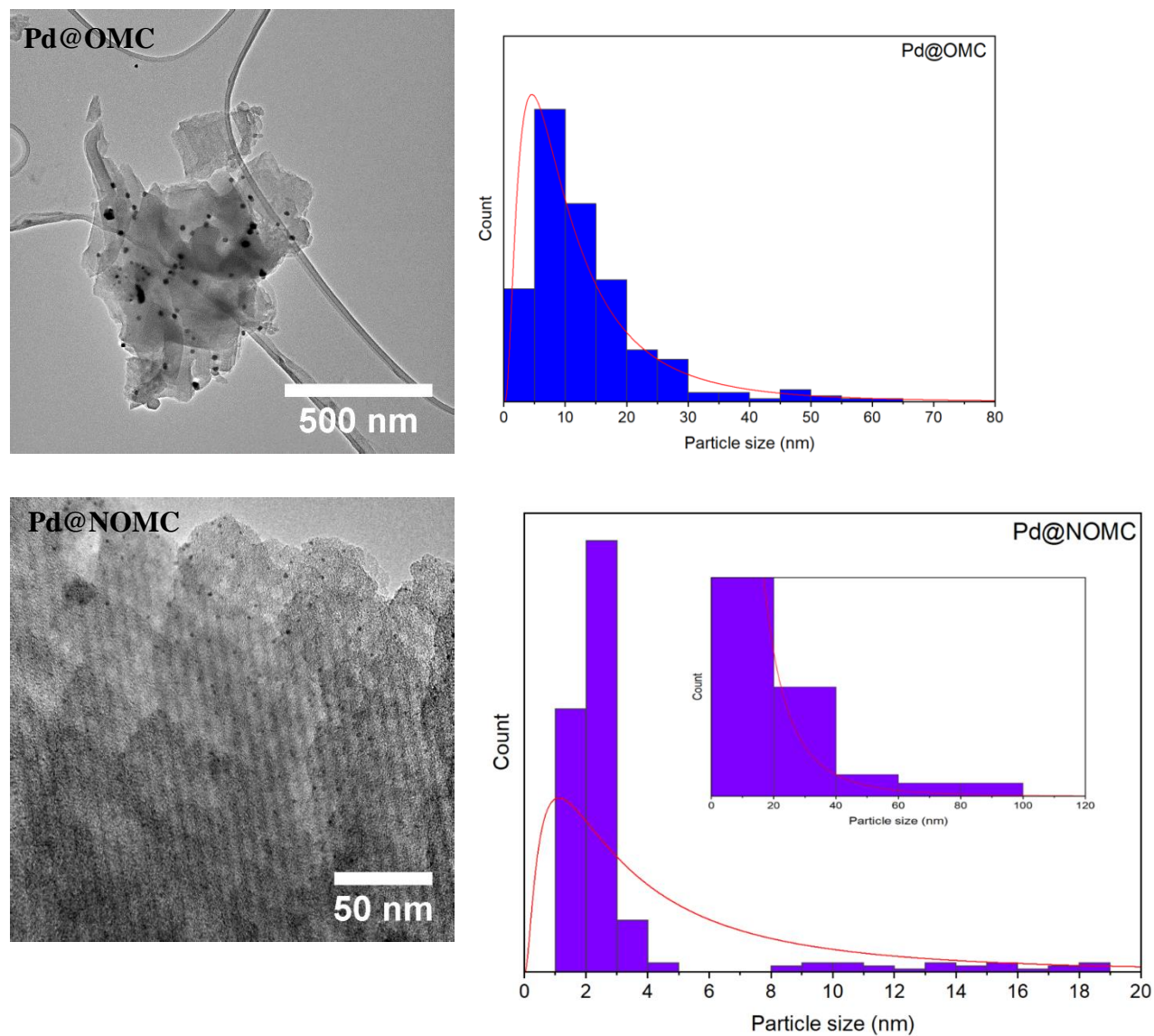
Figure A.3.1: Example of TEM images and histograms from each of the OMC and NOMC samples used in section 4.3.2. The images illustrated the samples appearance after exposure to reaction conditions. An expanded view of Pd@NOMC has been included, due to the presence of several larger particles.

A.4 BJH analysis of OMC and NOMC

BJH analysis of the desorption curve from N_2-physisorption of NOMC support.
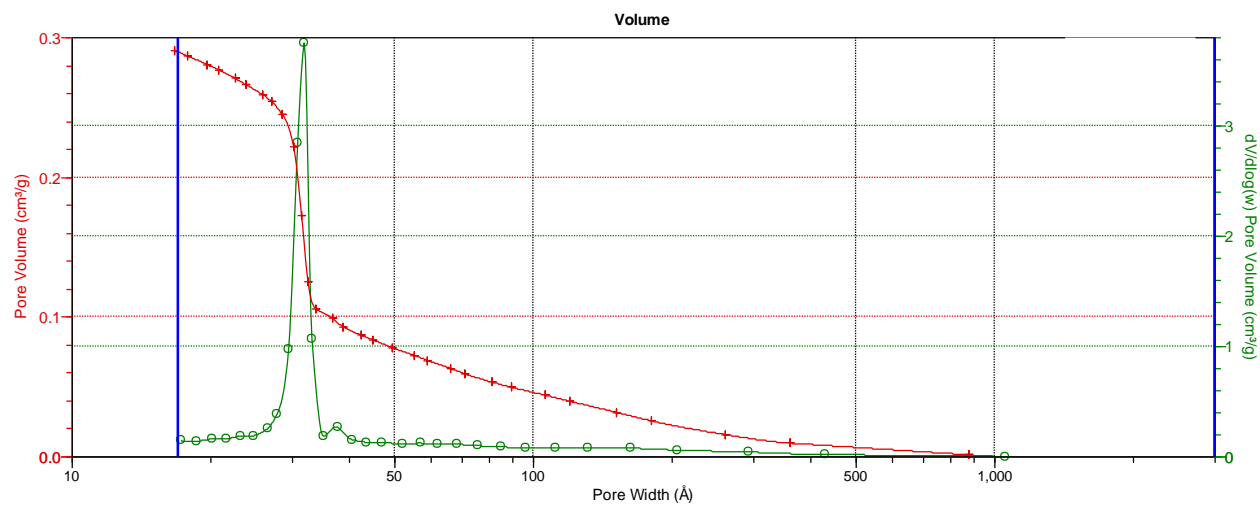
BJH analysis of the adsorption curve from N_2-physisorption of NOMC support.
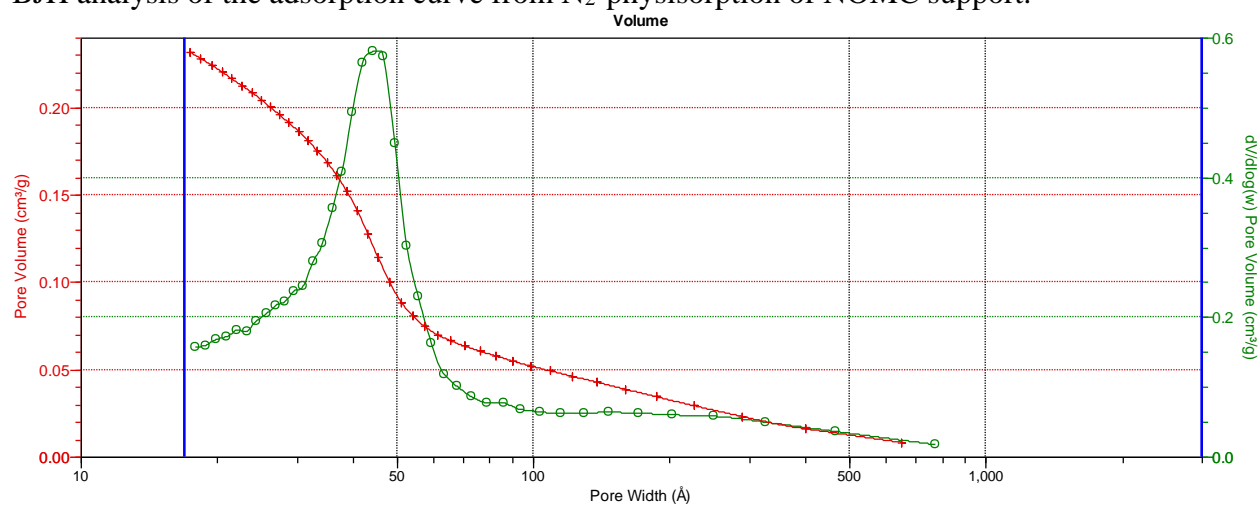
BJH analysis of the desorption curve from N$_2$-physisorption of OMC support.
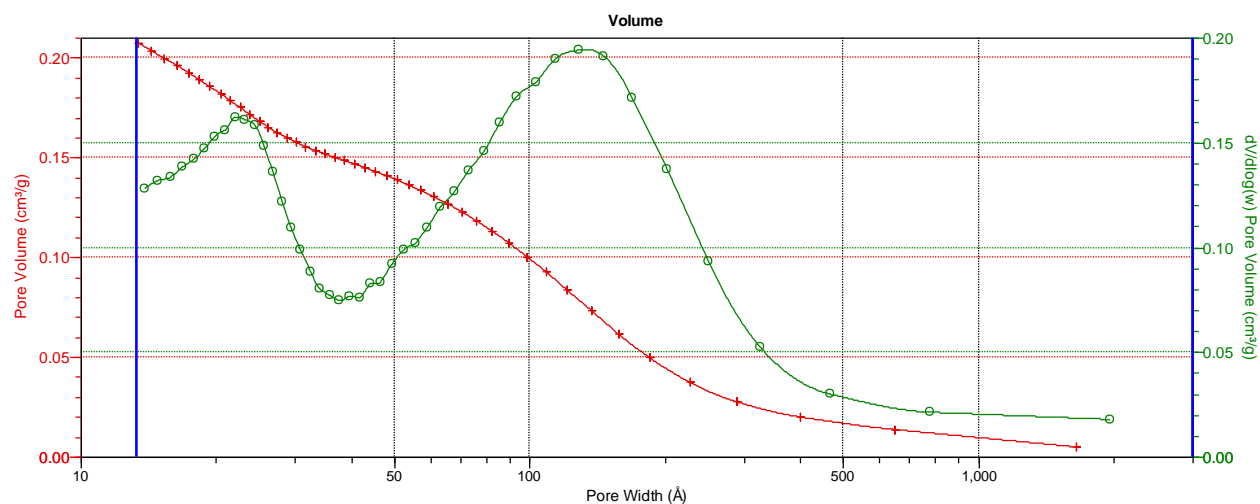
BJH analysis of the adsorption curve from N$_2$-physisorption of OMC support.
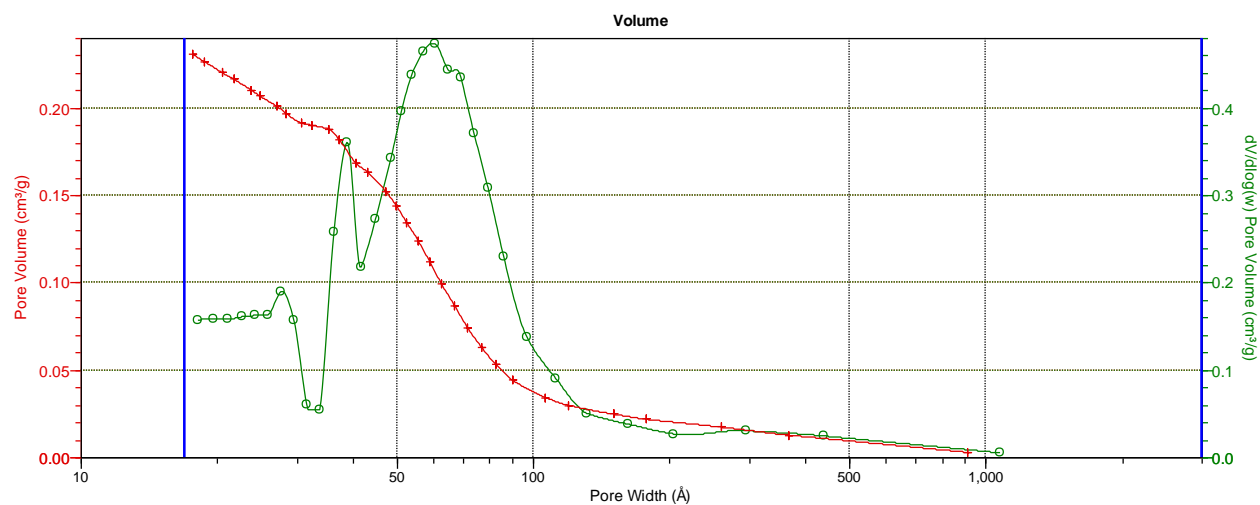
Figure A.4.1: BJH analysis of the OMC and NOMC materials acquired during N$_2$-physisorption. The results from NOMC indicated a more narrow distribution of pore sizes compared to OMC despite their similar appearance in electron microscopy images.

A.5 SAXS measurement of OMC and NOMC
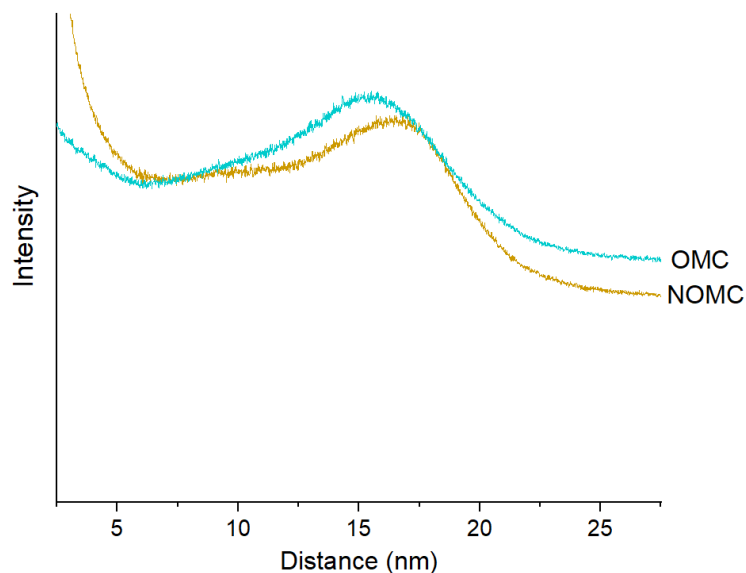
Figure A.5.1: SAXS analysis conducted by Niklas Bennedsen on the NOMC and OMC materials. A clear peak is observed at 15 nm for OMC and 17 nm for NOMC indicating a periodically spacing in the material attributed to the ordered pores.

Appendix B, supporting information for Chapter 5

B.1 XPS analysis of bpy-PP-POPs
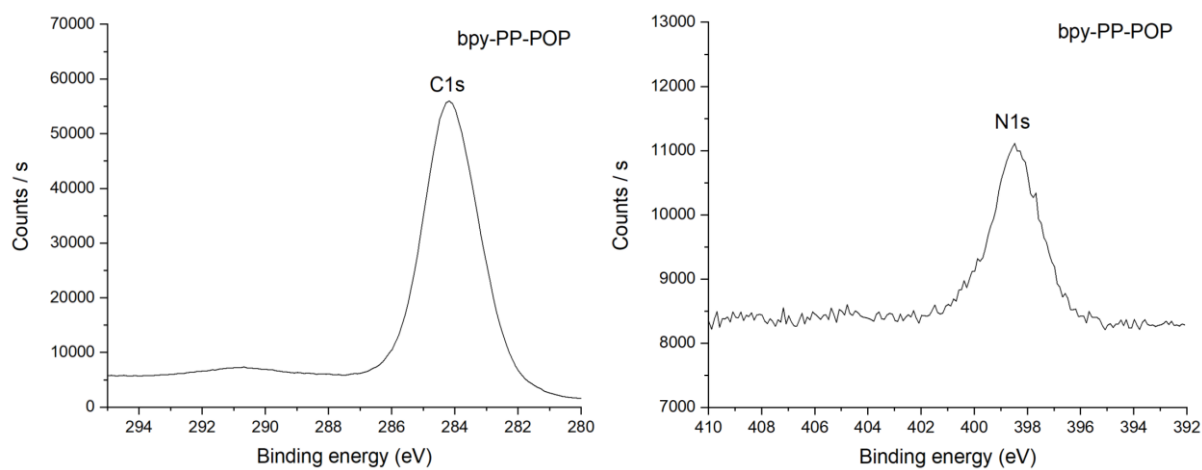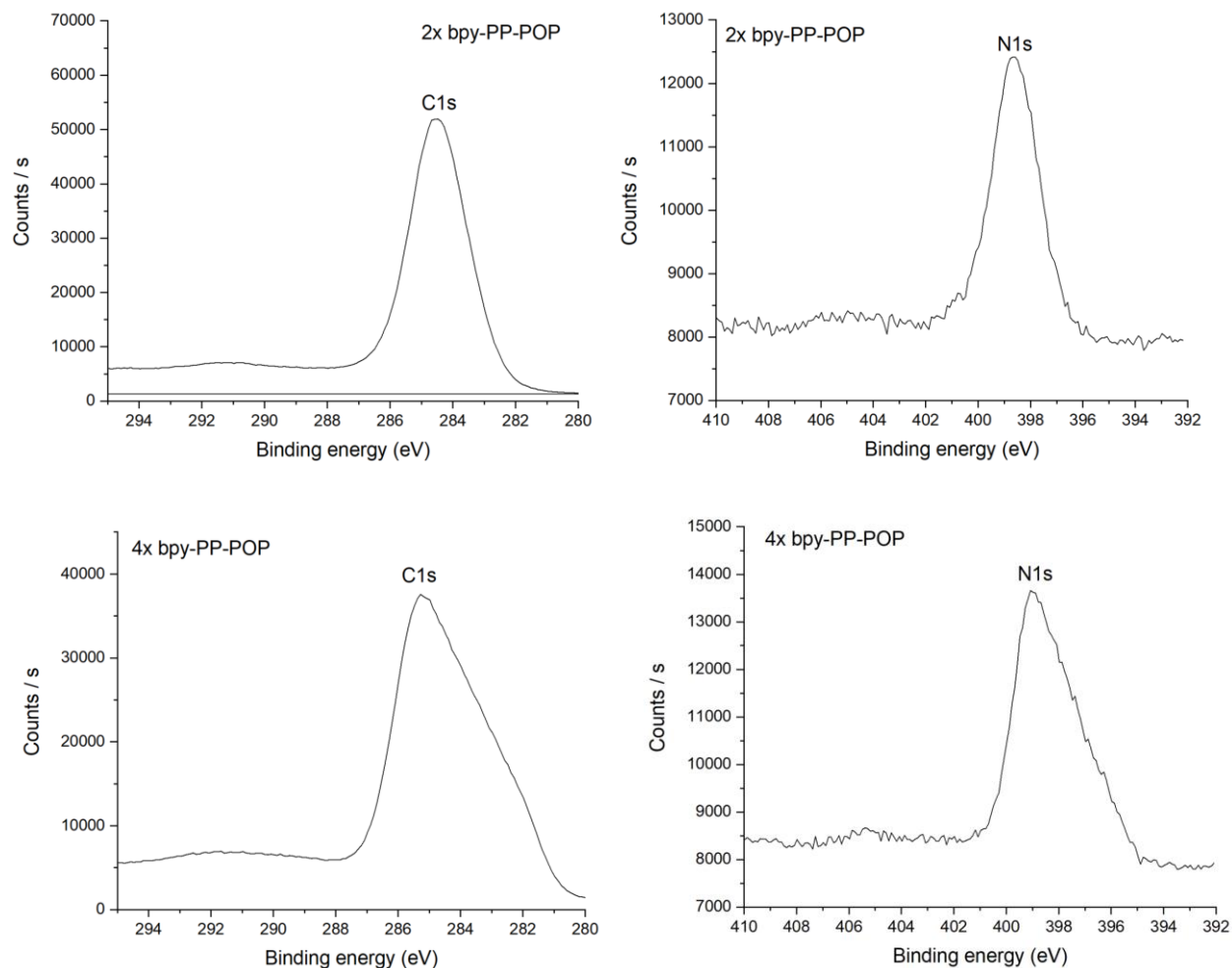
Figure B.1.1: XPS of the three bpy-PP-POP materials (bpy-PP-POP, 2x bpy-PP-POP and 4x bpy-PP-POP). The observed signal from nitrogen from all three samples (398.5 eV) is attributed to pyridinic nitrogen from the ligands incorporated in the POP.

B.2 XRD measurement of bpy-PP-POP
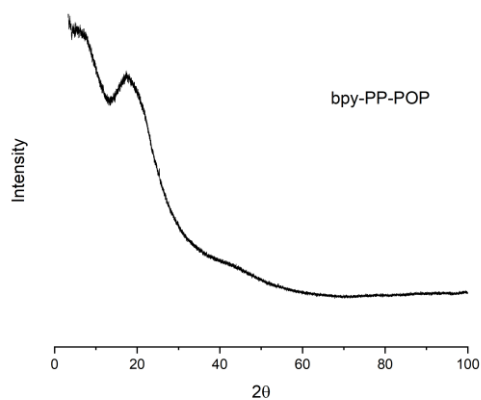
Figure B.2.1: The XRD diffractogram of bpy-PP-POP shows an amorphous material, which only has a broad peak below 30 °, as is common for amorphous carbon materials. There are no crystalline peaks, which indicates the complete removal of the palladium used for the synthesis.

B.3 STEM image indicating the presence of single atoms on bpy-PP-POP
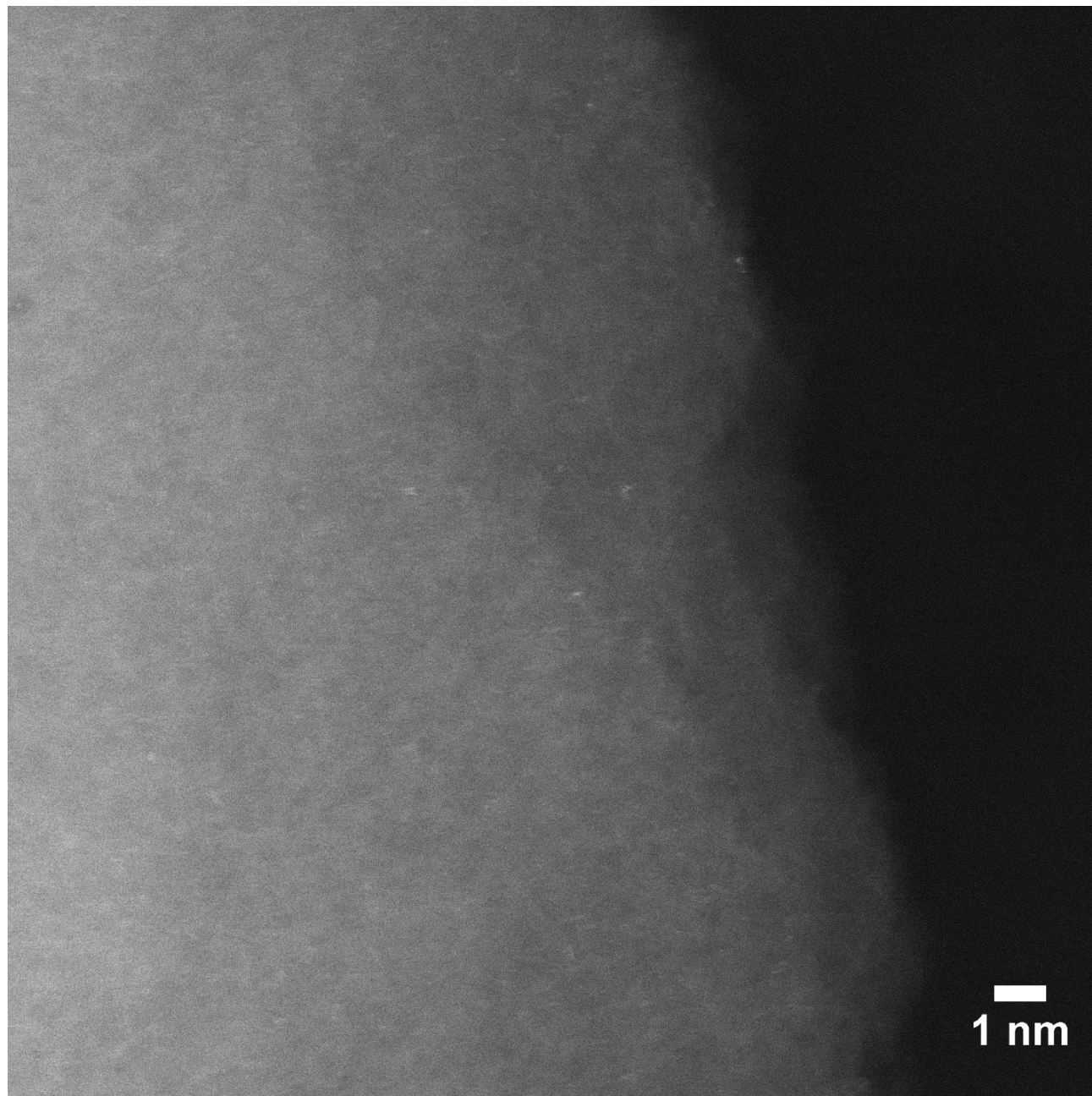
Figure B.3.1: High-resolution HAADF STEM image of bpy-PP-POP. Bright particles can barely be seen several places on the material believed to be single atoms of Ir.

Appendix C, supporting information for Chapter 6

C.1 Isotherms at different copper loadings
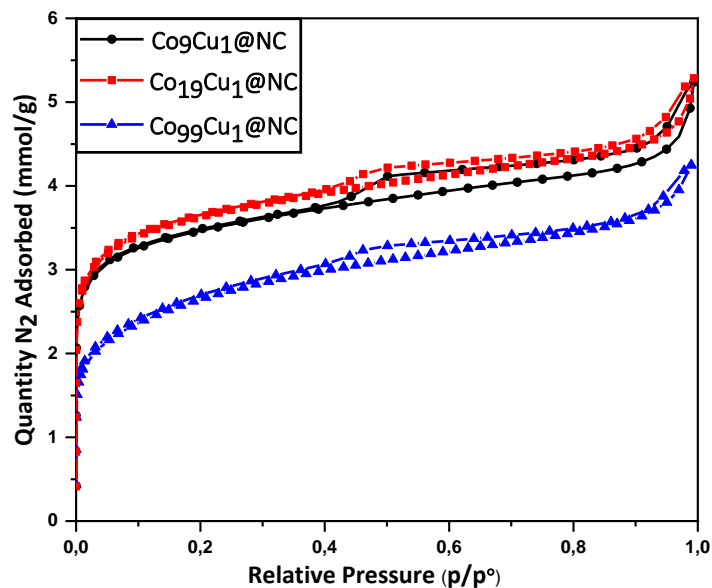
Figure C.1.1: Comparison of nitrogen physisorption isotherms from three of the $Co_xCu_y@NC$ covered in chapter 6. All three isotherms have a similar shape with some variation in initial adsorption.

C.2 BJH analysis of $Co_9Cu_1@NC$
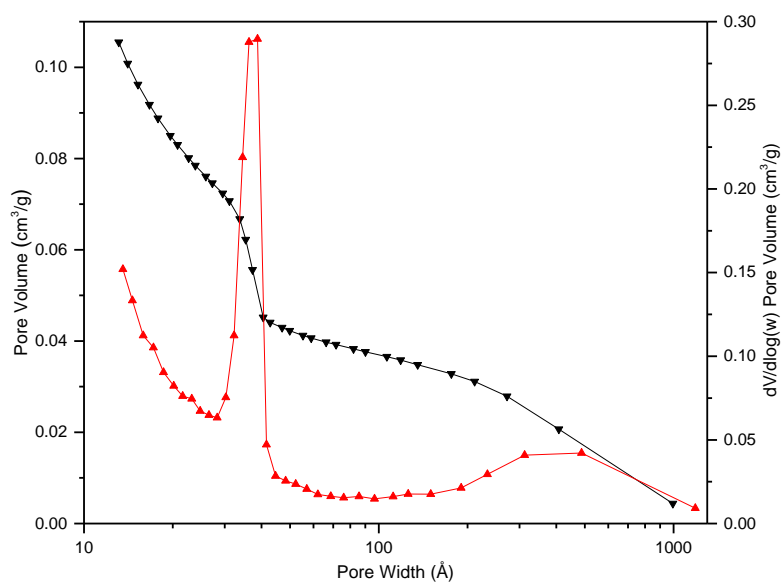
Figure C.2.1: The BJH adsorption data from the $Co_9Cu_1@NC$ sample. The results indicate that the sample mainly has pores of about 30 Å in size.

C.3 XRD of ZIF-67 before impregnation with copper
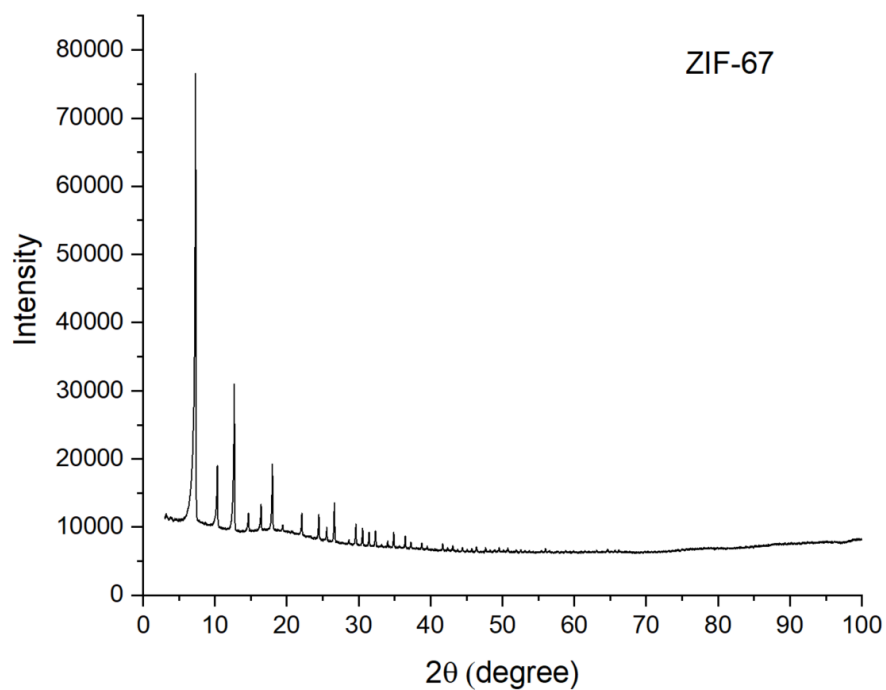
Figure C.3.1: XRD pattern recorded from the ZIF-67 precursor used for preparing all the Co_xCu_y@NC samples. The resulting pattern is in line with what is expected from this type of MOF.

C.4 Additional images and particle size distributions of all Co_xCu_y@NC catalysts
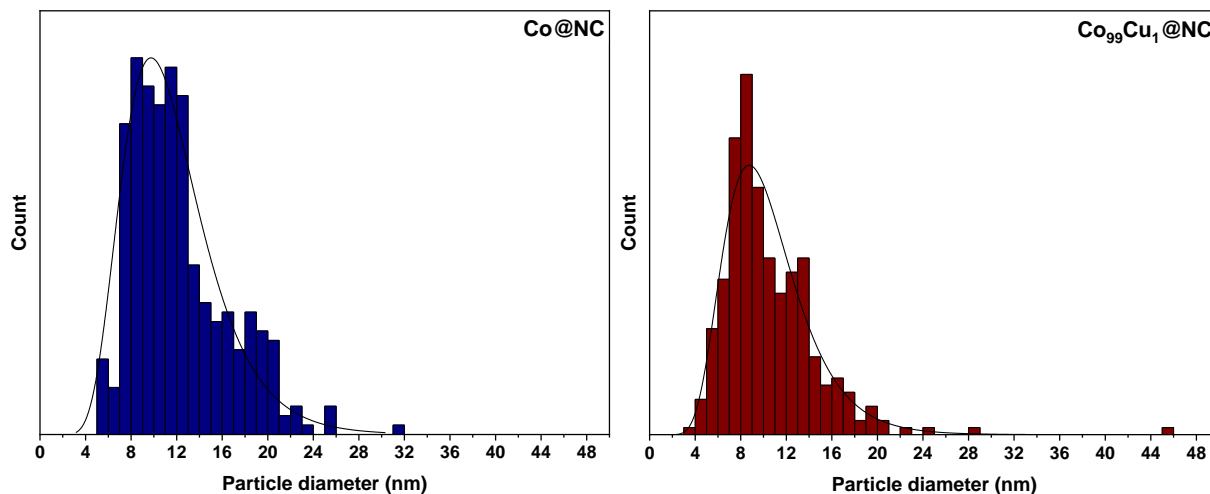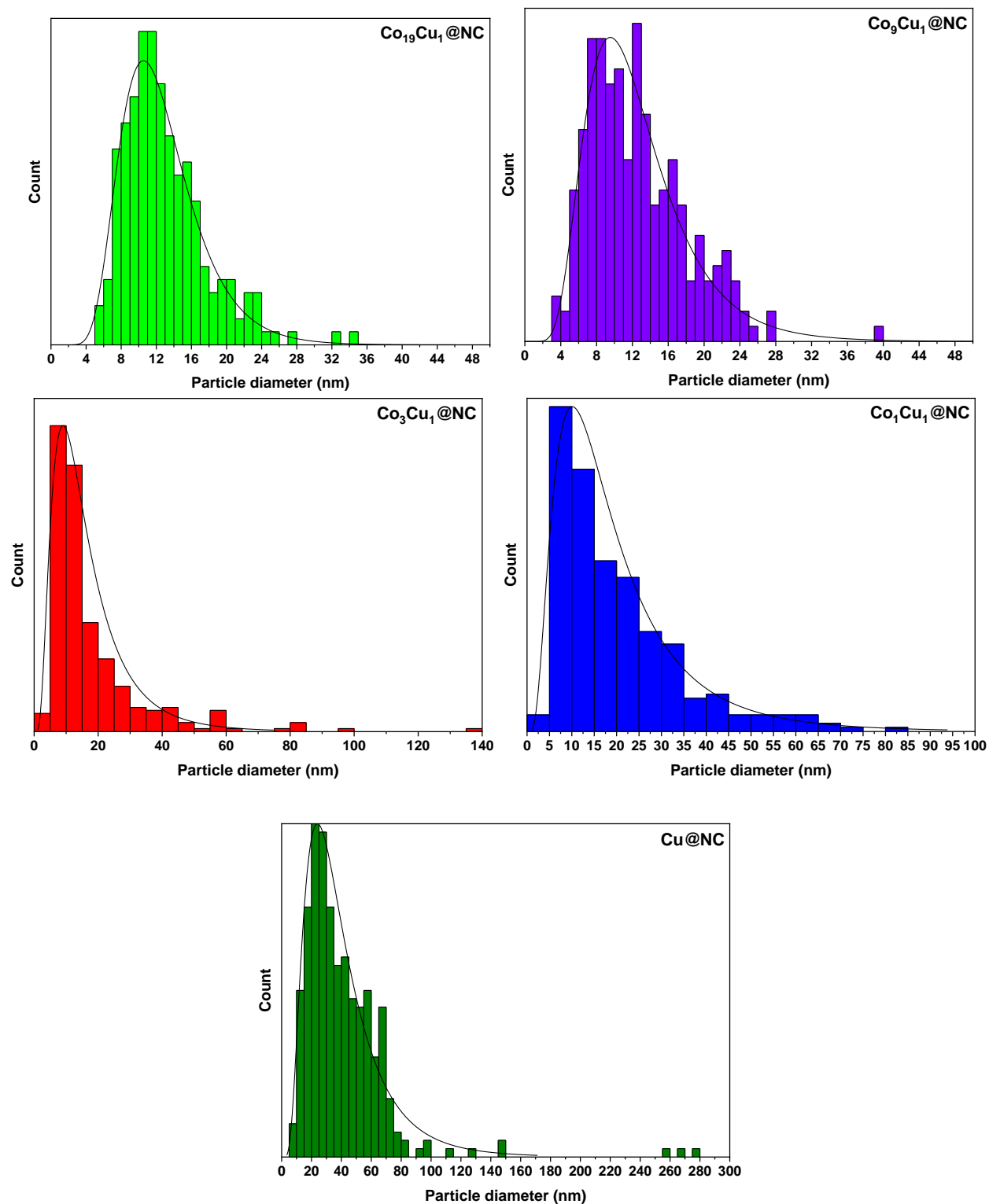
Figure C.4.1: Particle size distribution histograms for all the $Co_xCu_y@NC$ samples along with lines indicating a normal distribution.
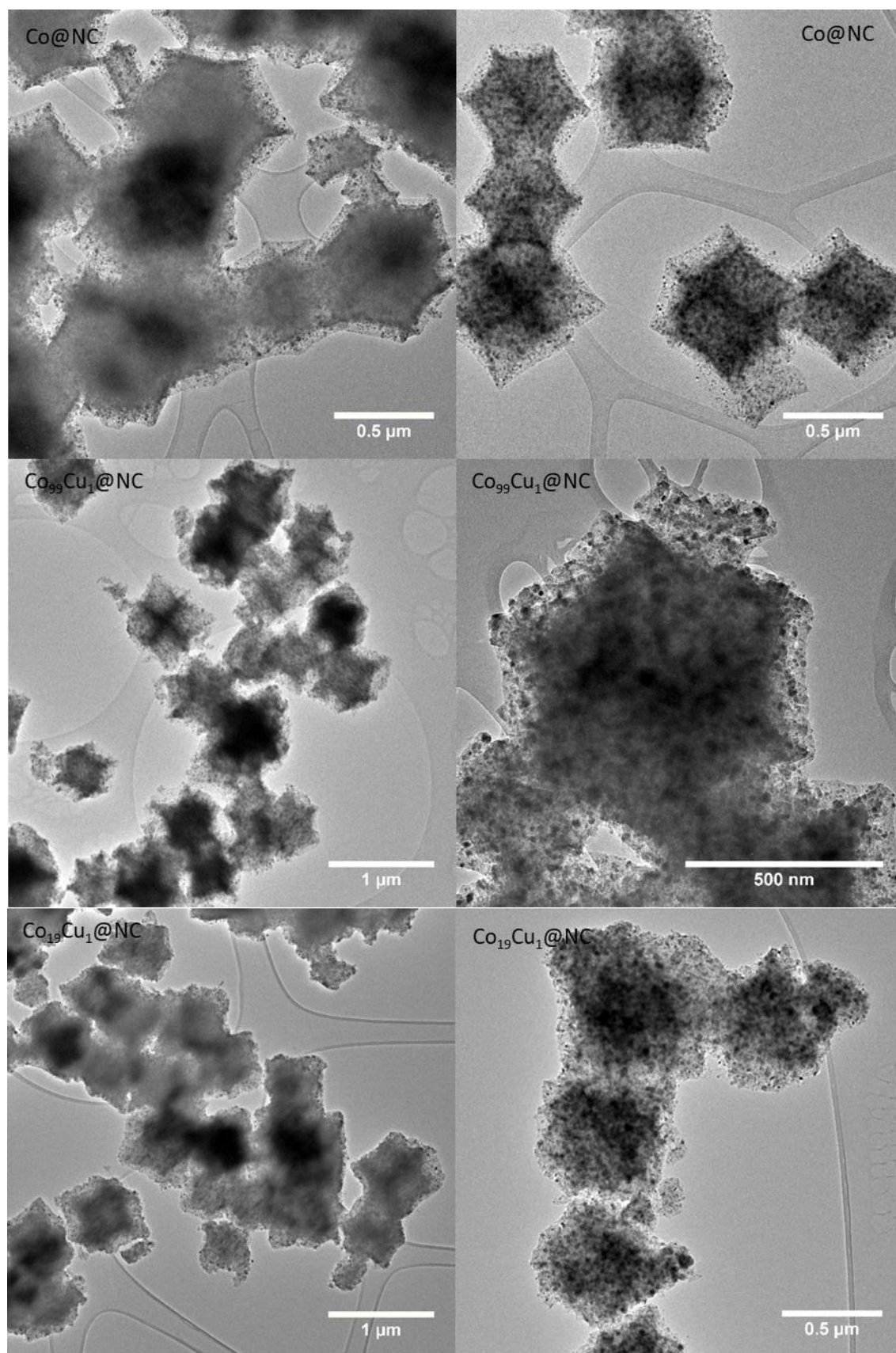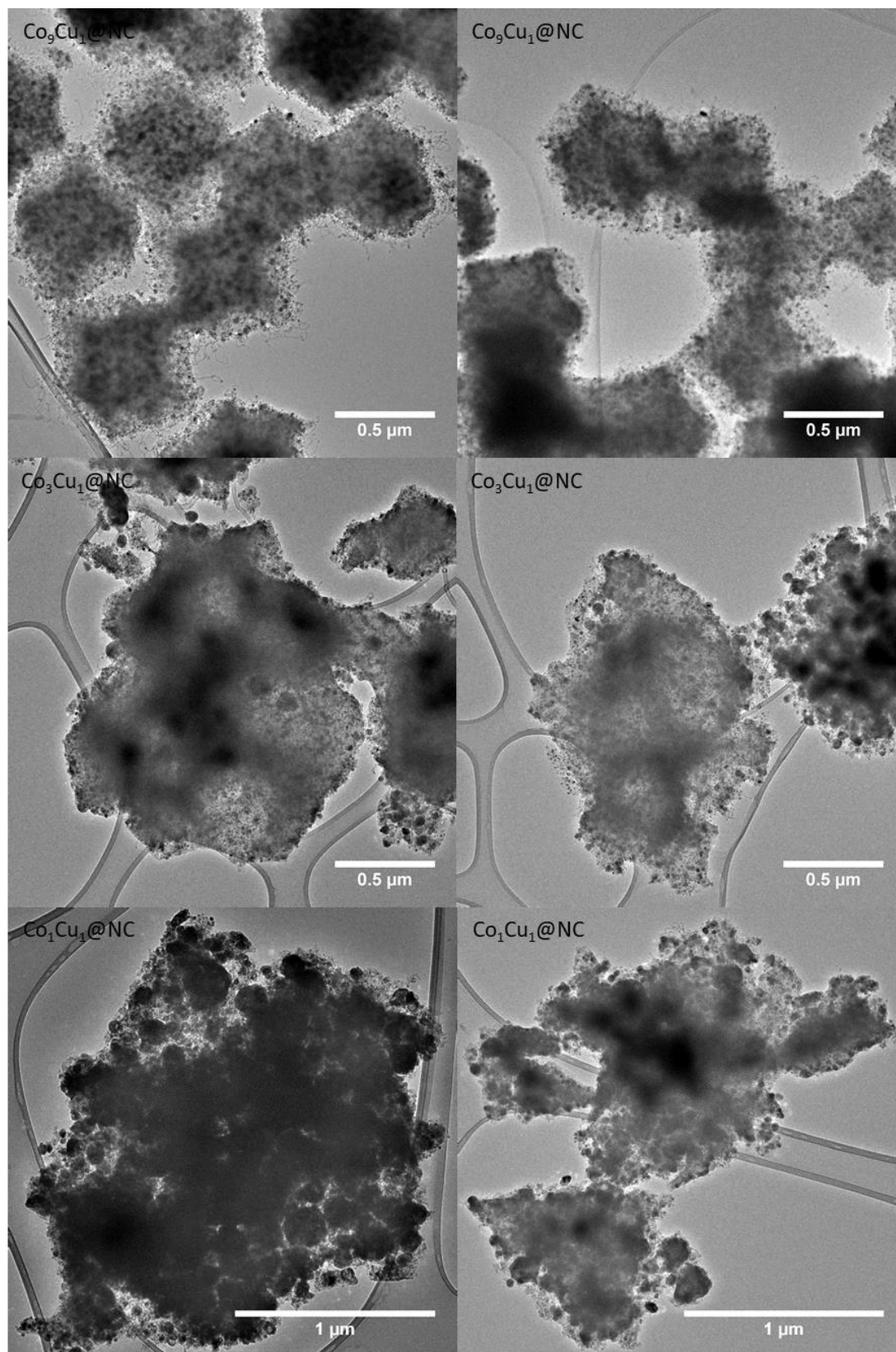
Figure C.4.2: Additional TEM images of all the Co$_x$Cu$_y$@NC samples. The images indicate that higher doping amounts of Cu destabilized the original dodecahedral structure.

C.5 TEM-EDS of Co_9Cu_1@NC
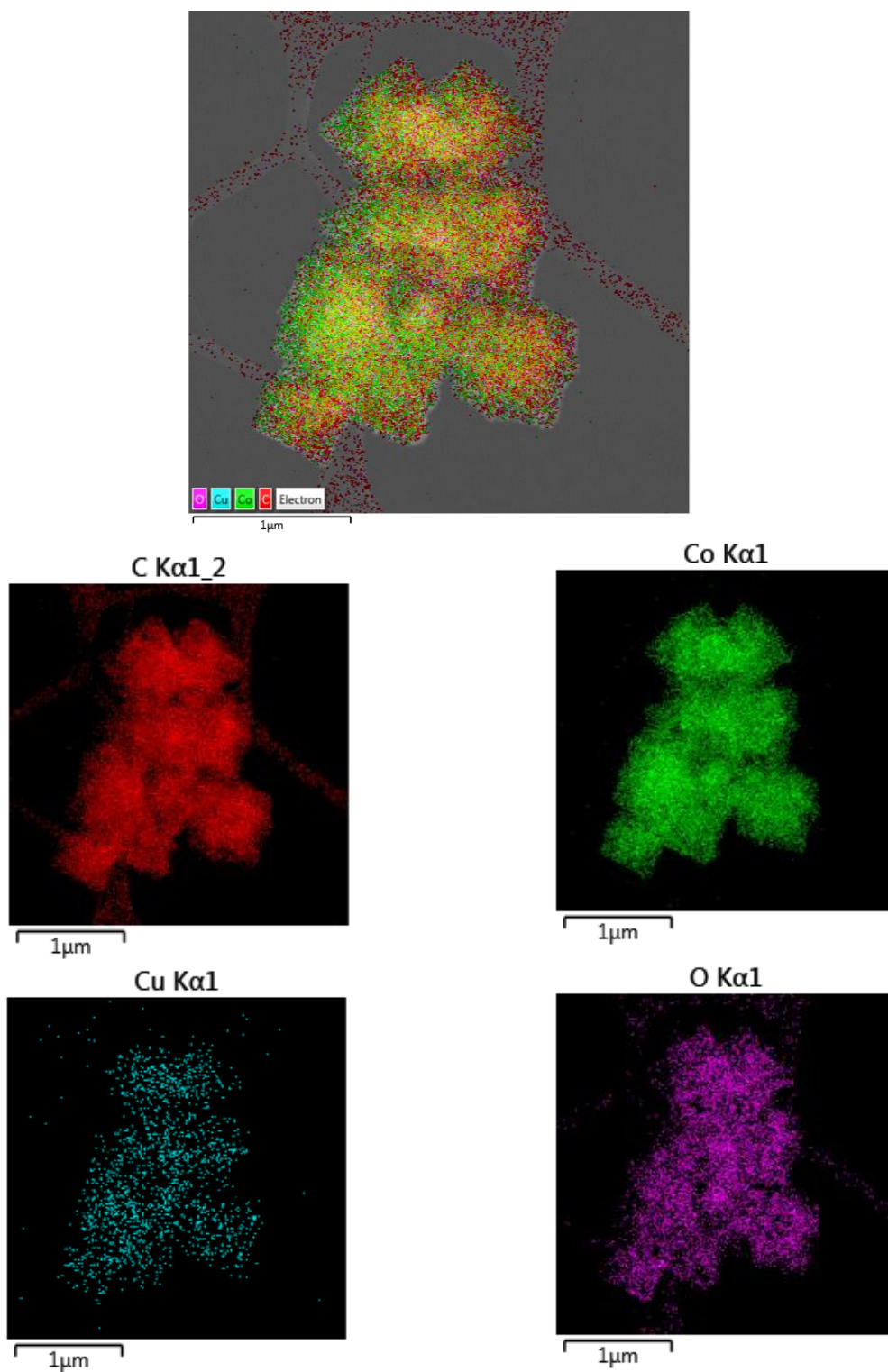
Figure C.5.1: TEM-EDS analysis conducted on Co_9Cu_1@NC showing an even distribution of both Co and Cu in the sample structure.

C.6 TEM-EDS of Co$_1$Cu$_1$@NC
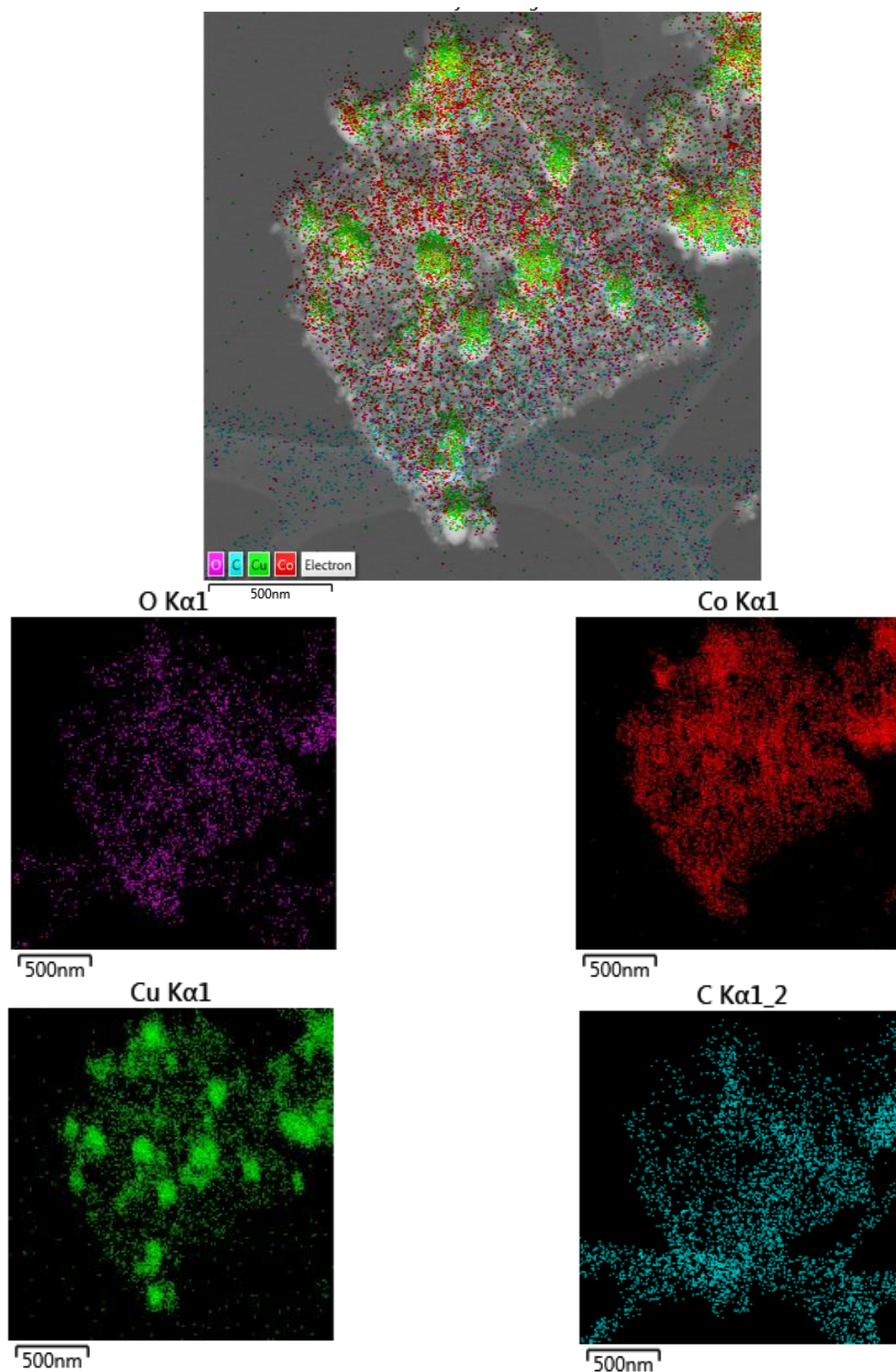
Figure C.6.1: TEM-EDS analysis conducted on Co$_1$Cu$_1$@NC showing agglomerates of Cu nanoparticles in the sample structure.

C.7 Deconvolution of nitrogen for Co_9Cu_1@NC sample
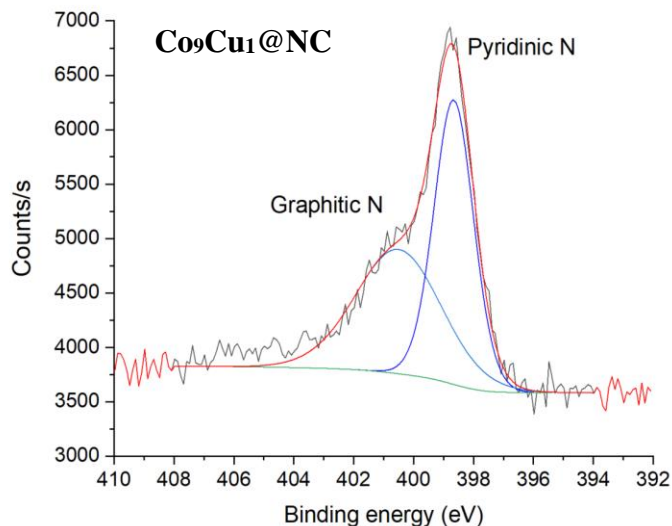
Figure C.7.1: Deconvolution of the N1S peak from XPS analysis of Co_9Cu_1@NC. Two peaks located at 398.5 eV and 400.8 eV are attributed to pyridinic nitrogen and graphitic nitrogen respectively.

C.8 Typical NMR spectrum from hydrosilylation of cyclohexanone
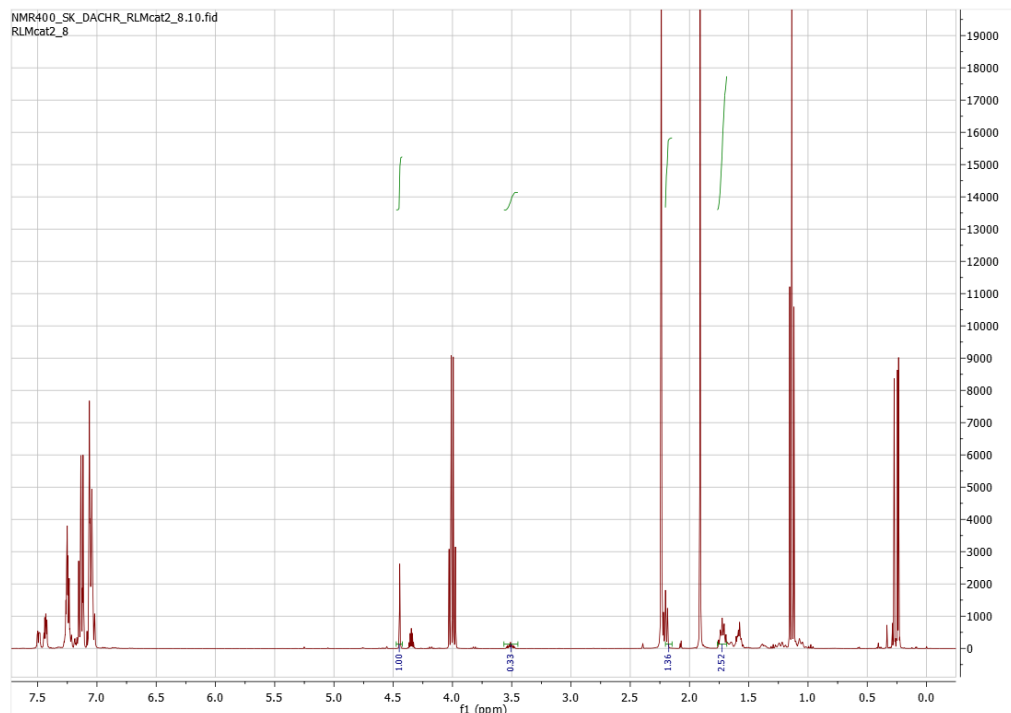
Figure C.8.1: Typical NMR spectrum used for estimating hydrosilylation product. Cyclohexanone has two usable peaks (roughly found at 1.61 ppm and 2.24 ppm), while the silylation product is quantified at 3.5 ppm. Dibenzyl ether was used as an internal standard (about 4.55 ppm).

C.9 Images of Co_9Cu_1@NC after hydrosilylation of cyclohexanone
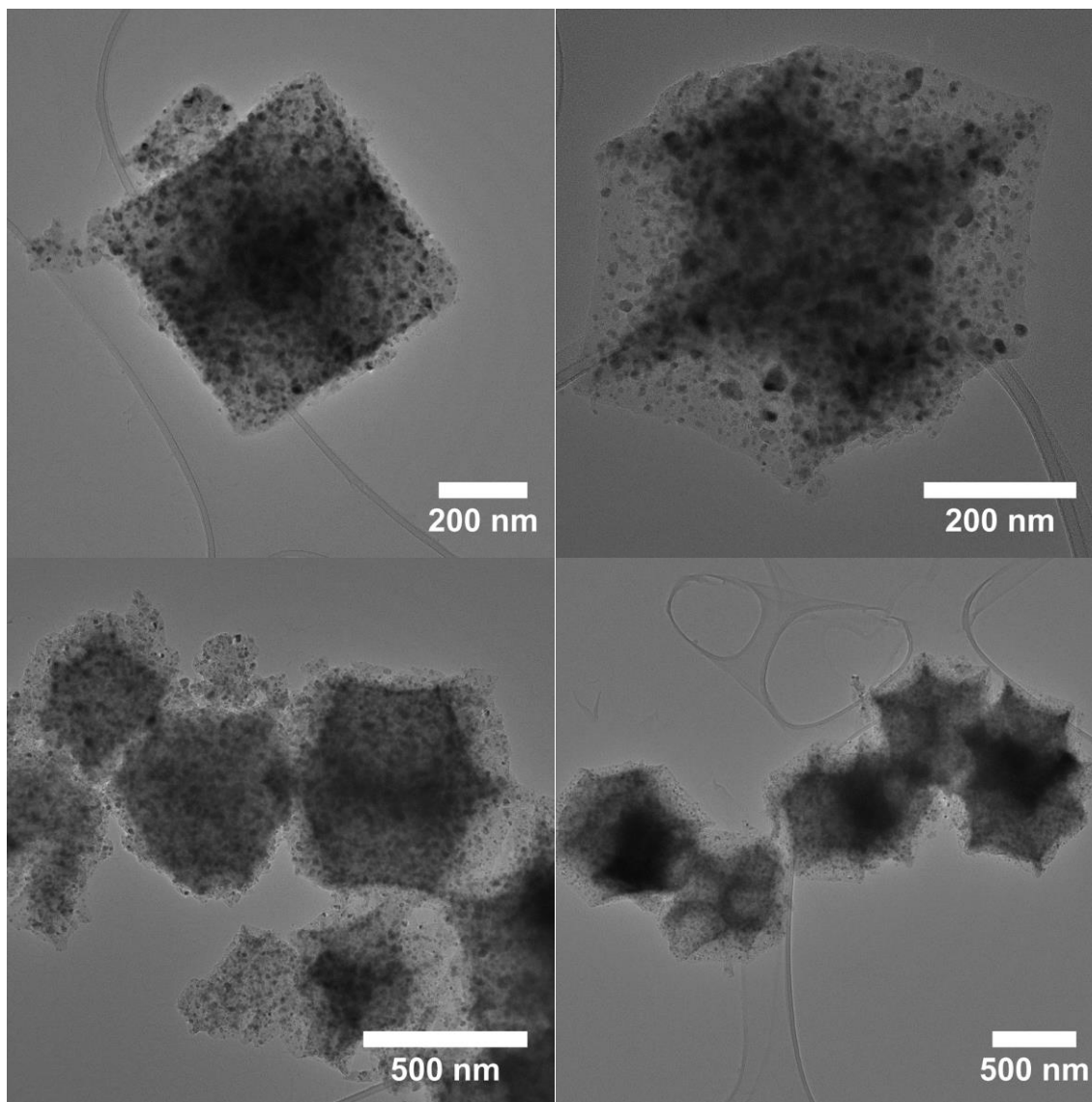
Figure C.9.1: Images of Co_9Cu_1@NC of a standard hydrosilylation reaction of cyclohexanone. The dodecahedral structure is maintained and no clear change in particle sizes or large agglomerates is observed.

Appendix D, Published articles

D.1 *Stabilization of Metal Nanoparticle Catalysts via Encapsulation in Mesoporous Zeolites by Steam-Assisted Recrystallization, ACS Applied Nano Materials.*

> Right and Permission: Reprinted (adapted) with permission from ACS Appl. Nano Mater. 2019, 2, 12, 8083–8091. Copyright 2019 American Chemical Society.

D.2 *The effect of active site distribution in bi-functional Pt-zeolite catalysts for ethane dehydroaromatization, Applied Catalysis A: General.*

> Right and Permission: Author retains right to include full articles in a thesis/dissertation (Elsevier)

D.3 *Study of CoCu Alloy Nanoparticles Supported on MOF-Derived Carbon for Hydrosilylation of Ketones, Catalysis Letters.*

> Right and Permission: Reprinted by permission from [Springer Nature Customer Service Centre GmbH]: [Springer Nature] Catalysis Letters [Study of CoCu Alloy Nanoparticles Supported on MOF-Derived Carbon for Hydrosilylation of Ketones, David B. Christensen et al., Copyright 2019]

D.4 *Selective formic acid dehydrogenation at low temperature over a RuO2/COF pre-catalyst synthesized on the gram scale, Catalysis Science and Technology.*

> Right and Permission: Adapted from [L. P. L. Gonçalves, D. B. Christensen, M. Meledina, L. M. Salonen, D. Y. Petrovykh, E. Carbó-Argibay, J. P. S. Sousa, O. S. G. P. Soares, M. F. R. Pereira, S. Kegnæs and Y. V. Kolen'ko, Catal. Sci. Technol., 2020, 10, 1991 DOI: 10.1039/D0CY00145G] with permission from The Royal Society of Chemistry.

D.5 *Heterogeneous production of formic acid by hydrogenation of CO2 using Ir-bpy embedded in polyphenylene POPs, submitted 2020.*

D.6 *Dehydrogenation of bioethanol using Cu nanoparticles supported on N-doped ordered mesoporous carbon, submitted 2020.*

D.7 *A Synergic Activity of Urea/Butyl Imidazolium Ionic Liquid Supported on UiO-66-NH2 Metal–Organic Framework for Synthesis of Oximes, Catalysis Letters.*

> Right and Permission: Reprinted by permission from [Springer Nature Customer Service Centre GmbH]: [Springer Nature] Catalysis Letters [A Synergic Activity of Urea/Butyl Imidazolium Ionic Liquid Supported on UiO-66-NH2 Metal–Organic Framework for Synthesis of Oximes, Saeed Askari et al., Copyright 2020]

Appendix D.1

Stabilization of Metal Nanoparticle Catalysts via Encapsulation in Mesoporous Zeolites by Steam-Assisted Recrystallization

Kristoffer H. Rasmussen, Farnoosh Goodarzi, David B. Christensen, Jerrik Mielby,* and Søren Kegnæs*

Technical University of Denmark, Kemitorvet bygning 207, 2800 Kgs Lyngby, Denmark

S *Supporting Information*

ABSTRACT: Zeolite encapsulated metal nanoparticle catalysts hold great promise for several green and sustainable processes, ranging from environmental remediation to renewable energy and biomass conversion. In particular, the microporous zeolite framework keeps the nanoparticles in a firm grip that can control selectivity and prevent sintering at high temperatures. While progress in the synthesis of mesoporous zeolites continues, the encapsulation of metal nanoparticles remains a challenge that often requires complex procedures and expensive additives. Here, we report a general method to encapsulate both base and noble metal nano-

Encapsulated metal nanoparticles

High selectivity

High conversion
High stability

particles inside the internal voids of a compartmentalized mesoporous zeolite prepared by carbon templating and steam-assisted recrystallization. This results in a remarkable shell-like morphology that facilitates the formation of small metal nanoparticles upon simple impregnation and reduction. When the materials are applied in catalysis, we for instance demonstrate that zeolite encapsulated Ni nanoparticles are highly active, selective, and stable catalysts for CO_2 methanation (49% conversion with 93% selectivity at 450 °C)—a reaction where catalysts often suffer from sintering due to the high reaction temperatures. While the introduction of Ni nanoparticles prior to the steam-assisted recrystallization results in the formation of inactive nickel phyllosilicates, noble metals such as Pt do not suffer from this limitation. Therefore, we also demonstrate the synthesis of an active catalyst prepared by the formation of Pt nanoparticles prior to the shell synthesis. We tested the zeolite encapsulated Pt nanoparticles for hydrogenation of linear and cyclic alkenes with increased chain length. The catalysts are active for hydrogenation of oct-1-ene (66% conversion) and cyclooctene (79% conversion) but inactive for the large cyclododecane (<1% conversion), which show that this type of catalyst is highly selective in size selective catalysis. All catalysts are characterized by XRD, TEM, XPS, and N_2 physisorption.

KEYWORDS: encapsulated nanoparticles, mesoporous zeolites, methanation, hydrogenation, steam-assisted recrystallization
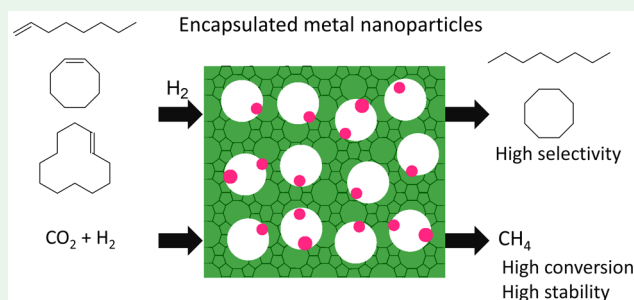
INTRODUCTION

Zeolites have many remarkable properties and find extensive use in heterogeneous catalysis.[1,2] They are well-known for their Lewis and Brønsted acidity[3,4] as well as their ability to encapsulate cations, complexes, and metals in their crystalline microporous framework.[5−7] In the particular case of metal nanoparticles, there may be several reasons to encapsulate them inside zeolites. For instance, the zeolite framework may control the nanoparticle size, which results in a high metal dispersion. The zeolite framework may also protect the nanoparticles against sintering caused by particle migration and coalescence[8−10] or impose a strict size and shape selectivity by excluding molecules (reactants, intermediates, or products) that are too large to diffuse in and out of the zeolite.[5,11−14] Furthermore, zeolite encapsulated metal nanoparticles may benefit from the unique metal−support interface that is in close proximity to the active sites of the zeolite framework.[15]

Although many of the properties of zeolites relates to their microporous framework, the micropores may also cause

limitations when it comes to large or bulky substrates. If the substrates and products are about the same size as the micropores, they will constantly be in contact with the pore wall, which will slow down the diffusion. For this reason, the rate of diffusion within a zeolite can be orders of magnitude lower than both molecular and Knudsen diffusion.[16] It is important to underline that the problem of diffusion is the same whether the reaction occurs on an acidic or metal active site inside the zeolite catalyst.

In general, there are two approaches to overcome diffusion limitations. The first approach is to increase the effective diffusivity by increasing the pore size of the zeolite. Over the past 20 years, much effort has therefore been devoted to the synthesis of large- and extra-large pore zeolites.[17] The second approach is to decrease the mean diffusion path length, either by decreasing the size of the zeolite crystals[18] or by introducing

Figure 1. Schematic outline of a general method to encapsulate metal nanoparticles in zeolites.

an additional system of mesopores.[19−22] The method to synthesize mesoporous zeolites typically includes dealumination,[23,24] desilication,[21,25−27] or templating using either hard[28−32] or soft templates.[33−36]

Despite great technological, environmental, and economic interest, general methods for the encapsulation of metal nanoparticles in zeolites are still not well established. In ge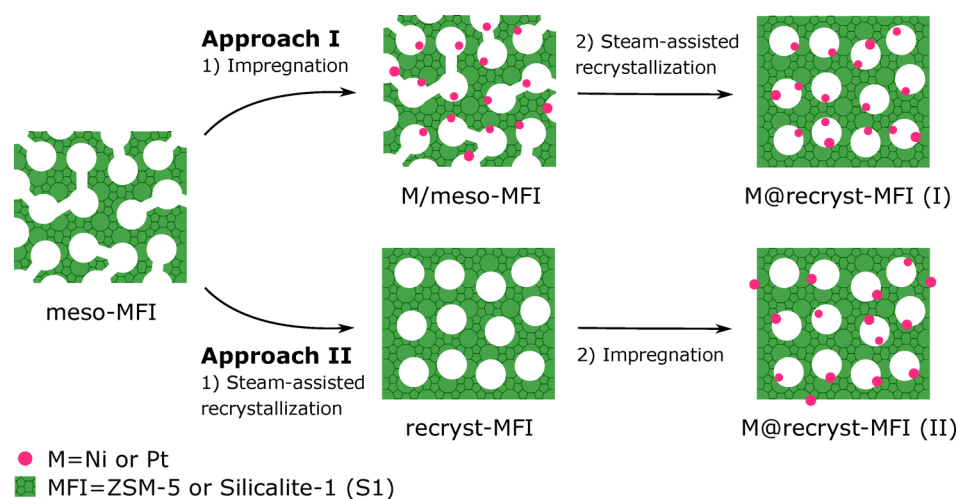neral, the poor diffusion of solvated metal precursors in small- and medium-pore zeolites (8- and 10-membered rings, respectively) preclude postsynthetic encapsulation by simple methods such as impregnation and ion exchange,[5,37] whereas the incorporation of metal nanoparticles during crystallization often relies on expensive additives or complicated reaction procedures.[10,38−40] Encapsulation of metal nanoparticles *in situ* in microporous zeolites have been accomplished by several research groups which provide the size selectivity from the zeolite network.[37−40] The encapsulation of metal nanoparticles in mesoporous zeolite catalysts is an area of much ongoing research.[13,41−45] For instance, Laprune et al.[42] recently encapsulated nickel phyllosilicates in multihollow silicalite-1 crystals. The encapsulated nickel phyllosilicates were then reduced to Ni nanoparticles and tested for methane steam reforming at 700 °C. Although the encapsulated Ni nanoparticles showed a high stability against sintering, the researchers also concluded that the catalytic activity of the encapsulated Ni nanoparticles suffered from poisoning by amorphous silica species remaining from the synthesis. Additionally, Li et al.[46] developed a way to encapsulate Pt in a macroporous nanoreactor with a microporous yolk−shell by first impregnating a conventional silicalite-1 zeolite, which then could undergo recrystallization to provide the encapsulated Pt in the macroporous interior of the zeolite providing sinter-stable nanoparticles. Generally, supporting metals in open mesopores enhance diffusion of molecules compared to conventional zeolites; however, it results in a lower size/shape selectivity for the reaction when compared to microporous zeolites.[47] Because of the size of the channels, introduction of the solvated metal precursors in mesopores by simple impregnation is easier compared to medium and small pore zeolites. Gu et al.[48] exploited the mesopores in a ZSM-5 zeolite to encapsulate Pt nanoparticles and then convert it into a microporous zeolite to provide size selective catalysis.

In our work, we present a general method to encapsulate metal nanoparticles inside a highly mesoporous zeolite interior with a microporous zeolite shell providing both size selectivity and sinter-stable metal particles. The mesoporous zeolite was prepared by carbon templating, which allowed for easy impregnation with metal precursors. Formation of a microporous shell with preservation of the highly mesoporous interior was accomplished by steam-assisted recrystallization, resulting in the remarkable compartmentalized zeolite. The synthesis allowed for supporting metal nanoparticles in a highly mesoporous interior while still benefiting from the micropores in the shell. Compared to conventional zeolite synthesis, steam-assisted crystallization also provides an attractive method to increase the yield, produce less waste, and avoid phase separation.[49−51] We demonstrate the successful encapsulation of both base and noble nanoparticles (Ni and Pt, respectively) and show the effect of supporting the metal both before and after the steam-assisted recrystallization. We tested the Ni containing zeolites in CO_2 methanation, which is a promising power-to-gas technology but suffers from sintering of metal particles at the high operating temperatures.[15] Here, we showed that encapsulation in the zeolite with the shell results in the most active with sinter-stable Ni particles.

The shell encapsulated Pt nanoparticles were tested for the size-selective hydrogenation of linear and cyclic alkenes and showed that the catalyst is highly selective in size selective catalysis. Figure 1 shows a schematic outline of the method.

■ EXPERIMENTAL SECTION

Synthesis of Mesoporous ZSM-5 and Silicalite-1 (S-1). Following the procedure by Jacobsen et al.,[29] a predried carbon template (Carbon Black Pearls, BP2000, 2 g) was impregnated with an aqueous solution of tetrapropylammonium hydroxide (TPAOH, 1 M, 7.2 mL) in a Teflon beaker. For ZSM-5, $NaAlO_2$ (0.016 g) was dissolved in the TPAOH solution prior to impregnation. The impregnated carbon template was left to dry at room temperature overnight. The template was then impregnated with tetraethyl orthosilicate (TEOS) (4.4 mL) and left to dry at room temperature overnight once more. The beaker with the carbon−silica composite material was then placed inside a Teflon-lined stainless steel autoclave filled with 15 mL of distilled water for the steam-assisted synthesis. The autoclave was heated to 180 °C and kept for 72 h. After cooling to room temperature, the solid material was collected by filtration and washed with water until neutral pH. The samples were dried at 80 °C

Table 1. Outline of the Prepared Zeolites, Synthesis Conditions, and Results from N$_2$ Physisorption Analysis

entry	sample	TPAOH[a]	TEOS[b]	surface area[c] (m^2/g)	pore vol[d] (cm^3/g)	micropore vol[e] (cm^3/g)
1	meso-S1			453	0.35	0.14
2	recryst-S1 (1:0)	1		449	0.32	0.13
3	recryst-S1 (1:1)	1	1	422	0.30	0.13
4	recryst-S1 (2:0)	2		451	0.33	0.12
5	recryst-S1 (2:2)	2	2	530	0.30	0.16
6	meso-ZSM-5			432	0.30	0.13
7	recryst-ZSM-5	1	1	440	0.31	0.09

^{a}1 = 3.6 mL and 2 = 7.2 mL of 1 M TPAOH to 1 g of meso-S1/meso-ZSM-5. ^{b}1= 2.3 mL and 2 = 4.6 mL of TEOS to 1 g of meso-S1/meso-ZSM-5. ^{c}Calculated by the BET method. ^{d}Calculated at relative pressure p/p_0 = 0.95. ^{e}Calculated by the t-plot method.
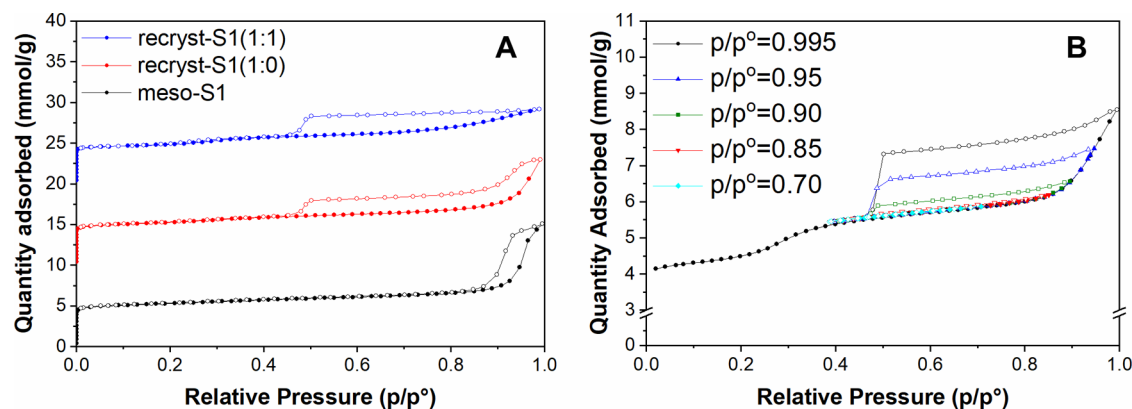
Figure 2. (A) N$_2$ physisorption isotherms of meso-S1 (black), recryst-S1(1:0) (red), and recryst-S1(1:1) (blue) and (B) hysteresis scan of recryst-S1(1:1).

for 12 h and finally calcined at 550 °C for 20 h to obtain a fine white solid product (meso-S1 or meso-ZSM-5).

Steam-Assisted Recrystallization (Synthesis of Recryst-ZSM-5 and Recryst-S1). The meso-ZSM-5 or meso-S1 (0.5 g) was ground in a mortar, impregnated with varying amounts of TPAOH and dried at room temperature overnight. The dry zeolites were then impregnated with varying amounts of TEOS and dried at room temperature overnight once more. The exact amounts and ratio of zeolite to TPAOH and TEOS are listed in Table 1. The dried zeolites were then placed in a Teflon beaker inside a Teflon-lined stainless steel autoclave containing 15 mL of water for the steam-assisted recrystallization. The autoclave was heated at 180 °C for 72 h. The product was collected by filtration, washed with water until neutral pH, dried at 80 °C for 12 h, and finally calcined at 550 °C for 20 h to obtain a fine white product.

Encapsulation of Metals (Approach I). As-synthesized meso-S1 or meso-ZSM-5 was dried in a vacuum oven at 60 °C overnight and then impregnated to incipient wetness with an aqueous solution of either Ni(NO$_3$)$_2$ (for a 5 wt % Ni zeolite) or H$_2$PtCl$_6$ solution (for a 1 wt % Pt zeolite). The impregnated samples were then dried at 80 °C for 12 h. The nickel-containing meso-ZSM-5 was calcined at 550 °C for 2 h to obtain NiO$_x$/meso-ZSM-5, while the platinum-containing meso-S1 was first calcined at 350 °C for 2 h with a 0.5 °C/min ramp in a muffle oven to achieve PtO$_x$/meso-S1. The metal oxide-containing sample was then subjected to steam-assisted recrystallization to grow a shell around the NiO$_x$/meso-ZSM-5 or PtO$_x$/meso-S1. The shell was grown according to the procedure described above using 0.5 g of zeolite, 1.8 mL of TPAOH, and 1.1 mL of TEOS. The calcination was limited to 4 h calcination at 550 °C. The calcined Ni-containing zeolite was reduced under 10% H$_2$ in N$_2$ at 750 °C for 2 h with a 5 °C/min ramp to obtain Ni@recryst-ZSM-5(I). The calcined Pt zeolite was reduced under hydrogen at 600 °C for 3 h with a 5 °C/min ramp to obtain Pt@recryst-S1(I). For encapsulation of Ni and Pt in meso-ZSM-5 and meso-S1, respectively, the Ni was reduced under 10% H$_2$ in N$_2$ at 500 °C for 2 h with 5 °C/min ramp after impregnation and drying at 80 °C to obtain Ni/meso-ZSM-5 while Pt

was reduced under hydrogen at 600 °C for 3 h with 5 °C/min ramp after calcination at 350 °C to obtain Pt/meso-S1.

Encapsulation of Metals (Approach II). The recryst-S1 and recryst-ZSM-5 zeolite were impregnated with H$_2$PtCl$_6$ and Ni(NO$_3$)$_2$ solution, respectively, to incipient wetness after drying in a vacuum oven at 60 °C overnight. Afterward, the samples were dried at 80 °C for 12 h. The Ni sample was reduced under 10% H$_2$ in N$_2$ at 500 °C for 2 h with a 5 °C/min ramp to obtain Ni@recryst-ZSM-5(II). The platinum-containing zeolite was first calcined at 350 °C for 2 h with a 0.5 °C/min ramp in a muffle oven (PtO$_x$@recryst-S1(II)) and then reduced under hydrogen at 600 °C for 3 h with 5 °C/min ramp to obtain Pt@recryst-S1(II).

■ **RESULTS AND DISCUSSION**

Figure 2, Table 1, and Figures S1–S5 compile the results from N$_2$ physisorption and X-ray powder diffractions (XRPD) analysis of all the prepared support materials. In particular, Table 1 shows the effect on the surface area and porosity by changing the ratio of TPAOH and TEOS during the steam-assisted recrystallization of the carbon templated mesoporous zeolites. In general, the addition of TEOS slightly decreased the total pore volume, while the surface area and micropore volume remained in the same range under all conditions. A significant increase in surface area and micropore volume was observed by the addition of large amounts of both TPAOH and TEOS in entry 5.

More detailed information about the morphology of the recrystallized zeolites is evident from the physisorption isotherms and the pore size distributions shown for meso-S1, recryst-S1(1:0), and recryst-S1(1:1) in Figure 2A and Figure S2, respectively.

As expected, the physisorption isotherms of all zeolites in Figure 2A show significant adsorption of N$_2$ at low relative pressures ($p/p°$ < 0.01) which is typical for microporous

zeolites. Furthermore, all three isotherms show a significant hysteresis loop at higher relative pressures. For meso-S1 (black), the hysteresis loop closes at around $p/p° = 0.85$, which indicates the presence of large and open mesopores.[52,53] According to the IUPAC classification,[54] the physisorption isotherm of meso-S1 is a type IV with an H1 hysteresis loop. Figure S2 shows the corresponding pore size distribution as calculated by BJH analysis of the desorption branch and shows that the carbon templating results in a broad distribution of mesopores around between 10 and 34 nm in diameter. This result is in good agreement with previous reports.[29,55] In contrast, the hysteresis loops of recryst-S1(1:0) and recryst-S1(1:1) (red and blue, respectively) modified by steam-assisted recrystallization are almost parallel until the forced closure point at around $p/p° = 0.45$. According to the IUPAC classification, these data correspond to type IV isotherms with type H2a hysteresis loops. This behavior indicates that the recrystallized zeolites have an ink-bottle-type porosity with a constricted system of internal voids and mesopores that are only accessible via the inherent zeolite micropores.[53,56] It is important to mention that the peaks around 3.8 nm in the pore size distribution are not related to actual mesopores but simply caused by cavitation and the so-called tensile strength effect at the forced closure point.[57,58] As expected, the same peaks are not evident from the corresponding pore size distribution as calculated from the adsorption branch (data not shown). While the change from type H1 to type H2a hysteresis loops indicates the successful synthesis of a microporous zeolite shell, the physisorption analysis also reveals that both TPAOH and TEOS are required to transform all open mesopores into fully enclosed compartments. While recryst-S1(1:0) has a total pore volume of 0.32 g/cm^3 and BJH analysis indicates some remaining open porosity in the mesoporous range, recryst-S1(1:1) has a total pore volume of 0.30 g/cm^3 and a relatively flat desorption branch until the forced closure point at $p/p° = 0.45$. Figure 2B shows the isotherms from a hysteresis scanning experiment performed on recryst-S1(1:1) to investigate the desorption branches at different partial pressures and degrees of filling in more detail. As expected, the flat shape of the desorption scans confirm that all the mesopores empty via cavitation controlled evaporation rather than pore blocking.[52,59,60]

Figure S1 shows the XRPD analysis of meso-S1, recryst-S1(1:0), and recryst-S1(1:1), respectively. The diffraction patterns of all other zeolite materials are shown in Figure S3. In general, the diffraction patterns show no significant differences between the parent and modified zeolites. This confirms that both carbon templating and steam-assisted recrystallization result in zeolites with the expected MFI structure and good crystallinity.[61] Furthermore, the diffraction patterns show no significant differences between the recrystallized samples prepared with different ratios of zeolite, TPAOH, and TEOS, which is in good agreement with the results from N$_2$ physisorption analysis reported in Table 1.

Figure 3 shows an SEM and TEM image of meso-S1 and recryst-S1(1:1), respectively. The SEM images show that the crystal size of both samples is around 1−2 μm, which confirms that the added TEOS crystallizes on the surface of the carbon templated zeolites rather than in new separate crystals. We therefore speculate that the carbon templated zeolite may function as effective seed crystals in this step. Furthermore, the SEM images show a significant difference in the surface features of the two samples. While the surface of meso-S1
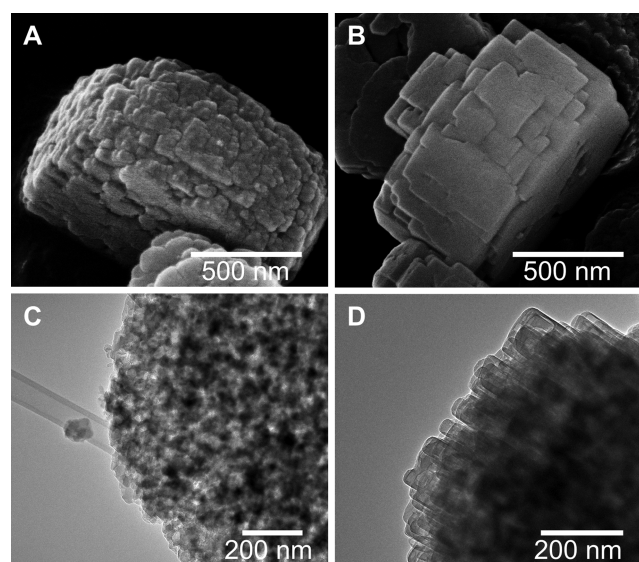
Figure 3. SEM and TEM images of meso-S1 (A, C) and recryst-S1(1:1) (B, D).

appears fluffy, which is typical for mesoporous zeolites and in good agreement with previous reports,[13,19,62,63] the surface of recryst-S1(1:1) appears more smooth with well-defined terraces. The same features are also evident from the TEM images, which also reveal more insight into the nature of the enclosed mesopores. While Figure 3C clearly shows the open porosity of the carbon-templated zeolite, Figure 3D exhibits how the steam-assisted crystallization has restructured the surface of the zeolite and transformed the open porosity into a large number of small and separate compartments. The thickness of the zeolite shell is typically in the range 10−30 nm.

On the basis of our previous experience with encapsulated metal nanoparticles, we speculated whether the steam-assisted recrystallization could offer a general method to encapsulate both base and noble metal nanoparticles in mesoporous zeolites. We therefore prepared a number of Ni and Pt catalysts by simple impregnation of the metal precursors on the mesoporous zeolites both before and after the steam-assisted recrystallization.

Figure 4 shows the TEM images of the Ni catalysts together with their corresponding particle size histogram fitted with a log-normal distribution. For comparison, Ni/meso-ZSM-5 was prepared by impregnation of carbon-templated meso-ZSM-5, Ni@recryst-ZSM-5(I) was prepared by impregnation of carbon-templated meso-ZSM-5 followed by steam-assisted recrystallization, and Ni@recryst-ZSM-5(II) was prepared by steam-assisted recrystallization of meso-ZSM-5 followed by impregnation. The nickel-containing catalysts were reduced under the as-mentioned conditions (see the Experimental Section).

The first TEM image in Figure 4 shows that a number of large Ni nanoparticles (up to 46 nm) were present on the external surface of Ni/meso-ZSM-5, which resulted in a relatively broad particle size distribution. In contrast, fewer Ni nanoparticles were present on the external surface area of Ni@recryst-ZSM-5(I) and Ni@recryst-ZSM-5(II), which resulted in smaller nanoparticles and more narrow size distributions. Furthermore, the TEM images also show that the enclosed porosity appeared to encapsulate a significant number of the
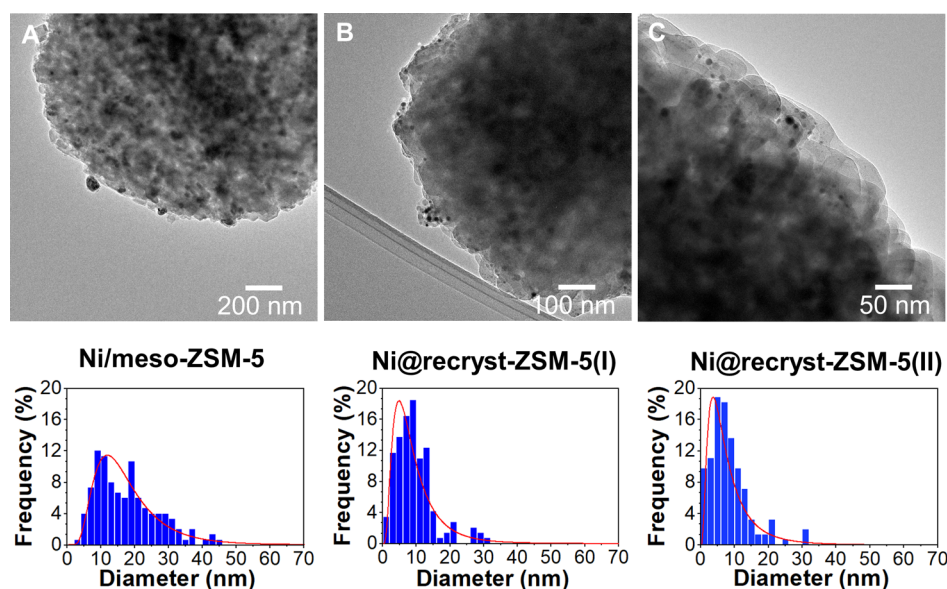
Figure 4. TEM images of (A) Ni/meso-ZSM-5, (B) Ni@recryst-ZSM-5(I), and (C) Ni@recryst-ZSM-5(II) together with their particle size distributions based on the measurement of >100 nanoparticles.

Summary of the catalytic results at 450 °C.

Catalyst	Conv.	Selec.	STY[a]
Ni/meso-ZSM-5	44%	84%	213
Ni@recryst-ZSM-5(I)	36%	66%	134
Ni@recryst-ZSM-5(II)	49%	93%	283

[a] Site time yield in mol CH_4/mol Ni h^{-1}
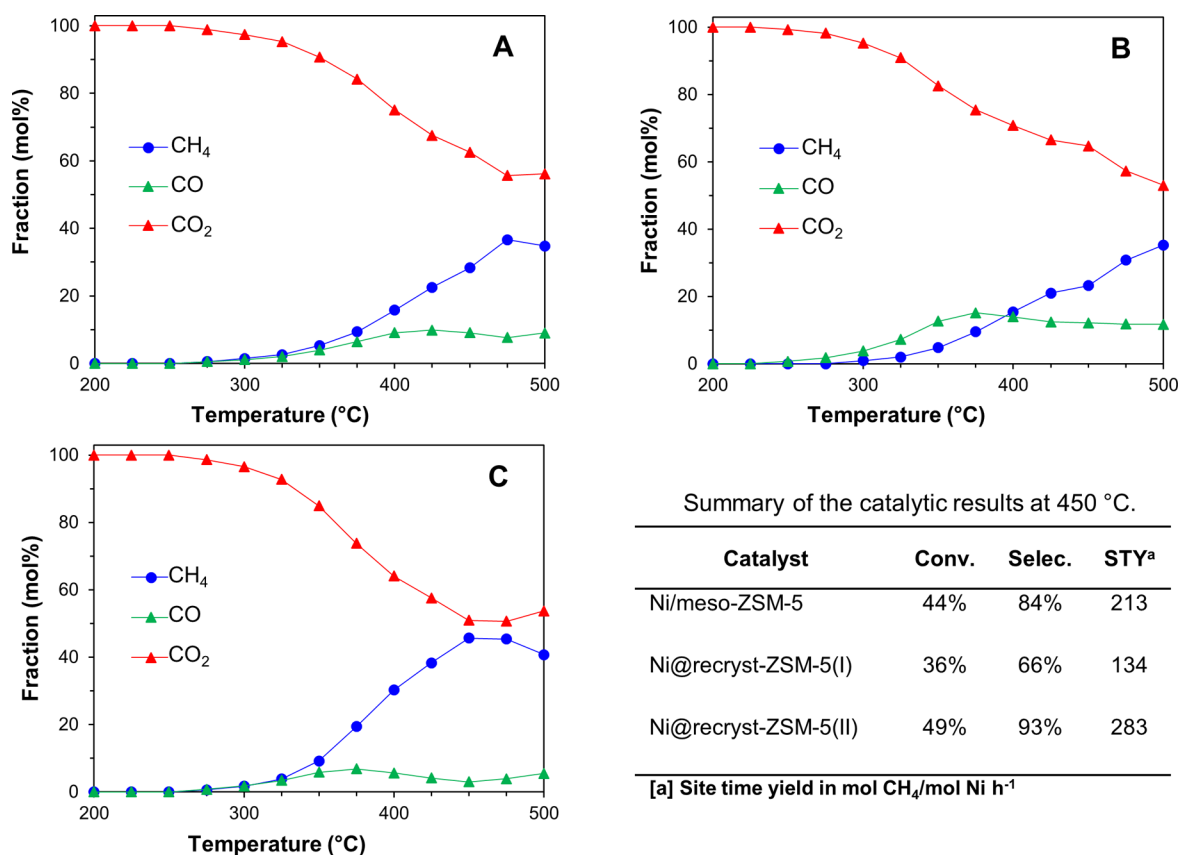
Figure 5. Product distribution as a function of the temperature for (A) Ni/meso-ZSM-5, (B) Ni@recryst-ZSM-5(I), and (C) Ni@recryst-ZSM-5(II) together with a summary of the catalytic activity at 450 °C.

Ni nanoparticles within the zeolite shell. The XRPD patterns of the three Ni catalysts are shown in Figure S6. Besides the characteristic diffraction pattern of ZSM-5, the XRD analysis also reveal some small peaks from Ni(111). Although the signals are too weak to confirm the average particle size by line broadening analysis, the results indicate that the Ni nano-

particles decrease in the order of Ni/meso-ZSM-5 > Ni@recryst-ZSM-5(II) > Ni@recryst-ZSM-5(I).

To compare the catalytic activity, we tested the Ni catalysts for high-temperature CO_2 methanation, which is an important reaction that is well-known to suffer from sintering.[64−66] Figure 5 A−C shows the molar fraction of CH_4, CO, and CO_2 as a function of the reaction temperature. A comparison of the
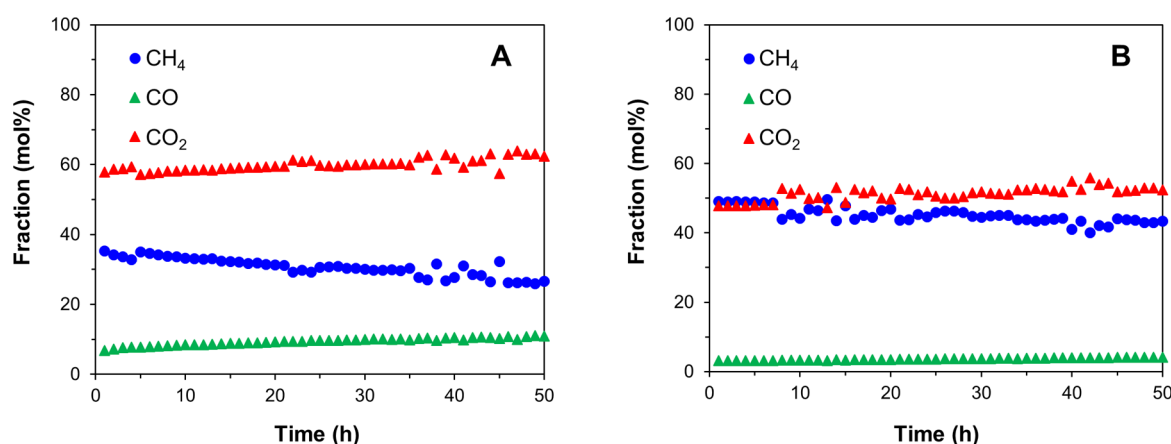
Figure 6. Catalytic stability for (A) Ni/meso-ZSM-5 and (B) Ni@recryst-ZSM-5(II) over 50 h at 450 °C.

product distribution at 450 °C shows that Ni@recryst-ZSM-5(II) results in 49% conversion and 93% selectivity, which is significantly higher than the other catalysts. Considering the similar particle size distributions of Ni@recryst-ZSM-5(II) and Ni@recryst-ZSM-5(I), we speculate that the alkaline and hydrothermal conditions under the steam-assisted recrystallization could result in the formation of nickel phyllosilicates (see Figure S10). It has previously been shown that these phyllosilicates are difficult to reduce into Ni nanoparticles and may decrease the catalytic activity.[6,42] Approach II (postimpregnation) does not suffer from the formation of these inactive species and is therefore the most effective method to encapsulate base metals such as Ni nanoparticles.

Figure 6 shows the catalytic activity of Ni/meso-ZSM-5 compared to Ni@recryst-ZSM-5(II) over 50 h at 450 °C. The results clearly show that Ni@recryst-ZSM-5(II) results not only in higher conversion and selectivity but also in higher stability over time.

Figure S12 shows the results from the TEM analysis of the spent catalysts after 50 h at 450 °C. The TEM image of Ni/meso-ZSM-5 shows the formation of large Ni nanoparticles on the surface of the catalysts, which indicates that severe sintering may explain the poor stability. In contrast, the TEM image of Ni@recryst-ZSM-5 shows that the zeolite-encapsulated nanoparticles appear to remain within the confined space of the small zeolite compartments. This indicates that the zeolite shell effectively prevents nanoparticle migration and coalescence on the surface of the catalyst, which results in a higher metal dispersion, a higher catalytic activity, and a higher thermal stability.

To investigate whether noble metal nanoparticles could be encapsulated by impregnation of the carbon-templated zeolite prior to the steam-assisted recrystallization, we then prepared Pt/meso-S1 and Pt@recryst-S1(I). As expected, the XRPD analysis shows the characteristic diffraction pattern of the MFI zeolite as well as an additional peak from Pt(111) at 39.6°[67] (see Figure S15). Figure S17 shows the XPS analysis for the Pt 4f orbitals in Pt/meso-S1 and Pt@recryst-S1(I). The difference in signal intensity indicates that significantly more Pt is present on the surface of Pt/meso-S1 than on the surface of Pt@recryst-S1(I). For comparison, ICP-OES analysis showed that the metal loading of Pt/meso-S1 and Pt@recryst-S1(I) was 0.8% and 0.7%, respectively. Because the change in metal loading can only account for 12.5% of the decrease in signal

intensity, we assign the rest of the decrease to a successful encapsulation of the Pt nanoparticles.

Figure 7 shows two representative STEM images of the Pt catalysts (see Figures S18 and S19 for more images). With the
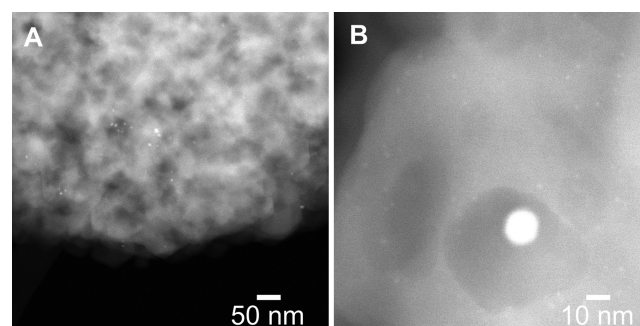
Figure 7. STEM images of Pt/meso-S1 (A) and Pt@recryst-S1(I) (B).

exception of a few larger nanoparticles on the surface of the catalyst, the STEM analysis shows that a large number of small nanoparticles are still present on Pt@recryst-S1(I) after the steam-assisted recrystallization.

To investigate the degree of encapsulation and the potential use for selective catalysis, we tested the two Pt catalysts for the shape-selective hydrogenation of linear and cyclic alkenes. The results in Table 2 clearly show that encapsulation of the Pt nanoparticles had a significant effect on the catalytic activity.

Table 2. Catalytic Results from the Hydrogenation of Alkenes[a]

catalyst	substrate	product	time (h)	conv[b] (%)
Pt/meso-S1	oct-1-ene	octane	1	99
	cis-cyclooctene	cyclooctane	1	99
	cyclododecene	cyclododecane	24	53
Pt@recryst-S1(I)	oct-1-ene	octane	1	6
	oct-1-ene	octane	24	66
	cis-cyclooctene	cyclooctane	1	8
	cis-cyclooctene	cyclooctane	24	79
	cyclododecene	cyclododecane	24	1

[a]Reaction conditions: alkene (1 mmol), catalyst (50 mg), decane (internal standard, 0.2 mmol), ethyl acetate (5 mL), 1 bar of H_2 room temperature. [b]Conversion determined by GC-FID.

ACS Applied Nano Materials   Article

As expected, the effect is most pronounced for cyclododecene, which is too large to enter the microporous zeolite. These results therefore confirm that the recrystallized zeolite encapsulates a large fraction of the Pt nanoparticles. For the two smaller molecules, oct-1-ene and cyclooctene, the decreased activity may be explained by a slower diffusion.[5,48] To investigate the effect of the preparation procedure, we also tried to encapsulate the Pt nanoparticle after the steam-assisted recrystallization (Pt@recryst-S1(II)), see the Supporting Information. This, however, resulted in a significantly lower size selectivity (see Table S2), which indicates an incomplete encapsulation of the Pt nanoparticles (Figure S20). For this reason, it appears that Approach I (preimpregnation) is the more effective method to encapsulate noble metals such as Pt nanoparticles.

CONCLUSION

A general steam-assisted recrystallization method was developed to encapsulate both base and noble metal nanoparticles inside the internal voids of compartmentalized mesoporous ZSM-5 or silicalite-1. For full coverage of mesoporous zeolite with a microporous layer, both TEOS and TPAOH were required. It was shown that encapsulated Ni nanoparticles, where Ni was introduced after steam-assisted recrystallizations (approach II), was the most active and stable catalyst for CO_2 methanation with a site time yield of 283 mol CH_4/mol Ni h^{-1}, whereas the zeolite encapsulated Ni nanoparticles prepared according to approach I suffer from the possible formation of inactive nickel phyllosilicates. Approach II offers a suitable way to obtain sinter-stable encapsulated base metals which can be used for high-temperature reactions.

Furthermore, it was demonstrated that the Pt catalyst prepared by introducing the Pt nanoparticles prior to the steam-assisted recrystallization (approach I) was more size selective in linear and cyclic alkenes hydrogenation and proves that the method is highly applicable for obtaining size selective catalysts. Therefore, we conclude that approach I is more effective for encapsulation of noble metals while approach II is more effective for encapsulation of base metals. The general method offers a new way for encapsulation of metals in hierarchical zeolite catalysts.

ASSOCIATED CONTENT

ⓢ Supporting Information

The Supporting Information is available free of charge at https://pubs.acs.org/doi/10.1021/acsanm.9b02205.

> Experimental characterization conditions, materials used for synthesis, reaction conditions and analysis for hydrogenation of alkenes and methanation, XRPD and N_2 physisorption of samples for shell optimization, XRPD and TEM images of Ni zeolites before and after stability test, XRPD and STEM images of Pt zeolites, textural properties of Pt@recryst-S1(II), XPS of Pt zeolites, catalytic results of Pt@recryst-S1(II) (PDF)

AUTHOR INFORMATION

Corresponding Authors
*E-mail: skk@kemi.dtu.dk. Tel: +45 45 25 24 02.
*E-mail: jjmie@kemi.dtu.dk. Tel: +45 45 25 23 63.
ORCID ⓞ
Jerrik Mielby: 0000-0001-6588-2495

Søren Kegnæs: 0000-0002-6933-6931

Notes
The authors declare no competing financial interest.

REFERENCES

(1) Čejka, J.; Mintova, S. Perspectives of Micro/Mesoporous Composites in Catalysis. *Catal. Rev.: Sci. Eng.* **2007**, *49* (4), 457−509.
(2) Davis, M. E.; Lobo, R. F. Zeolite and Molecular Sieve Synthesis. *Chem. Mater.* **1992**, *4* (4), 756−768.
(3) Corma, A. Inorganic Solid Acids and Their Use in Acid-Catalyzed Hydrocarbon Reactions. *Chem. Rev.* **1995**, *95* (3), 559−614.
(4) Saravanamurugan, S.; Tosi, I.; Rasmussen, K. H.; Jensen, R. E.; Taarning, E.; Meier, S.; Riisager, A. Facile and Benign Conversion of Sucrose to Fructose Using Zeolites with Balanced Brønsted and Lewis Acidity. *Catal. Sci. Technol.* **2017**, *7* (13), 2782−2788.
(5) Goel, S.; Zones, S. I.; Iglesia, E. Encapsulation of Metal Clusters within MFI via Interzeolite Transformations and Direct Hydrothermal Syntheses and Catalytic Consequences of Their Confinement. *J. Am. Chem. Soc.* **2014**, *136* (43), 15280−15290.
(6) Li, S.; Tuel, A.; Laprune, D.; Meunier, F.; Farrusseng, D. Transition-Metal Nanoparticles in Hollow Zeolite Single Crystals as Bifunctional and Size-Selective Hydrogenation Catalysts. *Chem. Mater.* **2015**, *27* (1), 276−282.
(7) Mielby, J.; Abildstrøm, J. O.; Wang, F.; Kasama, T.; Weidenthaler, C.; Kegnaes, S. Oxidation of Bioethanol Using Zeolite-Encapsulated Gold Nanoparticles. *Angew. Chem., Int. Ed.* **2014**, *53* (46), 12513−12516.
(8) Cui, T.-L.; Ke, W.-Y.; Zhang, W.-B.; Wang, H.-H.; Li, X.-H.; Chen, J.-S. Encapsulating Palladium Nanoparticles Inside Mesoporous MFI Zeolite Nanocrystals for Shape-Selective Catalysis. *Angew. Chem., Int. Ed.* **2016**, *55* (32), 9178−9182.
(9) Zhang, J.; Wang, L.; Zhu, L.; Wu, Q.; Chen, C.; Wang, X.; Ji, Y.; Meng, X.; Xiao, F.-S. Solvent-Free Synthesis of Zeolite Crystals Encapsulating Gold-Palladium Nanoparticles for the Selective Oxidation of Bioethanol. *ChemSusChem* **2015**, *8* (17), 2867−2871.
(10) Laursen, A. B.; Højholt, K. T.; Lundegaard, L. F.; Simonsen, S. B.; Helveg, S.; Schüth, F.; Paul, M.; Grunwaldt, J.-D.; Kegnaes, S.; Christensen, C. H.; Egeblad, K. Substrate Size-Selective Catalysis with Zeolite-Encapsulated Gold Nanoparticles. *Angew. Chem.* **2010**, *122* (20), 3582−3585.
(11) Miyake, K.; Inoue, R.; Nakai, M.; Hirota, Y.; Uchida, Y.; Tanaka, S.; Miyamoto, M.; Nishiyama, N. Fabrication of Pt Nanoparticles Encapsulated in Single Crystal like Silicalite-1 Zeolite as a Catalyst for Shape-Selective Hydrogenation of C6 Olefins. *Microporous Mesoporous Mater.* **2018**, *271*, 156−159.
(12) Goel, S.; Wu, Z.; Zones, S. I.; Iglesia, E. Synthesis and Catalytic Properties of Metal Clusters Encapsulated within Small-Pore (SOD, GIS, ANA) Zeolites. *J. Am. Chem. Soc.* **2012**, *134* (42), 17688−17695.
(13) Farrusseng, D.; Tuel, A. Perspectives on Zeolite-Encapsulated Metal Nanoparticles and Their Applications in Catalysis. *New J. Chem.* **2016**, *40* (5), 3933−3949.
(14) Højholt, K. T.; Laursen, A. B.; Kegnæs, S.; Christensen, C. H. Size-Selective Oxidation of Aldehydes with Zeolite Encapsulated Gold Nanoparticles. *Top. Catal.* **2011**, *54* (16−18), 1026−1033.

(15) Goodarzi, F.; Kang, L.; Wang, F. R.; Joensen, F.; Kegnæs, S.; Mielby, J. Methanation of Carbon Dioxide over Zeolite-Encapsulated Nickel Nanoparticles. *ChemCatChem* **2018**, *10* (7), 1566−1570.

(16) Christensen, C. H.; Johannsen, K.; Törnqvist, E.; Schmidt, I.; Topsøe, H.; Christensen, C. H. Mesoporous Zeolite Single Crystal Catalysts: Diffusion and Catalysis in Hierarchical Zeolites. *Catal. Today* **2007**, *128* (3-4), 117−122.

(17) Jiang, J.; Jorda, J. L.; Yu, J.; Baumes, L. A.; Mugnaioli, E.; Diaz-Cabanas, M. J.; Kolb, U.; Corma, A. Synthesis and Structure Determination of the Hierarchical Meso-Microporous Zeolite ITQ-43. *Science (Washington, DC, U. S.)* **2011**, *333* (6046), 1131−1134.

(18) Tosheva, L.; Valtchev, V. P. Nanozeolites: Synthesis, Crystallization Mechanism, and Applications. *Chem. Mater.* **2005**, *17* (10), 2494−2513.

(19) Pérez-Ramírez, J.; Christensen, C. H.; Egeblad, K.; Christensen, C. H.; Groen, J. C. Hierarchical Zeolites: Enhanced Utilisation of Microporous Crystals in Catalysis by Advances in Materials Design. *Chem. Soc. Rev.* **2008**, *37* (11), 2530−2542.

(20) Egeblad, K.; Christensen, C. H.; Kustova, M.; Christensen, C. H. Templating Mesoporous Zeolites. *Chem. Mater.* **2008**, *20*, 946−960.

(21) Ivanova, I. I.; Knyazeva, E. E. Micro-Mesoporous Materials Obtained by Zeolite Recrystallization: Synthesis, Characterization and Catalytic Applications. *Chem. Soc. Rev.* **2013**, *42* (9), 3671−3688.

(22) Abildstrøm, J. O.; Ali, Z. N.; Mentzel, U. V.; Mielby, J.; Kegnæs, S.; Kegnæs, M. Mesoporous MEL, BEA, and FAU Zeolite Crystals Obtained by in Situ Formation of Carbon Template over Metal Nanoparticles. *New J. Chem.* **2016**, *40* (5), 4223−4227.

(23) Janssen, A. H.; Koster, A. J.; de Jong, K. P. Three-Dimensional Transmission Electron Microscopic Observations of Mesopores in Dealuminated Zeolite Y. *Angew. Chem., Int. Ed.* **2001**, *40* (6), 1102−1104.

(24) Choifeng, C.; Hall, J. B.; Huggins, B. J.; Beyerlein, R. A. Electron Microscope Investigation of Mesopore Formation and Aluminum Migration in USY Catalysts. *J. Catal.* **1993**, *140* (2), 395−405.

(25) Ivanova, I. I.; Kuznetsov, A. S.; Ponomareva, O. A.; Yuschenko, V. V.; Knyazeva, E. E. Micro/Mesoporous Catalysts Obtained by Recrystallization of Mordenite. *Stud. Surf. Sci. Catal.* **2005**, *158*, 121−128.

(26) Chal, R.; Cacciaguerra, T.; van Donk, S.; Gérardin, C. Pseudomorphic Synthesis of Mesoporous Zeolite Y Crystals. *Chem. Commun.* **2010**, *46* (41), 7840−7842.

(27) Peréz-Ramírez, J.; Verboekend, D.; Bonilla, A.; Abelló, S. Zeolite Catalysts with Tunable Hierarchy Factor by Pore-Growth Moderators. *Adv. Funct. Mater.* **2009**, *19* (24), 3972−3979.

(28) Schmidt, I.; Boisen, A.; Gustavsson, E.; Ståhl, K.; Pehrson, S.; Dahl, S.; Carlsson, A.; Jacobsen, C. J. H. Carbon Nanotube Templated Growth of Mesoporous Zeolite Single Crystals. *Chem. Mater.* **2001**, *13* (12), 4416−4418.

(29) Jacobsen, C. J. H.; Madsen, C.; Houzvicka, J.; Schmidt, I.; Carlsson, A. Mesoporous Zeolite Single Crystals. *J. Am. Chem. Soc.* **2000**, *122* (29), 7116−7117.

(30) Han, S.; Wang, Z.; Meng, L.; Jiang, N. Synthesis of Uniform Mesoporous ZSM-5 Using Hydrophilic Carbon as a Hard Template. *Mater. Chem. Phys.* **2016**, *177*, 112−117.

(31) Zhang, Y.; Okubo, T. Synthesis of Mesoporous Aluminosilicate with Zeolitic Characteristics Using Vapor Phase Transport. *Chem. Commun.* **2005**, No. 21, 2719−2720.

(32) Abildstrøm, J. O.; Kegnæs, M.; Hytoft, G.; Mielby, J.; Kegnæs, S. Synthesis of Mesoporous Zeolite Catalysts by in Situ Formation of Carbon Template over Nickel Nanoparticles. *Microporous Mesoporous Mater.* **2016**, *225*, 232−237.

(33) Liu, F.; Willhammar, T.; Wang, L.; Zhu, L.; Sun, Q.; Meng, X.; Carrillo-Cabrera, W.; Zou, X.; Xiao, F. S. ZSM-5 Zeolite Single Crystals with b-Axis-Aligned Mesoporous Channels as an Efficient Catalyst for Conversion of Bulky Organic Molecules. *J. Am. Chem. Soc.* **2012**, *134* (10), 4557−4560.

(34) Wang, L.; Zhang, Z.; Yin, C.; Shan, Z.; Xiao, F.-S. Hierarchical Mesoporous Zeolites with Controllable Mesoporosity Templated from Cationic Polymers. *Microporous Mesoporous Mater.* **2010**, *131* (1−3), 58−67.

(35) Xiao, F.-S.; Wang, L.; Yin, C.; Lin, K.; Di, Y.; Li, J.; Xu, R.; Su, D. S.; Schlögl, R.; Yokoi, T.; Tatsumi, T. Catalytic Properties of Hierarchical Mesoporous Zeolites Templated with a Mixture of Small Organic Ammonium Salts and Mesoscale Cationic Polymers. *Angew. Chem., Int. Ed.* **2006**, *45* (19), 3090−3093.

(36) Wang, H.; Pinnavaia, T. J. MFI Zeolite with Small and Uniform Intracrystal Mesopores. *Angew. Chem., Int. Ed.* **2006**, *45* (45), 7603−7606.

(37) Wang, N.; Sun, Q.; Bai, R.; Li, X.; Guo, G.; Yu, J. In Situ Confinement of Ultrasmall Pd Clusters within Nanosized Silicalite-1 Zeolite for Highly Efficient Catalysis of Hydrogen Generation. *J. Am. Chem. Soc.* **2016**, *138* (24), 7484−7487.

(38) Moliner, M.; Gabay, J. E.; Kliewer, C. E.; Carr, R. T.; Guzman, J.; Casty, G. L.; Serna, P.; Corma, A. Reversible Transformation of Pt Nanoparticles into Single Atoms inside High-Silica Chabazite Zeolite. *J. Am. Chem. Soc.* **2016**, *138* (48), 15743−15750.

(39) Zhang, Y.; Kubů, M.; Mazur, M.; Čejka, J. Encapsulation of Pt Nanoparticles into IPC-2 and IPC-4 Zeolites Using the ADOR Approach. *Microporous Mesoporous Mater.* **2019**, *279*, 364−370.

(40) Liu, L.; Díaz, U.; Arenal, R.; Agostini, G.; Concepción, P.; Corma, A. Generation of Subnanometric Platinum with High Stability during Transformation of a 2D Zeolite into 3D. *Nat. Mater.* **2017**, *16* (1), 132−138.

(41) Kim, J. C.; Lee, S.; Cho, K.; Na, K.; Lee, C.; Ryoo, R. Mesoporous MFI Zeolite Nanosponge Supporting Cobalt Nanoparticles as a Fischer−Tropsch Catalyst with High Yield of Branched Hydrocarbons in the Gasoline Range. *ACS Catal.* **2014**, *4* (11), 3919−3927.

(42) Laprune, D.; Tuel, A.; Farrusseng, D.; Meunier, F. Highly Dispersed Nickel Particles Encapsulated in Multi-Hollow Silicalite-1 Single Crystals - Effects of Siliceous Deposits and Phosphorous Species on the Catalytic Performances. *ChemCatChem* **2017**, *9*, 2297−2307.

(43) Han, J.; Cho, J.; Kim, J. C.; Ryoo, R. Confinement of Supported Metal Catalysts at High Loading in the Mesopore Network of Hierarchical Zeolites, with Access via the Microporous Windows. *ACS Catal.* **2018**, *8* (2), 876−879.

(44) Gallas-Hulin, A.; Mielby, J.; Kegnæs, S. Efficient Production of Hydrogen from Decomposition of Formic Acid over Zeolite Incorporated Gold Nanoparticles. *ChemistrySelect* **2016**, *1* (13), 3942−3945.

(45) Rasmussen, K. H.; Mielby, J.; Kegnaes, S. Towards Encapsulation of Nanoparticles in Chabazite Through Interzeolite Transformation. *ChemCatChem* **2018**, *10* (19), 4380−4385.

(46) Li, S.; Boucheron, T.; Tuel, A.; Farrusseng, D.; Meunier, F. Size-Selective Hydrogenation at the Subnanometer Scale over Platinum Nanoparticles Encapsulated in Silicalite-1 Single Crystal Hollow Shells. *Chem. Commun.* **2014**, *50* (15), 1824−1826.

(47) Xu, D.; Lv, H.; Liu, B. Encapsulation of Metal Nanoparticle Catalysts Within Mesoporous Zeolites and Their Enhanced Catalytic Performances: A Review. *Front. Chem.* **2018**, DOI: 10.3389/fchem.2018.00550.

(48) Gu, J.; Zhang, Z.; Hu, P.; Ding, L.; Xue, N.; Peng, L.; Guo, X.; Lin, M.; Ding, W. Platinum Nanoparticles Encapsulated in MFI Zeolite Crystals by a Two-Step Dry Gel Conversion Method as a Highly Selective Hydrogenation Catalyst. *ACS Catal.* **2015**, *5* (11), 6893−6901.

(49) Zhou, J.; Hua, Z.; Zhao, J.; Gao, Z.; Zeng, S.; Shi, J. A Micro/Mesoporous Aluminosilicate: Key Factors Affecting Framework Crystallization during Steam-Assisted Synthesis and Its Catalytic Property. *J. Mater. Chem.* **2010**, *20* (32), 6764−6771.

(50) Matsukata, M.; Ogura, M.; Osaki, T.; Hari Prasad Rao, P. R.; Nomura, M.; Kikuchi, E. Conversion of Dry Gel to Microporous Crystals in Gas Phase. *Top. Catal.* **1999**, *9*, 77−92.

ACS Applied Nano Materials

(51) Naik, S. P.; Chiang, A. S. T.; Thompson, R. W. Synthesis of Zeolitic Mesoporous Materials by Dry Gel Conversion under Controlled Humidity. *J. Phys. Chem. B* **2003**, *107* (29), 7006−7014.

(52) Thommes, M.; Cychosz, K. A. Physical Adsorption Characterization of Nanoporous Materials: Progress and Challenges. *Adsorption* **2014**, *20* (2), 233−250.

(53) Thommes, M. Physical Adsorption Characterization of Nanoporous Materials. *Chem. Ing. Technol.* **2010**, *82* (7), 1059−1073.

(54) Thommes, M.; Kaneko, K.; Neimark, A. V.; Olivier, J. P.; Rodriguez-Reinoso, F.; Rouquerol, J.; Sing, K. S. W. Physisorption of Gases, with Special Reference to the Evaluation of Surface Area and Pore Size Distribution (IUPAC Technical Report). *Pure Appl. Chem.* **2015**, *87* (9−10), 1051−1069.

(55) Christensen, C. H.; Johannsen, K.; Schmidt, I.; Christensen, C. H. Catalytic Benzene Alkylation over Mesoporous Zeolite Single Crystals: Improving Activity and Selectivity with a New Family of Porous Materials. *J. Am. Chem. Soc.* **2003**, *125* (44), 13370−13371.

(56) Groen, J. C.; Pérez-Ramírez, J. Critical Appraisal of Mesopore Characterization by Adsorption Analysis. *Appl. Catal., A* **2004**, *268* (1−2), 121−125.

(57) Groen, J. C.; Peffer, L. A.; Pérez-Ramírez, J. Pore Size Determination in Modified Micro- and Mesoporous Materials. Pitfalls and Limitations in Gas Adsorption Data Analysis. *Microporous Mesoporous Mater.* **2003**, *60* (1−3), 1−17.

(58) Janssen, A. H.; Koster, A. J.; de Jong, K. P. On the Shape of the Mesopores in Zeolite Y: A Three-Dimensional Transmission Electron Microscopy Study Combined with Texture Analysis. *J. Phys. Chem. B* **2002**, *106* (46), 11905−11909.

(59) Cychosz, K. A.; Guillet-Nicolas, R.; García-Martínez, J.; Thommes, M. Recent Advances in the Textural Characterization of Hierarchically Structured Nanoporous Materials. *Chem. Soc. Rev.* **2017**, *46* (2), 389−414.

(60) Rasmussen, C. J.; Vishnyakov, A.; Thommes, M.; Smarsly, B. M.; Kleitz, F.; Neimark, A. V. Cavitation in Metastable Liquid Nitrogen Confined to Nanoscale Pores. *Langmuir* **2010**, *26* (12), 10147−10157.

(61) Pulikkal Thumbayil, R.; Mielby, J.; Kegnæs, S. Pd Nanoparticles Encapsulated in Mesoporous HZSM-5 Zeolite for Selective One-Step Conversion of Acetone to Methyl Isobutyl Ketone. *Top. Catal.* **2019**, *62* (7−11), 678−688.

(62) Chen, H.; Zhang, X.; Zhang, J.; Wang, Q. Controllable Synthesis of Hierarchical ZSM-5 for Hydroconversion of Vegetable Oil to Aviation Fuel-like Hydrocarbons. *RSC Adv.* **2017**, *7* (73), 46109−46117.

(63) Wang, Z.; Li, C.; Cho, H. J.; Kung, S.-C.; Snyder, M. A.; Fan, W. Direct, Single-Step Synthesis of Hierarchical Zeolites without Secondary Templating. *J. Mater. Chem. A* **2015**, *3* (3), 1298−1305.

(64) Lucchini, M. A.; Testino, A.; Kambolis, A.; Proff, C.; Ludwig, C. Sintering and Coking Resistant Core-Shell Microporous Silica-Nickel Nanoparticles for CO Methanation: Towards Advanced Catalysts Production. *Appl. Catal., B* **2016**, *182*, 94−101.

(65) Wang, W.; Chu, W.; Wang, N.; Yang, W.; Jiang, C. Mesoporous Nickel Catalyst Supported on Multi-Walled Carbon Nanotubes for Carbon Dioxide Methanation. *Int. J. Hydrogen Energy* **2016**, *41* (2), 967−975.

(66) Rostrup-Nielsen, J. R.; Pedersen, K.; Sehested, J. High Temperature Methanation Sintering and Structure Sensitivity. *Appl. Catal., A* **2007**, *330* (1−2), 134−138.

(67) Shah, M. A. Growth of Uniform Nanoparticles of Platinum by an Economical Approach at Relatively Low Temperature. *Sci. Iran.* **2012**, *19* (3), 964−966.

Appendix D.2

The effect of active site distribution in bi-functional Pt-zeolite catalysts for ethane dehydroaromatization

Farnoosh Goodarzi[a], David Benjamin Christensen[a], Finn Joensen[b], Søren Kegnæs[a], Jerrik Mielby[a,*]

[a] DTU Chemistry, Technical University of Denmark, Kemitorvet 207, 2800 Kgs, Lyngby, Denmark
[b] Haldor Topsøe A/S, Haldor Topsøes Allé 1, 2800 Kgs, Lyngby, Denmark

ARTICLE INFO

ABSTRACT

The direct conversion of ethane to higher-valued petrochemical feedstock such as benzene, toluene and xylenes (BTX) has become more economically attractive because of the recent shale gas revolution. The selectivity towards BTX and catalyst deactivation represent significant technical challenges in this process. In this work, we synthesized a series of bi-functional Pt on acidic ZSM-5 catalysts to investigate the effect of platinum nanoparticle distribution and location on selectivity and deactivation. The best catalyst was Pt encapsulated in desilicated ZSM-5 that remained stable after 15 h of reaction resulting in 60% higher conversion and 75% higher BTX selectivity than Pt supported on conventional acidic ZSM-5 zeolite.

1. Introduction

Aromatics such as benzene, toluene and xylenes (BTX) are high-valuable raw materials for manufacturing industries [1]. ZSM-5 with microporous three-dimensional channel structure is the primary catalyst applied in the direct conversion of light alkanes such as ethane into aromatics (dehydroaromatization). The pore size of around 5.4 Å in the ZSM-5 zeolite, which has similar size as BTX molecules, makes this zeolite the perfect size selective catalyst for BTX. Acidic ZSM-5 zeolite is usually combined with effective hydrogenating metals such as Pt [2,3], Pd [4] and Ru [5] or metal cations (e.g. Zn, Ga) [6–8], to achieve higher catalytic activity.

Despite the excellent performance of conventional acidic ZSM-5, the small size of the pores imposes a diffusion barrier that leads to severe coke formation in the micropores and catalyst deactivation [9,10]. To address this drawback, different solutions have been proposed to minimize the mean diffusion path length [10–13]. The introduction of mesopores can suppress coke formation by facilitating the molecular diffusion. Mesopores can be created during synthesis by using hard or soft templates [14–16] or via post-synthetic approaches such as alkali/acid treatments [17–19]. In addition, the presence of mesopores can increase the external surface area to facilitate the dispersion of supported metal nanoparticles [20,21].

Previous reports have indicated that the proximity of the metal and acid sites influences the conversion, selectivity and deactivation in the direct transformation of ethane to aromatics. For instance, Reschetilowski et al. [2] proposed that higher dispersion and smaller particle size of Pt leads to closer proximity of metal and acid sites, which increases the electron deficiency of the metal. The authors suggested that this stabilizes the chemisorbed platinum-ethylene complex, which assists consecutive reactions that convert the olefin intermediates into coke and consequently leads to rapid deactivation. Furthermore, Steinberg et al. [22] investigated the importance of the catalyst bed and demonstrated that the optimum packing has Pt/ZSM-5 in the top bed and pure acidic ZSM-5 in the bottom bed. The authors therefore concluded that dehydroaromatization is initiated in the first bed and the process is followed by aromatization on the bottom bed. Based on these results, Xiang et al. [23] recently suggested that for combining these beds into one catalyst bed, an optimum design would be a catalyst that consists of a core of Pt on acidic ZSM-5 with a shell of pure acidic ZSM-5. Despite previous investigations on Pt/ZSM-5, the importance of the metal and acid site distribution is still not fully understood because of the lack of proper model catalysts. Based on our previous work with metal nanoparticles and mesoporous zeolites [20,21], we therefore decided to encapsulate Pt in the core of a hierarchical ZSM-5 catalyst.

Here, we prepared four ZSM-5 zeolites with similar strong acid site concentration but different morphology and pore size distribution in order to investigate the effect of the metal nanoparticles size, location and distribution and proximity of Pt and acid sites. The zeolites were
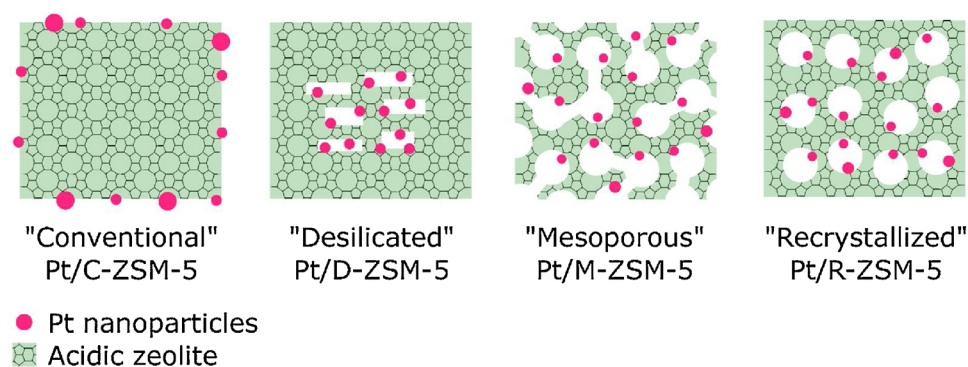

Fig. 1. Schematic illustration of the four different catalysts. From left to right: Pt supported on conventional ZSM-5 (Pt/C-ZSM-5), Pt supported on desilicated ZSM-5 (Pt/D-ZSM-5), Pt supported on mesoporous carbon-templated ZSM-5 (Pt/M-ZSM-5) and Pt supported on steam-assisted recrystallized mesoporous ZSM-5 (Pt/R-ZSM-5).

then impregnated with Pt and tested for the direct conversion of ethane into BTX by dehydroaromatization. The first catalyst is conventional ZSM-5 with Pt primarily located on the zeolite external surface (Pt/C-ZSM-5), please see Fig. 1. The second catalyst is selectively desilicated ZSM-5, where mesopores and voids are created inside the zeolite framework and platinum is mainly located inside these voids (Pt/D-ZSM-5). The third and fourth catalysts are Pt encapsulated in mesoporous ZSM-5 (Pt/M-ZSM-5) and steam-assisted recrystallized mesoporous ZSM-5 with Pt surrounded by a thin microporous shell of ZSM-5 (Pt/R-ZSM-5), respectively. Under the same reaction conditions, Pt/D-ZSM-5 exhibited the highest catalytic activity and remained stable for over 15 h of conversion. Furthermore, the catalyst accommodated the largest amount of coke.

2. Experimental

Tetrapropylammonium hydroxide (TPAOH, Sigma-Aldrich, 1.0 M in H_2O) and tetraethyl orthosilicate (TEOS, Sigma-Aldrich, ≥99.0 %) were used as the structure directing agent (SDA) and silicon source, respectively, in all of the syntheses.

2.1. Synthesis

2.1.1. Conventional ZSM-5 (C-ZSM-5)

For synthesis of conventional ZSM-5 (C-ZSM-5) with Si/Al ratio of 100, 0.016 g of sodium aluminate ($NaAlO_2$, Sigma-Aldrich, anhydrous) was dissolved in 7.26 ml TPAOH. Then 4.46 mL of TEOS was added dropwise to the solution while stirring in a Teflon beaker. The mixture was stirred for 1 h and then heated in a Teflon-lined stainless steel autoclave at 180 °C for 24 h under autogenous pressure. The product was separated from the liquid phase by filtration, washed several times with distilled water, dried at 80 °C overnight and then calcined for 20 h at 550 °C to yield NaZSM-5. NaZSM-5 was ion exchanged as described in Section 2.1.5 to achieve C-ZSM-5.

2.1.2. Selectively desilicated ZSM-5 (D-ZSM-5)

1.0 g of NaZSM-5 was added to a solution of 0.7 g cetyltrimethylammonium bromide (CTAB, as surfactant) in 50 ml ammonium hydroxide (15 % ammonia in H_2O) and stirred for 3 h at room temperature. The mixture was then heated in a Teflon-lined stainless steel autoclave at 90 °C for 24 h under autogenous pressure. Product was washed and calcined for 10 h at 550 °C to yield desilicated NaZSM-5. Finally, the product was ion exchanged as described in Section 2.1.5 to achieve D-ZSM-5.

2.1.3. Mesoporous ZSM-5 (M-ZSM-5)

Following the procedure by Jacobsen et al. [14] mesoporous ZSM-5 was synthesized using carbon black particles (BP-2000), with average particle diameter of 12 nm, as hard template. First, 0.016 g of sodium aluminate was dissolved in 7.26 mL TPAOH and then 2 g of carbon black was impregnated with the solution in a Teflon beaker and dried

overnight at room temperature. The dried mixture was impregnated with 4.46 mL of TEOS and dried overnight at room temperature. The Teflon beaker was placed in a Teflon-lined stainless steel autoclave and 15 ml of distilled water was added into the autoclave, around the beaker, to produce saturated steam. The autoclave was heated at 180 °C for 72 h. After the autoclave was quenched, synthesized powder was collected, washed with distilled water, dried at 80 °C for 24 h and finally calcined at 550 °C for 20 h to yield mesoporous NaZSM-5. The sample was ion exchanged as described in Section 2.1.5 to achieve M-ZSM-5.

2.1.4. Steam-assisted recrystallized mesoporous ZSM-5 (R-ZSM-5)

The as-synthesized mesoporous NaZSM-5 was pulverized in a mortar, dried in vacuum oven at 80 °C overnight. First, 0.016 g of sodium aluminate was dissolved in 7.26 mL TPAOH and used for impregnating 1 g of the ZSM-5 powder in a Teflon beaker. The mixture was mixed for 15 min and dried overnight at room temperature. Then the material was impregnated with 4.46 mL TEOS again and dried overnight at room temperature. The beaker was placed in a Teflon-lined stainless steel autoclave and 15 ml of distilled water was added into the autoclave, around the beaker, to produce saturated steam. The autoclave was heated at 180 °C for 72 h. After the autoclave was quenched, synthesized powder was collected, washed with distilled water, dried at 80 °C for 24 h and finally calcined at 550 °C for 20 h to yield steam-assisted recrystallized NaZSM-5. The product was ion exchanged as described in Section 2.1.5 to achieve R-ZSM-5.

2.1.5. Ion exchange protocol and impregnation of the zeolites

All ZSM-5 samples were ion exchanged by stirring 1 g of zeolite in 80 ml of 1 mol/L ammonium nitrate aqueous solution at 80 °C for 1 h. The process was repeated three times while the last ion exchange was carried out overnight. The powder was washed, dried in the oven for 12 h at 80 °C and calcined for 10 h at 550 °C to achieve protonated ZSM-5 zeolites. Prior to metal impregnation, the zeolite powder was placed in vacuum oven at 50 °C overnight. The zeolite powder was impregnated with H_2PtCl_6 solution in water until incipient wetness. Finally, the powder was dried at 80 °C for 12 h, calcined at 350 °C (heating ramp of 0.5 °C/min) for 3 h and reduced in H_2 at 600 °C for 3 h to achieve 1 wt% Pt in ZSM-5 zeolite.

2.2. Characterizations

Powder X-ray diffraction was performed for all Pt on acidic ZSM-5 catalysts and pure acidic ZSM-5 zeolites on a Huber G670 diffractometer operated in transmission mode with Cu $K_{\alpha 1}$ irradiation from a focusing quartz monochromator.

Inductively coupled plasma optical emission spectroscopy (ICP-OES) was done for elemental analysis on an Agilent 720 ICP-OES spectrometer to determine the amount of Si, Al and Pt.

Transmission electron microscopy (TEM) was performed on a FEI Tecnai T20 G2 microscope operated at 200 KV to investigate crystal size

and morphology of the samples and platinum location on different ZSM-5 supports.

N$_2$ physisorption was operated for protonated ZSM-5 zeolites at liquid nitrogen temperature on a 3FLEX surface area and porosimetry analyzer. Prior to the test, samples were outgassed under vacuum at 400 °C overnight. The specific surface area (S$_{BET}$) was calculated by the BET method. Micropore volumes (V$_{micro}$) were determined using *t*-plot method. The total pore volumes (V$_{total}$) and the external surface were calculated from the amount of adsorbed nitrogen at the relative pressure of P/P° = 0.95.

Temperature programmed desorption of ammonia (NH$_3$-TPD) was measured by ammonia TPD on a Mettler Toledo TGA-DSC1. Prior to the analysis, the samples were heated to 500 °C in a mix flow of N$_2$ and Ar. Afterwards, samples were cooled down to 150 °C and NH$_3$ was purged for 30 min followed by flushing with inert gases for 3 h to remove physically adsorbed NH$_3$. Eventually, desorption of NH$_3$ was carried out by increasing the temperature to 500 °C with a heating ramp of 5 °C/min.

The amount of coke was quantified by thermo-gravimetric analysis (TGA) on a Mettler Toledo equipment. The catalysts were heated at a rate of 5 °C min^{-1} in synthetic air to 700 °C.

2.3. Catalytic test

Ethane dehydroaromatization experiments were performed in a continuous fixed bed stainless steel reactor with an inner diameter of 9 mm at 550 °C and under 2 barg pressure. The reactor and thermowells, which were in contact with the stream, were coated with SilcoNert®1000 [24] (Silicosteel®, thickness of 100 − 500 nm). Catalyst fraction size was between 0.6 − 1 mm and 1.0 g of the fractionated catalyst was loaded into the reactor. All of the catalysts were pretreated at 550 °C for 1 h under 12 N L h^{-1} flow of N$_2$ to remove impurities and any traces of oxygen from the catalysts. The gas was then switched to 10 % ethane in N$_2$ with total flow of 3 NL h^{-1} corresponding to a gas hourly space velocity (GHSV) of 0.3 NL$_{Ethane}$/g$_{cat}$ /h. The outlet gases were analyzed online in an Agilent 7890B gas chromatograph equipped with two capillary columns of CP-Al$_2$O$_3$-KCl (25m × 0.32mm × 5 µm) and HP-INNOWax, (30 mm × 0.32 mm × 0.25 µm), a thermal conductivity detector (TCD) and two flame ionization detectors (FID). The conversion and products selectivity were calculated based on carbon mole balance.

3. Results and discussion

3.1. Characterization results

The X-ray diffraction (XRD) patterns of all the platinum containing ZSM-5 catalysts and pure conventional ZSM-5 zeolite are shown in Fig. 2. As expected, the patterns show that all ZSM-5 samples were
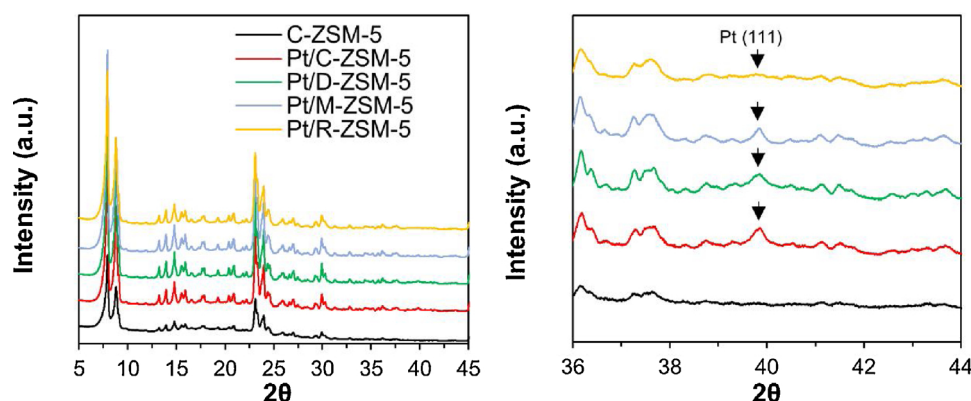
Fig. 3. N$_2$ physisorption analysis with offset of 2 mmol/g between isotherms for conventional (C-ZSM-5), selectively desilicated (D-ZSM-5), mesoporous ZSM-5 (M-ZSM-5) and steam-assisted recrystallized mesoporous ZSM-5 (R-ZSM-5) performed at 77 K.

crystalline and had the characteristic peaks of the ZSM-5 zeolite framework. In addition, a very weak peak appeared around 2θ = 39.9° in all of the ZSM-5-supported Pt samples except for Pt/R-ZSM-5. We assign this peak to the diffraction from Pt (111). The absence of the Pt (111) peak in Pt/R-ZSM-5 indicates that the nanoparticles are smaller than in the other samples. Furthermore, we found that the diffraction peak of Pt (111) is slightly broader in Pt/D-ZSM-5, indicating that the nanoparticles in this sample are smaller than in Pt/M-ZSM-5 and Pt/C-ZSM-5.

Fig. 3 shows the N$_2$ physisorption analysis of all ZSM-5 zeolites without platinum. The isotherms are type I for both C-ZSM5 and D-ZSM-5 with a small step around P/P° = 0.15. This step is not related to pores in the MFI materials, but a result of the so-called fluid-to-crystalline like phase transition of the adsorbed nitrogen [25]. Moreover, D-ZSM-5 has a small H4 hysteresis loop at P/P° above the forced closure at around P/P° = 0.45, which is attributed to the created internal voids and mesopores in the sample with broad pore size distribution [20,21]. Figure S1 shows the pore size distribution (PSD) obtained from BJH analysis of the desorption branch which confirms that PSD in the D-ZSM-5 is between 6–70 nm. However, M-ZSM-5 shows a type IV isotherm with a hysteresis loop at P/P° > 0.8. Typically, this loop is assigned to mesopores [26] and BJH analysis shows that PSD is between 5–50 nm (Figure S1). Similarly, R-ZSM-5 exhibits a type IV isotherm but

Fig. 2. XRD patterns of the prepared catalysts (normal (left) and zoomed in (right)).
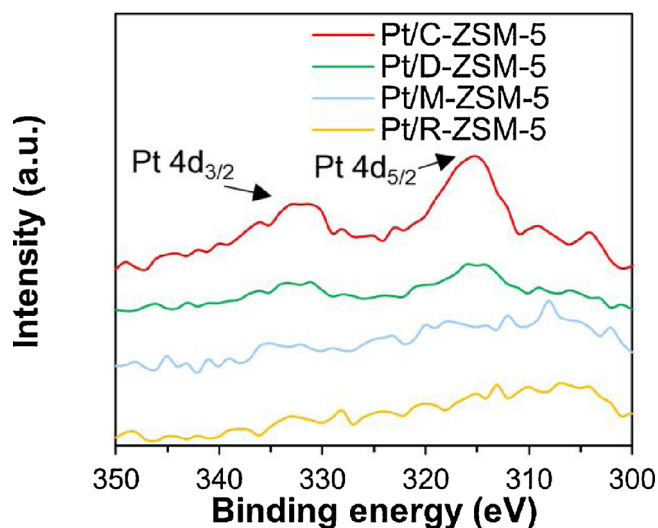
Fig. 4. XPS of the Pt on different support.

with hysteresis loop of H2a that has a steep closing at around P/ $P° = 0.45$. This well-known phenomenon is referred to as an inkbottle-type of porosity and indicates that the mesopores are only accessible through the inherent zeolite micropores [27]. Based on these results, the four ZSM-5 zeolites have different types of pore systems and different pore size distributions. All textural properties of the ZSM-5 supports are summarized in Table S1. The results show that the

modified zeolites D-ZSM-5, M-ZSM-5 and R-ZSM-5 have a higher external surface area and total pore volume than C-ZSM-5, while the microporous surface area remain in the same range (Fig. 4).

Elemental analysis results obtained from ICP-OES revealed that all four catalysts have similar Pt content of about 0.7 wt% as well as a similar Si/Al ratios of around 100 (See Table S2). X-ray photoelectron spectroscopy (XPS) analysis of Pt/C-ZSM-5 shows two weak peaks from Pt $4d_{5/2}$ and $4d_{3/2}$. This indicates that Pt particles are present on the surface of this sample. The other samples showed no detectable peaks between $300 - 350$ eV, which confirms that a significant part of the platinum nanoparticles were encapsulated in the interior of the zeolites.

The TEM images in Fig. 5 illustrate very different zeolite morphologies as well as dispersion and location of the Pt nanoparticles. The C-ZSM-5 and D-ZSM-5 have the typical coffin-shape morphology for the MFI structure with average crystal size of 250 nm. Moreover, in D-ZSM-5 the created voids and mesopores are obvious inside the zeolite crystals. As for M-ZSM-5 and R-ZSM-5, the crystals are larger in size (around 1000 nm), which are more clear in Figs. S4 and S5. Fig. 5d also shows reconstructed surface via steam-assisted recrystallization around R-ZSM-5 that makes the surface smoother, while M-ZSM-5 has a rough surface (Fig. 5c). The Pt nanoparticles are rather large in Pt/C-ZSM-5 (around 10–50 nm) compared to other samples. Furthermore, metal nanoparticles are agglomerated and mostly situated on the surface of the Pt/C-ZSM-5. In the Pt/D-ZSM-5 where Pt nanoparticles are encapsulated in the desilicated ZSM-5, the small metal nanoparticles (less than 10 nm) are well distributed in the zeolite voids and mesopores inside the interior region of the zeolite crystal. In the case of Pt/M-ZSM-5, the Pt particles are difficult to detect in the TEM images due to the
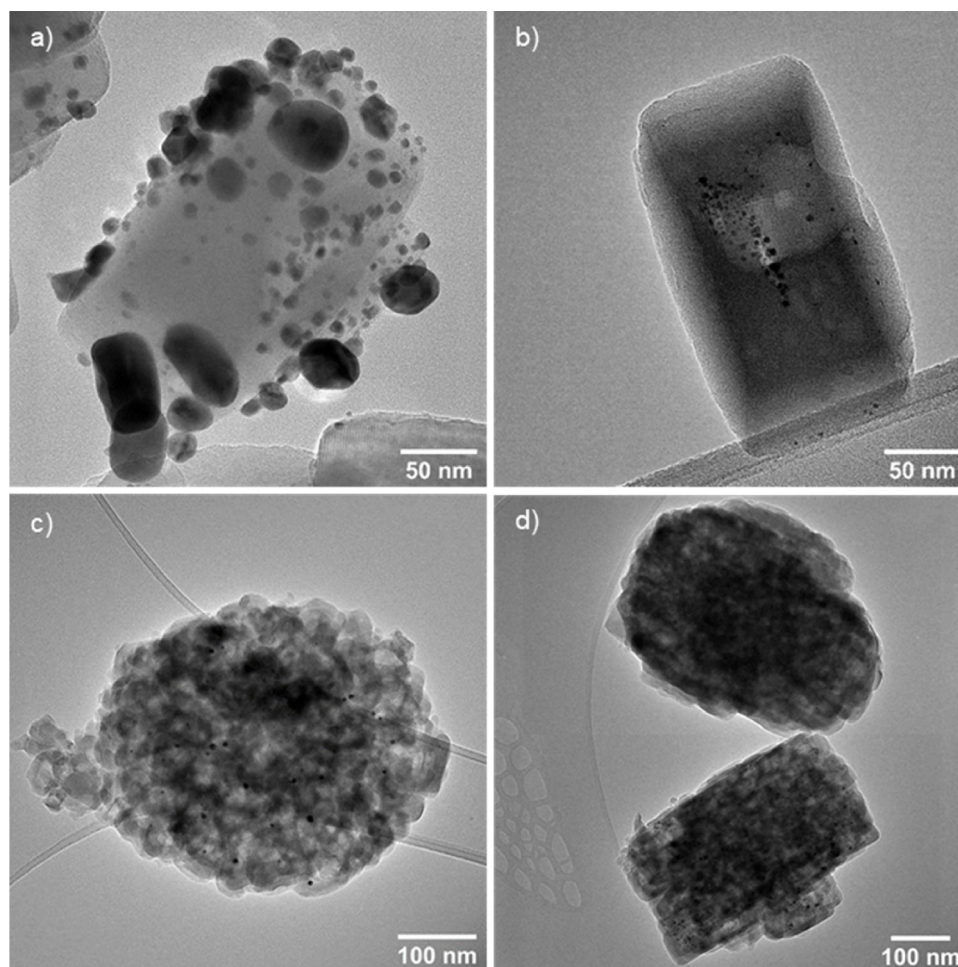
Fig. 5. TEM images of a) Pt/C-ZSM-5, b) Pt/D-ZSM-5, c) Pt/M-ZSM-5 and d) Pt/R-ZSM-5, respectively.

thickness of the zeolite particles. However, we speculate that Pt nanoparticles are situated inside the mesoporous ZSM-5 crystals since there are no particles found on the external surface. For Pt/R-ZSM-5 sample, Pt nanoparticles (smaller than 10 nm) are well dispersed inside the zeolite and encapsulated by the thin shell surrounding them. The observed size of Pt nanoparticles in TEM are in good agreement with XRD results (more TEM images are presented in SI). In addition, the TEM images confirm XPS analysis results that Pt nanoparticles are mainly located on the surface of Pt/C-ZSM-5, whereas for the other samples the metal particles are primarily located in the interior.

NH$_3$-TPD shows that the concentration of strong acid sites is similar in all ZSM-5 catalysts considering the degree of uncertainty for the analysis, which is 0.02 mmol/g (Table 1).

Table 1
Distribution of weak and strong acidic sites as determined by NH$_3$-TPD.

Catalyst	Weak acid sites[a] (mmol/g)	Strong acid sites[b] (mmol/g)	Total acid Sites (mmol/g)
C-ZSM-5	0.040	0.069	0.109
D-ZSM-5	0.039	0.081	0.120
M-ZSM-5	0.052	0.104	0.156
R-ZSM-5	0.040	0.086	0.126

[a] Density of acid sites determined by NH$_3$-TPD for NH$_3$ desorbed at $180-280\,°C$.
[b] Density of acid sites determined by NH$_3$-TPD for NH$_3$ desorbed at $280-550\,°C$.

3.2. Catalytic results

We tested the four catalysts for the direct dehydroaromatization of ethane into BTX-type aromatics. Fig. 6a shows the conversion as function of the time-on-stream at 550 °C. The overall catalytic behavior of all four catalysts is that their initial conversion begins to decrease over time with different rates. Among the catalysts, Pt/D-ZSM-5 resulted in the highest activity and selectivity towards BTX during the 15 h experiment. The least active catalyst is Pt/M-ZSM-5 that showed low conversion, low selectivity and significant deactivation. Based on a previous study by Reschetilowski *et al.* [2], it is likely that this catalyst is less active firstly due to the large size of Pt nanoparticles and secondly because metal nanoparticles are located inside the mesopores and not in the zeolite framework. This means that platinum nanoparticles are situated distant from Brønsted acid sites.

The selectivity of the catalysts towards the desired BTX products in Fig. 6b shows that Pt/D-ZSM-5 has the highest selectivity, which is about 38% and it increases slightly over time to about 42%. In contrast, the Pt/M-ZSM-5 shows the lowest selectivity towards BTX and decreases from 20% to below 10% after 6 h. In spite of the same conversion of ethane over Pt/C-ZSM-5 and Pt/R-ZSM-5 during the first 5 h of reaction, the latter catalyst exhibits a more stable and higher conversion. In addition, the BTX selectivity of Pt/R-ZSM-5 is higher, and significantly more stable, only decreasing from 36% to 33% while BTX selectivity drops from 28% to 21% for Pt/C-ZSM-5. Direct conversion of ethane to aromatics is thermodynamically limited by the initial reaction, which is dehydrogenation of ethane into ethylene. Therefore, ethylene is required to be transformed to aromatics to overcome the thermodynamic limitation and increase the overall conversion [28]. As NH$_3$-TPD results showed similar strong acid site concentration for all four zeolites, it may be assumed that the consumption of ethylene is favored by the close proximity of metal and acid sites which catalyzes the oligomerization and cyclization transformation [29,30]. For this reason, both distribution and location of metal active sites in the catalysts probably play a crucial role with respect to both activity and BTX selectivity. This would explain the higher selectivity for Pt/D-ZSM-5

and Pt/R-ZSM-5 where Pt nanoparticles are more evenly distributed in the interior and surrounded by ZSM-5 framework compared to the other two catalysts in which nanoparticles are located on the external surface as shown in TEM. Furthermore, we believe that Pt/D-ZSM-5 gives the highest conversion and BTX selectivity compared to Pt/R-ZSM-5 due to the optimum location of Pt nanoparticles, which is in the inner region. This also confirms the discussed mechanism in the literature [22] that first ethane dehydrogenates on the metal nanoparticles active sites. Subsequently, ethylene reacts further on zeolite Brønsted acid sites, while diffusing out of the catalyst, to convert into BTX. Therefore, if Pt nanoparticles are not distributed near the framework (i.e. close proximity to the acid sites), the conversion will be limited, which is projected more clearly in Pt/C-ZSM-5.

Fig. 7 shows the selectivity towards different by-products: methane, ethylene, propane, propylene, butane, butenes and heavy aromatics such as naphthalene derivatives. Methane formation is the consequence of higher conversion and BTX selectivity that involves more secondary reactions. Therefore, the catalysts Pt/D-ZSM-5 and Pt/R-ZSM-5 with higher conversion and BTX selectivity have higher selectivity to methane. Ethylene product is lower in these catalysts compared to Pt/C-ZSM-5 and Pt/M-ZSM-5, which also confirms that ethylene is consumed more efficiently in these catalysts to form aromatics. Olefins and alkanes consisting of C$_3$ and C$_4$ are considered as secondary products, which is why their production reaches a maximum and then declines as the result of their further transformation in all of the catalysts. In general, a small amount of heavy aromatics are formed over all of the catalysts but the selectivity towards these products is too small for comparison.

The TGA results in Fig. 8 indicate that the most active catalyst of Pt/D-ZSM-5 has the largest amount of coke content around 12.6 wt% while Pt/R-ZSM-5 contains the least amount of coke (1.3 wt%). It is likely that higher porosity of Pt/R-ZSM-5 enhances the diffusion to suppress the coke formation more effectively than Pt/D-ZSM-5, which has less voids and mesopores. It is remarkable however, that the desilicated sample maintains superior activity and selectivity throughout, despite the high amount of coke deposition. Carbon deposition on Pt/M-ZSM-5 and Pt/R-ZSM-5 zeolites are almost similar, although the latter catalyst exhibited higher conversion and selectivity towards BTX. Based on the small coke content of these two catalysts, the main reason for the deactivation in Pt/M-ZSM-5 might be sintering and loss of metal active sites rather than coking. Furthermore, Pt/C-ZSM-5 has high content of deposited coke (around 10%), which indicates that the decrease in activity and selectivity was mainly caused by pore blockage. Based on all above discussed results, Pt/D-ZSM-5 is the most active and selective catalyst that preserved its activity which we may attribute to successful metal encapsulation in the core region and presence of mesoporosity which provides accessibility to the active sites.

4. Conclusion

Four platinum containing acidic ZSM-5 with similar strong acid site concentration but different morphology, where metal nanoparticles are located in different regions of zeolite, were synthesized and tested in the direct conversion of ethane to aromatics. The two catalysts, Pt on conventional ZSM-5 and Pt on mesoporous ZSM-5, in which Pt nanoparticles were larger and located distant from the acid sites showed the least activity and selectivity towards BTX. Furthermore, the conversion and selectivity decreased after 15 h.

Desilicated ZSM-5 and recrystallized ZSM-5-encapsulated Pt nanoparticles showed significantly higher activity and selectivity towards BTX. The metal active sites in these catalysts were sitting in close proximity to the acid sites. Furthermore, in desilicated ZSM-5-encapsulated Pt, where Pt nanoparticles are situated mainly in the core of zeolite surrounded by zeolite framework, resulted in highest conversion
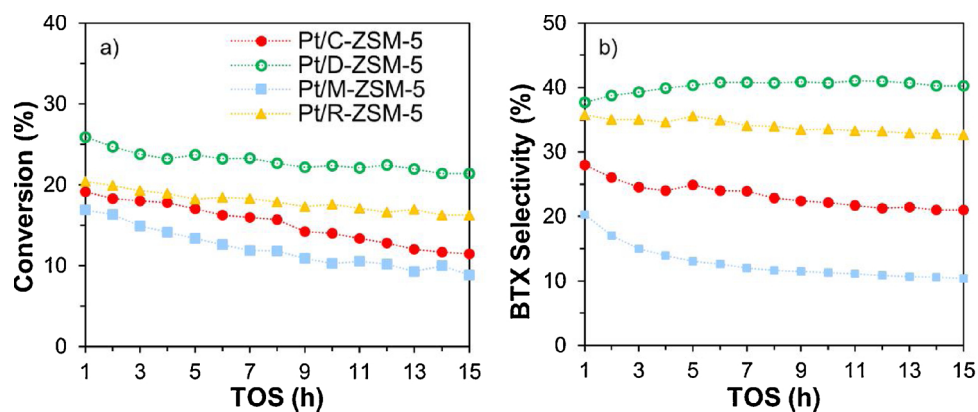
Fig. 6. Ethane conversion and BTX selectivity for different catalysts at 550 °C, 2 barg and GHSV = 0.3 h^{-1}.
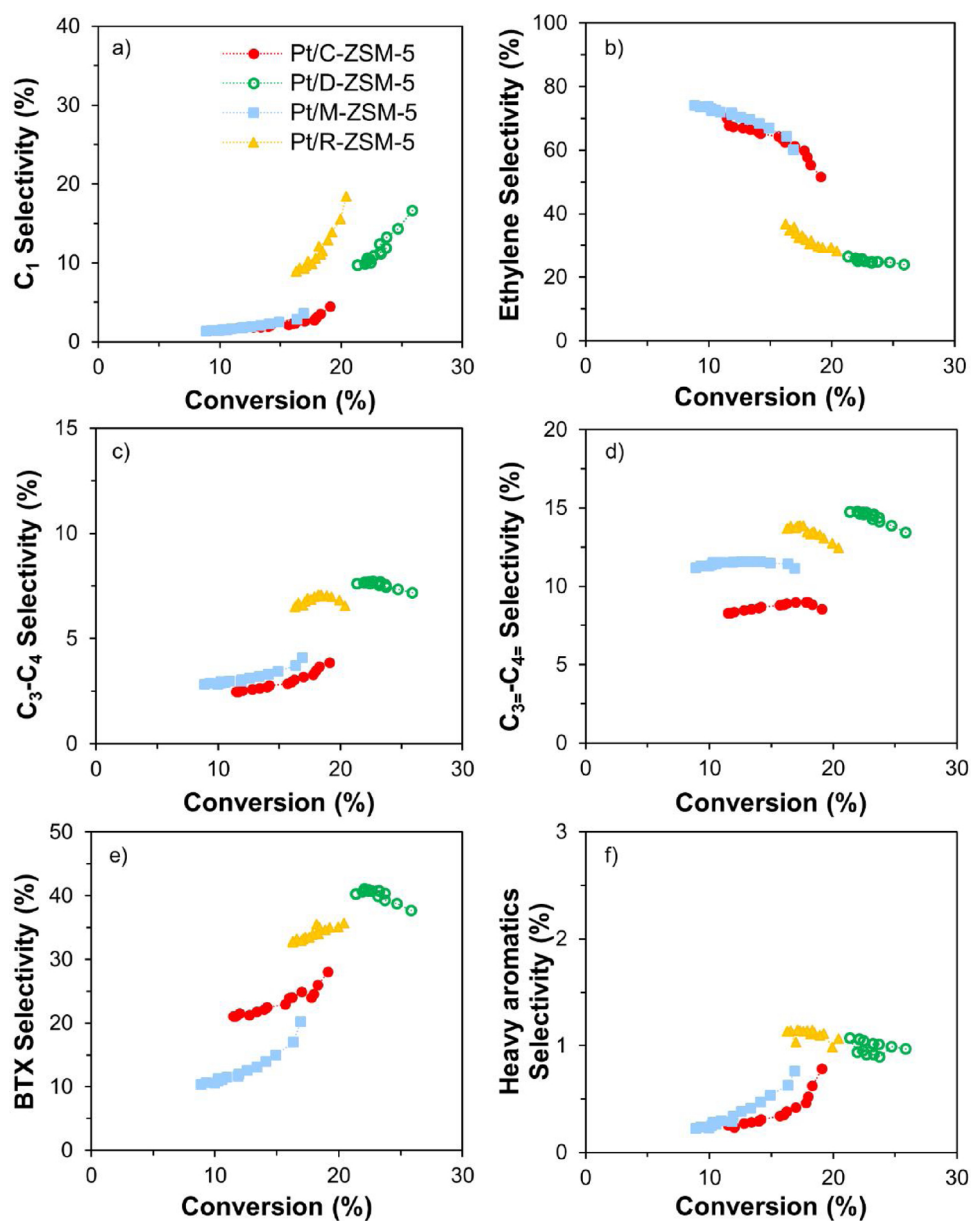

Fig. 7. Selectivity towards methane, ethylene, alkanes, olefins, BTX and heavy aromatics for the different catalysts at 550 °C, 2 barg and GHSV = 0.3 h^{-1}.
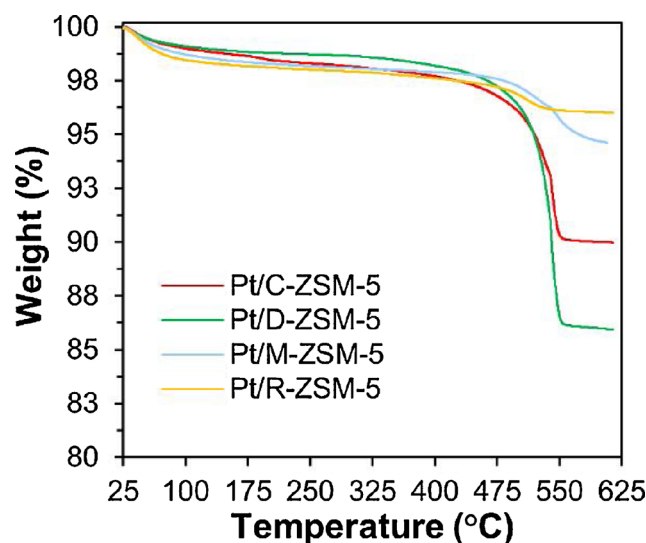
Fig. 8. TGA results of catalysts with heating ramp of 5°/min in synthetic air.

of ethane and selectivity towards BTX. The BTX selectivity of this catalyst was significantly stable because of presence of mesopores despite containing the highest amount of coke. Desilicated ZSM-5 encapsulated Pt catalyst proved to be the optimum design for the bi-functional Pt/ZSM-5 catalyst. Thus, we believe the new design of the synthesized catalyst holds promise to achieve a selective and stable catalyst for ethane dehydroaromatization.

CRediT authorship contribution statement

Farnoosh Goodarzi: Investigation, Formal analysis, Visualization, Writing - original draft. **David Benjamin Christensen:** Investigation. **Finn Joensen:** Formal analysis, Methodology, Supervision, Resources. **Søren Kegnæs:** Formal analysis, Project administration, Supervision, Resources. **Jerrik Mielby:** Formal analysis, Conceptualization, Writing - review & editing.

Acknowledgements

Appendix A. Supplementary data

Supplementary material related to this article can be found, in the online version, at doi:https://doi.org/10.1016/j.apcata.2019.117383.

References

[1] A.A. Dergachev, A.L. Lapidus, Russ. J. Gen. Chem. 79 (2009) 1244–1251, https://doi.org/10.1134/S1070363209060413.
[2] W. Reschetilowski, U. Mroczek, K.H. Steinberg, K.P. Wendlandt, Appl. Catal. 78 (1991) 257–264, https://doi.org/10.1016/0166-9834(91)80110-I.
[3] O.V. Chetina, T.V. Vasina, V.V. Lunin, Appl. Catal. A Gen. 131 (1995) 7–14, https://doi.org/10.1016/0926-860X(95)00126-3.
[4] U. Mroczek, W. Reschetilowski, K. Pietzsch, K.H. Steinberg, React. Kinet. Catal. Lett. 43 (1991) 539–544, https://doi.org/10.1007/BF02064725.
[5] U. Mroczek, F. Roessner, K.H. Steinberg, React. Kinet. Catal. Lett. 43 (1991) 559–563, https://doi.org/10.1007/BF02064728.
[6] O.P. Keipert, D. Wolf, P. Schulz, M. Baerns, Appl. Catal. A Gen. 131 (1995) 347–365, https://doi.org/10.1016/0926-860X(95)00148-4.
[7] T. Liang, H. Toghiani, Y. Xiang, Ind. Eng. Chem. Res. (2018), https://doi.org/10.1021/acs.iecr.8b03735 acs.iecr.8b03735.
[8] V.B. Kazansky, I.R. Subbotina, N. Rane, R.A. Van Santen, E.J.M. Hensen, Phys. Chem. Chem. Phys. 7 (2005) 3088–3092, https://doi.org/10.1039/b506782k.
[9] J. Glatthorn, E. Feldmann, V. Tabaku, C. Leuschner, P. Meyer, BMC Ecol. 18 (2018) 493–502, https://doi.org/10.1186/s12898-018-0203-y.
[10] L. Su, L. Liu, J. Zhuang, H. Wang, Y. Li, W. Shen, Y. Xu, X. Bao, Catal. Letters 91 (2003) 155–168, https://doi.org/10.1023/B:CATL.0000007149.48132.5a.
[11] I.I. Ivanova, E.E. Knyazeva, Chem. Soc. Rev. 42 (2013) 3671–3688, https://doi.org/10.1039/c2cs35341e.
[12] J.C. Groen, W. Zhu, S. Brouwer, S.J. Huynink, F. Kapteijn, J.A. Moulijn, J. Pérez-Ramírez, J. Am. Chem. Soc. 129 (2007) 355–360, https://doi.org/10.1021/ja065737o.
[13] M.Y. Gim, C. Song, T.H. Kim, J.H. Song, D.H. Kim, K.Y. Lee, I.K. Song, Mol. Catal. 439 (2017) 134–142, https://doi.org/10.1016/j.mcat.2017.07.001.
[14] C.J.H. Jacobsen, C. Madsen, J. Houzvicka, I. Schmidt, A. Carlsson, J. Am. Chem. Soc. 122 (2000) 7116–7117, https://doi.org/10.1021/ja000744c.
[15] H. Wang, T.J. Pinnavaia, Angew. Chemie - Int. Ed. 45 (2006) 7603–7606, https://doi.org/10.1002/anie.200602595.
[16] H. Chen, M. Yang, W. Shang, Y. Tong, B. Liu, X. Han, J. Zhang, Q. Hao, M. Sun, X. Ma, Ind. Eng. Chem. Res. 57 (2018) 10956–10966, https://doi.org/10.1021/acs.iecr.8b00849.
[17] M. Ogura, S. Shinomiya, J. Tateno, Y. Nara, M. Nomura, E. Kikuchi, M. Matsukata, Appl. Catal. A Gen. 219 (2001) 33–43, https://doi.org/10.1016/S0926-860X(01)00645-7.
[18] J.C. Groen, J.A. Moulijn, J. Pérez-Ramírez, Microporous Mesoporous Mater. 87 (2005) 153–161, https://doi.org/10.1016/j.micromeso.2005.07.050.
[19] M. Ogura, S. Shinomiya, J. Tateno, Y. Nara, E. Kikuchi, M. Matsukata, Chem. Lett. 29 (2000) 882–883, https://doi.org/10.1246/cl.2000.882.
[20] F. Goodarzi, L. Kang, F.R. Wang, F. Joensen, S. Kegnæs, J. Mielby, ChemCatChem. 10 (2018) 1566–1570, https://doi.org/10.1002/cctc.201701946.
[21] J. Mielby, J.O. Abildstrøm, F. Wang, T. Kasama, C. Weidenthaler, S. Kegnæs, Angew. Chemie - Int. Ed. 53 (2014) 12513–12516, https://doi.org/10.1002/anie.201406354.
[22] K.H. Steinberg, U. Mroczek, F. Roessner, Appl. Catal. 66 (1990) 37–44, https://doi.org/10.1016/S0166-9834(00)81625-5.
[23] Y. Xiang, H. Wang, J. Cheng, J. Matsubu, Catal. Sci. Technol. 8 (2018) 1500–1516, https://doi.org/10.1039/c7cy01878a.
[24] SilicoNert, (2019). https://silcotek.de/coating.
[25] P.L. Llewellyn, J.P. Coulomb, Y. Grillet, J. Patarin, H. Lauter, H. Reichert, J. Rouquerol, Langmuir 9 (1993) 1846–1851, https://doi.org/10.1021/la00031a036.
[26] A.H. Janssen, I. Schmidt, C.J.H. Jacobsen, A.J. Koster, K.P. de Jong, Microporous Mesoporous Mater. 65 (2003) 59–75, https://doi.org/10.1016/j.micromeso.2003.07.003.
[27] J.C. Groen, J. Pérez-Ramírez, Appl. Catal. A Gen. 268 (2004) 121–125, https://doi.org/10.1016/j.apcata.2004.03.031.
[28] Y. Xiang, H. Wang, J. Cheng, J. Matsubu, Catal. Sci. Technol. 8 (2018) 1500–1516, https://doi.org/10.1039/C7CY01878A.
[29] M.S. Scurrell, Appl. Catal. 32 (1987) 1–22, https://doi.org/10.1016/S0166-9834(00)80612-0.
[30] A. Hagen, F. Roessner, Catal. Rev. - Sci. Eng. 42 (2000) 403–437, https://doi.org/10.1081/CR-100101952.

Appendix D.3

Study of CoCu Alloy Nanoparticles Supported on MOF-Derived Carbon for Hydrosilylation of Ketones

David B. Christensen[1] · Rasmus L. Mortensen[1] · Søren Kramer[1] · Søren Kegnæs[1]

Abstract

Carbonized zeolitic imidazolate frameworks (ZIFs) show potential as mesoporous heterogeneous catalysts with high metal loadings. ZIF-67 and ZIF-8 were used to create mono- and bimetallic CoCu particles supported on nitrogen-doped carbon via self-assembly in methanol at room temperature, followed by carbonization at 675 °C. A Cu precursor, $Cu(NO_3)_2 \cdot 2H_2O$, was impregnated into the ZIF-67 before carbonization to obtain bimetallic catalysts. Nanoalloy particles with different CoCu ratio were synthesized and characterized using XRD. The materials were further characterized using TEM, SEM, XRF and nitrogen physisorption. The different alloys were tested in conversion of cyclohexanone to the corresponding silyl ether. Complete conversion of cyclohexanone at 90 °C for 24 h were obtained. The catalyst $Co_{99}Cu_1$@NC gave a 60% increase in yield over a pure Co analogue.
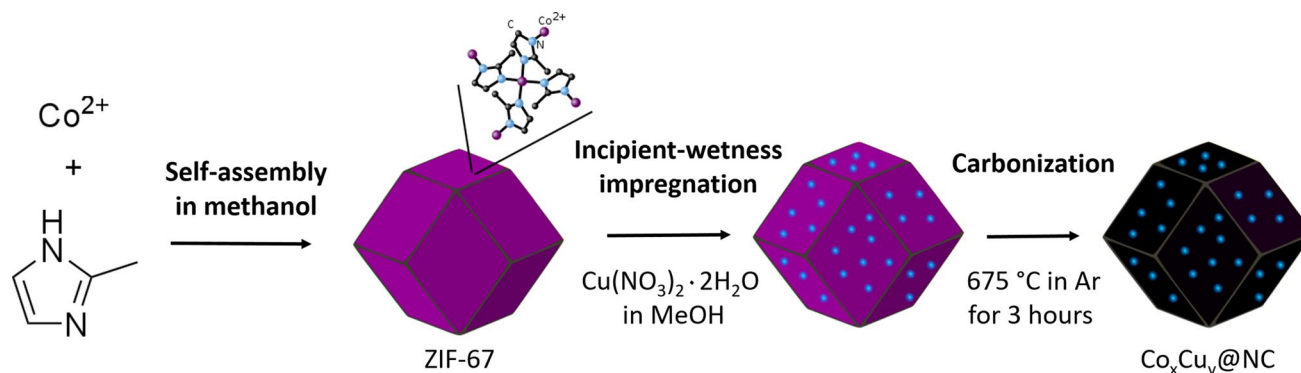
Keywords Hydrosilylation · MOF · ZIF-67 · Carbonization · Bimetallic alloy

Graphic Abstract

✉ Søren Kegnæs
skk@kemi.dtu.dk

1 Department of Chemistry, Technical University of Denmark, Kemitorvet 207, 2800 Kgs. Lyngby, Denmark

1 Introduction

The synthesis of new heterogeneous catalysts containing earth-abundant metals offers a way to create cheaper, more sustainable alternatives to more traditional catalysts containing precious metals like Pd, Pt or Ru [1–5]. One of the challenges of using earth-abundant metals is that they usually have much lower activities compared to their precious metal counterparts. This can often be circumvented by creating base metal nanoalloys [6–11]. According to Sabatier's Principle, there is an optimal adsorption energy between the reactant and the active site. This is usually illustrated in

the form of a volcano plot [12, 13]. An alloy will have an adsorption energy somewhere in between its components. Using this principle, alloys may achieve properties similar or sometimes superior to those of pure precious metals [8, 14–16]. However, it can be challenging to synthesize the desired alloyed nanoparticles in the right ratio and uniform distributed in the catalyst.

Metal–organic frameworks (MOFs) have attracted a lot of attention recently, due to the ease of synthesis, high porosity and surface area [17, 18]. MOFs are easily made by mixing a metal salt with an organic linker in an appropriate solvent. Recently, there has been interest in the use of MOF derivatives as the structural template for making a new class of heterogeneous catalysts [19–21]. MOF derived carbon materials have been known at least since 2007, where MOF-5 was pyrolysed with polymerized furfuryl alcohol to make a nanoporous carbon with good hydrogen uptake and electrochemical properties [22]. Since then, different types of MOF-derived nanomaterials have been tested for use in sensing, gas-/energy-storage and catalysis with good performance [23, 24]. One method is to carbonize the MOF, creating a carbonaceous support material. Due to the high structural stability of the original MOF, much of the structure, pore volume and specific surface area is preserved after carbonization [25–27]. The material gains increased thermal and chemical stability, but loses the functionalities of the ligands [28–30]. The carbonization process also help with the reduction of the metal ions present in the ZIF structure to form metal nanoparticles. MOF-derived carbons have been tested for several purposes such as oxygen reduction reaction, Li-ion batteries, gas storage and as a support material for heterogeneous catalysts [31–33].

Zeolitic imidazolate framework (ZIF) materials are a group of MOFs with attractive properties, due to their structural similarities to zeolites [34, 35]. A great number of ZIF structures have been reported over the last decade, mimicking both known zeolite structures and added new topologies [21, 35, 36]. Synthesis of ZIF with more than one metal and with different metal ratios can be difficult and time-consuming. By using incipient-wetness impregnating on the porous ZIF with a secondary metal precursor before carbonization, bimetallic alloy nanoparticles are expected to be formed inside the new carbon support. Previously a 50/50 CoNi alloy has been synthesized using a similar procedure [37]. Data from XRD indicated the formation of uniform alloy nanoparticles between Co and Ni in the carbonized ZIF-67.

Herein we present a simple way to synthesize cobalt–copper nanoalloys on nitrogen-doped carbon in a variety of loadings using ZIF-67 as a carbon-, cobalt-, nitrogen-containing platform. Cobalt containing ZIF-67 was impregnated with a different Cu solution before carbonization. In total were seven different catalysts synthesized with different amounts of cobalt and copper. The synthesized materials were characterized using XRD, TEM, SEM, XRF and nitrogen physisorption. The catalytic activities of the produced materials were compared using a model reaction, conversion of cyclohexanone to the corresponding silyl ether. The reaction is typically run using a homogenous precious metal catalyst [38–40].

The synthesis method benefits from the presence of nitrogen in the 2-methylimidazole in the ZIF, creating a natural nitrogen-doping of the resulting carbon. Nitrogen-doping of carbon is a common way of tuning the electronic properties of carbon materials, often utilized in the development of electro-catalysts for fuel cells and other electronic devices [41]. However, the positive effect of nitrogen-doping is not limited to electrochemical reactions as number of other reactions have seen increased yield due to the presence of nitrogen [42–46].

2 Experimental Section

A total of seven types of catalysts were synthesized with expected Co/Cu ratios of 99:1, 19:1, 9:1, 3:1, 1:1 as well as a pure Co and pure Cu variant. The samples are labelled as $Co_xCu_y@NC$, were x and y indicate the expected amount of Co compared to Cu and NC = nitrogen-doped carbon. According to the empirical formula, $C_8H_{10}N_4Co$, the ZIF-67 is expected to contain 26.7 wt% Co before carbonization, which serves as the basis for the calculating the amount of Cu needed. The basic procedure for ZIF-67 has been used in previous work [37].

2.1 Materials

All chemicals were obtained from Sigma-Aldrich with no further purification. 2-methylimidazole, cobalt nitrate hexahydrate ($Co(NO_3)_2 \cdot 6H_2O > 98\%$), methanol ($MeOH \geq 99\%$), zinc nitrate hexahydrate ($Zn(NO_3)_2 \cdot 6H_2O \geq 99\%$), copper(II) nitrate hemi(pentahydrate) ($Cu(NO_3)_2 \cdot 2.5H_2O$), cyclohexanone, dimethylphenylsilane ($HSiMe_2Ph \geq 98\%$), toluene, dibenzylether, ethylacetate, D-chloroform ($CDCl_3$ 99.8 atom % D), triethylsilane ($HSi(C_2H_5)_3$ 99%).

2.2 Synthesis of ZIF-67 and ZIF-8

ZIF-67 was synthesized according to previous work by Lou et al. [47]. In a 1L Erlenmeyer flask a solution of 2-methylimidazole in MeOH (3.2840 g in 250 mL) and a solution of $Co(NO_3)_2 \cdot 6\ H_2O$ in MeOH (2.9104 g in 250 mL) were mixed at room temperature. The mixture was stirred for 5 min, aged for 24 h. The cobalt containing ZIF-67 was collected by centrifugation and dried in an oven at 80 °C. The typical yield was 0.5 g.

ZIF-8 was synthesized using the same metal to ligand ratio. A solution of 2-methylimidazole in MeOH (3.2840 g in 250 mL) and a solution of $Zn(NO_3)_2 \cdot 6H_2O$ (2.9748 g in 250 mL) were mixed at room temperature. The mixture was stirred for 5 min, aged for 24 h. The zinc containing ZIF-8 was collected by centrifugation and dried in an oven at 80 °C. The typical yield was 0.8 g.

2.3 Synthesis of $Co_xCu_Y@NC$

Different amounts of $Cu(NO_3)_2 \cdot 2.5H_2O$ were dissolved in 85 µL MeOH. Dried ZIF-67 was impregnated to incipient-wetness to make each of the desired Co/Cu ratios. The resulting powders were flushed at room temperature using Ar for 30 min. followed by carbonization at 675 °C heated at a rate of 5 °C/min. in Ar for 3 h.

2.4 Synthesis of Cu@NC

As a reference material Cu@NC was synthesized. A solution of $Cu(NO_3)_2 \cdot 2.5H_2O$ in MeOH (45.4 mg in 340 µL) was prepared. 170 µL of the solution was used for incipient wetness impregnation of the dried ZIF-8. The resulting powder was followed by flushing in Ar for 30 min. at room temperature. The impregnated powder was then carbonized at 900 °C heated at rate 5 °C/min. for 3 h. The increased temperature is required in order to remove the Zn in the ZIF-8 and incorporate Cu in the structure.

2.5 Material Characterization

XRF data was acquired using a PanAnalytical epsilon 3-XL directly on the powdered catalyts without any prior treatment. TEM images was acquired on a FEI Tecnai T20 G2 instrument from Thermo Fisher Scientific. Powdered samples were placed on holey carbon grids with no prior treatment. SEM was carried out on a FEI Quanta 200 ESEM FEG on powdered samples placed on carbon grids. XRD was acquired using Cu-Kα from a focusing quartz monochromator and a Huber G670 Guinier camera. The samples were loose powders and run for one hour.

2.6 Catalytic Measurements

The catalytic performances of the catalysts were compared using the hydrosilylation reaction of cyclohexanone. The experiments used solutions of 1 mmol cyclohexanone/mL and 1.2 $HSiMe_2Ph$/mL in toluene prepared in glovebox together with 10 mg $Co_xCu_y@NC$ catalyst. The vials were sealed with teflon caps and allowed to react outside the glovebox at 90 °C, stirred at a rate of 600 RPM. The products were quantified by NMR. ^{1}H-NMR data was acquired on a Bruker Ascend 400 (400 Hz).

3 Results and Discussion

Each of the seven $Co_xCu_y@NC$ catalysts synthesized were characterized using a number of different techniques along with the original ZIF-67 material for comparison.

In order to form the cobalt–copper alloyed particles on nitrogen-doped carbon, the ZIF-67 impregnated with Cu precursor was carbonized in Ar at high temperature.
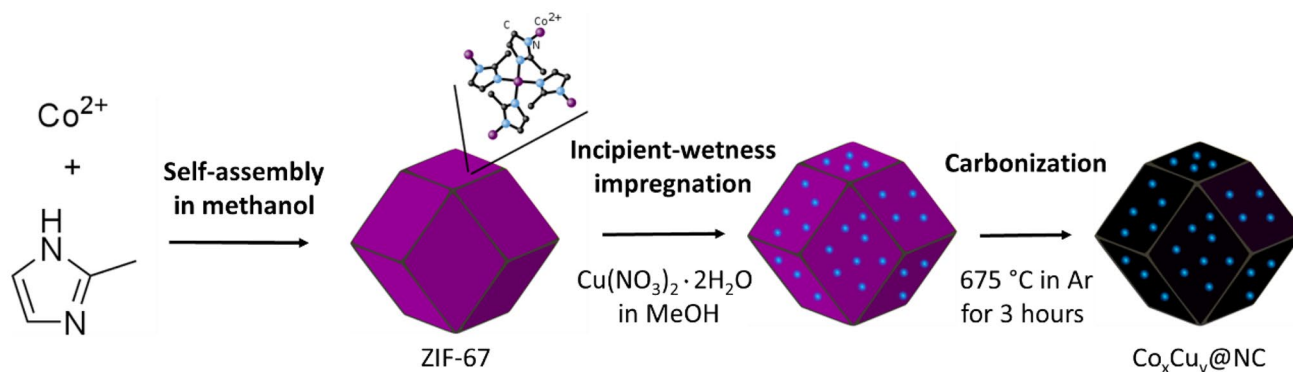
Fig. 1 Schematic representation of a typical synthesis of Cu-doped carbonized ZIF-67
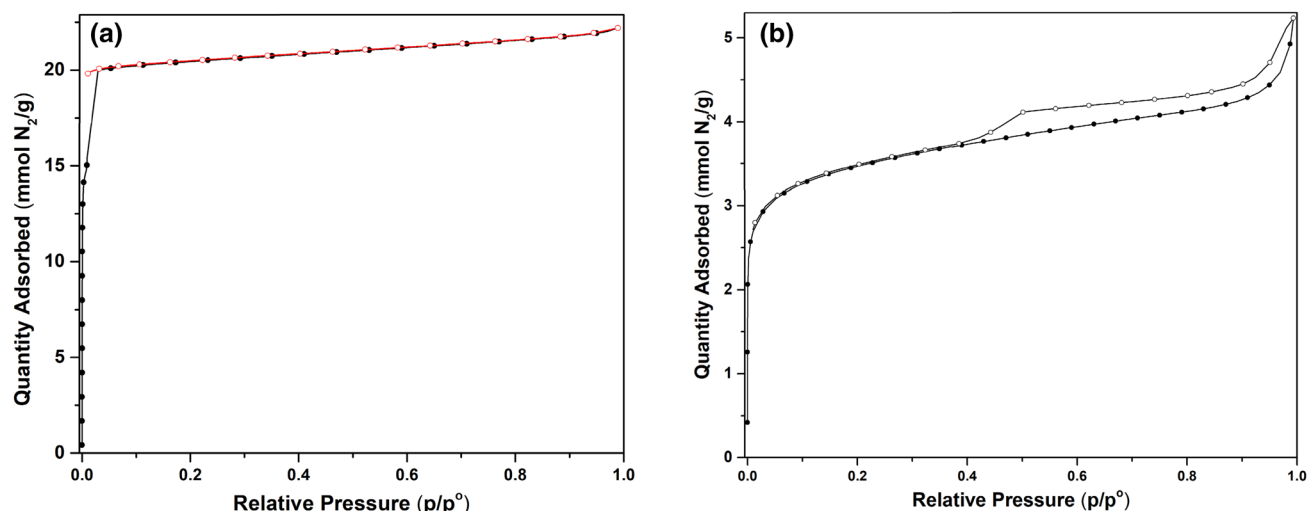
Fig. 2 N_2-physisorption isotherm of synthesized ZIF-67 (**a**) and Co_9Cu_1@NC-675 (**b**)

The decomposition during carbonization was investigated using TGA (see Supporting Information, S1). ZIF-67 starts to decompose at around 480 °C and has lost about 40% of its total mass at 600 °C. Based on ICP-OES the content of pure ZIF-67 is about 26 wt% as is expected from it empirical formular ($C_8H_{10}N_4Co$). After carbonization at 600 °C, the Co content increases to about 30 wt% (see Supporting Info, S2) (Fig. 1).

Nitrogen physisorption of the synthesized ZIF-67 and the derived carbon material is shown in Fig. 2. ZIF-67 originally had a typical type I isotherm indicating a microporous material. After impregnation with 10% copper and subsequent carbonization, the isotherm becomes a type II with a clear hysteresis loop indicative of mesopores in the structure.

ZIF-67 shows a high surface area of 1364 m^2/g (BET), and a pore volume of 0.762 cm^3/g (Single Point Adsorption) similar to what has been reported in other work [19, 48]. After impregnation and carbonization, the surface area and total pore volume drops significantly. Co_9Cu_1@NC-675 had a BET surface area of 244 m^2/g and a total pore volume of 0.079 cm^3/g. BJH adsorption and comparison of isotherms at different copper loadings can be found in Supporting Information S3–S5.

The change in structure from ZIF-67 to porous carbon support is apparent in SEM. In Fig. 3 it is clear that the polyhedral shape of the original ZIF-67 is distorted after
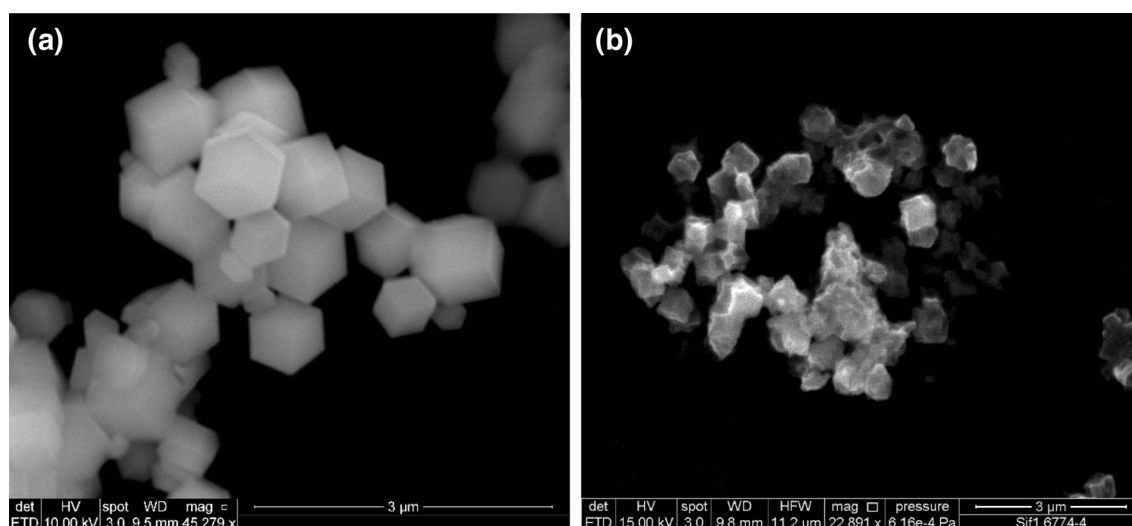
Fig. 3 SEM images showing the polyhedral shape of the catalysts, which clearly seen for ZIF-67 (**a**), however it has been somewhat distorted after carbonization at 675 °C as seen for Co_9Cu_1@NC (**b**)
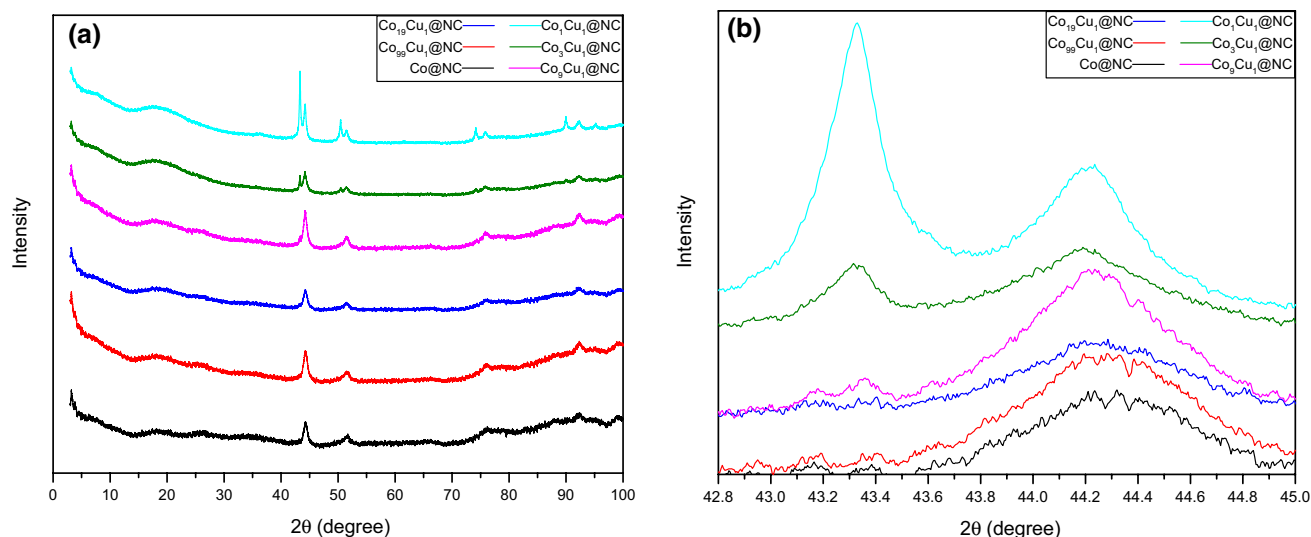
Fig. 4 XRD pattern of synthesized nitrogen-doped carbon catalyst. **a** Shows the full range of angles measured, showing none of the many characteristic peaks of ZIF-67 between 5 and 40°. **b** Features a zoom-in on the Co(111) and Cu(111) peaks. The Co(111) is clearly seen shifting downward at higher Cu loadings

Table 1 CoCu ratios determined using XRF

Entry	Catalyst	Cu(NO₃)₂·2.5H₂O added/100 mg ZIF-67	Cu/Co ratio
1	Co@NC	–	–
2	$Co_{99}Cu_1$@NC	1.05 mg	1/65.67
3	$Co_{19}Cu_1$@NC	5.55 mg	1/15.67
4	Co_9Cu_1@NC	11.7 mg	1/7.93
5	Co_3Cu_1@NC	35.1 mg	1/2.62
6	Co_1Cu_1@NC	105.2 mg	1/0.90
7	Cu@NC	–	–

impregnation with Cu and subsequent carbonization. The overall particle size seems reduced from the original 1 µm to about 700 nm.

XRD was performed to confirm the formation of CoCu alloyed particles. Each of the catalysts (Fig. 4) show characteristic peaks of Co at 44.32, 51.70, 75.8 and 92.1°. At higher loadings of Cu, its (111) peak becomes visible at 43.31°, along with additional peaks at 50.4, 74.1, 89.9 and 95.2°. The Co (111) peak at 44.32° shifts towards a lower diffraction angle of 44.20°, when the metal content is above 25% Cu. None of the typical peaks associated with ZIF-67 between 5 and 40° can be seen here [42, 49]. The peaks were identified using data from the ICDD. According to Vegard's Law, the location of the alloy peak can be linearly related to its composition. Based on the Co

(111) peak, the particles were estimated to contain roughly 10% Cu. The Cu (111) peak is not notably shifted from the location of pure copper, indicating the presence of pure copper particles. Even with an equal amount of Co and Cu, the nanoparticles seemingly consist of CoCu particles containing 10% Cu and a larger amount of separate almost pure Cu nanoparticles.

Characterization using XRF was used to confirm the CoCu ratio of the synthesized catalyst (see Table 1). The results show good control over CoCu ratio using simple incipient wetness impregnation. In general the amount of Co is lower than expected. This may be due to a slightly lower content of Co in the parent ZIF-67 material. The nitrogen species present in the structure were examined using XPS (see Supporting Info, S4 and S5). The nitrogen content in the surface was found to be about 4% for the carbonized ZIF (Entry 1), while the materials containing added copper (Entry 2–6) had an increased content ranging from 7.8 to 11%. The nitrogen peaks indicated equal amounts of graphitic and pyradinic nitrogen with the exception of Entry 1, which also showed a fair amount of pyrrolic nitrogen (31.9%) and less graphitic nitrogen (12.5%).

TEM images of the carbonized ZIFs show that the dodecahedral shape of ZIF-67 is retained after carbonization (Fig. 5). This matches what has previously been reported by Zou et al. [50] The size of the dodecahedra's range from 0.6 to 1.4 µm, seemingly increasing in size with higher loadings of Cu. The metal nanoparticles are clearly seen distributed

across the carbon support. The size of the metal nanoparticles mainly range from 8 to 20 nm.

TEM also shows the influence of the higher Cu loading on the overall structure of the carbon matrix. The dodecahedral structure seemingly increases in size with higher loadings of Cu. As the amount of added Cu increases, the carbon structure loses much of its dodecahedral structure as can be seen from Co_3Cu_1@NC and Co_1Cu_1@NC. STEM–EDS shows how the large particles generated when doping with more Cu are mostly pure Cu particles, while at lower loadings a good dispersion of both Cu and Co is seen (see Supporting Info, S13-14).

3.1 Hydrosilylation of Cyclohexanone

In order to compare the activities of the synthesized Co_xCu_y@NC catalysts, the hydrosilylation of Cyclohexanone (1a) was chosen as a model reaction. The same amount of catalyst was used for each of the reactions. The results from the hydrosilylation of cyclohexanone (1a) can be seen in Table 2. Using the carbon catalyst derived directly from ZIF-67 (Entry 1) yields 21% of the silyl ether product under the given conditions. The purely copper containing Cu@NC derived from ZIF-8 (Entry 7) affords a much lower yield of only 9%. Similar, low yields where observed for commercial Cu and Pt on carbon (Supporting Info S17). A clear improvement in reactivity is seen when the two are combined to form CoCu alloy nanoparticles. Even $Co_{99}Cu_1$@NC shows an increase in yield from 21 to 35% compared to Co@NC. When using much higher Cu loadings like those found

Fig. 5 TEM images of all ZIF-67 derived catalysts. As more Cu is added, the polyhedral structure starts to break down. **a** Co@NC, **b** $Co_{99}Cu_1$@NC **c** $Co_{19}Cu_1$@NC **d** Co_9Cu_1@NC **e** Co_3Cu_1@NC **f** Co_1Cu_1@NC. (Cu@NC can be found in Supporting Info S10–S12 along with histograms and additional images of all catalysts)

Table 2 Experimental results from hydrosilylation of cyclohexanone

Entry	Catalyst	Yield (%)	Conversion (%)
1	Co@NC	21	38
2	$Co_{99}Cu_1$@NC	35	41
3	$Co_{19}Cu_1$@NC	38	45
4	Co_9Cu_1@NC	72	72
5	Co_3Cu_1@NC	100	100
6	Co_1Cu_1@NC	100	100
7	Cu@NC	9	29

Yield based on NMR

Fig. 6 Time study of Co_9Cu_1@NC for the hydrosilylation of cyclohexanone

brought the yield down to a few percent (1b). Acetophenone readily reactants to form the silyl ether. Induction effects affects the yield as demonstrated by the addition of different groups in the para position. A methyl group brings the silyl ether yield down to 75% (1d). The combination of a longer alkyl chain on the ketone and an ether group in the para position lowers the yield down to 57% (1e). The introduction of electron withdrawing group, fluorine, brings the yield down to 46% (1f). Additionally, when a large bulky group was added at the end of the alkyl, the yield was lower than for any of the other acetophenones (1g). TEM of the Co_9Cu_1@NC after reaction show no notable differences to the fresh catalyst (Supporting Info, S15-16). The catalyst show partly deactivation when reused first time. However, the deactivation seemed to stabilise when reused further times (Supporting S18).

in Co_3Cu_1@NC and Co_1Cu_1@NC complete conversion is achieved.

Co_9Cu_1@NC was selected for a time study (Fig. 6) and scope for a range of hydrosilylation reactions (Table 3). The time study shows the reaction occurs with no induction period and fits with an overall 1st order reaction (Fig. 7). Cyclohexanone (1a) gave good yields under these conditions. However, the addition of a t-butyl group

4 Conclusion

MOF derived carbon materials combine the advantages of a stable porous materials with a high metal loading. The present work shows that using simple preparation methods, bimetallic CoCu alloy nanoparticles incorporated in mesoporous carbon can be synthesized with good control of the metallic ratio. The nanoparticles are well-distributed with an average size of about 10 nm. The Co_xCu_y@NC675 catalysts show high yield for a simple hydrosilylation reaction compared to catalysts containing only Co or Cu. Under relatively mild conditions, complete conversion of cyclohexanone to the silane when the CuCo ratio is 1/2.62 or above.

Table 3 Experimental results from substrate scope of hydrosilylation using Co_9Cu_1@NC

Yield based on NMR

Fig. 7 Linear fit of time study indicating an overall 1st order reaction hydrosilylation of cyclohexanone

Compliance with Ethical Standards

Conflict of interest The authors declare that they have no conflict of interest.

References

1. Roundtable NRC (US) CS (2012) The role of the chemical sciences in finding alternatives to critical resources. National Academies Press, Washington, DC
2. Wang D, Astruc D (2017) The recent development of efficient Earth-abundant transition-metal nanocatalysts. Chem Soc Rev 46(3):816–854
3. Armbrüster M, Kovnir K, Friedrich M, Teschner D, Wowsnick G, Hahne M et al (2012) $Al_{13}Fe_4$ as a low-cost alternative for palladium in heterogeneous hydrogenation. Nat Mater 11(8):690–693
4. Fihri A, Bouhrara M, Nekoueishahraki B, Basset JM, Polshettiwar V (2011) Nanocatalysts for Suzuki cross-coupling reactions. Chem Soc Rev 40(10):5181–5203
5. Gorbanev YY, Kegnæs S, Hanning CW, Hansen TW, Riisager A (2012) Acetic acid formation by selective aerobic oxidation of aqueous ethanol over heterogeneous ruthenium catalysts. ACS Catal 2(4):604–612
6. Tan Y, Wang H, Liu P, Shen Y, Cheng C, Hirata A et al (2016) Versatile nanoporous bimetallic phosphides towards electrochemical water splitting. Energy Environ Sci 9(7):2257–2261
7. Yan Y, Du JS, Gilroy KD, Yang D, Xia Y, Zhang H (2017) Intermetallic nanocrystals: syntheses and catalytic applications. Adv Mater. https://arxiv.org/abs/1702.08137
8. Pye DR, Mankad NP (2017) Bimetallic catalysis for C-C and C-X coupling reactions. Chem Sci 8(3):1705–1718
9. Jellinek J (2008) Nanoalloys: tuning properties and characteristics through size and composition. Faraday Discuss 138:11–35
10. Rovik AK, Klitgaard SK, Dahl S, Christensen CH, Chorkendorff I (2009) Effect of alloying on carbon formation during ethane dehydrogenation. Appl Catal A 358(2):269–278
11. Kramer S, Mielby J, Buss K, Kasama T, Kegnæs S (2017) Nitrogen-doped carbon-encapsulated nickel/cobalt nanoparticle catalysts for Olefin migration in allylarenes. ChemCatChem 9(15):2930–2934
12. Deutschmann O, Knözinger H, Kochloefl K, Turek T (2005) Heterogeneous catalysis and solid catalysts. Ullmann's encyclopedia of industrial chemistry. Wiley, Hoboken, pp 7–14
13. Balandin AA (1969) Modern state of the multiplet theory of heterogeneous catalysis. Adv Catal Rel Subj 19:1–210
14. Calle-Vallejo F, Tymoczko J, Colic V, Huy Vu Q, Pohl M, Morgenstern K et al (2015) Finding optimal surface sites on heterogeneous catalysts by counting nearest neighbors. Science (80-) 350(6257):185–190
15. Studt F, Abild-Pedersen F, Wu Q, Jensen AD, Temel B, Grunwaldt JD et al (2012) CO hydrogenation to methanol on Cu-Ni catalysts: theory and experiment. J Catal 293:51–60. https://doi.org/10.1016/j.jcat.2012.06.004
16. Shi J (2013) On the synergetic catalytic effect in heterogeneous nanocomposite catalysis. Chem Rev 113:2139–2181
17. Manna K, Ji P, Lin Z, Greene FX, Urban A, Thacker NC et al (2016) Chemoselective single-site Earth-abundant metal catalysts at metal-organic framework nodes. Nat Commun 7:1–11. https://doi.org/10.1038/ncomms12610
18. Howarth AJ, Liu Y, Li P, Li Z, Wang TC, Hupp JT et al (2016) Chemical, thermal and mechanical stabilities of metal-organic frameworks. Nat Rev Mater 1(15018):1–15
19. Zhong G, Liu D, Zhang J (2018) The application of ZIF-67 and its derivatives: Adsorption, separation, electrochemistry and catalysts. J Mater Chem A 6(5):1887–1899
20. Park KS, Jin SA, Lee KH, Lee J, Song I, Lee BS et al (2016) Characterization of zeolitic imidazolate framework-derived polyhedral carbonaceous material and its application to electrocatalyst for oxygen reduction reaction. Int J Electrochem Sci 11(11):9295–9306
21. Chen B, Yang Z, Zhu Y, Xia Y (2014) Zeolitic imidazolate framework materials: recent progress in synthesis and applications. J Mater Chem A 2(40):16811–16831
22. Liu B, Shioyama H, Akita T, Xu Q (2008) Metal-organic framework as a template for porous carbon synthesis. J Am Chem Soc 130(16):5390–5391
23. Dang S, Zhu Q-L, Xu Q (2018) Nanomaterials derived from metal–organic frameworks. Nat Rev Mater 3(1):17075. https://www.nature.com/articles/natrevmats201775
24. Liang Z, Zhao R, Qiu T, Zou R, Xu Q (2019) Metal organic framework derived materials for electrochemical energy applications. EnergyChem 1(1):1–32
25. Li W, Zhang A, Jiang X, Chen C, Liu Z, Song C et al (2017) Low temperature CO_2 methanation: ZIF-67-derived Co-based porous carbon catalysts with controlled crystal morphology and size. ACS Sustain Chem Eng 5(9):7824–7831
26. Gadipelli S, Guo ZX (2015) Tuning of ZIF-derived carbon with high activity, nitrogen functionality, and yield—a case for superior CO_2 capture. Chemsuschem 8(12):2123–2132
27. Zacho SL, Gajdek D, Mielby J, Kegnæs S (2019) Synthesis of nano-engineered catalysts consisting of Co_3O_4 nanoparticles confined in porous SiO_2. Top Catal. https://doi.org/10.1007/s11244-019-01134-9
28. Liu B, Shioyama H, Jiang H, Zhang X, Xu Q (2010) Metal-organic framework (MOF) as a template for syntheses of nanoporous carbons as electrode materials for supercapacitor.

Carbon NY 48(2):456–463. https://doi.org/10.1016/j.carbon.2009.09.061

29. Zacho SL, Mielby J, Kegnæs S (2018) Hydrolytic dehydrogenation of ammonia borane over ZIF-67 derived Co nanoparticle catalysts. Catal Sci Technol 8(18):4741–4746

30. Torad NL, Hu M, Kamachi Y, Takai K, Imura M, Naito M et al (2013) Facile synthesis of nanoporous carbons with controlled particle sizes by direct carbonization of monodispersed ZIF-8 crystals. Chem Commun 49(25):2521–2523

31. Shi X, Song H, Li A, Chen X, Zhou J, Ma Z (2017) Sn-Co nanoalloys embedded in porous N-doped carbon microboxes as a stable anode material for lithium-ion batteries. J Mater Chem A 5(12):5873–5879. https://doi.org/10.1039/C7TA00099E

32. Zhou YX, Chen YZ, Cao L, Lu J, Jiang HL (2015) Conversion of a metal-organic framework to N-doped porous carbon incorporating Co and CoO nanoparticles: direct oxidation of alcohols to esters. Chem Commun 51(39):8292–8295

33. Jiang H-L, Liu B, Lan Y-Q, Kuratani K, Akita T, Shioyama H et al (2011) From metal-organic framework to nanoporous carbon: toward a very high surface area and hydrogen uptake. J Am Chem Soc 133(31):11854–11857

34. Li PZ, Aranishi K, Xu Q (2012) ZIF-8 immobilized nickel nanoparticles: highly effective catalysts for hydrogen generation from hydrolysis of ammonia borane. Chem Commun 48(26):3173–3175

35. Phan A, Doonan CJ, Uribe-Romo FJ, Knobler CB, O'Keeffe M, Yaghi OM (2010) Synthesis, structure, and carbon dioxide capture properties of zeolitic imidazolate frameworks. Acc Chem Res 43(1):58–67

36. Pimentel BR, Parulkar A, Zhou EK, Brunelli NA, Lively RP (2014) Zeolitic imidazolate frameworks: next-generation materials for energy-efficient gas separations. Chemsuschem 7(12):3202–3240

37. Bennedsen NR, Kramer S, Mielby JJ, Kegnæs S (2018) Cobalt-nickel alloy catalysts for hydrosilylation of ketones synthesized by utilizing metal-organic framework as template. Catal Sci Technol 8(9):2434–2440

38. Marciniec B, Maciejewski H, Pietraszuk C, Pawluc P (2013) Hydrosilylation—a comprehensive review on recent advances. Springer, New York

39. Ojima I, Nagai Y (1974) Asymmetric reduction of ketones via hydrosilylation catalyzed by a Rhodium(I) complex with chiral phosphine ligands. Ii. on the mechanism of the induction of asymmetry. Chem Lett 3(3):223–228. https://www.journal.csj.jp/doi/10.1246/cl.1974.223

40. Lewis LN, Stein J, Gao Y, Colborn RE, Hutchins G (1997) Platinum catalysts used in the silicone industry. Platin Matals Rev 41(2):66–75

41. Wang W, Dang J, Zhao X, Nagase S (2016) Formation mechanisms of graphitic-N: oxygen reduction and nitrogen doping of graphene oxides

42. Yusran Y, Xu D, Fang Q, Zhang D, Qiu S (2017) MOF-derived Co@N-C nanocatalyst for catalytic reduction of 4-nitrophenol to 4-aminophenol. Microporous Mesoporous Mater. 241:346–354. https://doi.org/10.1016/j.micromeso.2016.12.029

43. Wang G, Cao Z, Gu D, Pfänder N, Swertz A (2016) Nitrogen-doped ordered mesoporous carbon supported bimetallic PtCo nanoparticles for upgrading of biophenolics. Angew Chemie - Int Ed. 55(31):8850–8855

44. Wang Y, Wang C, Wang Y, Liu H, Huang Z (2016) Superior sodium-ion storage performance of Co_3O_4@nitrogen-doped carbon: derived from a metal-organic framework. J Mater Chem A 4(15):5428–5435. https://doi.org/10.1039/C6TA00236F

45. Zacharska M, Podyacheva OY, Kibis LS, Boronin AI, Senkovskiy BV, Gerasimov EY et al (2015) Ruthenium clusters on carbon nanofibers for formic acid decomposition: effect of doping the support with nitrogen. ChemCatChem 7(18):2910–2917

46. Kramer S, Hejjo F, Rasmussen KH, Kegnæs S (2018) Silylative pinacol coupling catalyzed by nitrogen-doped carbon-encapsulated nickel/cobalt nanoparticles: evidence for a silyl radical pathway. ACS Catal 8(2):754–759

47. Hu H, Guan B, Xia B, Lou XW (2015) Designed formation of Co_3O_4/$NiCo_2O_4$ double-shelled nanocages with enhanced pseudocapacitive and electrocatalytic properties. J Am Chem Soc 137(16):5590–5595

48. Yang H, He XW, Wang F, Kang Y, Zhang J (2012) Doping copper into ZIF-67 for enhancing gas uptake capacity and visible-light-driven photocatalytic degradation of organic dye. J Mater Chem 22(41):21849–21851

49. Qian J, Sun F, Qin L (2012) Hydrothermal synthesis of zeolitic imidazolate framework-67 (ZIF-67) nanocrystals. Mater Lett 82:220–223. https://doi.org/10.1016/j.matlet.2012.05.077

50. Xia W, Zhu J, Guo W, An L, Xia D, Zou R (2014) Well-defined carbon polyhedrons prepared from nano metal-organic frameworks for oxygen reduction. J Mater Chem A 2(30):11606–11613

COMMUNICATION

Selective formic acid dehydrogenation at low temperature over a RuO₂/COF pre-catalyst synthesized on the gram scale†

Liliana P. L. Gonçalves, [iD] [ab] David B. Christensen,[c] Maria Meledina,[de]
Laura M. Salonen, [iD] [a] Dmitri Y. Petrovykh, [iD] [a] Enrique Carbó-Argibay,[a]
Juliana P. S. Sousa,[a] O. Salomé G. P. Soares,[b] M. Fernando R. Pereira, [iD] [b]
Søren Kegnæs [iD] *[c] and Yury V. Kolen'ko [iD] *[a]

A pre-catalyst, consisting of RuO₂ nanoparticles and clusters anchored on TpBD-Me₂ COF, was synthesized. During catalytic formic acid dehydrogenation, RuO₂ undergoes *in situ* reduction to metallic Ru, forming an active and selective catalyst, which outperforms the commercial **Ru–C** catalyst. The chemical structure of the COF supporting material is maintained during stability testing.

Formic acid (FA) is an important chemical that is used, for example, in silage and animal feed, leather and tanning industries, and pharmaceutical and food industries. More interestingly, FA can be used as a fuel for direct FA fuel cells (DFAFCs), which generate electrical energy. Alternatively, FA can be used as a H₂ carrier *via* dehydrogenation to CO₂ and H₂, with the resultant H₂ used as a fuel for hydrogen fuel cells.[1,2]

Compared to other H₂ carriers, FA possesses high gravimetric and volumetric capacity (4.4 wt% and 53.4 g L⁻¹), and is liquid under ambient conditions, which makes it a promising practical H₂ carrier. Furthermore, FA can be produced directly from biomass or CO₂, which allows a carbon-neutral cycle for the production and storage of renewable hydrogen.[1,2] In addition, FA could be used as a sustainable carbon monoxide source.[3]

Depending on the catalyst and the reaction conditions, the decomposition of FA can produce H₂ and CO₂ through dehydrogenation, or the alternative production of CO can occur.[2] Therefore, the selectivity of the catalyst is crucial in order to obtain the delivered product. Homogeneous and heterogeneous catalysts have been proposed both in the liquid[4–6] and gas[7–15] phase for FA dehydrogenation. Most of the catalysts, however, exhibit selectivities <100% in the gas phase.

The most used catalysts for FA decomposition reaction are Pd-,[4,9–11] Au-,[7–9] and Pt-based[12,13] catalysts due to the high conversion and selectivity that they achieve. High activity and selectivity have been obtained also with Ru, which has been primarily investigated in the liquid phase as a homogeneous catalyst,[5,6] and less extensively as a heterogeneous[13,15] or immobilized-complex[14] catalyst. In contrast, for gas-phase FA dehydrogenation, studies of Ru-based catalysts are scarce when compared to Pd-, Pt-, Au-, and Ni-based catalysts.[13,15] Hence, we were interested in investigating RuO₂ nanoparticles (NPs) supported on TpBD-Me₂ (Fig. S1a and b†) covalent organic framework (COF) as a pre-catalyst for this reaction. We envisioned that such a pre-catalyst would eventually provide an active and selective catalytic system due to *in situ* reduction of RuO₂ to Ru under reaction conditions.

COFs are crystalline porous materials with tunable pore structure. Owing to their high surface area, regular porosity, and structural uniformity, this class of materials is an interesting candidate to be used as catalyst support.[16–18] Specifically, COFs themselves have been used as organocatalysts[19] and as supports for metals,[16–18] providing high dispersion of the active catalyst.[20] Unfortunately, the amount of COF that is synthesized per batch in a typical solvothermal synthesis is only in the order of tens to a few hundreds of milligrams, which hinders their use in

[a] *International Iberian Nanotechnology Laboratory (INL), Avenida Mestre José Veiga, 4715-330 Braga, Portugal. E-mail: yury.kolenko@inl.int*

[b] *Laboratory of Separation and Reaction Engineering – Laboratory of Catalysis and Materials (LSRE-LCM), Faculdade de Engenharia, Universidade do Porto, Rua Dr. Roberto Frias, 4200-465 Porto, Portugal*

[c] *DTU Chemistry, Technical University of Denmark, Kemitorvet 207, 2800 Kgs. Lyngby, Denmark. E-mail: skk@kemi.dtu.dk*

[d] *Central Facility for Electron Microscopy, RWTH Aachen University, D-52074 Aachen, Germany*

[e] *Forschungszentrum Jülich GmbH, Ernst Ruska-Centre (ER-C 2), D-52425 Jülich, Germany*

This journal is © The Royal Society of Chemistry 2020

Catal. Sci. Technol., 2020, **10**, 1991–1995 | **1991**

systematic studies and real applications. Furthermore, there is a scarcity of using COFs for heterogeneous gas phase catalysis.[17]

In the current study, we employed the TpBD-Me$_2$ COF, hereafter referred to as **COF**, synthesized using a procedure[21] developed in our group that beneficially yields *ca.* 2 g of the crystalline **COF** material in one batch. This specific **COF** was selected because of its high stability under harsh conditions[22] and high N-content that can be beneficial for the FA dehydrogenation reaction.[12,15]

In the **COF** synthesis protocol, 1,3,5-triformylphloroglucinol (Tp)[23] self-assembles with *o*-tolidine (BD-Me$_2$) to yield TpBD-Me$_2$[21] as an orange solid (Fig. S1†). We further anchored RuO$_2$ NPs on the as-synthesized **COF** using a method reported elsewhere.[24] Briefly, RuCl$_x \cdot x$H$_2$O is used as a precursor and the NPs are precipitated using NaOH.

We began by investigating the crystallinity of the obtained materials. The distances derived from the small-angle X-ray scattering (SAXS) pattern of **COF** (Fig. 1a) correspond well to those reported in the literature for TpBD-Me$_2$.[25] Importantly, the crystallinity of **COF** was maintained after anchoring the RuO$_2$ NPs (Fig. 1a). Inductively coupled plasma-optical emission spectroscopy (ICP-OES) shows that the Ru loading is 2.4%. The specific surface area (S_{BET}) of **COF** was estimated to be 520 m^2 g^{-1} (Fig. S2a and Table S1†), consistent with the literature.[21,25] After precipitating RuO$_2$ onto TpBD-Me$_2$, the S_{BET} increases to 630 m^2 g^{-1} due to the anchoring of high surface area RuO$_2$ NPs, which results in augmentation of the overall texture of **Ru-COF**. We further characterized the surface chemistry of the as-synthesized materials using X-ray photoelectron spectroscopy (XPS) (Fig. 1b, S3 and Table S2†). In **Ru-COF**, the main Ru 3p$_{3/2}$ component is at the binding energy (BE) of 462.8 eV (Fig. 1b), which matches the value reported for the hydrated RuO$_2$ catalyst prepared *via* an analogous procedure (further information in the ESI†).[26–29]

We used annular dark-field scanning transmission electron microscopy (ADF-STEM) imaging coupled with energy-dispersive X-ray spectroscopy (STEM-EDX) mapping to investigate the morphology and the chemical composition of the synthesized **COF** and **Ru-COF**.[30–32] Fig. 2a shows the ADF-STEM overview of agglomerated ≈10–50 nm **COF** particles. An ordered honeycomb structure is clearly visualized in Fig. 2b, confirming the crystalline state of **COF** with a pore size of ≈6.1 Å. An ADF-STEM image of the **Ru-COF** pre-catalyst is shown in Fig. 2c. The bright contrast features correspond to Ru-rich NPs of ≈1.2 nm in diameter (Fig. 2d) anchored on COF, along with single Ru atoms and clusters of few-atoms spread within the COF support (Fig. 2c). Together with this, some of the Ru-rich NPs form agglomerates of ≈10 nm in size (Fig. S4†). Considering the estimated particle size, the dispersion of the NPs is ≈100% (ESI†), suggesting that all the Ru should be available for the catalytic reaction. Fig. S5† shows an ADF-STEM image of the **Ru-COF** pre-catalyst together with corresponding STEM-EDX maps evidencing the bright contrast particles to be Ru-rich.

Having confirmed the presence of ≈1.2 nm RuO$_2$ NPs anchored on the crystalline COF, we tested the **Ru-COF** pre-catalyst in a light-off gas-phase FA dehydrogenation experiment and compared it with a **Ru–C** commercial catalyst with a particle size <2 nm (ESI†). The yield of H$_2$ (Y_{H_2}) is shown in Fig. 3a while the conversion of FA (X) and selectivity to H$_2$ (S_{H_2}) are summarized in Fig. S7a and b.† In the first cycle, the catalyst exhibits high activity towards FA dehydrogenation from 120 °C onwards, reaching 50% conversion at 155 °C (Fig. S7a†) and a maximum Y_{H_2} of 97% at 200 °C (Fig. 3a). Importantly, the catalyst outperforms the

Fig. 1 (a) SAXS patterns of **COF**, **Ru-COF**, and **Ru-COF** after the stability test. (b) High-resolution XPS data for the Ru 3p$_{3/2}$ region of **Ru-COF** and **Ru-COF** after the stability test (symbols: raw data; black lines: overall fits; coloured lines: fits of individual components; grey dashed lines: background).

Fig. 2 (a) ADF-STEM image of **COF**, together with the magnified area (b) indicated by a white square in (a) and the corresponding fast Fourier transform (FFT) in the inset; (c) ADF-STEM image of the **Ru-COF** pre-catalyst, along with (d) a high resolution image of a RuO$_2$ NP.

1992 | *Catal. Sci. Technol.*, 2020, **10**, 1991–1995

This journal is © The Royal Society of Chemistry 2020

Fig. 3 Comparison of the catalytic performance of the synthesized **Ru-COF** and commercial **Ru–C** control catalyst in the dehydrogenation of FA. Light-off curves for (a) H_2 yield (Y_{H_2}) as a function of reaction temperature; (b) stability test performed at 120 °C for 25 h, monitoring Y_{H_2} as a function of time; (c) comparison of the H_2 selectivity (S_{H_2}) as a function of conversion (X), for our catalyst (**Ru-COF**), the commercial catalyst tested (**Ru–C**) and state-of-the-art catalysts for gas-phase FA dehydrogenation.

commercial **Ru–C** control catalyst, showing a higher X at a lower temperature and a higher maximum Y_{H_2}. The S_{H_2} remained nearly constant ($\approx$98%) during the first cycle across the full range of the tested temperatures (Fig. S7b†). In a negative control, no activity for FA dehydrogenation was observed when **COF** was used as catalyst (data not shown), confirming that the active phase is Ru-based. In the second catalytic run, a loss of $\approx$40% in activity was observed for both our **Ru-COF** catalyst and **Ru–C**; however, for our catalyst, the S_{H_2} increased to $\approx$100% (Fig. 3a and S7†).

Next, we performed a long time-on-stream stability test. Since reasonable deactivation was observed at temperatures above 120 °C (Fig. S7c†), the stability tests were carried out at this temperature (Fig. 3b). During the first hour after reaching 120 °C, the catalyst achieves $\approx$24% Y_{H_2}. Afterwards, the Y_{H_2} shows a slight decrease over the following 23 h, becoming stable at $\approx$11%, with the amount of CO generated (data not shown) being much lower than that at higher temperatures and close to the detection limit, marking the selectivity of our catalyst. The reference **Ru–C** catalyst exhibited a similar behaviour; however, the Y_{H_2} was generally about half of that of our catalyst. Notably, as the reactions are conducted at low temperatures, the S_{H_2} is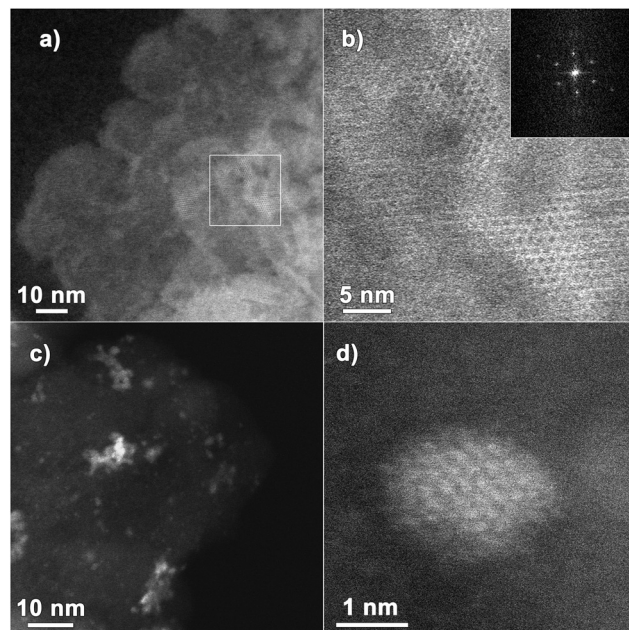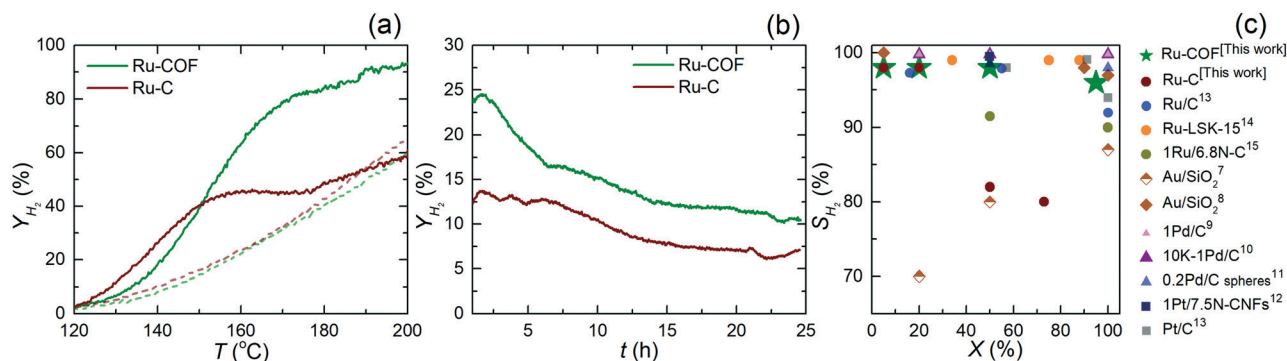 most likely determined by the water-gas shift equilibrium, leading to the low amount of CO observed, and consequently, to high selectivity towards hydrogen.

To gain insight into the possible active catalytic phase, we analyzed our catalyst after stability testing by SAXS, ADF-STEM, and XPS. The SAXS pattern shows that the COF crystallinity is lost after the long time FA dehydrogenation (Fig. 1a). At the same time, XPS analysis of the sample after the catalytic testing (Fig. 1b and S3†) indicates that the chemical structure of the COF support remains largely unchanged (ESI†).[33] These results suggest that the loss of crystallinity is due to delamination of the 2D COF into 1D COF sheets, rather than a modification of its chemical structure (ESI†). XPS also confirms that the RuO_2 NPs are reduced to metallic Ru under the reaction conditions (ESI†); however, some of the RuO_2, likely in the core of the particles,

is not fully reduced. Notably, ADF-STEM suggests sintering of the Ru NPs and clusters during catalytic testing, leading to $\approx$2.4 nm average size (Fig. S6†).

The complementary characterization techniques provide consistent insights into the catalytic process: we believe that the ultrasmall RuO_2 NPs are rapidly reduced to metallic Ru under the reaction conditions,[27,34] and the metallic Ru further acts as the active site for the dehydrogenation of FA, as we envisioned originally. The consequent decrease in activity during the catalytic reaction (Fig. 3b) is most likely related to the sintering of the active Ru NPs (Fig. S6†). The loss of crystallinity and the associated delamination of COF (ESI†)[35] under the same conditions suggest this as one of the mechanisms that can promote the mobility and sintering of Ru. We observe a similar deactivation in the commercial **Ru–C** catalyst also likely associated with the increased size of Ru NPs.

The selectivity values determined for our catalyst at conversions of 5%, 20%, 50%, and 95% (125, 140, 155, and 200 °C, respectively) are shown in Fig. 3c as a function of conversion and compared to state-of-the-art catalysts used for gas phase FA dehydrogenation. In all range of conversions, our catalyst exhibits selectivity values similar to those reported for high performance Ru-, Au-, Pd-, and Pt-based catalysts,[8–14] and higher selectivity than those reported for **Ru–C** and Au–SiO_2 catalysts.[7,15] Significantly, our **Ru-COF** catalyst exhibits higher Y_{H_2} = 50% at 150 °C and $S_{H_2} \approx$ 98% at X = 50%, than those reported by Solymosi et al. for the **Ru–C** catalyst (Y_{H_2} = 15% at 150 °C and S_{H_2} = 95% at X = 66%),[13] by Zacharska and co-workers for Ru supported on N-doped C nanofibers ($Y_{H_2} \approx$ 15% at 150 °C and S_{H_2} = 91.5% at X = 50%),[15] and a higher yield and similar selectivity as reported by Jia et al. for Pt supported on N-doped C nanofibers ($Y_{H_2} \approx$ 30% at 150 °C and S_{H_2} = 99.5% at X = 50%).[12] Notably, the aforementioned reports employ a lower FA feed concentration and in the case of the aforementioned work of Solymosi et al., a higher catalyst amount.[12,13,15]

The high N content of our COF support (9.9 wt%, ESI†) likely contributes to the high activity of the catalyst via two

This journal is © The Royal Society of Chemistry 2020

Catal. Sci. Technol., 2020, **10**, 1991–1995 | **1993**

mechanisms. First, N-doping of a C nanofiber support has been reported to increase the activity of the Ru catalyst.[15] In a second effect, reported for a Pt catalyst on a similar N-doped C nanofiber support, the improved activity of the catalyst in the FA dehydrogenation reaction was associated with the presence of sub-nm Pt clusters, the formation of which was promoted by the N-doping.[12] While analogous formation of sub-nm Ru clusters has not been observed for Ru supported on N-doped C nanofibers,[15] the combination of our method for the formation of the Ru catalyst and of the N-containing COF support does produce sub-nm Ru clusters with high dispersion over COF (Fig. 2c and S5†). Accordingly, we believe that both of the previously reported beneficial effects of N in the C support[12,15] contribute to the high selectivity observed for our catalyst. The exact influence of the N-content in the COF support on the catalyst performance is the subject of the ongoing research efforts.

In summary, TpBD-Me$_2$ COF was successfully synthesized and used as a support for RuO$_2$ NPs. **COF** presents a high surface area, well-defined porosity with a honeycomb structure as shown by ADF-STEM, and a high N-content of 9.9 wt% from constituent organic building blocks. These features allowed the precipitation of well-dispersed RuO$_2$ NPs as well as small RuO$_2$ clusters and single Ru atoms on the COF support, which were found to provide a good **Ru-COF** pre-catalyst for the *in situ* formation of an active and selective Ru catalyst for the FA dehydrogenation reaction.

The ruthenium phase in the **Ru-COF** pre-catalyst was confirmed to be hydrated RuO$_2$ by XPS analysis, which was further reduced to metallic Ru during the initial stage of catalytic testing, thus forming the active sites for the dehydrogenation of FA. The COF support maintained its chemical structure after 25 h of catalytic testing at 120 °C, as confirmed by XPS, although a loss of crystallinity of the support and some degree of sintering of the Ru NPs were observed.

The results obtained in this investigation provide an ambitious benchmark for further studies for the development of COF-supported catalysts for the FA dehydrogenation reaction, as well as for other gas-phase dehydrogenation reactions at low temperatures. A particularly promising direction for future work indicated by our results is the selective synthesis of single Ru atom catalysts supported on COF for (de)hydrogenation.

Conflicts of interest

There are no conflicts to declare.

Acknowledgements

Notes and references

1 A. K. Singh, S. Singh and A. Kumar, *Catal. Sci. Technol.*, 2016, **6**, 12–40.

2 X. Wang, Q. Meng, L. Gao, Z. Jin, J. Ge, C. Liu and W. Xing, *Int. J. Hydrogen Energy*, 2018, **43**, 7055–7071.

3 W. Supronowicz, I. A. Ignatyev, G. Lolli, A. Wolf, L. Zhao and L. Mleczko, *Green Chem.*, 2015, **17**, 2904–2911.

4 Y. Kim and D. H. Kim, *Appl. Catal., B*, 2019, **244**, 684–693.

5 Y. Pan, C.-L. Pan, Y. Zhang, H. Li, S. Min, X. Guo, B. Zheng, H. Chen, A. Anders, Z. Lai, J. Zheng and K.-W. Huang, *Chem. – Asian J.*, 2016, **11**, 1357–1360.

6 C. Guan, D.-D. Zhang, Y. Pan, M. Iguchi, M. J. Ajitha, J. Hu, H. Li, C. Yao, M.-H. Huang, S. Min, J. Zheng, Y. Himeda, H. Kawanami and K.-W. Huang, *Inorg. Chem.*, 2017, **56**, 438–445.

7 J. Mielby, A. J. Kunov-Kruse and S. Kegnæs, *J. Catal.*, 2017, **345**, 149–156.

8 A. Gazsi, T. Bánsági and F. Solymosi, *J. Phys. Chem. C*, 2011, **115**, 15459–15466.

9 D. A. Bulushev, S. Beloshapkin and J. R. H. Ross, *Catal. Today*, 2010, **154**, 7–12.

10 L. Jia, D. A. Bulushev and J. R. H. Ross, *Catal. Today*, 2016, **259**, 453–459.

11 D. A. Bulushev, L. G. Bulusheva, S. Beloshapkin, T. O'Connor, A. V. Okotrub and K. M. Ryan, *ACS Appl. Mater. Interfaces*, 2015, **7**, 8719–8726.

12 L. Jia, D. A. Bulushev, O. Yu. Podyacheva, A. I. Boronin, L. S. Kibis, E. Yu. Gerasimov, S. Beloshapkin, I. A. Seryak, Z. R. Ismagilov and J. R. H. Ross, *J. Catal.*, 2013, **307**, 94–102.

13 F. Solymosi, Á. Koós, N. Liliom and I. Ugrai, *J. Catal.*, 2011, **279**, 213–219.

14 A. Beloqui Redondo, F. L. Morel, M. Ranocchiari and J. A. van Bokhoven, *ACS Catal.*, 2015, **5**, 7099–7103.

15 M. Zacharska, O. Yu. Podyacheva, L. S. Kibis, A. I. Boronin, B. V. Senkovskiy, E. Yu. Gerasimov, O. P. Taran, A. B. Ayusheev, V. N. Parmon, J. J. Leahy and D. A. Bulushev, *ChemCatChem*, 2015, **7**, 2910–2917.

16 S.-Y. Ding, J. Gao, Q. Wang, Y. Zhang, W.-G. Song, C.-Y. Su and W. Wang, *J. Am. Chem. Soc.*, 2011, **133**, 19816–19822.

17 D. Mullangi, S. Nandi, S. Shalini, S. Sreedhala, C. P. Vinod and R. Vaidhyanathan, *Sci. Rep.*, 2015, **5**, 10876.

18 G.-J. Chen, X.-B. Li, C.-C. Zhao, H.-C. Ma, J.-L. Kan, Y.-B. Xin, C.-X. Chen and Y.-B. Dong, *Inorg. Chem.*, 2018, **57**, 2678–2685.

19 Y. Zhi, P. Shao, X. Feng, H. Xia, Y. Zhang, Z. Shi, Y. Mu and X. Liu, *J. Mater. Chem. A*, 2018, **6**, 374–382.

20 S. Kandambeth, K. Dey and R. Banerjee, *J. Am. Chem. Soc.*, 2019, **141**, 1807–1822.

21 A. Mellah, S. P. S. Fernandes, R. Rodríguez, J. Otero, J. Paz, J. Cruces, D. D. Medina, H. Djamila, B. Espiña and L. M. Salonen, *Chem. – Eur. J.*, 2018, **24**, 10601–10605.

1994 | *Catal. Sci. Technol.*, 2020, **10**, 1991–1995

This journal is © The Royal Society of Chemistry 2020

22 S. Kandambeth, A. Mallick, B. Lukose, M. V. Mane, T. Heine and R. Banerjee, *J. Am. Chem. Soc.*, 2012, **134**, 19524–19527.

23 J. H. Chong, M. Sauer, B. O. Patrick and M. J. MacLachlan, *Org. Lett.*, 2003, **5**, 3823–3826.

24 N. Mizuno and K. Yamaguchi, *Catal. Today*, 2008, **132**, 18–26.

25 S. Chandra, S. Kandambeth, B. P. Biswal, B. Lukose, S. M. Kunjir, M. Chaudhary, R. Babarao, T. Heine and R. Banerjee, *J. Am. Chem. Soc.*, 2013, **135**, 17853–17861.

26 K. Yamaguchi, T. Koike, J. W. Kim, Y. Ogasawara and N. Mizuno, *Chem. – Eur. J.*, 2008, **14**, 11480–11487.

27 D. J. Morgan, *Surf. Interface Anal.*, 2015, **47**, 1072–1079.

28 H. G. Manyar, D. Weber, H. Daly, J. M. Thompson, D. W. Rooney, L. F. Gladden, E. H. Stitt, J. J. Delgado, S. Bernal and C. Hardacre, *J. Catal.*, 2009, **265**, 80–88.

29 P. P. T. Krause, H. Camuka, T. Leichtweiss and H. Over, *Nanoscale*, 2016, **8**, 13944–13953.

30 Ernst Ruska-Centre for Microscopy and Spectroscopy with Electrons (ER-C), A. Kovács, R. Schierholz and K. Tillmann, *Journal of Large-Scale Research facilities (JLSRF)*, 2016, **2**, A43.

31 Ernst Ruska-Centre for Microscopy and Spectroscopy with Electrons (ER-C), K. Tillmann, J. Barthel and L. Houben, *Journal of Large-Scale Research facilities (JLSRF)*, 2015, **1**, A34.

32 Ernst Ruska-Centre for Microscopy and Spectroscopy with Electrons (ER-C), M. Heggen, M. Luysberg and K. Tillmann, *Journal of Large-Scale Research facilities (JLSRF)*, 2016, **2**, A42.

33 E. H. Lock, D. Y. Petrovykh, P. Mack, T. Carney, R. G. White, S. G. Walton and R. F. Fernsler, *Langmuir*, 2010, **26**, 8857–8868.

34 T. Weber, M. J. S. Abb, O. Khalid, J. Pfrommer, F. Carla, R. Znaiguia, V. Vonk, A. Stierle and H. Over, *J. Phys. Chem. C*, 2019, **123**, 3979–3987.

35 D. N. Bunck and W. R. Dichtel, *J. Am. Chem. Soc.*, 2013, **135**, 14952–14955.

This journal is © The Royal Society of Chemistry 2020

Catal. Sci. Technol., 2020, **10**, 1991–1995 | **1995**

Appendix D.5

1 **Heterogeneous formic acid production by hydrogenation**

2 **of CO_2 catalyzed by Ir-bpy embedded in polyphenylene**

3 **porous organic polymers**

4 Niklas R. Bennedsen[a], David B. Christensen[a], Rasmus L. Mortensen[a], Bolun Wang[b], Ryan Wang[b],

5 Søren Kramer*[a], and Søren Kegnæs*[a]

6 [a]Department of Chemistry, Technical University of Denmark, 2800 Kgs. Lyngby, Denmark.

7 [b]Department of Chemical Engineering, University College London, Torrington Place, WC1E

8 London, United Kingdom.

9 E-mail addresses: sokr@kemi.dtu.dk (S. Kramer), skk@kemi.dtu.dk (S. Kegnæs).

10 **Abstract:**

11 Heterogeneous single-site catalysis has gained significant attention as a platform for creating more

12 efficient and selective catalysts that can help improve current and new technologies. A promising

13 class of single-site catalysts are porous organic polymers (POPs) due to their high stability,

14 porosity, and functional freedom which can mimic the catalytic activity and selectivity of

15 homogeneous organometallic catalysts. These properties of the POP-based systems make them very

16 attractive as catalysts for hydrogenation of CO_2 to formate, which can be used as a green and

17 renewable hydrogen carrier beyond utilizing CO_2 as a valuable chemical instead of emitting it to the

18 atmosphere. So far, the hydrogenation of CO_2 have predominately relied on homogeneous catalysts,

19 but heterogeneous POP-based catalytic systems have emerged as an appealing platform for

20 circumventing the disadvantages of homogeneous catalysts such as difficult catalyst recovery and

21 recyclability. Furthermore, the rigid structure of certain POPs can be exploited to prevent undesired

22 catalyst deactivation mechanisms. In this study, five POPs were synthesized containing different

23   ligands and ligand densities. The POPs were assessed in the hydrogenation of CO_2 where the active

24   catalysts were made in-situ by mixing $IrCl_3$ and the POPs. One of the Ir/POP catalysts provided a

25   turn-over number (TON) >20,000, which is among the highest for POP-based systems. The

26   corresponding homogeneous Ir(III)/ligand system did not show the same activity thus highlighting

27   that POP-systems can provide unique catalytic performances different from apparently similar

28   homogeneous systems. Thorough characterization (CO_2- and N_2-physisorption, TGA, CHN-

29   analysis, XRD, XPS, SEM, and TEM) was performed before and after the catalytic reaction in order

30   to reveal the material properties. Notably, the developed Ir/POP system also showed catalytic

31   activity for the decomposition of formic acid into H_2. Given the high TON for formic acid

32   production and the capability to also catalyze the dehydrogenation of formic acid, the developed

33   Ir/POP system can help enable the implementation formic acid as a sustainable hydrogen energy

34   carrier.

35   **Keywords**: CO_2 utilization, heterogeneous catalyst, porous organic polymers, hydrogenation of

36   CO_2, hydrogen capture and release.

1) Introduction

Designing novel porous materials with active single-sites have been of high interest for the past decades in the field of heterogeneous catalysis to access more efficient and selective catalysts.[1] Porous organic polymers (POPs) have received significant attention as single-site catalysts for their high stability, porous nature, and high functional freedom.[2] POPs can easily be synthetically modified with many different functionalities, in contrast to other materials such as metal- or covalent organic frameworks, aluminosilicates, and metaloxides where compositional restraints and/or required crystallinity can hinder the incorporation of different functionalities.[3] These functionalities can be organometallic ligands with the ability to immobilize metals and thereby form active heterogeneous catalysts.[4] Furthermore, the coordination of metals to POP-based ligand sites can also prevent classical deactivation mechanism thereby providing unique catalytic activities.[5] Finally, the heterogeneous skeleton of POPs facilitates its easy recovery and reuse for future and sustainable applications.

Utilization of carbon dioxide (CO_2) have been targeted as an attractive strategy to diminish its emission to the atmosphere and contribution to the climate change as a greenhouse gas.[6] A promising application is the transformation of CO_2 into more valuable chemicals with examples such as formic acid (FA), methanol, and methane.[7] The interest for renewable formation of FA has increased tremendously over the past decades due to its high volumetric capacity of hydrogen (H_2) that can be released through selective decomposition.[8] This makes FA an attractive organic liquid hydrogen carrier (LOHC), which can remove the otherwise need for high pressure containers in storage and transportation of H_2.[9] The released H_2 can be used as an excellent green, renewable, and sustainable source of energy with its a high gravimetric energy density, which can replace the need for fossil fuels and thereby diminish the environmental impact currently seen throughout the world.[10] The formation of FA by hydrogenation of CO_2 provides a neutral carbon

61   balance and helps in the utilization of CO_2 as a valuable resource.[7c,11] Although the

62   hydrogenation transformation is not thermodynamically favourable, the reaction can be driven by

63   trapping the generated FA as formate.[12] Currently, state-of-the-art homogeneous catalysts for

64   hydrogenation of CO_2 to formate use precious metal-based catalyst, such as Ir, Rh, Ru, and Pd in

65   alkaline aqueous media.[13] Although these homogeneous precious metal catalysts provide high

66   turnover numbers (TON), they do not have the same green and sustainable properties as

67   heterogeneous catalysts. Thus, novel and active heterogeneous catalysts are very attractive for

68   accommodating the demands for FA as a green and sustainable hydrogen carrier, which helps the

69   utilization of CO_2.

70   The most frequently used industrial catalysts are immobilized metal nanoparticles on porous

71   supports, but these catalysts lack activity and selectivity in the formation of formate.[7a] Given the

72   unique properties of POPs containing organometallic single-sites, these new materials hold promise

73   for addressing the issues with activity and selectivity for heterogeneous catalysis. So far, there are

74   only sparse reports on the use of POPs for formic acid production from CO_2; however, these reports

75   already display very promising results.[14,15,16] For example, in the state-of-the-art, Yoon et al.

76   have demonstrated that an iridium containing phenanthroline-based POP catalyst can afford a TON

77   of 14,330 for the hydrogenation of CO_2 to formate.[14d]

78   We have previously developed a polyphenylene (PP) POP which did not contain organometallic

79   ligand sites.[17] Instead of single-site catalysis the PP was used as a support material for Pd

80   nanoparticles. Recently, Wang et al. have shown that a sulfonated PP can hydrate alkyne bonds

81   showing the versatility of such a material.[18] Yet, as the PP POP is made up exclusively of

82   aromatic sp^2-carbons, it is very robust, and this feature could make it ideal for applications in high-

83   pressure reactions like the hydrogenation of CO_2 to formate.

84   Here, we report the synthesis of novel PP-based POPs with organometallic ligands, bipyridine or

85   phenanthroline, incorporated into the polymer skeleton. Upon in situ ligation to iridium, the best Ir-

86   POP can catalyze hydrogenation of CO_2 to formate with a TON >20,000 under reaction conditions

87   comparable to previous literature reports (140 °C, 56 bar 1:1 $H_2:CO_2$). The influence on the TON of

88   varying the ligand and ligand density is examined. The synthesized materials are characterized by

89   TGA, CO_2- and N_2-physisorpion, SEM, STEM, TEM, XPS, and CHN-analysis. In addition, post-

90   reaction characterization is conducted to assess material changes during the catalytic reaction.

91   Interestingly, the corresponding homogeneous catalysts led to much lower TONs, thus highlighting

92   the essential role of the POP in the catalytic performance. Finally, we demonstrate that the same

93   catalyst is active in the selective dehydrogenation of FA. This is the first reported POP catalyst

94   system capable of both forming and decomposing FA selectively, accordingly it can help advancing

95   H_2 as a renewable and sustainable energy source.

96   **2) Results and Discussion**

97   **2.1) Synthesis and characterization**

98   In our new PP POP synthesis, 1,2,4,5-tetrabromobenzene, 1,4-phenylenediboronic acid, and the

99   corresponding N-based ligand are coupled through a Suzuki cross-coupling in the presence of

100   catalytic Pd(PPh$_3$)$_4$ (Scheme 1).[17] Palladium traces are removed by oxidation and EDTA-

101   complexation yielding the PP with the desired ligand. The polymerization allows for easy tuning of

102   the resulting POP by changing the ratio between the brominated building blocks (N-based ligand

103   and 1,2,4,5-tetrabromobenzene). A demonstration thereof was done by synthesizing POPs with

104   either bipyridine or phenanthroline functionality and by increasing the amount of ligand

105   incorporated into the POP skeleton. As a result, five different POPs were synthesized and

106   abbreviated based on their properties; bpy = bipyridine, Phen = phenanthroline, prefix numbers

107   indicate change of the ligand concentration in the synthesis relative to the original POP.
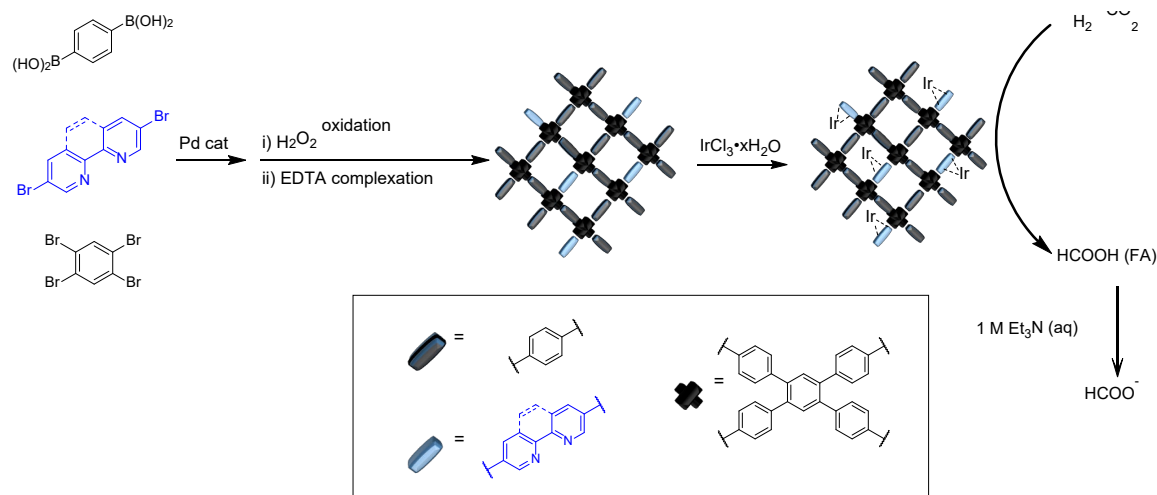
Scheme 1. Illustration of the synthesis and catalytic reaction of the PP-POPs.

108

109   One of the characteristics of the synthesized POPs is that the polymerization technique only forms

110   aromatic sp^2-carbons resulting in polymers which are more chemically and physically stable than

111   other polymers.[2d] The expected high thermal stability was also observed by thermogravimetric

112   analysis (Figure 1a). The POPs are seemingly stable in air up to 400 °C and a significant mass loss

113   is only observed above 500°C. An amorphous structure is seen in XRD (Figure S2), but the polymer

114   appears homogeneous in structure with similar morphology throughout the whole sample in SEM

115   (Figure 1b). The nitrogen content of the synthesized POPs was assessed by CHN-analysis and XPS

116   (Figure 1c). Both analyses reveal an increase in nitrogen content in our series of bpy-based POPs

117   with bpy-PP-POP having the lowest nitrogen content and 4xbpy-PP-POP the highest; however, the

118   increase does not match the expected 1 : 2 : 4 ratio but rather a 1 : 1.5 : 2.5 ratio based on the CHN

119   values. The adsorption properties were examined by N_2-physisorption initially where none of the

120   POPs containing ligands showed any porosity (Figure S3). Notably, the change of adsorbent to CO_2

121   instead of N_2 showed that all the POPs are porous and capable of adsorbing CO_2 (Figure 1d).[19]

122   Furthermore, a clear trend was observed as increasing the bpy density in the POP decreases the

123   porosity. XPS analysis of the carbon in the polymer confirms that only one signal is present

124   corresponding to C-C bonds with no indication of oxidation from the H_2O_2 treatment (Figure S5).

125   The nitrogen in the bpy-PP-POP is present as only one specie that has a binding energy

126   corresponding to pyridinic nitrogen (Figure 1e).[20] The introduction of more bipyridine sites or

127   replacing bpy with Phen into the skeleton (2xbpy-PP-POP, 4xbpy-PP-POP, or Phen-PP-POP) did

128   not show any significant difference from the bpy-PP-POP material (see Figure S6). These results

129   are in agreement with the synthesized material being a polyphenylene POP with either bpy or Phen

130   functionality in the skeleton (see Table S2 for additional values from CHN-analysis and Figure S7

131   for a TEM image).

POP	CHN-analysis N (mass %)	XPS N (mass %)	Nitrogen content relative to bpy-PP-POP
bpy-PP-POP	3.28%	4.91%	1.0
2xbpy-PP-POP	4.90%	6.30%	1.5
4xbpy-PP-POP	8.22%	9.62%	2.5
Phen-PP-POP	3.81%	2.12%	1.2
PP-POP	0.46%	0.00%	0.1
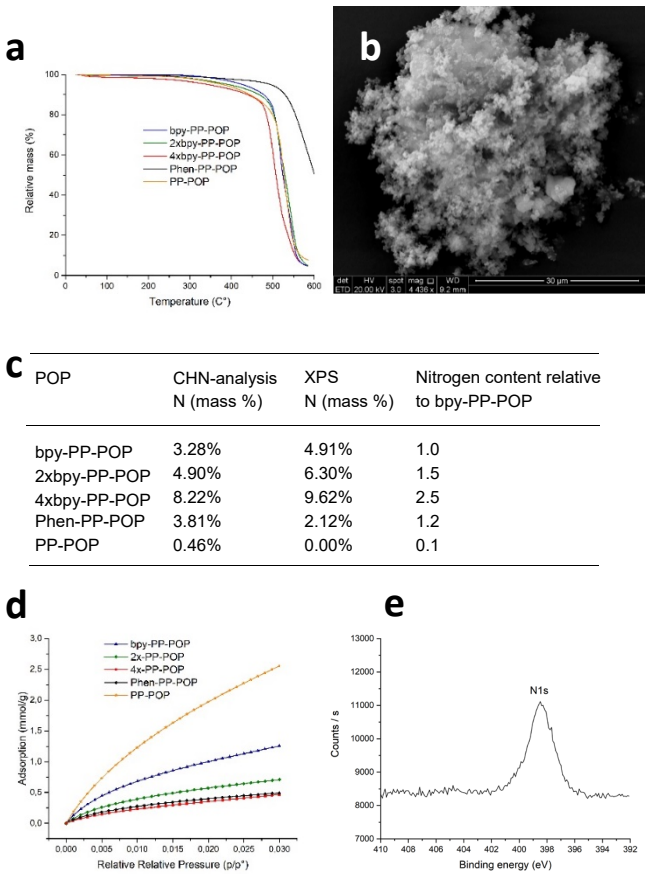
Figure 1. Characterization of synthesized POP. a) The thermal stability evaluated from TGA. b) SEM image of the bpy-PP-POP. c) Compositional analysis of the nitrogen content of the POPs. d) CO_2-adsorption isotherms of the POPs. e) XPS signal from the N1s scan shown for the bpy-PP-POP.

132

2.2) Hydrogenation of CO_2

134 With four different POPs containing organometallic ligand sites in hand, we tested the POPs in the

135 catalytic hydrogenation of CO_2 to formate. In our test setup, the POP and an iridium precursor were

136 mixed in a 1M aqueous solution of Et_3N inside a steel reactor. The total pressure inside the reactor

137 was regulated to 56 bar of CO_2 and H_2 in a 1:1 ratio before being heated to the specified

138 temperature (an example of the pressure profile during an experiment is shown in Figure S9). The

139 POPs with either phenanthroline or bipyridine in the skeleton both showed activity in the formation

140 of FA, but the POP based on bipyridine displayed superior activity (Table 1, entry 1 and 2).

141 Lowering the iridium concentration to 10 μM for the bpy-PP-POP provided an impressive TON of

142 20,041 (entry 3). The addition of more POP did not improve the catalytic performance (entry 4).

143 Replacing the original POP with derivatives that have a higher concentration of bipyridine in the

144 skeleton (2xbpy-PP-POP and 4xbpy-PP-POP) led to significantly lower TONs (entry 5 and 6). This

145 may be correlated to their inferior porosity seen from the CO_2-adsorption experiment. Increasing the

146 reaction time to 48 hours did not improve the yield (entry 7). Switching the iridium precursor from

147 $IrCl_3$ to $[IrCp*Cl]_2$ or $[Ir(cod)MeO]_2$ did not provide higher activity (entry 8 and 9). Lowering the

148 reaction temperature to 120 °C decreased the activity significantly (entry 10). A test reaction with

149 commercially available material of iridium nanoparticles on carbon (Ir/C) showed no significant

150 catalytic activity (entry 11).

151 **Table 1.** The catalytic performance of the synthesized POPs in the presence of an iridium precursor

152 for the hydrogenation of CO_2 to formate.

$$CO_2 + H_2 \xrightarrow[\substack{1\ M\ Et_3N\ (aq)\ (5mL), \\ 24\ h,\ 140\ °C}]{\substack{[Ir],\ ligand \\ 56\ bar\ (1:1\ CO_2:H_2)}} HCO_2^-$$

| Entry	Ligand	[Ir] (conc.)	Yield[a]	TON[b]
1	Phen-PP-POP	$IrCl_3•xH_2O$ (100 µM)	12%	1336
2	bpy-PP-POP	$IrCl_3•xH_2O$ (100 µM)	42%	4676
3	bpy-PP-POP	$IrCl_3•xH_2O$ (10 µM)	18%	20041
4[c]	bpy-PP-POP	$IrCl_3•xH_2O$ (10 µM)	16%	17814
5[d]	2xbpy-PP-POP	$IrCl_3•xH_2O$ (10 µM)	5%	5567
6[d]	4x-bpy-PP-POP	$IrCl_3•xH_2O$ (10 µM)	5%	5567
7[e]	bpy-PP-POP	$IrCl_3•xH_2O$ (10 µM)	15%	16701
8	bpy-PP-POP	[IrCp*Cl]₂ (10 µM)	12%	13360
9	bpy-PP-POP	[Ir(cod)MeO]₂ (10 µM)	10%	11134
10[f]	bpy-PP-POP	$IrCl_3•xH_2O$ (10 µM)	2%	2227
11[g]	-	Ir/C (100 µM)	3%	3340
12[d]	2,2'-bipyridine	$IrCl_3•xH_2O$ (10 µM)	<1%	-
13[h]	-	K[IrbpyCl₄] (10 µM)	2%	2227
14[i]	bpy-PP-POP + 2,2'-bipyridine	$IrCl_3•xH_2O$ (10 µM)	6%	6080
15	bpy-PP-POP (used)	-	12%	13361
16	bpy-PP-POP (used)	$IrCl_3•xH_2O$ (10 µM)	17%	18928
17	-	-	<1%	-
18	-	$IrCl_3•xH_2O$ (10 µM)	<1%	-
19	bpy-PP-POP	-	6%	6680

153

154 [a]Yield quantified by ^{1}H-NMR using D_2O as solvent and Et_3N as a standard. [b]TON calculated by the following equation: the n(formate)/n(Ir)

155 where n(formate) is given by yield*n(Et_3N) and the total amount of iridium is estimated based on a iridium content of 52% for the $IrCl_3•xH_2O$

156 salt. [c]Twice the normal amount of POP. [d]The overall amount of bipyridine was kept constant. [e]Reaction time was 48 hours. [f]The reaction

157 temperature was decreased to 120 °C. [g]Commercially available Ir/C. [h]The K[IrbpyCl₄] complex was synthesized according to reported

158 literature.[22] [i]The amount of added 2,2'-bipyridine is 1 equivalent of the added iridium.

159

160 To compare our heterogeneous catalyst system with the corresponding homogeneous catalyst

161 system, we performed the CO_2 hydrogenation with $IrCl_3•xH_2O$/2,2'-bipyridine (entry 12).

162 Surprisingly, this homogeneous catalyst system did not display any significant activity indicating

163 that the incorporation of the ligand into the POP skeleton is crucial for achieving high TONs for this

164 transformation. Also, the use of a homogeneous monobipyridine iridium complex as catalyst was

165 unsuccessful (entry 13). To gain further insight into the potential reason for the beneficial effect of

166 the POP, we added 2,2'-bipyridine to a reaction with bpy-PP-POP (entry 14). Notably, the reaction

167 was significantly inhibited by the presence of the homogeneous ligand. Previous reports have

168   indicated that common deactivation mechanisms e.g. formation of inactive dimers and saturated

169   complexes can be avoided with the incorporation of the ligand into a rigid POP backbone, and also

170   that active complexes can only be formed with POP-based ligands providing unique properties for

171   catalysis.[5,21] Accordingly, we hypothesize that the rigid bpy-PP-POP stabilizes a catalytically

172   active Ir/mono-bpy species and prevents the formation of more stable yet inactive bis- or

173   trischelated Ir/bpy species and dimers, which can be accessed readily under homogeneous

174   conditions (Scheme 2).

175
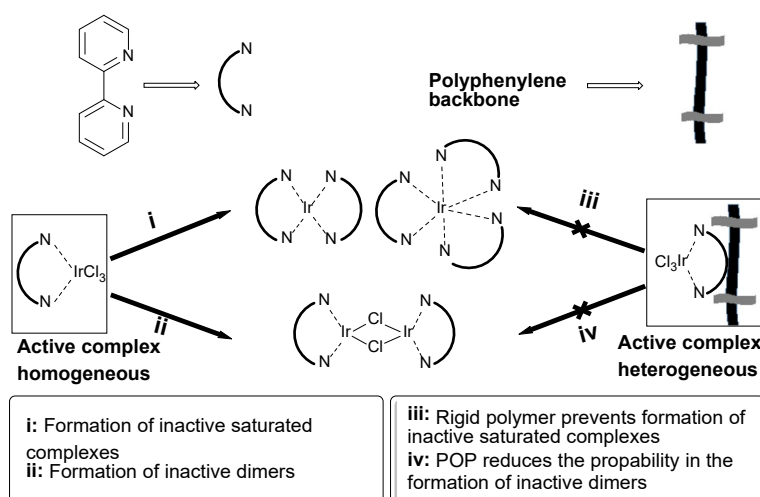
176   **Scheme 2.** Potential deactivation pathways for homogeneous systems which are made inaccessible

177   by the rigid structure of the POP.

178

179   To investigate the recyclability of the bpy-PP-POP catalyst material, it was recovered by

180   centrifugation and rinsed with water. Subsequently, the recovered catalyst material was subjected to

181   a fresh solution of Et_3N under CO_2 and H_2 pressure. The POP-based catalyst material is still active,

182   but a loss of yield is observed (Table 1, entry 15). However, the original activity can be recovered

183   by the addition of fresh $IrCl_3 \cdot xH_2O$ (entry 16). Control experiments showed that the reactor and

184   IrCl$_3$•xH$_2$O are not active by itself (entries 17-18). The bpy-PP-POP alone does show some activity,

185   but it is less active than in the presence of iridium (entry 19).

186   The used bpy-PP-POP catalyst was characterized by STEM to identify potential changes in the

187   material and help clarifying possible deactivation mechanisms (Figure 2). The STEM images of the

188   used catalyst reveal the presence of iridium nanoparticles that are distributed throughout the whole

189   sample and have a very narrow size distribution (2-4 nm). Albeit, Iridium nanoparticles on carbon

190   have previously shown to be inactive for the hydrogenation of CO$_2$ under our conditions (Table 1,

191   entry 11). XRF analysis reveals the presence of approximately 1 µM iridium in a filtrated reaction

192   mixture (see Table S3). These two observations suggest that the observed catalytic deactivation

193   observed upon recycling can arise from either/both decomposition of Ir(III) into nanoparticles or

194   from metal leaching. Yet, the addition of fresh IrCl$_3$•xH$_2$O can re-establish the activity showcasing

195   the robustness of the POP itself.
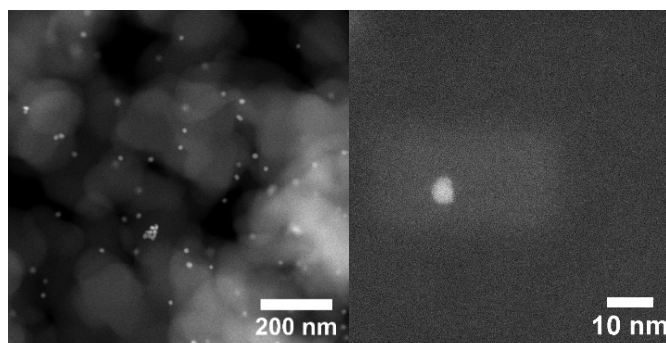
Figure 2. STEM images of the used bpy-PP-POP
showing the presence of small iridium nanoparticles.

196

197   The observed inability of the corresponding homogeneous catalyst systems to replicate the high

198   TON obtained with the POP supports the intended heterogeneous nature of the catalyst.

199   Nonetheless, homogeneous species which can only be formed in the presence of the POP could

200   potentially be catalytically active in the hydrogenation. To investigate this possibility, a filtration

201   experiment was carried out (Scheme 3). The reaction was stopped after 2 hours, filtered to remove

202   the POP from the reaction mixture, and started again by refilling with CO_2 and H_2. The very limited

203   activity in the liquid phase shows that the origin of the catalytic activity is heterogeneous in nature.

$$CO_2 + H_2 \xrightarrow{\substack{\text{1) IrCl}_3 \cdot \text{xH}_2\text{O (10 }\mu\text{M), 111 mg} \\ \text{bpy-PP-POP, 1 M Et}_3\text{N (aq)} \\ \text{(5mL), 2 h, 140 °C} \\ \\ \text{2) Filtration} \quad \text{and CO} \\ \text{3) Applying H}_2 \qquad _2 \\ \text{pressure, 140 °C, 22 h}}} HCO_2^-$$

204   **2 h:**   1.4%
                                                                                          24 h: 2.3%
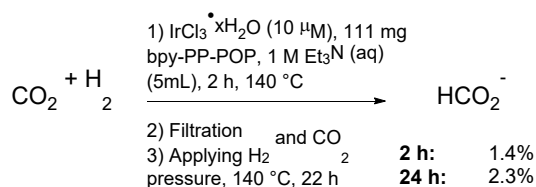
205   **Scheme 3.** Filtration experiment with the obtained yield after either 2 or 24 h at 140 °C.

206

207   **2.3) Selective dehydrogenation of formic acid**

208   The path towards a sustainable and renewable future utilization of FA as hydrogen energy carrier

209   requires both the formation and selective dehydrogenation of FA. Reports of systems that can

210   catalyze both directions are rare and highly attractive.[21] In that perspective, we tested if our bpy-

211   PP-POP/IrCl$_3$-system was active in the dehydrogenation of FA. In our setup, the dehydrogenation of

212   FA is conducted in a continuous vapour phase setup by bubbling FA with a stream of nitrogen and

213   passing the saturated gas stream over a fixed reactor bed. The yield of H_2 is then measured while the

214   temperature of the reactor bed is increased. Notably, activity was observed at temperatures from

215   160 °C illustrating the potential of our POP as a multifunctional catalyst capable of both forming

216   and decomposing FA (Figure 3). Performing the decomposition of FA with minimal formation of

217   CO is crucial to avoid poisoning of the state-of-the-art platinum catalysts used in the fuel cells, and

218   therefore this reaction is typically carried out at low temperatures to get very high selectivity.[24]

219   Remarkably, our POP-based system is very selective up to 190 °C (CO < 0.01%; Figure S11).
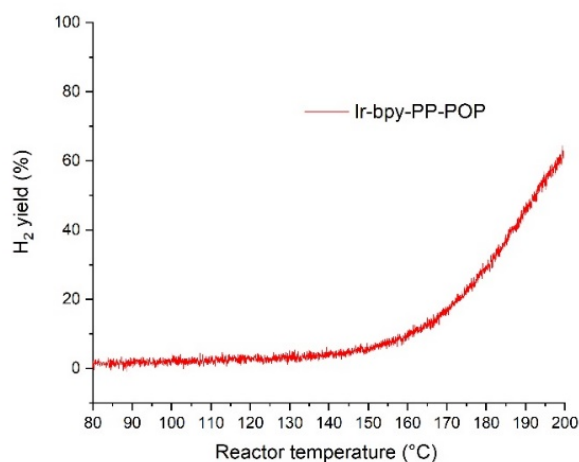
220

221   **Figure 3.** Activity plot with the yield of H_2 as a function of temperature in the decomposition of

222   FA.

223

224   **3) Conclusions**

225   In summary, we have made a series of polyphenylene-based POPs with different ligand types and

226   concentration of the ligand in the skeleton of the POP. The POPs are amorphous with excellent

227   thermal stability up to at least 400 °C in air. The synthesized POPs were assessed in the

228   hydrogenation of CO_2 to form FA as a renewable hydrogen energy carrier creating a neutral carbon

229   balance and utilization the abundant CO_2. The results show that both ligand type and concentration

230   of the ligand affects the catalytic performance. The best catalytic performance was observed with

231   bpy-PP-POP which led to a TON >20,000. The beneficial effect of incorporating the bipyridine

232   ligand into a POP structure was clearly demonstrated with the much lower activity achieved for the

233   corresponding homogeneous iridium-bipyridine systems. A decrease in activity was observed when

234   recycling the catalyst material, however, the activity can be recovered by introducing fresh iridium

235   to the reaction mixture, thus demonstrating the robustness of the POP. Electron microscopy

236   revealed that the most likely deactivation mechanism is formation of inactive iridium nanoparticles.

237   Finally, we demonstrated that our catalytic system can also selectively decompose FA into H_2

238   thereby highlighting the potential of POP catalysts in the implementation of FA as a renewable

239   energy source.

240   **Acknowledgments**

245

246   **References**

247   1   a) C. Copéret, M. Chabanas, R. Saint-Arroman, J.-M. Basset, J.-M. Angew. Chem. Int. Ed. 42 (2003)156

248   https://doi.org/10.1002/anie.200390072, b) J. Thomas, R. Raja, D. Lewis, Angew. Int. Ed. 44 (2005) 6456

249   https://doi.org/10.1002/anie.200462473, c) J. Pelletier, J.-M. Basset, Acc. Chem. Res. 49 (2016) 664

250   https://doi.org/10.1021/acs.accounts.5b00518, d) X. Cui, W. Li, P. Ryabchuk, K. Junge, M. Beller, Nat Chemistry

251   1 (2018) 385 https://doi.org/10.1038/s41929-018-0090-9, e) M. Wasson, C. Buru, Z. Chen, T. Islamoglu, O.

252   Farha, Appl. Catal. A-Gen. 586 (2019) 117214 https://doi.org/10.1016/j.apcata.2019.117214.

253   2   a) P. Kaur, J. Hupp, S. Nguyen, ACS Catal. 1 (2011) 819 https://doi.org/10.1021/cs200131g, b) Y. Zhang, N.

254   Riduan, Chem. Soc. Rev. 41 (2012) 2083 https://doi.org/10.1039/C1CS15227K, c) Q. Sun, Z. Dai, X. Meng, F.-

255   S. Xiao, Chem. Soc. Rev. 44 (2015) 6018 https://doi.org/10.1039/C5CS00198F, d) S. Kramer, N. Bennedsen, S.

256   Kegnæs, ACS Catal. 8 (2018) 6961 https://doi.org/10.1021/acscatal.8b01167.

257   3   a) Y. Ma, W. Tong, H. Zhou, S. Suib, Microporous and Mesoporous Materials 37 (2000) 243

258   https://doi.org/10.1016/S1387-1811(99)00199-7, b) Y. Wang, H. Arandiyan, J. Scott, A. Bagheri, H. Dai, R.

259   Amal, J. Mater. Chem. A. 5 (2017) 8825 https://doi.org/10.1039/C6TA10896B, c) A. Dhakshinamoorthy, A.

260   Asiri, H. Garcia, ACS Catal. 9 (2019) 1081 https://doi.org/10.1021/acscatal.8b04506, d) L. Gonçalves, D.

261   Christensen, M. Meledina, L. Salonen, D. Petrovykh, J. Sousa, O. Soares, M. Pereira, S. Kegnæs, Y. Kolen'ko,

262   Catal. Sci. Technol. 10 (2020) 1991 https://doi.org/10.1039/D0CY00145G.

263   4   a) W. Wang, A. Zheng, P. Zhao, C. Xia, F. Li, ACS Catal. 4 (2014) 321 https://doi.org/10.1021/cs400983y, b)

264   X. Wang, S. Lu, J. Li, Y. Liu, C. Li, Catal. Sci. Technol. 5 (2015) 2585 https://doi.org/10.1039/C5CY00038F, c)

265   Z. Dai, Q. Sun, X. Liu, C. Bian, Q. Wu, S. Pan, L. Wang, X. Meng, F. Deng, F.-S. Xiao, J. Catal. 338 (2016)

266   202 https://doi.org/10.1016/j.jcat.2016.03.005, d) Y. Xu, T. Wang, Z. He, M. Zhou, W. Yu, B. Shi, K. Huang,

267   Appl. Catal. Gen-A, 541 (2017) 112 https://doi.org/10.1016/j.apcata.2017.05.005, e) R. Cai, X. Ye, Q. Sun, Q.

268   He, Y. He, S. Ma, X. Shi, ACS Catal. 7 (2017) 1087 https://doi.org/10.1021/acscatal.6b03211.

269   5   a) S. Kraft, R. Sánchez, A. Hock, ACS Catal. 3 (2013) 826, b) T. Iwai, T. Harada, H. Shimada, K. Asano, M.

270   Sawamura, ACS Catal. 7 (2017) 1681 https://doi.org/10.1021/acscatal.6b02988.

271   6   a) M. Aresta, A. Dibenedetto, A. Angelini, Journal of CO_2 Utilization 3-4 (2013) 65

272   https://doi.org/10.1016/j.jcou.2013.08.001, b) M. Aresta, A. Dibenedetto, A. Angelini, Chem. Rev. 114 (2014)

273   1709 https://doi.org/10.1021/cr4002758, c) A. Parvez, M. Afzal, T. Hebb, Journal of CO_2 Utilization 40 (2020)

274   101217 https://doi.org/10.1016/j.jcou.2020.101217.

275   7   a) G. Gunasekar, K. Park, K.-D. Jung, S. Yoon, Inorg. Chem. Front. 3 (2016) 882

276   https://doi.org/10.1039/C5QI00231A, b) X. Su, J. Xu, B. Liang, H. Duan, B. Hou, Y. Huang, Journal of Energy

277   Chemistry 25 (2016) 553 https://doi.org/10.1016/j.jechem.2016.03.009, c) A. Álverez, A. Bansode, A. Urakawa,

278   A. Bavykina, T. Wezendonk, M. Makkee, J. Gascon, F. Kapteijn, Chem. Rev. 117 (2017) 9804

279   https://doi.org/10.1021/acs.chemrev.6b00816, d) S. Dang, H. Yang, P. Gao, H. Wang, X. Li, W. Wei, Y. Sun,

280   Catalysis Today 330 (2019) 61 https://doi.org/10.1016/j.cattod.2018.04.021.

281   8   a) A. Klerke, S. Klitgaard, R. Fehrmann, Catal. Lett. 130 (2009), 541 https://doi.org/10.1007/s10562-009-9964-

282   4, b) A. Züttel, P. Mauron, S. Kato, E. Callini, M. Holzer, J. Huang, Chimia 69 (2015) 264

283   https://doi.org/10.2533/chimia.2015.264, c) A. Singh, S. Singh, A. Kumar, Catal. Sci. Technol. 6 (2016) 12

284   https://doi.org/10.1039/C5CY01276G, d) A. Gallas-Hulin, J. Mielby, S. Kegnæs, ChemistrySelect 1 (2016)

285   3941 https://doi.org/10.1002/slct.201600831, e) H. Kawanami, Y. Himeda, G. Laurenczy, Adv. Inorg. Chem. 70

286   (2017) 395 https://doi.org/10.1016/bs.adioch.2017.04.002, f) J. Eppinger, K.-W. Huang, ACS Energy Lett. 2

287   (2017) 188, g) K. Müller, K. Brooks, T. Autrey, Energy Fuels 31 (2017) 12603, h) J. Mielby, A. Kunov-Kruse,

288   S. Kegnæs, J. Catal. 345 (2017) 149 https://doi.org/10.1016/j.jcat.2016.11.020, i) S. Zacho, J. Mielby, S.

289   Kegnæs, Catal. Sci. Technol. 8 (2018) 4741 https://doi.org/10.1039/C8CY01500G, j) H. Zhong, M. Iguchi, M.

290   Chatterjee, Y. Himeda, Q. Xu, H. Kawanami, Adv. Sustainable Syst. 2 (2018) 1700161

291   https://doi.org/10.1002/adsu.201700161.

292   9   a) P. Preuster, C. Papp, P. Wasserscheid, Acc. Chem. Res. 50 (2017) 74

293   https://doi.org/10.1021/acs.accounts.6b00474, b) P. Aakko-Saksa, C. Cook, J. Kiviaho, T. Repo, J. Power

294   Sources 396 (2018) 803 https://doi.org/10.1016/j.jpowsour.2018.04.011, c) M. Niermann, S. Drünert, M.

295   Kaltschmitt, K. Bonhoff, Energy Environ. Sci. 12 (2019) 290 https://doi.org/10.1039/C8EE02700E, d) M.

296   Niermann, A. Beckendorff, M. Kaltschmitt, K. Bonhoff, Int. J. Hydrogen Energy 44 (2019) 6631

297   https://doi.org/10.1016/j.ijhydene.2019.01.199, e) P. Modisha, C. Ouma, R. Garidzirai, P. Wasserscheid, D.

298   Bessarabov, Energy Fuels, 33 (2019) 2778 https://doi.org/10.1021/acs.energyfuels.9b00296.

299   10 J. Abe, A. Popoola, E. Ajenifuja, O. Popoola, Int. J. Hydrogen Energ. 44 (2019) 15072

300   https://doi.org/10.1016/j.ijhydene.2019.04.068.

301   11 W.-H. Wang, Y. Himeda, J. Muckerman, E. Fujita, Adv. Inorg. Chem. 66 (2014) 189

302   https://doi.org/10.1016/B978-0-12-420221-4.00006-8.

303   12 C. Jia, J. Gao, Y. Dai, J. Zhang, Y. Yang, J. Energy. Chem. 25 (2016) 1027

304   https://doi.org/10.1016/j.jechem.2016.10.003.

305   13 a) Y. Himeda, Eur. J. Inorg. Chem. (2007) 3927 https://doi.org/10.1002/ejic.200700494, b) R. Tanaka, M.

306   Yamashita, K. Nozaki, J. Am. Chem. Soc. 131 (2009) 14168 https://doi.org/10.1021/ja903574e, c) S. Sanz, A.

307   Azua, E. Peris, Dalton Trans. 39 (2010) 6339 https://doi.org/10.1039/C003220D, d) W. Wang, S. Wang, X. Ma,

308   J. Gong, Chem. Soc. Rev. 40 (2011) 3703 https://doi.org/10.1039/C1CS15008A.

309   14 For examples with POPs see: a) N. McNamara, J. Hicks, ChemSusChem 7 (2014) 1114

310   https://doi.org/10.1002/cssc.201301231, b) Z.-Z. Yang, H. Zhang, B. Yu, Y. Zhao, G. Ji, Z. Liu, Chem.

311   Commun. 51 (2015) 1271 https://doi.org/10.1039/C4CC08295H, c) X. Shao, X. Yang, J. Xu, S. Liu, S. Miao, X.

312   Liu, X. Su, H. Duan, Y. Huang, T. Zhang, Chem. 5 (2019) 693 https://doi.org/10.1016/j.chempr.2018.12.014, d)

313   G. Gunasekar, S. Yoon, J. Mater. Chem. A. 7 (2019) 14019 https://doi.org/10.1039/C9TA03807H.

314   15 For examples with COFs see: a) K. Park, G. Hariyanandam, N. Prakash, K.-D. Jung, S. Yoon, ChemSusChem 8

315   (2015) 3410 https://doi.org/10.1002/cssc.201500436, b) G. Hariyanandam, D. Hyun, P. Natarajan, K.-D. Jung,

316   S. Yoon, Catal. Today 265 (2016) 52 https://doi.org/10.1016/j.cattod.2015.10.037, c) K. Park, G. Gunasekar, S.-

317   H. Kim, H. Park, S. Kim, K. Park, K.-D. Jung, S. Yoon, Green Chem. 22 (2020) 1639

318   https://doi.org/10.1039/C9GC03685G.

319   16 For examples with MOFs see: a) D. Sun, Y. Fu, W. Liu, L. Ye, D. Wang, L. Yang, X. Fu, Z. Li, Chem. Eur. J.

320   19 (2013) 14279 https://doi.org/10.1002/chem.201301728, b) M. Chambers, X. Wang, N. Elgrishi, C. Hendon,

321   A. Walsh, J. Bonnefoy, J. Canivet, E. Quadrelli, D. Farrusseng, C. Mellot-Draznieks, M. Fontecave,

322   ChemSusChem 8 (2015) 603 https://doi.org/10.1002/csse.201403345, c) H. Fei, M. Sampson, Y. Lee, C.

323   Kubiak, S. Cohen, Inorg. Chem. 54 (2015) 6821 https://doi.org/10.1021/acs.inorgchem.5b00752, d) B. An, L.

324   Zeng, M. Jia, Z. Li, Z. Lin, Y. Song, Y. Zhou, J. Cheng, C. Wang, W. Lin, J. Am. Chem. Soc. 139 (2017) 17747

325   https://doi.org/10.1021/jacs.7b10922, e) E. Gutterød, S. Øien-Ødegaard, K. Bossers, A.-E. Nieuwelink, M.

326   Manzoli, L. Braglia, A. Lazzarini, E. Borfecchia, S. Ahmadigoltapeh, B. Bouchevreau, B. Lønstad-Bleken, R.

327   Henry, C. Lamberti, S. Bordiga, B. Weckhuysen, K. Lillerud, U. Olsbye, Ind. Eng. Chem. Res. 56 (2017) 13206

328   https://doi.org/10.1021/acs.iecr.7b01457, f) P. Tshuma, B. Makhubela, L. Öhrström, S. Bourne, N. Chatterjee, I.

329   Beas, J. Darkwa, G. Mehlana, RSC. Adv. 10 (2020) 3593 https://doi.org/10.1039/C9RA09938G.

330   17 F. Wang, J. Mielby, F. Richter, G. Wang, G. Prieto, T. Kasama, C. Weidenthaler, H.-J. Bongard, S. Kegnæs, A.

331   Fürstner, F. Schüth, Angew. Chem. Int. Ed. 53 (2014) 8645 https://doi.org/10.1002/anie.201404912.

332   18 Y. Liu, B. Wang, L. Kang, A. Stamatopoulos, H. Gu, F. Wang, Chem. Mater. 32 (2020) 4375

333   https://doi.org/10.1021/acs.chemmater.0c01763.

334   19 J. Zhang, Z. Xia, L. Dai, Sci. Adv. 1 (2015) e1500564 https://doi.org/10.1126/sciadv.1500564.

335   20 a) K. Cychosz, M. Thommes, Engineering 4 (2018) 559 https://doi.org/10.1016/j.eng.2018.06.001, b) M.

336   Alkordi, R. Haikal, Y. Hassan, A.-H. Emwas, Y. Belmabkhout, J. Mater. Chem. A 3 (2015) 22584

337   https://doi.org/10.1039/C5TA05297A.

338   21 T. Iwai, T. Harada, K. Hara, M. Sawamura, Angew. Chem. Int. Ed. 52 (2013) 12322

339   https://doi.org/10.1002/anie.201306769.

340   22 J. Lee, Y. Liou, W. Huang, Inorg. Chim. Acta 319 (2001) 83 https://doi.org/10.1016/S0020-1693(01)00437-6.

341   23 a) J. Hull, Y. Himeda, W.-H. Wang, B. Hasiguchi, R. Periana, D. Szalda, J. Muckerman, E. Fujita, Nat.

342   Chemistry 4 (2012) 383 https://doi.org/10.1038/nchem.1295, b) J. Lee, J. Ryu, J. Kim, S.-W. Nam, J. Han, T.-H.

343   Lim, S. Gautam, K. Chae, C. Yoon, J. Mater. Chem. A 2 (2014) 9490 https://doi.org/10.1039/C4TA01133C.

344   24 D. Mellmann, P. Sponholz, H. Junge, M. Beller, M. Chem. Soc. Rev. 45 (2016) 3954

345   https://doi.org/10.1039/C5CS00618J.

Appendix D.6

WILEY-VCH

COMMUNICATION

Dehydrogenation of bioethanol using Cu nanoparticles supported on N-doped ordered mesoporous carbon

Rouzana Pulikkal Thumbayil, [a] David Benjamin Christensen, [a] Jerrik Mielby, [a] and Søren Kegnæs*[a]

[a]   Dr. R.P. Thumbayil, D.B. Christensen, Dr. J. Mielby, Prof. S. Kegnæs
        Department of Chemistry,
        Technical University of Denmark
        Kemitorvet 207, 2800 Kgs. Lyngby (Denmark)
        E-mail: skk@kemi.dtu.dk

        Supporting information for this article is given via a link at the end of the document.

Abstract: Carbon supported Cu nanoparticles have a remarkable selectivity towards the catalytic dehydrogenation of bioethanol to acetaldehyde, which is an interesting alternative to the preparation from ethylene. In this work, we prepared a series of catalysts comprised of Cu nanoparticles supported on N-doped ordered mesoporous carbons to investigate the catalytic effect of nitrogen content. Our study shows that N-doping has a significant effect on the dispersion of Cu nanoparticles and that the highest content of N results in the highest activity. Furthermore, we show that the combined effects of strong metal-support interactions and nano-confinement is an effective method to prevent thermal and steam induced sintering. In contrast, we find no evidence that N-doping activates the substrate or change the rate-determining step. At 260 °C, the best catalyst results in >99% selectivity and a site-time yield of 175 $mol_{acetaldehyde}/mol_{Cu}/h$. Under these conditions, the catalysts are stable for more than 12 h using an aqueous solution of 10% ethanol as feed.

Introduction

Considering the critical need to reduce the emission of CO_2, the chemical industry must gradually rely on renewable energy and biomass rather than fossil fuel resources. One such example could be the synthesis of acetaldehyde via dehydrogenation or partial oxidation of bioethanol, [1,2] which is an interesting alternative to the preparation from ethylene (the Wacker process). Acetaldehyde is used for the production of acetic acid, ethyl acetate, acetic anhydride, pyridine, vinyl acetate and other commercially important products. [3,4] In the past, the dehydrogenation of ethanol to acetaldehyde was typically performed at 260-290 °C using copper chromite catalysts. Unfortunately, these catalysts suffer from co-formation of several by-products, including ethyl acetate, acetic acid and crotonaldehyde. [5-7] Because of their high selectivity towards acetaldehyde, supported copper catalysts, such as Cu-SiC, [5] Cu/Zeolites, [8] Cu-SiO$_2$, [9,10] Cu-Al$_2$O$_3$, [11] Cu-ZnO-Al$_2$O$_3$, [12] Cu/carbon, [13] or Cu/GO, [14] have therefore sparked renewed interest. Cu supported on carbon materials are currently among the most selective catalysts [13,15] because of the relatively inert carbon surface, which limits secondary reactions such as esterification, aldol condensation or ketonization. [9] However, the weak metal-support interactions and the relatively low melting point of copper make the carbon-supported catalysts particularly prone to sintering. Furthermore, copper easily gets oxidized in air, which results in fast deactivation. [16-20] Encapsulation of nanoparticles to a confined space has proven to be a promising way to stabilize nanoparticle during catalytic reactions. [19] Additionally, the inert surface of mesoporous carbon can help minimize side reactions to increase the selectivity towards acetaldehyde. [9,13]

It has previously been shown that N-doping can increase the metal-support interactions between the metal nanoparticles and the carbon support. [20,21] For instance, Bulushev et al. reported N-doping of carbon and the use of the material as a support for Cu nanoparticles in the catalytic decomposition of formic acid. [22] The use of graphitic-nitrogen for the stabilization of Cu nanoparticles in different N-doped carbon supports such as polyacrylonitrile-based porous carbon (PPC), commercial microporous carbon (CMC) are also reported for dehydrogenation of ethanol to acetaldehyde. Morales et al. reported Cu supported on graphite and reduced graphene oxide functionalized with nitrogen groups for bioethanol as feed. [14] However, the nature and catalytic effect of N-doping on activity and stability of Cu nanoparticles are still not fully understood.

In order to investigate the effect of N-doping, we supported Cu-nanoparticles on three ordered mesoporous carbon materials with different N-content. We then tested the catalysts for the Cu-catalyzed dehydrogenation of bioethanol to acetaldehyde to compare the catalytic activity, selectivity and stability over time. The influence of N-doping on the activation energy of catalysts and reaction mechanism were also studied using Arrhenius plot and in-situ DRIFTS. Additionally, the catalytic activity of commercially available Cu supported on activated carbon (3Cu/AC) were also studied to compare the performance of the synthesized catalysts. In contrast to the ordered mesoporous carbon support, the carbon support in 3Cu/AC is microporous. [23,24]

Three ordered mesoporous carbon with different N-loading were synthesized by changing the carbon-nitrogen precursors. They are abbreviated as NMC-0, NMC-2 and NMC-7, where 0, 2 and 7 refers to the approximate percentage of nitrogen. Figure 1 shows the synthesis of the three ordered mesoporous carbons with different carbon-nitrogen precursors. Synthesis of NMC-7 uses 3-aminophenol (3-AMP) and hexamethylenetetramine (HMTA) as the precursors responsible for the high N-content of
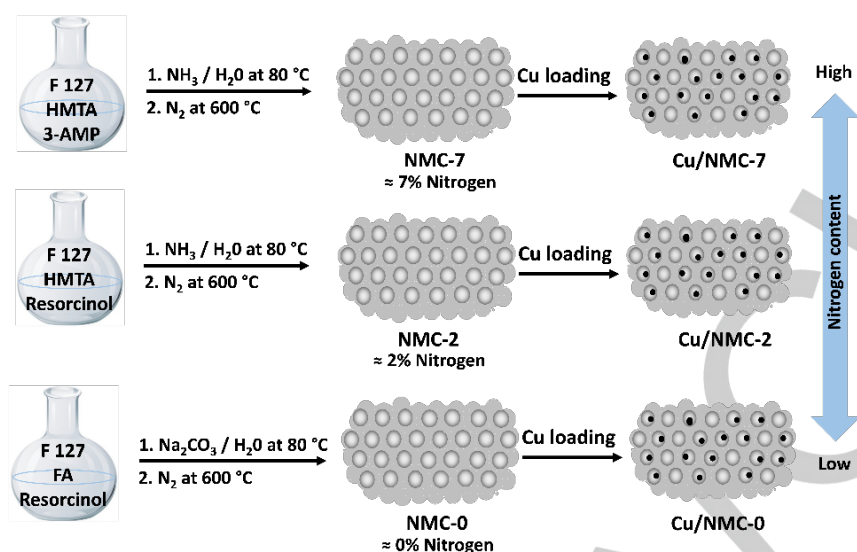
COMMUNICATION

Figure 1. Synthesis route of Cu/NMC-0, Cu/NMC-2 and Cu/NMC-7.

ordered mesoporous carbon. [25] In NMC-2 synthesis, 3-AMP was replaced with resorcinol (with no N-functional group) whereas both 3-AMP and HMTA was exchanged with N-free reagents such as resorcinol, formaldehyde (FA) and Na_2CO_3 for the synthesis of NMC-0.

Results and Discussion

Commercially available copper on activated carbon support was used as a reference to compare the performance of the synthesized materials. Figure 2 shows the N_2 physisorption isotherms of the as-synthesized mesoporous carbon supports and copper on activated carbon. As expected, the physisorption isotherm of the NMCs showed the characteristic type IV isotherm with a H4 hysteresis loop, which is typically associated with capillary condensation in mesoporous materials. [26,27] The hysteresis loop closes around $p/p_0 = 0.3$, 0.38 and 0.45 for NMC-0,

NMC-2 and NMC-7 respectively. The high uptake at low p/p_0 shows the presence of microporous textures in ordered mesoporous carbon. [28] Physisorption analysis of the commercial copper on activated carbon catalyst (3Cu/AC) showed a typical type I isotherm with no significant mesoporosity. As expected, the specific surface area and porosity decreased for all catalysts after loading with Cu nanoparticles, see Table 1. The surface area increased in the order of NMC-7 < NMC-0 < NMC-2, which indicates some
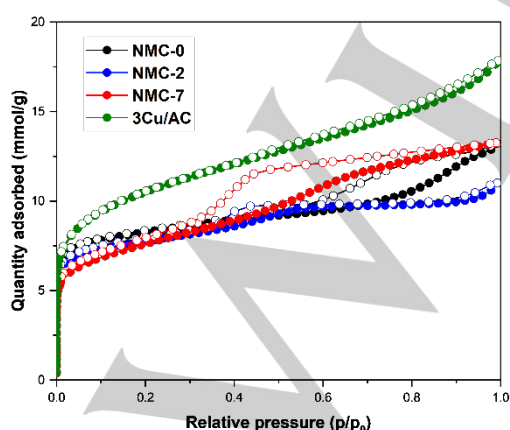

Figure 2. N_2 Physisorption isotherm of mesoporous carbon supports and 3Cu/AC.

Table 1. N_2 Physisorption Data for synthesised materials.

Catalyst	V_{total}[a] (cm³g⁻¹)	V_{micro}[b] (cm³g⁻¹)	S_{BET}[c] (m²g⁻¹)
NMC-0	0.411	0.17	590
3Cu/NMC-0	0.388	0.12	512
NMC-2	0.478	.11	602
1Cu/NMC-2	0.458	0.09	542
3Cu/NMC-2	0.296	0.15	504
8Cu/NMC-2	0.275	0.15	476
NMC-7	0.529	0.09	578
1Cu/NMC-7	0.349	0.11	484
3Cu/NMC-7	0.323	0.10	413
8Cu/NMC-7	0.319	0.08	400
3Cu/AC	0.584	0.16	811

[a] V_{total} determined from the adsorption isotherm branch at around $p/p_0 = 0.95$

[b] V_{micro} calculated by the t-plot method

[c] S_{BET} calculated from BET surface area plot

WILEY-VCH

COMMUNICATION

changes in the textural properties of the different NMC. [29,20] The pore size distribution of all materials is shown in Figure S1. The results show that NMC-2 and NMC-7 are quite similar with a narrow pores size distribution around 5-6 nm, while NMC-0 has a broader size distribution around 10 nm in diameter.

Table 2 shows the carbon and nitrogen content of the support materials determined by elemental analysis. Nitrogen content of NMC-7 is approximately 9.4 wt% while that of NMC-0 is 0.4 wt%. The metal loading in the catalyst were measured by ICP-OES to confirm that the amount of copper precursor used during the synthesis was appropriate. The result confirms the copper loading in the three materials, 3Cu/NMC-0, 3Cu/NMC-2 and 3Cu/NMC-7 to be 2.94, 2.95, 2.8 wt % respectively.

Table 2. Elemental CHN analysis of mesoporous carbon support.

Catalyst	Carbon (%)	Nitrogen (%)	Hydrogen (%)
3Cu/NMC-0	89.9	0.4	9.7
3Cu/NMC-2	86.1	1.5	12.4
3Cu/NMC-7	84.1	9.4	6.5

Figure 3(a) shows the XRD pattern of the prepared catalysts and 3Cu/AC and Figure 3(b) zoom in the Cu(111) peak in three as-synthesized catalysts. Materials with same copper loading (3wt%), 3Cu/NMC-0, 3Cu/NMC-2, 3Cu/NMC-7 and 3Cu/AC shows the characteristic XRD pattern of Cu(111) plane at $2\theta = 43.2°$. However, the intensity of the peak decreases with increase in the N-content of mesoporous carbon. We attribute this to the highly dispersed copper particle on the N-doped carbon. [30,31] In addition to Cu(111) peak, a weak diffraction peak was observed corresponding to $Cu_2O(111)$ for 3Cu/NMC-0, 3Cu/NMC-2 and 3Cu/AC. However, no XRD pattern were observed for mesoporous carbon and therefore confirms the amorphous nature of the ordered mesoporous carbons (Figure S2). Figure S3 shows the XRD pattern of various metal loading on NMC-2 and NMC-7 such as 1 and 8 wt% of copper. In general, the intensity of the Cu(111) peak at 43.2° increases
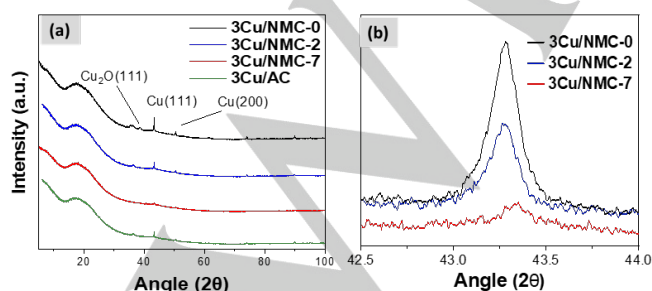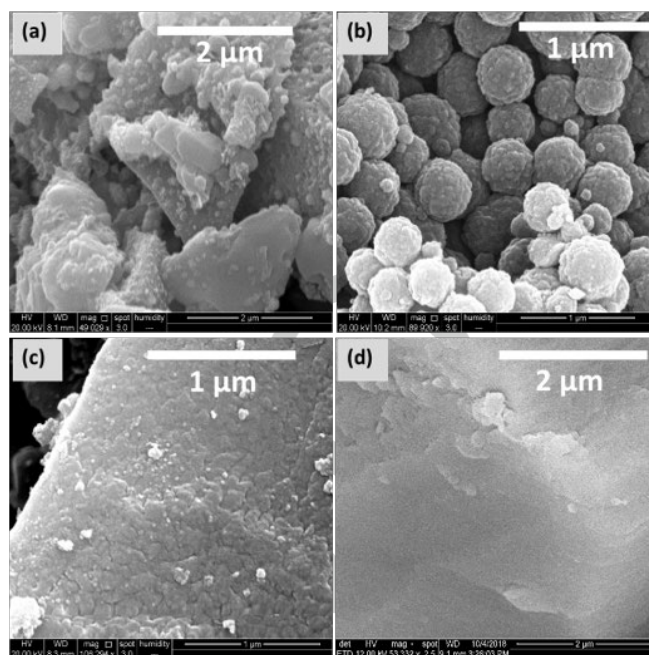

Figure 4. SEM Images of a) 3Cu/NMC-0, b) 3Cu/NMC-2, c) 3Cu/NMC-7 and d) 3Cu/AC.

with the copper loading. The morphology of the materials is analyzed using SEM and is shown in Figure 4. Interestingly, the morphology of the NMC-2 carbon support showed a uniform and spherically shaped mesoporous carbon structures, which are quite different from NMC-0 and NMC-7. This difference in the structure of NMCs is likely due to the difference in the precursors of polymers. The SEM image for 3Cu/AC showed even structures without any visible mesoporosity or channel like structures.

The TEM images of as-synthesized materials in Figure 5 shows uniform and highly ordered mesopores throughout the materials. The measured pore widths are in the range of 5-6 nm for NMC-7, NMC-2 and 8-10 nm for NMC-0, which agree well with the results from the N_2 physisorption analysis. The TEM image of 3Cu/AC in Figure 5(d) shows the particles with average size of 22.1 nm. Figure 5(a-c) shows the TEM images of 3Cu/NMC-0, 3Cu/NMC-2 and 3Cu/NMC-7. With the exception of a few large particles on the external surface of the catalysts, the images show a high dispersion of Cu particles distributed throughout the ordered mesoporous carbons. The size distribution based on the measurement of >200 Cu particles are shown in Figure S4. Most particles in 3Cu/NMC-7 are small with an average particle size of around 6.4 nm. The TEM image of 3Cu/NMC-0 shows both small and large nanoparticles with an average size of particles around 12.4 nm. The copper nanoparticles in 3Cu/NMC-2 has an average size of 11.5 nm. In general, the average size of the nanoparticles increases in the order 3Cu/NMC-7 < 3Cu/NMC-2 < 3Cu/NMC-0. The HAADF image of 3Cu/NMC-7 shown in Figure S5 confirms the confinement of uniformly distributed copper nanoparticles owing to the high nitrogen content. The TEM images for the other materials such as

Figure 3. a) XRD Pattern of 3Cu/NMC-0, 3Cu/NMC-2, 3Cu/NMC-7 and 3Cu/AC b) Cu(111) zoom in.
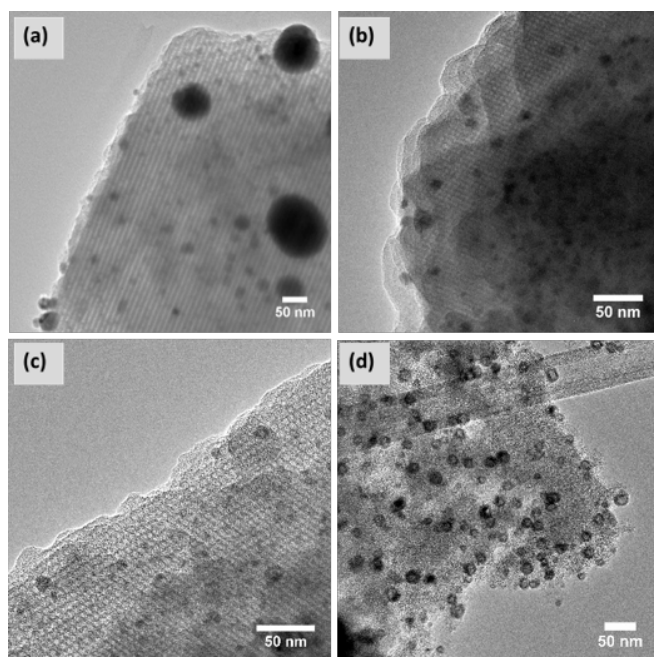
COMMUNICATION

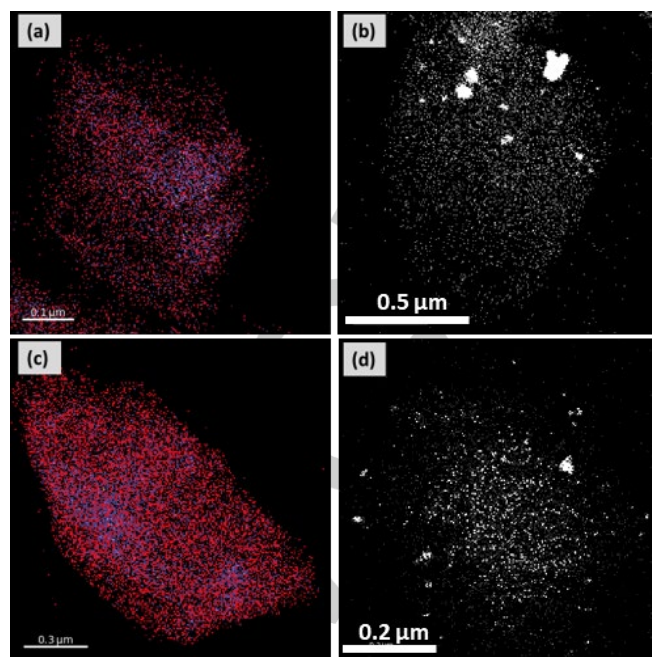**Figure 5.** TEM Images of a) 3Cu/NMC-0, b) 3Cu/NMC-2, c) 3Cu/NMC-7 and d) 3Cu/AC.

Figure 6. EDX Element distribution of a) N in NMC-2 b) Cu in 3Cu/NMC-2 c) N in NMC-7 and d) Cu in 3Cu/NMC-7.

1Cu/NMC-2, 8Cu/NMC-0, 8Cu/NMC-2, 1Cu/NMC-7 and 8Cu/NMC-7 are shown in Figure S5.

The reducibility of the copper particles on 3Cu/NMC-0, 3Cu/NMC-2 and 3Cu/NMC-7 as compared to 3Cu/AC was investigated by H_2-TPR, see Figure S6. The H_2-TPR profile show differences in the shape, number and temperature range of the peaks for the three materials. The difference in the shape of the peaks indicates the presence of more than one type of copper species in the materials. [32] Notably, the TPR profile of the materials showed peaks below 300 °C. This may be explained by the presence of small and well-dispersed copper nanoparticles that are easily reduced.[32,33] In contrast, the high-temperature peak above 400 °C in TPR of 3Cu/AC indicates the presence of large copper oxide nanoparticles that are difficult to reduce. [34]

Figure 6 shows the surface elemental composition of 3Cu/NMC-2 and 3Cu/NMC-7 as determined by EDX analysis. Figure 6(a) and 6(c) shows the N mapping in NMC-2 and NMC-7 respectively, where the N signals are evenly distributed on the surface of ordered mesoporous carbon. However, the intensity of N signal is relatively less in NMC-2 in comparison to NMC-7 and this can be attributed to the nitrogen loading in each sample. Figure 6(b) and 6(d) shows the Cu mapping in NMC-2 and NMC-7, respectively, where the intensity of the Cu photopeak is uniform for both 3Cu/NMC-2 and 3Cu/NMC-7.

Additionally, the surface composition of catalyst materials was conducted using XPS to analyze the and oxidation state of copper nanoparticles on the surface of the carbon support. Deconvolution of the N1s spectra shows the difference in nitrogen species on the different materials (NMC-2 and NMC-7) before and after adding Cu as shown in Figure 7.

The peaks are typically attributed to 4 different types of nitrogen corresponding to pyridinic-N (N1 398.2 eV), pyrrolic-N (N2 399.9 eV), quaternary-N (N3 400.7 eV) and pyridine N-oxide (N4 402.7eV) for NMC-7 [20] Cu loading on the mesoporous carbon support (NMC-7) results in a significant change in the spectra. These changes in N1s spectra of the catalysts are listed in Table S1. Figure 7(b and d) shows that both the N1 and N2 peaks shifted by 0.2 - 1 eV towards higher binding energy. This can be attributed to the strong interaction of Cu with nitrogen species. [35,36] The interaction of Cu species with pyridinic-N results in decrease in the
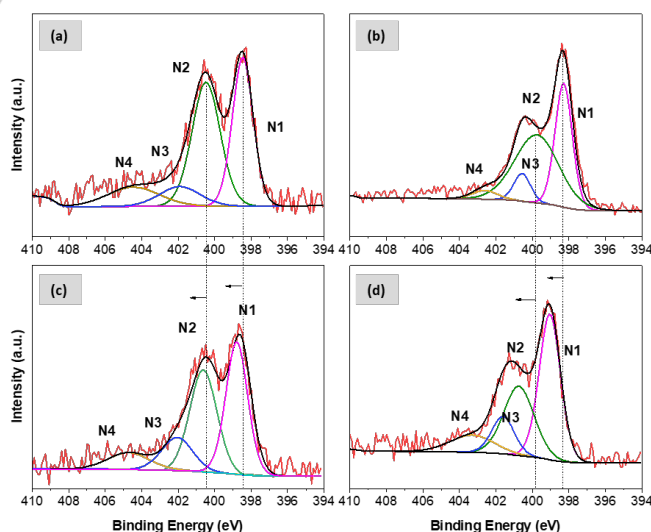

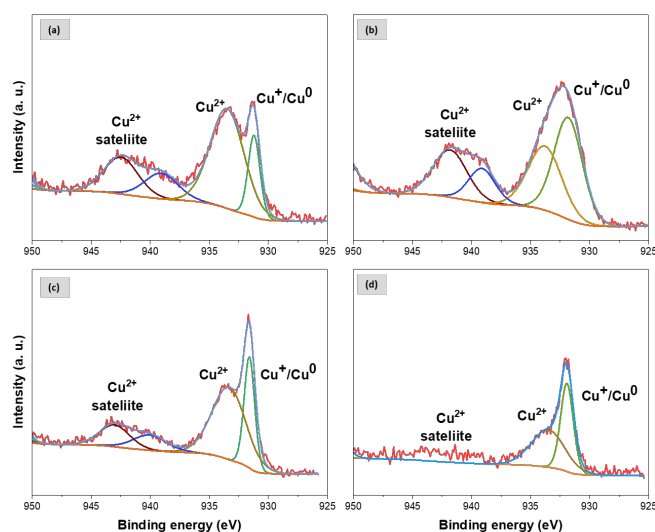**Figure 7.** XPS N1s spectra of a) NMC-2, b) NMC-7, c) 3Cu/NMC-2 and d) 3Cu/NMC-7.

WILEY-VCH

COMMUNICATION

Figure 8. XPS Cu 2p$_{3/2}$ spectra of a) 3Cu/AC, b) 3Cu/NMC-0, c) 3Cu/NMC-2 and d) 3Cu/NMC-7.

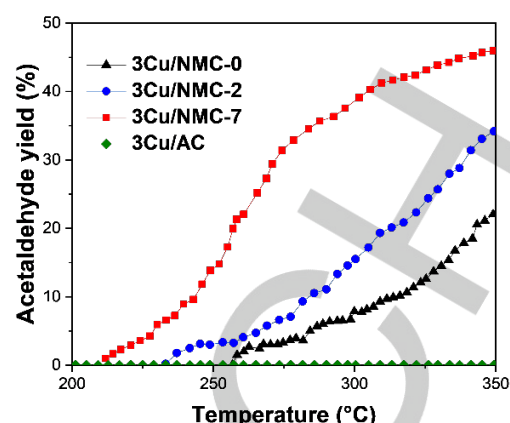**Figure 9.** Effect of temperature on the catalytic activity for 3Cu/AC, 3Cu/NMC-0, 3Cu/NMC-2 and 3Cu/NMC-7 using 10% ethanol as reactant feed

relative intensity of N2 over N3 after impregnating Cu over NMC-7. This further reinforces the strong interaction between copper and nitrogen in Cu loaded samples. The interaction of Cu with NMC-2 resulted in the small decrease in the N2 and N3 peaks. These factors could attribute to the effect of N-doping on Cu. [20,37]

Figure 8 shows the XPS analysis of the Cu 2p$_{3/2}$ photopeaks of 3Cu/NMCs and 3Cu/AC. The materials 3Cu/NMC-2 and 3Cu/NMC-7 showed a narrow Cu$^+$/CuO peaks in XPS and the intensity of Cu^{2+} satellite peak was less in both samples. However, the samples 3Cu/AC and 3Cu/NMC-0 showed broad and large Cu^{2+} satellite peak. The results show a strong interaction of Cu and N species in N-doped catalysts. Moreover, the Cu^{2+} satellite peak around 942 eV was negligibly small for 3Cu/NMC-7, which supports the interaction of Cu and nitrogen in 3Cu/NMC-7. [20,14,38] Additionally, Cu LMM spectra were analyzed, and the spectra are shown in Figure S7. 3Cu/NMC-0, 3Cu/NMC-2 and 3Cu/AC had broad peaks in the Cu$^+$,Cu^0 region.However, the intensity of Cu LMM spectra were too weak to deconvolute to distinguish between Cu$^+$ or Cu^0. [39]

The surface content of C, N, O and Cu in 3Cu/NMC-0, 3Cu/NMC-2, 3Cu/NMC-7 and 3Cu/AC based on XPS are given in the Table 3. The data (C and N) are in good

agreement with the expected composition from the mesoporous carbon precursors used in the synthesis. All materials showed characteristic peaks of copper on the surface of the impregnated catalysts. However, the results showed a lower surface concentration of Cu on NMC-7 confirming higher encapsulation of copper nanoparticles by mesoporous carbon support. XPS data for all as-synthesized catalysts are given in Table S2 and S3.

Catalytic activity test: The catalysts were tested for the dehydrogenation of bioethanol (10% ethanol + 90% water reaction feed) at a gas hourly space velocity, GHSV= 21250 h^{-1}. Figure 9 shows the yield of acetaldehyde against temperature for as-synthesized catalysts and 3Cu/AC. As shown in the figure, the commercial Cu catalyst 3Cu/AC was completely inactive and did not show any catalytic activity for the dehydrogenation reaction. We speculate that the lack of activity of 3Cu/AC was due to the fast oxidation of exposed copper sites or by steam-induced sintering of Cu nanoparticles. [40,41] The yield of acetaldehyde for all synthesized catalysts increased with the temperature. 3Cu/NMC-7 showed a significantly higher acetaldehyde yield than 3Cu/NMC-0 and 3Cu/NMC-2, which demonstrates the positive effect of nitrogen content and/or the small size of copper nanoparticles on ethanol conversion. The possible influence of pore diffusion on the reaction rate of the catalysts was estimated using Weisz-Prater calculations found in Table S4. The result showed negligible pore diffusion limitations with Weisz-Prater Criterion <1.

Figure S8 shows the catalytic activity results for all other catalysts, including 1Cu/NMC-2, 1Cu/NMC-7, 8Cu/NMC-0, 8Cu/NMC-2 and 8Cu/NMC-7. In general, the yield of acetaldehyde increased with the temperature and reaches up to 57% yield of acetaldehyde at 350 °C for 1Cu/NMC-7 and 48% yield of acetaldehyde for 1Cu/NMC-2. Above 99% selectivity towards acetaldehyde was observed for all catalysts irrespective of the N-content of the ordered mesoporous carbon support. Table S5 summarizes the conversion of ethanol for different catalysts at 350 °C. Furthermore, Figure S9 compares the catalytic activity of 3Cu/NMC-7 carbonized at 600, 700 and 800 °C, respectively. 3Cu/NMC-7 carbonized at 600 °C and 700 °C

Table 3. XPS Data for as-synthesized materials..

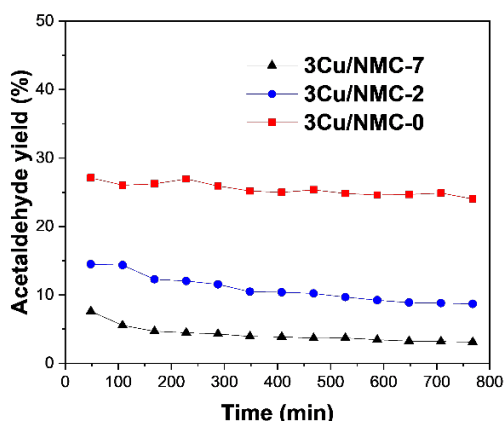| Catalyst	Carbon (%)	Oxygen (%)	Nitrogen (%)	Copper (%)
3Cu/AC	92.3	6.7	0	1.0
3Cu/NMC-0	82.4	16.4	0	1.2
3Cu/NMC-2	88.6	8.8	1.5	1.1
3Cu/NMC-7	87.8	5.3	6.8	0.1

COMMUNICATION

Figure 10. Stability test at 260 °C for as-synthesized catalysts with 10% ethanol feed

exhibited similar activity towards ethanol conversion possibly due to a balance between the influence of surface area of carbon support and nitrogen content, while the material carbonized at 800 °C showed less activity possibly due to the decrease in nitrogen content. The catalytic activity test was also carried out using pure ethanol under similar GHSV and the results are shown in Figure S10. The as-synthesized catalysts showed identical catalytic performance as that of 10% ethanol whereas 3Cu/AC showed some ethanol conversion from 260 °C.

Figure 10 shows the stability of 3Cu/NMC-0, 3Cu/NMC-2 and 3Cu/NMC-7 tested at 260 °C for 800 minutes. All catalyst showed high selectivity above 99% throughout the reaction interval. The catalyst 3Cu/NMC-7 retained around 93% of its initial activity even after 800 minutes whereas the catalysts 3Cu/NMC-2 and 3Cu/NMC-0 retained 68% and 40% of the initial activity, respectively. The high stability of 3Cu/NMC-7 is possibly due to the small and highly dispersed copper nanoparticles combined with high nitrogen content present in the catalyst. 3Cu/NMC-7 also showed higher stability when tested at higher temperature (320 °C) as shown in Figure S11(a). The stability test is also conducted with pure ethanol at the same flowrate (GHSV = 21250 h^{-1}) using 3Cu/AC and 3Cu/NMC-7. Figure S11(b) shows the stability test of 3Cu/NMC-7 as compared to 3Cu/AC. The higher stability of 3Cu/NMC-7 strengthens the evidence for a strong stabilization effect of doped nitrogen against sintering of copper nanoparticles. Stability of the catalysts with 8 wt% Cu using 8Cu/NMC-7 and 8Cu/NMC-2 are also tested at 260 °C
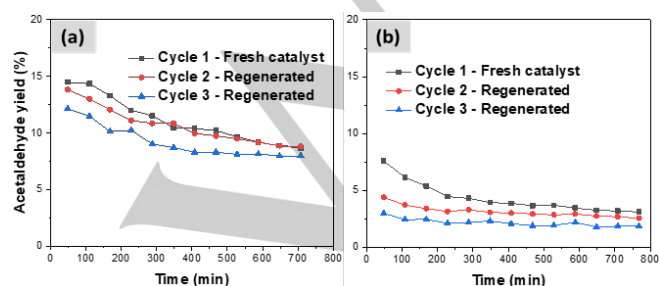
with the results shown in Figure S11(c). 8Cu/NMC-7 showed good stability and it retained nearly 80% of its initial activity after 800 minutes. In general, the loss of activity was less in the case of catalysts with high nitrogen content and can attribute to the strong Cu and support interaction.

The reusability of the catalysts was tested by regenerating the catalysts using an in-situ reduction at 450 °C for 2 hours under H$_2$. The regenerated catalysts were then subjected to the same catalytic test. Figure 11(a) and 11(b) show the re-usability of 3Cu/NMC-2 and 3Cu/NMC-0, respectively. The regenerated catalyst 3Cu/NMC-2 showed 95% and 84% of initial activity over fresh catalyst in cycle 2 and cycle 3. For comparison, 3Cu/NMC-0 showed acetaldehyde yields of 60% and 37% from its initial activity over fresh catalyst in cycle 2 and cycle 3, respectively. The reusability results for the catalyst 3Cu/NMC-7 are shown in Figure S11(d).

Figure 12 shows the TEM images of the spent catalysts analyzed after the stability tests. The TEM image of 3Cu/NMC-0 showed both small and big particles with an average particle size 15.4 nm. In contrast, the TEM image of used 3Cu/NMC-7 with the highest content of N showed well dispersed nanoparticles with no significant change in the particle size distribution. Figure 13 shows the histogram of the particle size distribution of 3Cu/NMC-7 before and after the catalytic activity test. This shows the confinement of copper nanoparticles in the mesoporous carbon of 3Cu/NMC-7. The average size of Cu nanoparticles in 3Cu/AC was increased from 22.1 nm to 34 nm after the stability test and shows higher migration of Cu nanoparticles in 3Cu/AC as compared to the as-synthesized catalysts. Figure S12 shows the particle size distribution of 3Cu/NMC-0, 3Cu/NMC-2 and 3Cu/AC after the stability test.
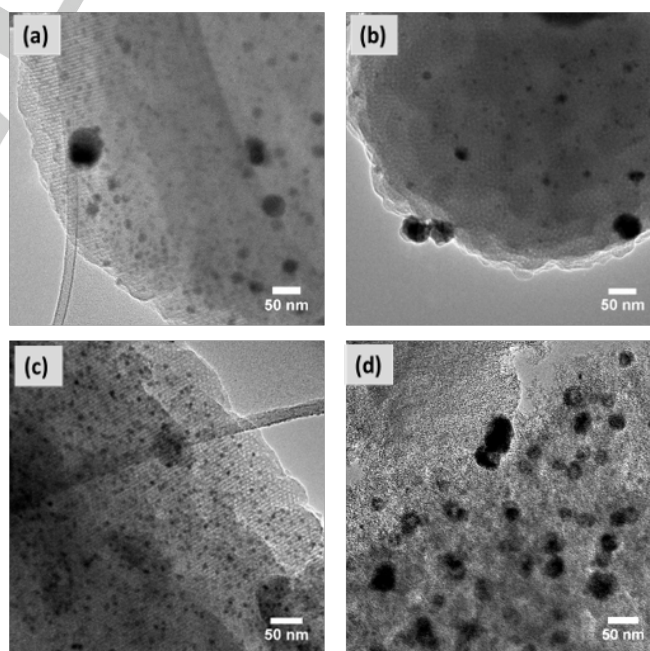

Figure 11. Reusability tests of catalysts a) 3Cu/NMC-2 and b) 3Cu/NMC-0.

Figure 12. TEM Image after stability test for a) 3Cu/NMC-0, b) 3Cu/NMC-2, c) 3Cu/NMC-7 and d) 3Cu/AC.
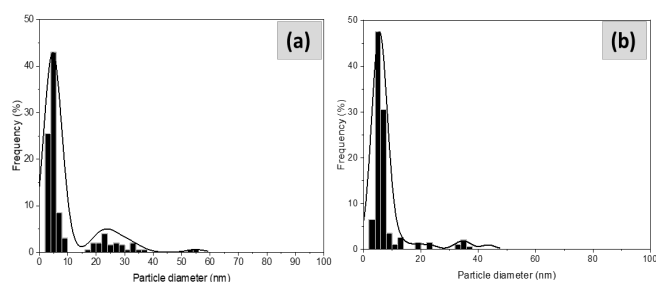
COMMUNICATION

Figure 15. Arrhenius plot of reaction rate over temperature of as-synthesized catalyst.

Figure 14 shows the XRD pattern of the catalysts after the stability test. Compared to the XRD patterns of the fresh catalysts, the intensity of Cu(111) diffraction peak was increased. The intensity of Cu(111) peak increased in the order 3Cu/NMC-7 < 3Cu/NMC-2 ≈ 3Cu/AC < 3Cu/NMC-0. The results are a clear indication of the confinement of small nanoparticles in ordered mesoporous carbon combined with stabilizing effect of copper nanoparticles by nitrogen doping in 3Cu/NMC-7. This stabilization effect due to nitrogen doping is not found in 3Cu/NMC-0 resulting in the sintering of copper nanoparticles during the reaction, a well-known reason for deactivation of copper nanoparticles in dehydrogenation reaction of ethanol. [42,43] The appearance of the typical diffraction peak of $Cu_2O(111)$ further support that surface oxidation may contribute to the deactivation of the catalysts. In line with the previous results, the effect is most significant for the catalysts with no or low nitrogen content.

Figure 15 shows the Arrhenius plots for the catalysts with 3 wt% Cu loading. The apparent activation energies of catalysts are around 86.1, 81.6 and 81.2 kJ/mol for 3Cu/NMC-0, 3Cu/NMC-2 and 3Cu/NMC-7, respectively. This indicates that the N-doping has no effect on the rate-limiting step and can be related to the dispersion of the Cu nanoparticles. The lowering of the light-off temperature is expected to be caused by an increase in active sites, due to the improved distribution of Cu. The particle measurements
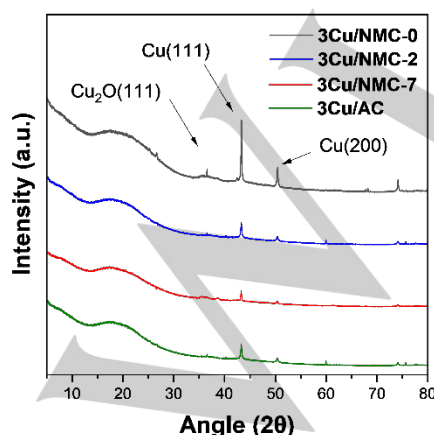
of the N-doped catalysts showed a lower average particle size providing more active sites for the dehydrogenation to occur. At 260 °C, the site-time yield (STY) of the catalysts are 14.6, 39.1 and 175 $mol_{acetaldehyde}/mol_{Cu}/h$ for 3Cu/NMC-0, 3Cu/NMC-2 and 3Cu/NMC-7, respectively. The catalyst 3Cu/NMC-7 was also tested at a high GHSV 26500 and 45450 h^{-1} where STY increased to 202 and 265 $mol_{acetaldehyde}/mol_{Cu}/h$. To the best of our knowledge, catalytic activity of 3Cu/NMC-7 showed best STY of similar catalysts reported. Table S6 shows comparison on activity of catalysts in recently published literature.

In order to investigate the effect of nitrogen in the reaction mechanism, we studied the mechanism on the surface of catalysts by in-situ DRIFTS at temperatures between 50 to 350 °C. The in-situ DRIFTS studies were conducted on 3Cu/NMC-7 and 3Cu/NMC-2. The in-situ DRIFT spectra of 3Cu/NMC-7 and 3Cu/NMC-0 are given in Figure S13(a) and (b). The detailed explanation on major observations from the spectra are given the supporting info. With the spectra of both 3Cu/NMC-7 and 3Cu/NMC-0 showing similar behavior through the temperature range, we can confirm that dehydrogenation of ethanol to acetaldehyde follows similar reaction mechanism with ethoxy formation as an intermediate. Furthermore, nitrogen has no role in defining the mechanism of dehydrogenation reaction.

Conclusion

In this work, we report the synthesis of an efficient and highly selective catalyst for the conversion of bioethanol to acetaldehyde via selective dehydrogenation. The catalyst is comprised of Cu nanoparticles supported on N-doped ordered mesoporous carbon prepared by carbonization of a templated polymer by increasing the amount of N in the polymer precursors, we were able to increase the amount of N in the carbon support from 0 to 7%. The ordered mesoporous carbon with the highest amount of N resulted in the highest Cu loading and, consequently, the highest catalytic activity and stability. We contribute this effect to increased metal-support interactions. Under the given

Figure 14. XRD patterns after stability test.

COMMUNICATION

reaction condition, 3Cu/NMC-7 resulted in a high yield of acetaldehyde with a STY of 175 $mol_{acetaldehyde}/mol_{Cu}/h$, more than 99% selectivity. Furthermore, the N-doped carbon prevent deactivation by surface oxidation or steam induced sintering in the presence of water. In situ DRIFTS studies confirm that the formation of acetaldehyde occurs via an ethoxy intermediate independent but does not indicate that the N-doping activates the ethanol or change the rate-determining step.

Experimental section

Materials: All chemicals and materials are used as received from Sigma-Aldrich with no further purification. Pluronic® F-127(M_n ~ 12 500), 3-aminophenol (3AMP, 98%), hexamethylenetetramine (HMTA, 99%), formaldehyde (FA, 37%), resorcinol (≥99.0%) ammonia (28% aqueous solution, ≥99.99%), sodium carbonate (≥99.0%), ethanol (EtOH >99.8%), copper on activated carbon (3 wt%, 3Cu/AC), copper nitrate hemipentahydrate ($Cu(NO_3)_2\cdot 2.5H_2O$, ≥99.99%).

Synthesis of NMC-0: F-127 (8.8 g) is dissolved in deionized water (208 mL) at room temperature followed by adding resorcinol (4.4 g) and formaldehyde 37% (8.85 mL) by stirring at room temperature. Na_2CO_3 (20 mg) is then added and stirred at 80 °C for 24 hours. The precipitate is collected by centrifugation and washed with deionized water three times. The reddish-brown product is dried at 80 °C overnight and then carbonized at 600 °C in argon atmosphere for 3 hours with a heating ramp of 1 °C/min.

Synthesis of NMC-2: F-127 (8.8 g) is dissolved in deionized water (208 mL) at room temperature followed by adding resorcinol (4.4 g) and hexamethylenetetramine (2.8 g) by stirring at room temperature. NH_3 solution 28% (8 ml) is then added and the mixture is stirred at 80 °C for 24 hours. The precipitate is collected by centrifugation and washed with deionized water three times. The reddish-brown product is dried at 80 °C overnight and then carbonized at 600 °C under argon atmosphere for 3 hours with a heating ramp of 1 °C/min.

Synthesis of NMC-7: The synthesis of NMC-7 was based on a modified version of the procedure reported by Guozhu Shen. [25] F-127 (8.8 g) is dissolved in deionized water (208 mL) at room temperature followed by adding 3-aminophenol (4.4 g) and hexamethylenetetramine (2.8 g) by stirring at room temperature. NH_3 solution 28% (8 ml) is then added and the mixture is stirred at 80 °C for 24 hours. The precipitate is collected by centrifugation and washed with deionized water three times. The reddish-brown product is dried at 80 °C overnight and then carbonized at 600 °C under argon atmosphere for 3 hours with a heating ramp of 1 °C/min.

The same procedure is repeated to prepare two additional NMC-7 samples with carbonisation temperatures of 700 °C and 800 °C, respectively.

Synthesis of xCu/NMC-y: The carbon-supported catalysts are prepared by incipient wetness impregnation using $Cu(NO_3)_2$ as metal precursor and ethanol as solvent. The appropriate amount of $Cu(NO_3)_2\cdot 2.5H_2O$ is mesoporous carbon support (0.485 g) followed by thorough mixing. The resulting material is reduced under a flow of pure H_2 at 450 °C for 2 hours with a heating ramp of 5 °C/min. The same procedure is used to prepare catalyts with 1, 3 and 8 wt% of Cu. The catalysts are named xCu/NMC-y, where x represent the Cu loading and y represent the weight percentage of nitrogen in the mesoporous carbon support.

Catalytic activity test: The catalysts were tested in a fixed-bed quartz tubular reactor under atmospheric pressure. 50 mg of the catalyst (1Cu/NMC-7) without fractionation (approx. particle size < 100 μm) was mixed with fractionated quartz (300-355 μm) and loaded in the reactor. The catalyst was then reduced using 10% H_2 in N_2 gas (100 ml/min) for 90 minutes at 450 °C a heating ramp of 5 °C/min under atmospheric pressure. The gas was then switched to pure N2 (50 ml/min) and the temperature was then lowered to 350 °C. An aqueous solution of 10% ethanol was introduced using a micro pump and the preheated gas mixture is then passed through the reactor with a gas hourly space velocity (GHSV) 21250 h^{-1}. The conversion and selectivity were quantified using an online GC equipped with a flame ionization detector (FID). Gas samples from the reaction outlet were collected and analyzed using GC-MS. The procedure was repeated with pure ethanol. Ethanol flow was adjusted using a syringe pump to get the GHSV similar to the experiment with 10% ethanol.

Characterization: X-ray powder diffraction (XRD) patterns are recorded using a Huber G670 powder diffractometer and Cu-Kα radiation (λ = 1.54056 nm). The diffraction patterns are recorded from 2θ = 5-100°. A Micrometrics 3Flex physisorption instrument is used to record the nitrogen adsorption-desorption isotherm at 77K. The total surface area is determined by the BET method, the total pore volume is determined from a single-point read at 0.95 p/p_0, the microporous volume is calculated from the t-plot and the pore-size distribution are calculated according to the BJH method. Prior to physisorption analysis, the samples are degassed at 200 °C in vacuum for overnight. Scanning electron microscopy (SEM) analysis is performed using a QUANTA FEG 400 SEM instrument and transmission electron microscopy (TEM) analysis is performed using a Tecnai T20 instrument operated at 200 kV. Prior to the analysis, the samples are directly dispersed on a lacey carbon grid. High-angle annular dark-field scanning transmission electron microscopy (HAADF-STEM) analysis is performed on an aberration-corrected JEOL ARM300CF instrument operated at 300 kV. X-ray photoelectron spectroscopy (XPS) is carried out using an angle-resolved XPS instrument Thermo Scientific™ K-Alpha™ spectrometer. All XPS spectra were collected on reduced catalysts. However, the samples were exposed to air after reduction during transfer.

The Cu loading is determined by inductively coupled plasma optical emission spectroscopy using Thermo Scientific™

COMMUNICATION

iCAP™ 7200 ICP-OES. Samples (20 mg) are first treated with 20 mL of aqua regia to dissolve the Cu and then diluted accordingly. The concentration is determined from a calibration line made from a commercial ICP standard. The elemental composition of the mesoporous N-doped carbon support is determined with a Thermo scientific FlashSmart™ Elemental Analyzer. The reduction temperature of the supported Cu nanoparticle are analyzed by temperature-programmed reduction (H_2-TPR) using a Micromeritics Autochem-II instrument. Samples are heated up to 500 °C at a ramp of 10 °C per minute in 5% H_2 in Ar gas flow (50 mL/min). The H_2 consumption is monitored using a thermal conductivity detector (TCD). A cold trap with dry ice is used to trap the water formed during the reduction with H_2. Diffuse reflectance infrared Fourier transform spectroscopy (DRIFTS) is performed on a Thermo Nicolet 6700 FTIR using a reactor and Praying Mantis diffuse reflectance accessory from Harrick Scientific Products. Prior to the analysis, the catalysts are mixed with KBr. The catalyst is then reduced at a temperature of 450 °C for 2 hours followed by a collection of background IR spectra under a flow of N_2. After cooling to 50 °C the N_2 is bubbled through ethanol to introduce the reactant into the reactor. IR spectra are then collected in a temperature range between 50 – 300 °C. Spectra are recorded continuously every 30 seconds until saturation of ethanol on the surface of the catalysts. The flow of ethanol is stopped afterwards followed by passing N_2 on the catalyst surface. Spectra are recorded for every 30 seconds for around 20 to 30 minutes during this process. The same procedure is repeated for temperature 100, 200, 300 and 350 °C. Spectra of pure ethanol on KBr pellet is also recorded in order to differentiate between the DRIFTS peaks of gaseous ethanol and the ethanol on catalyst surface.

Acknowledgements

Keywords: Dehydrogenation • N-doping • Heterogeneous catalysis • DRIFTS • Cu nanoparticles

[1]   C. H. Christensen, B. Jørgensen, J. Rass-Hansen, K. Egeblad, R. Madsen, S. K. Klitgaard, S. M. Hansen, M. R. Hansen, H. C. Andersen, A. Riisager, *Angew. Chemie - Int. Ed.* **2006**, *45*, 4648–4651.
[2]   R. Harun, M. K. Danquah, G. M. Forde, *J. Chem. Technol. Biotechnol.* **2010**, *85*, 199–203.
[3]   J. Mielby, J. O. Abildstrøm, F. Wang, T. Kasama, C. Weidenthaler, S. Kegnæs, *Angew. Chemie - Int. Ed.* **2014**, *53*, 12513–12516.
[4]   Y. Y. Gorbanev, S. Kegnæs, C. W. Hanning, T. W. Hansen, A. Riisager, *ACS Catal.* **2012**, *2*, 604–612.
[5]   M. Y. Li, W. D. Lu, L. He, F. Schüth, A. H. Lu, *ChemCatChem* **2019**, *11*, 481–487.
[6]   M. Kuwahara, M. Nishioka, M. Yoshida, K. ichi Fujita, *ChemCatChem*

[7]   G. M. Lari, K. Desai, C. Mondelli, J. Pérez-Ramírez, *Catal. Sci. Technol.* **2016**, *6*, 2706–2714.
[8]   S. Velu, L. Wang, M. Okazaki, K. Suzuki, S. Tomura, *Microporous Mesoporous Mater.* **2002**, *54*, 113–126.
[9]   Q. N. Wang, L. Shi, W. Li, W. C. Li, R. Si, F. Schüth, A. H. Lu, *Catal. Sci. Technol.* **2018**, *8*, 472–479.
[10] M. Ohira, H. Liu, D. He, Y. Hirata, M. Sano, T. Suzuki, T. Miyake, *J. Japan Pet. Inst.* **2018**, *61*, 205–212.
[11] F. Zaccheria, N. Ravasio, R. Psaro, A. Fusi, *Chem. - A Eur. J.* **2006**, *12*, 6426–6431.
[12] J. C. Serrano-Ruiz, R. Luque, A. Sepúlveda-Escribano, *Chem. Soc. Rev.* **2011**, *40*, 5266–5281.
[13] J. Ob-eye, P. Praserthdam, B. Jongsomjit, *Catalysts* **2019**, *9*, 66.
[14] M. V. Morales, E. Asedegbega-Nieto, B. Bachiller-Baeza, A. Guerrero-Ruiz, *Carbon N. Y.* **2016**, *102*, 426–436.
[15] W. D. Lu, Q. N. Wang, L. He, W. C. Li, F. Schüth, A. H. Lu, *ChemNanoMat* **2018**, *4*, 505–509.
[16] C. Wang, G. Garbarino, L. F. Allard, F. Wilson, G. Busca, M. Flytzani-Stephanopoulos, *ACS Catal.* **2016**, *6*, 210–218.
[17] L. Liu, A. Corma, *Chem. Rev.* **2018**, *118*, 4981–5079.
[18] G. Garbarino, P. Riani, M. Villa García, E. Finocchio, V. Sanchez Escribano, G. Busca, *Catal. Today* **2019**, 0–1.
[19] A. B. Laursen, K. T. Højholt, L. F. Lundegaard, S. B. Simonsen, S. Helveg, F. Schüth, M. Paul, J. D. Grunwaldt, S. Kegnœs, C. H. Christensen, et al., *Angew. Chemie - Int. Ed.* **2010**, *49*, 3504–3507.
[20] P. Zhang, Q. N. Wang, X. Yang, D. Wang, W. C. Li, Y. Zheng, M. Chen, A. H. Lu, *ChemCatChem* **2017**, *9*, 505–510.
[21] S. Kramer, F. Hejjo, K. H. Rasmussen, S. Kegnæs, *ACS Catal.* **2018**, *8*, 754–759.
[22] D. A. Bulushev, A. L. Chuvilin, V. I. Sobolev, S. G. Stolyarova, Y. V. Shubin, I. P. Asanov, A. V. Ishchenko, G. Magnani, M. Riccò, A. V. Okotrub, et al., *J. Mater. Chem. A* **2017**, *5*, 10574–10583.
[23] G. de Falco, F. Montagnaro, M. Balsamo, A. Erto, F. A. Deorsola, L. Lisi, S. Cimino, *Microporous Mesoporous Mater.* **2018**, *257*, 135–146.
[24] Y. Yang, Y. Qian, C. Xu, J. Jiang, X. Chen, *Appl. Mech. Mater.* **2012**, *184–185*, 1466–1470.
[25] G. Shen, X. Sun, H. Zhang, Y. Liu, J. Zhang, A. Meka, L. Zhou, C. Yu, **2015**, 24041–24048.
[26] R. A. W. Sing, K.S.W., Everet, D. H., Haul, *Pure Appl. Chem.* **1985**, *57*, 603–619.
[27] F. Goodarzi, L. Kang, F. R. Wang, F. Joensen, S. Kegnæs, J. Mielby, *ChemCatChem* **2018**, *10*, 1566–1570.
[28] M. Thommes, K. Kaneko, A. V. Neimark, J. P. Olivier, F. Rodriguez-Reinoso, J. Rouquerol, K. S. W. Sing, *Pure Appl. Chem.* **2015**, *87*, 1051–1069.
[29] P. Zhang, L. Wang, S. Yang, J. A. Schott, X. Liu, S. M. Mahurin, C. Huang, Y. Zhang, P. F. Fulvio, M. F. Chisholm, et al., *Nat. Commun.* **2017**, *8*, 1–10.
[30] X. H. Li, K. Wan, Q. B. Liu, J. H. Piao, Y. Y. Zheng, Z. X. Liang, *Cuihua Xuebao/Chinese J. Catal.* **2016**, *37*, 1562–1567.
[31] E. A. Redina, A. A. Greish, I. V. Mishin, G. I. Kapustin, O. P. Tkachenko, O. A. Kirichenko, L. M. Kustov, *Catal. Today* **2015**, *241*, 246–254.
[32] R. X. Zhou, X. Y. Jiang, J. X. Mao, X. M. Zheng, *Appl. Catal. A Gen.* **1997**, *162*, 213–222.
[33] C. Xia, J. Chen, F. Cui, X. Zhang, H. Kang, Z. Huang, *Chem. Mater.* **2008**, *20*, 5090–5099.
[34] R. Poreddy, C. Engelbrekt, A. Riisager, *Catal. Sci. Technol.* **2015**, *5*, 2467–2477.
[35] Y. Xie, C. Zhang, X. He, J. W. Su, T. Parker, T. White, M. Griep, J. Lin, *Appl. Surf. Sci.* **2019**, *464*, 344–350.
[36] A. Diacon, E. Rusen, A. Mocanu, L. C. Nistor, *Sci. Rep.* **2017**, *7*, 10345.
[37] Y. Gao, J. Li, L. Wang, et al. *Nanotechnology.* **2020**, 31(5), 055705
[38] J. C. Bauer, G. M. Veith, L. F. Allard, Y. Oyola, S. H. Overbury, S. Dai, *ACS Catal.* **2012**, *2*, 2537–2546.
[39] M. Galbiati, A. Stoot, D. Mackenzie, et al. *Sci Rep.* **2017**, 7, 39770
[40] G. Di. M. R. Dabera, M. Walker, A. M. Sanchez, H. J. Pereira, R. Beanland, R. A. Hatton, *Nat. Commun.* **2017**, *8*, DOI 10.1038/s41467-017-01735-6.

WILEY-VCH

COMMUNICATION

[41] T. Mitsudome, Y. Mikami, K. Ebata, T. Mizugaki, K. Jitsukawa, K. Kaneda, *Chem. Commun.* **2008**, *2*, 4804–4806.

[42] E. Santacesaria, G. Carotenuto, R. Tesser, M. Di Serio, *Chem. Eng. J.* **2012**, *179*, 209–220.

[43] J. M. Conesa, M. V. Morales, C. López-Olmos, I. Rodríguez-Ramos, A. Guerrero-Ruiz, *Appl. Catal. A Gen.* **2019**, *576*, 54–64.

WILEY-VCH

COMMUNICATION

Appendix D.7

A Synergic Activity of Urea/Butyl Imidazolium Ionic Liquid Supported on UiO-66-NH$_2$ Metal–Organic Framework for Synthesis of Oximes

Saeed Askari[1] · Mohammad Jafarzadeh[1] · David Benjamin Christensen[2] · Søren Kegnæs[2]
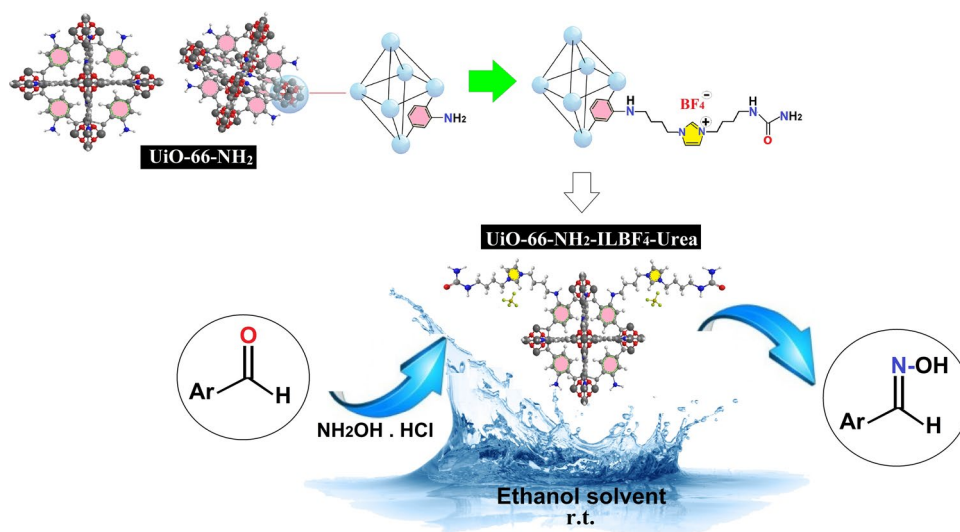
Abstract

An efficient supported ionic liquid catalyst is designed for condensation reaction of aldehydes and ketones. The Zr-based metal–organic framework (MOF), UiO-66-NH$_2$, was initially functionalized with *N,N′*-dibutyl imidazolium ionic liquid (UiO-66-NH$_2$-ILBr$^-$), and then urea was attached to the ionic liquid (IL) to form a task-specific IL. Bromide was exchanged with tetrafluoroborate and the catalyst exhibits excellent performance for the synthesis of oximes. The ionic liquid/urea coupling showed a synergistic effect on the efficiency of the reaction. The supported catalyst system was recycled simply by filtration and reused for five times without significant decrease in its activity. The catalyst was characterized with PXRD, FTIR, TGA, XPS, BET, FE-SEM, EDS, elemental mapping and elemental analysis (CHN).

Graphic Abstract

MOF/IL/urea catalytic system was used for the synthesis of oximes

✉ Mohammad Jafarzadeh
  m.jafar@razi.ac.ir

Extended author information available on the last page of the article

1 Introduction

Supported ionic liquids (SILs) and supported ionic liquid phase (SILPs) have attracted some interests due to their unique properties and activities compared to conventional ionic liquids (ILs) [1, 2]. A SILP material is defined as a thin and multilayer film (a few nanometer thick) of the ionic

liquid physisorbed on the surface of porous materials [3], while in SILs a monolayer of an ionic liquid is covalently immobilized on the surface (sometimes called as supported ionic liquid-like phase; SILLP) [1]. These concepts diminish the typical issue of the ILs such as high cost, large volume usage, high viscosity (cause difficulty in mass transfer and reactant diffusion) [4], and the need for liquid–liquid extraction for their recovery. Heterogenization of ILs on support materials (e.g. silica, alumina, titania, activated carbon, polymer) [5–7] not only reduce the amount of ionic liquid, provide short diffusion distance (due to a nanometer thickness) [4], makes for easier handling, recycling and long-term stability of ionic liquids [6], and reduce potential risk to the environment due their poor biodegradability [1], but also promotes the performance of the hybrid materials in their applications [6].

Although, SILPs have some advantages such as easy preparation and simple operation particularly in fixed-bed reactors for gas phase reactions, but they suffer from pore blocking and instability in the reaction medium especially in liquid phase. The IL can be removed from the surface (leaching) by force of mechanical stirring and/or dissolving in reaction media [1, 8, 9]. In contrast, by covalent grafting of ILs to the functional groups on the surface of the support, the stability and durability of SILs in organic syntheses may improve significantly. SILs have been used as hosts for organocatalysts [10], metal-complexes [8], and metal nanoparticles [6, 11] and generated task-specific ionic liquids (TSILs) [12–15] and specifically the concept of supported ionic liquid catalysts (SILC) [9, 16–18]. Metal–organic frameworks (MOFs), as class of promising porous materials, have been employed as suitable supports for immobilizing ILs [19, 20] and catalysts [21, 22] due to their high surface area, large pore volume, and available/accessible pores [23]. A synergic effect arising from their hybridization have previously been shown to enhance the efficiency of the catalytic reactions [19, 20]. MOF/TSIL hybrid materials have been used for various organic reactions such as acetalization of benzaldehydes with glycol [24], selective oxidation of cyclohexenes [25] and benzyl alcohols [26, 27], adsorptive desulfurization [28, 29], Knoevenagel condensation [30], cycloaddition of CO_2 with epoxides [31–33] and synthesis of biodiesels [34].

Oximes are important intermediates for synthesis of nitriles [35], amides (Beckmann rearrangement) [36–38], nitrones, hydroximinoyl chlorides, and chiral α-sulfinyl oximes [39]. They are also used for preparation of carbonyl compounds [40] and metal complexes [41], protecting carbonyl compounds, inhibiting enzymes [42] and manufacturing of pharmaceutical products and insecticides [43]. Although various methods have been developed recently for the synthesis of oximes such as decomposition of tosylhydrazones [44], oxidation of methylarenes (in the presence of a nitrogen source) [45], oxidation of primary amines [46], ammoximation of different ketones and aldehydes using polyoxometalates [47, 48], and transoximation [49], but the conventional method is still considered due to the simplicity of the procedure. Oximes are generally synthesized via a condensation reaction of carbonyl compounds (aldehydes and ketones) with hydroxylamine in acidic or basic conditions [50]. Since hydroxylamine is dangerous to handle and use [51], hydroxylamine hydrochloride is generally employed to generate in-situ hydroxylamine in the reaction medium, with only water and HCl as by-products [50]. Besides conventional conditions for the synthesis of oximes, microwave-assisted [52], ultrasonic [42], and mechanochemical [53] methods have been also developed. ILs have found much interest as an alternative reaction media for the synthesis of oximes [54–56]. It is expected that the application of SILs in the synthesis of oximes can find some benefits in an aspect of economic and environment.

In the present work, zirconium-based MOF, UiO-66-NH₂, is modified by a post-synthesis with imidazolium bromide (ILBr⁻) for the preparation of supported ionic liquid on the surface of the MOF. The SIL was further functionalized with urea to prepare a TSIL. Urea offers basic sites and hydrogen bond donors [57] for catalyzing organic synthesis of oximes, similar to the glycine-catalyzed synthesis in the previous report [58]. However, the urea-functionalized SIL serves as a catalyst and medium in this work. It is expected that the functionalized MOF exhibits heterogeneous characteristics for the IL and the base.

2 Experimental

2.1 Synthesis of 1,3-Bis-(4-bromo-butyl)-3*H*-imidazol-1-ium Bromide (ILBr⁻)

The preparation of the ionic liquid was adopted from a previously reported method [59]. Imidazole (290 mg, 4.3 mmol) was dissolved in THF (4 mL), and then a solution of sodium hydride (135 mg, 5 mmol) in THF (3 mL) was slowly added at 0 °C. After 45 min of stirring at room temperature, 1,4-dibromobutane (0.51 mL, 4.3 mmol) was added slowly to the above solution and stirred for 2 days. The product was extracted from the reaction mixture using ethyl acetate. In the second step, the product was dissolved in THF and stirred for 45 min. 1,4-dibromobutane (0.55 mL, 4.6 mmol) was then added into the mixture and refluxed for 2 days. The final product was isolated by extraction using ethyl acetate. The products were identified by ¹H and ¹³C NMR and the spectra were compared with data for a similar structure [60] (refer to Supporting Information for details).

2.2 Preparation of UiO-66-NH$_2$-ILBF$_4^-$-Urea

UiO-66-NH$_2$ was prepared according the method reported in the literature [61, 62]. The prepared UiO-66-NH$_2$ (0.1 g) was dispersed in 10 mL DMF in a round-bottomed flask using sonication for 5 min. Next, (0.03 mmol, 10 mg) 1,3-bis-(4-bromo-butyl)-3*H*-imidazol-1-ium bromide was added to the mixture, and the solution was stirred under reflux for 24 h. Next, (0.06 mmol, 3.6 mg) urea was added to the mixture to form Task Specific Ionic Liquid (TSIL). After 24 h stirring under reflux, the precipitate was isolated by centrifugation. The product (UiO-66-NH$_2$-ILBr$^-$-urea) was washed with DMF, water and ethanol. The supported ionic liquid phase was dried at 80 °C in an oven for 24 h. In the next step, an anion exchange was carried out by addition of sodium tetrafluoroborate (0.175 g, 1.5 mmol) to the solution of UiO-66-NH$_2$-ILBr$^-$-urea (0.1 g) in acetone (2 mL) followed by stirred at room temperature for 24 h. The exchanged IL was then filtered and washed with H$_2$O (3 × 10 mL), EtOH (3 mL), Et$_2$O (2.5 mL), and acetone (2.5 mL). The resulting UiO-66-NH$_2$-ILBF$_4^-$-urea was dried at 50 °C in an oven overnight to give the final product.

2.3 General Procedure for the Synthesis of Oximes

0.05 g of UiO-66-NH$_2$-ILBF$_4^-$-urea dispersed in 1 mL ethanol was added to a mixture of benzaldehyde (1 mmol, 0.11 mL) and hydroxylamine hydrochloride (1.5 mmol, 0.1 g). Stirring at 25 °C (room temperature) was continued until the benzaldehyde was consumed, as monitored by thin layer chromatography (TLC). After completion of the reaction, the reaction mixture was added to 10 mL water and extracted with ether (3 × 10 mL). Further purification was accomplished by washing it with ethyl acetate and *n*-hexane. The organic products were identified by ^{1}H and ^{13}C Nuclear Magnetic Resonance (NMR, Bruker 400 MHz) spectroscopy, by comparing with data in the literature [63]. The catalyst was washed with water and ethanol, and dried at 60 °C in an oven overnight. The catalyst was reused for several times under the same reaction conditions.

2.4 Spectral Data

2.4.1 Entry 1 (Benzaldehyde Oxime)

^{1}H NMR (400 MHz, d_6-DMSO): δ (ppm) 8.14 (s, 1H), 7.77–7.75 (d, 2H), 7.40–7.38 (m, 1H), 7.03–7.0 (dd, 2H); ^{13}C NMR (100 MHz, d_6-DMSO): δ (ppm) 167.52, 151.64, 131.88, 129.71, 126.84, 118.02, 115.06.

2.4.2 Entry 2 (2-Hydroxylbenzaldehyde Oxime)

^{1}H NMR (400 MHz, d_6-DMSO): δ (ppm) 8.33 (s, 1H), 7.49–7.47 (dd, 1H), 7.25–7.21 (dd, 1H), 6.90–6.86 (m, 2H); ^{13}C NMR (100 MHz, d_6-DMSO): δ (ppm) 156.42, 147.96, 130.93, 128.30, 119.80, 118.72, 116.46.

2.4.3 Entry 3 (2-Methylbenzaldehyde Oxime)

^{1}H NMR (400 MHz, d_6-DMSO): δ (ppm) 8.29 (s, 1H), 7.67–7.64 (dd, 1H), 7.50–7.35 (td, 1H), 7.08–7.06 (d, 1H), 6.98–6.94 (t, 1H), 3.41 (s, 3H); ^{13}C NMR (100 MHz, d_6-DMSO): δ (ppm) 157.26, 143.86, 131.23, 125.88, 121.38, 121.07, 112.19, 56.10. (Figure S10, Supporting Information).

2.4.4 Entry 4 (3,4,5-Trimethoxybenzaldehyde Oxime)

^{1}H NMR (400 MHz, CDCl$_3$): δ (ppm) 8.08 (s, 1H), 6.84 (s, 2H), 3.90 (s, 9H); ^{13}C NMR (100 MHz, CDCl$_3$): δ (ppm) 153.48, 150.21, 139.71, 127.40, 104.12, 60.95, 56.18. (Figure S11, Supporting Information).

2.4.5 Entry 5 (Cinnamaldehyde Oxime)

^{1}H NMR (400 MHz, d_6-DMSO): δ (ppm) 7.58–7.56 (d, 1H), 7.42–7.39 (dd, 2H), 7.38–7.36 (t, 1H), 7.33–7.32 (dd, 2H), 7.29 (d, 1H), 6.98–6.95 (d, 1H); ^{13}C NMR (100 MHz, d_6-DMSO): δ (ppm) 147.68, 138.35, 136.36, 129.50, 129.36, 127.67, 116.59.

2.4.6 Entry 6 (4-Nitrobenzaldehyde Oxime)

^{1}H NMR (400 MHz, d_6-DMSO): δ (ppm) 8.31 (s, 1H), 8.27–8.24 (dd, 2H), 7.88–7.84 (dd, 2H); ^{13}C NMR (100 MHz, d_6-DMSO): δ (ppm) 147.97, 147.29, 139.96, 127.80, 124.45.

2.4.7 Entry 7 (3-Nitrobenzaldehyde Oxime)

^{1}H-NMR (400 MHz, d_6-DMSO): δ (ppm) 8.42–8.41 (t, 1H), 8.32 (s, 1H), 8.23–8.20 (dd, 1H), 8.06–8.03 (dd, 1H), 7.72–7.68 (t, 1H); ^{13}C NMR (100 MHz, d_6-DMSO): δ (ppm) 148.57, 147.04, 135.39, 132.77, 130.79, 124.11, 121.26.

2.4.8 Entry 8 (2-Chlorobenzaldehyde Oxime)

^{1}H NMR (400 MHz, d_6-DMSO): δ (ppm) 8.37 (s, 1H), 7.83–7.81 (dd, 1H), 7.52–7.50 (dd, 1H), 7.45–7.42 (dd, 1H), 7.40–7.38 (dd, 1 H); ^{13}C NMR (100 MHz,

d_6-DMSO): δ (ppm) 144.99, 132.64, 131.40, 130.74, 130.29, 128.01, 127.26.

2.4.9 Entry 9 (4-Methoxybenzaldehyde Oxime)

^{1}H NMR (400 MHz, d_6-DMSO): δ (ppm) 8.06 (s, 1H), 7.96–7.93 (d, 1H), 7.53–7.51 (d, 1H), 7.31 (d, 1H), 6.99–6.95 (t, 1H), 3.79 (s, 3H); ^{13}C NMR (100 MHz, d_6-DMSO): δ (ppm) 160.25, 148.07, 144.71, 132.76, 128.28, 114.64, 114.13, 55.66. (Figure S12, Supporting Information).

2.4.10 Entry 10 (Acetophenone Oxime)

^{1}H NMR (400 MHz, d_6-DMSO): δ (ppm) 7.32–7.27 (dd, 2H), 7.21–7.19 (dd, 2H), 7.18 (t, 1H), 1.64 (s, 3H); ^{13}C NMR (100 MHz, d_6-DMSO): δ (ppm) 155.05, 138.11, 128.90, 126.60, 13.50.

2.4.11 Entry 11 (Cyclohexanone Oxime)

^{1}H NMR (400 MHz, d_6-DMSO): δ (ppm) 2.40–2.37 (t, 2H), 2.17–2.14 (m, 2H), 1.58–1.52 (m, 6H); ^{13}C NMR (100 MHz, d_6-DMSO): δ (ppm) 159.35, 31.80, 27.03, 25.72, 24.53.

2.5 Characterization Techniques

Powder X-ray diffraction (PXRD) was used to study the crystalline nature of the MOF (UiO-66-NH_2) before and after modification (fresh and reused catalyst) by a Rigaku D-Max C III diffractometer (Cu Kα, λ = 1.5418 Å). Infrared spectra were recorded by a Fourier transform infrared spectroscopy (FT-IR), from a Bruker vector 22 spectrometer,

using KBr pellets. The chemical composition of the modified MOF was examined by a CHN elemental analyzer (Euro EA—HEKAtech GmbH) under N_2 gas flow and X-ray photoelectron spectroscopy (XPS) on a Kratos Axis Ultra-DLS spectrometer (Al K_α source). The data was analyzed using the CasaXPS software. The thermal stability and organic species loading were studied by thermogravimetric analysis (TGA; Perkin Elmer STA 6000) at a heating rate of 10 °C min^{-1} under nitrogen flow. The morphology and elemental analysis were carried out by a field emission scanning electron microscope (FE-SEM; FEI NOVA NanoSEM 450) equipped with energy dispersive X-ray spectroscopy (EDX). Platinum spurring was carried out on the samples before analysis to avoid undesirable electron charging. The BET (Brunauer–Emmett–Teller) specific surface area and adsorption BJH (Barrett–Joyner–Halenda) pore size/volume of the samples were measured by an automatic porosimeter (Micromeritics, Tristar II 3020). The samples were degassed under vacuum overnight before analysis. TEM images was acquired on a FEI Tecnai T20 G2 instrument at 200 kV from Thermo Fisher Scientific. Powdered samples were placed on holey carbon grids with no prior treatment.

3 Results and Discussion

3.1 Preparation and Characterization of UiO-66-NH_2-$ILBF_4^-$-Urea Catalyst

After synthesizing the ionic liquid, 1,3-bis-(4-bromo-butyl)-3H-imidazol-1-ium bromide ($ILBr^-$), the UiO-66-NH_2 was functionalized by $ILBr^-$ and followed by urea. The reaction pathway to prepare UiO-66-NH_2-$ILBr^-$-urea is given

Scheme 1 Preparation of $ILBr^-$ and UiO-66-NH_2-$ILBr^-$-urea
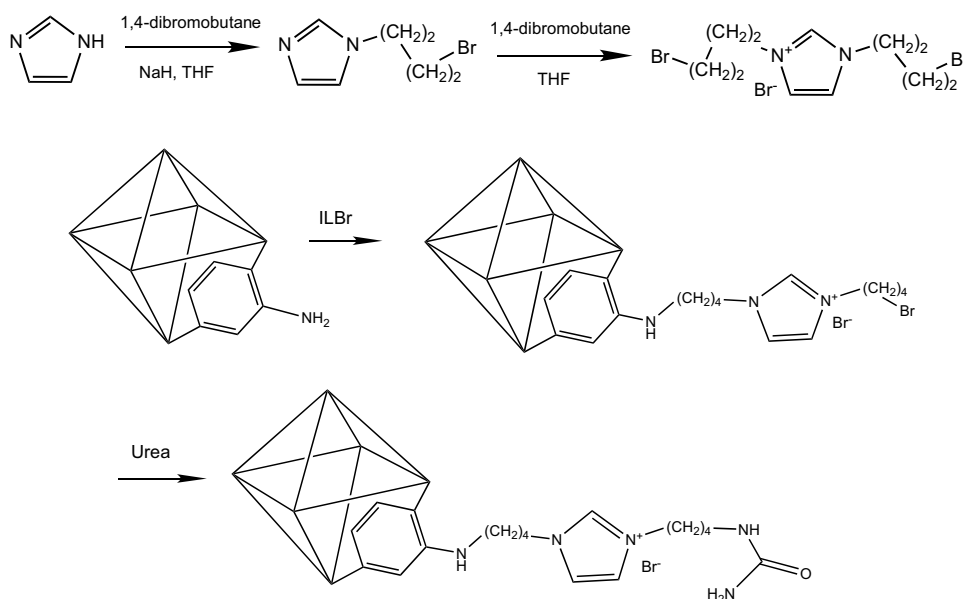
in Scheme 1. In addition, UiO-66-NH$_2$-ILBF$_4^-$-urea was prepared via an anion exchange, Br$^-$ replaced by BF$_4^-$. The preparation steps were monitored by applying different characterization techniques.

XRD was used to study the crystalline structure of the UiO-66-NH$_2$ after functionalization by ILBr$^-$ and grafting by urea (Fig. 1a). The characteristic diffraction of the UiO-66-NH$_2$ was observed at angles of 14.7°, 17.4°, 22.2°, 25.7°, 30.6°, 31.1°, 35.9°, 37.7°, 40.1°, 43.6°, 50.5°, and 56.8° corresponding to the (222), (400), (511), (600), (711), (731), (820), (751), (664), (933), (955), and (12 42) planes, respectively [64]. The UiO-66-NH$_2$-ILBF$_4^-$-urea showed isostructural and similar pattern to that of the pristine MOF, indicating that the post-synthesis maintained the crystalline structure of the frameworks. Additional diffractions at 17.95°, 28.7°, 29.25°, and 47.9° were observed and could be attributed to IL-Urea.

The functionalization of the MOF was investigated by FT-IR (Fig. 1b). The characteristic peaks related to the N–H stretch of primary amines (3457 cm^{-1} and 3351 cm^{-1}), carbonyl stretch (1661 cm^{-1}), C–N stretch (1259 cm^{-1}), and Zr–O stretch (600–800 cm^{-1}) were observed [64]. A stretching vibration at 503 cm^{-1} was attributed to CH$_2$–Br after attachment of ILBr$^-$ to the ligand of the MOF. For UiO-66-NH$_2$-ILBF$_4^-$-urea, the bands at 3370 and 3215 cm^{-1} were related to the stretching vibration of N–H in amines, while the band at 1630 cm^{-1} is attributed to the amide group in urea. Bands at 1590 cm^{-1} and 1460 cm^{-1} were assigned to the C=N and imidazolium ring, respectively.

Figure 1c, d demonstrated the N$_2$ adsorption–desorption isotherm and pore size distribution of the MOF. The isotherm showed a type IV hysteresis that is a characteristic pattern for mesoporous materials, while a fast adsorption at low pressure is consistence with microporous materials. Figure 1d showed a uniform distribution of the pore size in the framework. The surface area and porosity of the UiO-66-NH$_2$-ILBF$_4^-$-urea were determined (Table 1). As expected, the surface area and pore size/volume were reduced after modification of UiO-66-NH$_2$. The BET surface area, total pore volume, and average pore size were obtained to be 600 m^2 g^{-1}, 0.39 cm^3 g^{-1}, and 0.9 nm, respectively. The pore size of 0.9 nm belongs to the microporous materials according to the IUPAC classification of porous materials [65].
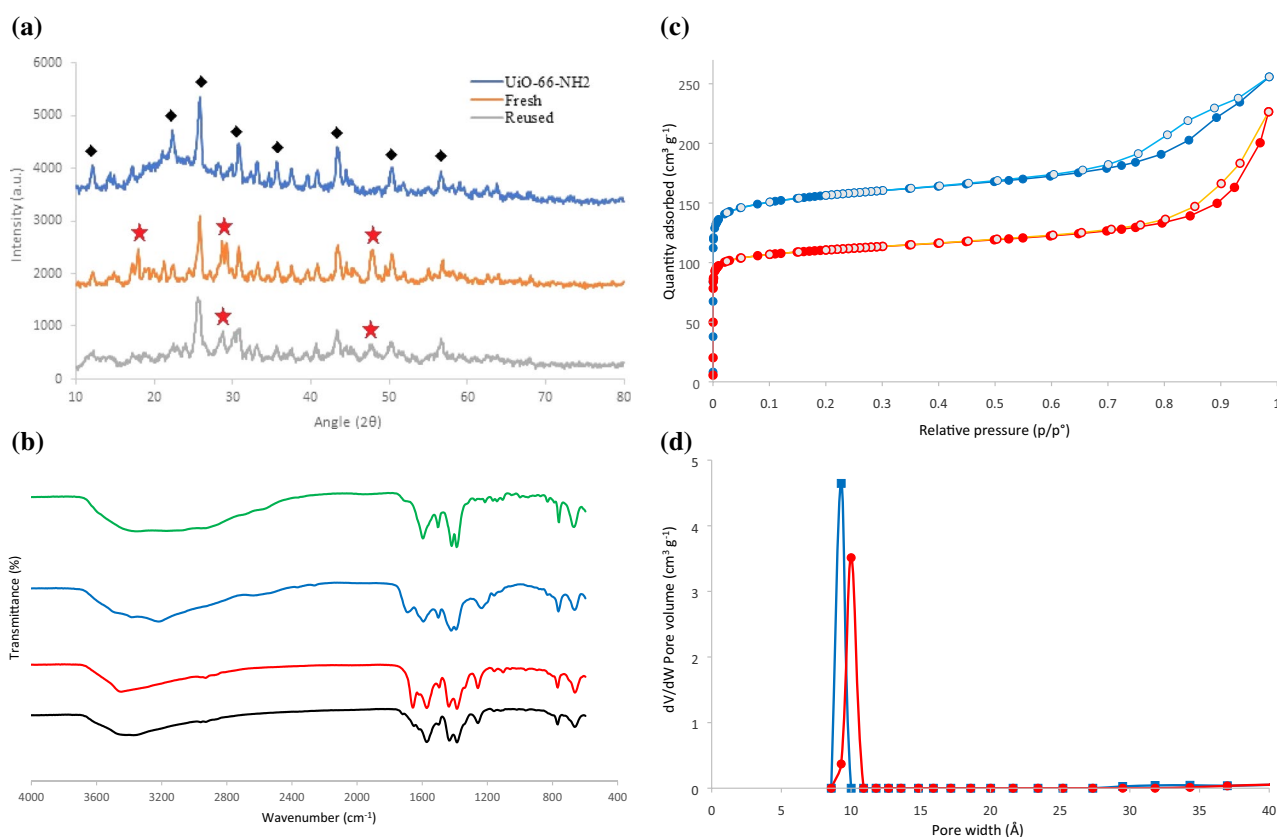

Fig. 1 **a** PXRD patterns of UiO-66-NH$_2$-ILBF$_4^-$-urea in fresh and reused (after five times recycling), and **b** FT-IR spectra of UiO-66-NH$_2$ (black), UiO-66-NH$_2$-ILBr$^-$ (red), fresh UiO-66-NH$_2$-ILBF$_4^-$-urea (blue) and reused UiO-66-NH$_2$-ILBF$_4^-$-urea (green). **c** N$_2$ adsorption–desorption isotherm and **d** pore size distribution of the fresh (blue) and reused (red), after five times recycling, UiO-66-NH$_2$-ILBF$_4^-$-urea. The solid spheres are referred to adsorption and the gray ones are for desorption

Table 1 Surface area and porosity of the UiO-66-NH$_2$-ILBF$_4^-$-urea in fresh and recycled forms

	UiO-66-NH$_2$	UiO-66-NH$_2$-ILBF$_4^-$-urea (fresh)	UiO-66-NH$_2$-ILBF$_4^-$-urea (recycled)
BET surface area (m^2 g^{-1})	1280	601	427
Total pore volume (cm^3 g^{-1})	0.60	0.39	0.34
Average pore size (nm)	1.89	0.93	1.0

Table 2 Elemental compositions of the UiO-66-NH$_2$, UiO-66-NH$_2$-ILBr$^-$ and UiO-66-NH$_2$-ILBr$^-$-urea

MOFs	CHN (At%)		XPS (At%)				
	C	N	Zr	O	C	N	Br
UiO-66-NH$_2$	21.28	4.49	2.88	31.47	60.72	4.84	–
UiO-66-NH$_2$-ILBr$^-$	24.28	5.65	2.41	23.32	64.07	2.60	7.60
UiO-66-NH$_2$-ILBr$^-$-urea	18.39	3.48	7.61	30.12	37.46	0.9	23.90

CHN analysis was used to determine the amount of organic species loading on the surface of the MOFs (Table 2). The results showed that the content of carbon and nitrogen increased after modification of the UiO-66-NH$_2$ with ionic-liquid. The atomic percentage of carbon and nitrogen decreased after grafting urea to the ionic liquid, which can be related to the presence of heavy elements (i.e. Br) in the structure. XPS was also employed for detection the elements and their quantities (Table 2). The presence of relevant elements (Zr, O, C, N, Br) in the structure of the MOF and the ionic liquid on the surface was verified. There is a difference in the elemental compositions obtained from CHN and XPS techniques due to their different operations applied for the analysis. In CHN, the content of selected elements (e.g. C, N, H) in the entire bulk of the samples is measured, while in XPS, almost all elements (except H) in the selected points of the samples in the surface and sub-layer with thickness < 10 nm is analyzed. Figures S7–S9 (Supporting Information) display the XPS surveys of UiO-66-NH$_2$, UiO-66-NH$_2$-ILBr$^-$ and UiO-66-NH$_2$-ILBr$^-$-urea, respectively. For UiO-66-NH$_2$ (Figure S5), the N 1s peak at 397 eV was attributed to NH$_2$ groups on the organic linkers. For the supported ILs, the O 1s peaks at 531 and 530.5 eV were assigned to the C=O groups in the linker and the urea, respectively (Figure S6 and S7), while the peak at 182 eV corresponded to the Br 3p in the C–Br bond (Figure S8). High-resolution XPS and the relevant deconvolution, in Fig. 2a, exhibited two components for the N peak. The peaks at ~ 401 and ~ 399.5 eV were assigned to the cationic N and the neutral N (–NH$_2$), respectively [66]. The peak at 401 eV confirms the presence of the imidazolium ring in the IL-supported UiO-66-NH$_2$ [67]. High-resolution XPS of the C 1s peak consists of three fitted peaks at binding energies of 283 and 284 and 290 eV (Fig. 2b). The peak at 283 eV was attributed to the C–C aliphatic (alkyl groups of the IL), while the peak at 284 eV was for C–N, C=C, and C=N

(in the linker and the imidazolium rings) [68]. The peak at 290 eV was also found to be correlated to the C=O in the linker and the urea [69].

The thermal stability and mass loading of ionic-liquid and urea into the framework were studied by TGA. In Fig. 3, The UiO-66-NH$_2$-ILBF$_4^-$ and UiO-66-NH$_2$-ILBF$_4^-$-urea showed almost similar thermal stability with the UiO-66-NH$_2$. An initial weight loss of ~ 5% and ~ 10% was found for UiO-66-NH$_2$-ILBF$_4^-$ and UiO-66-NH$_2$-ILBF$_4^-$-urea, respectively at below ~ 100 °C, while ~ 20% weight loss observed for the pristine MOF. The initial weight loss is related to the removal of the residual solvent (e.g. water and/or ethanol) from the pores. Moreover, an additional weight loss was observed at ~ 180–250 °C for the modified MOFs, relating to the escape of DMF coordinated to the nodes. Such event was not observed for the UiO-66-NH$_2$ because the MOF activation via a solvent extraction was efficient in removal of DMF. At temperature above 250 °C, slight reduction in the weight might be attributed to the thermal decomposition of the IL [70] and also urea groups in the modified MOFs, and removal of residual coordinated DMF inside the micropore of the UiO-66-NH$_2$ and partial degradation of the MOF structures ~ 400 °C. A further weight loss at ~ 500 °C was observed for the modified and pristine MOFs due to the framework degradation to ZrO$_2$ [64].

The TEM and SEM images (Fig. 4a, b) showed irregular round-shaped particles for UiO-66-NH$_2$-ILBF$_4^-$-urea with sizes ranging from 50 to 100 nm. The EDS confirms the existence of the elements incorporated in the MOF (Fig. 4c). Zr (5.5%), O (17.3%), C (35.6%), N (7.6%), B (9.8%), and F (24.0%) were found. The result confirms the presence of B and F (corresponding to BF$_4^-$) along with other elements in the structure. The trace amount of Br inferred an almost complete replacement of Br$^-$ with BF$_4^-$ within anion exchange. The elemental mapping demonstrated a homogeneous distribution of elements in the frameworks (Fig. 4d).

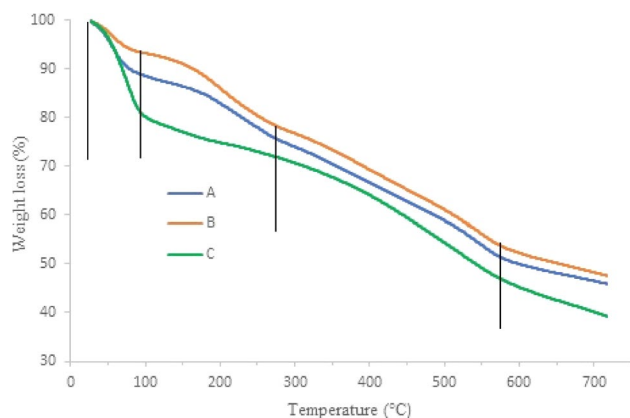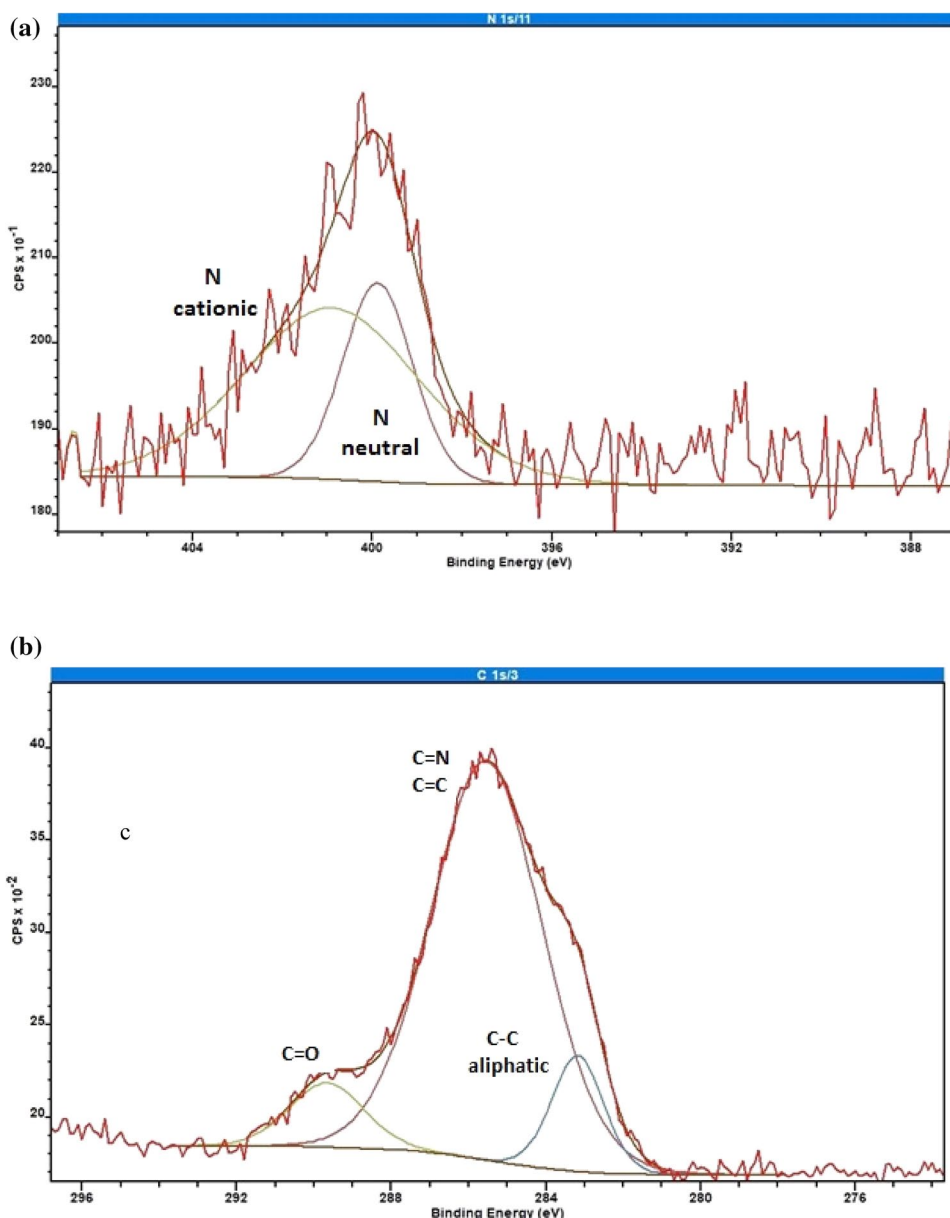**Fig. 2** High resolution XPS of **a** N 1 s for UiO-66-NH$_2$-ILBr$^-$ and **b** C 1s for UiO-66-NH$_2$-ILBr$^-$-urea

3.2 Synthesis of Oximes Using UiO-66-NH$_2$-ILBF$_4$$^-$-Urea Heterogeneous Catalyst

A zirconium MOF with incorporated IL and urea (UiO-66-NH$_2$-ILBF$_4$$^-$-urea) was used as a platform for catalyzing organic reactions. In the current work, the synthesis of oximes was selected due to the simplicity of the procedure (highly crystalline compound [39]), an efficient condensation reaction, and an interesting intermediate with broad applications. Oxime is basically an imine with a general formula: RR′C = NOH, where R is an alkyl and R′ could be hydrogen (to form aldoxime) and/or alkyl (to form ketoxime). The condensation reaction between benzaldehyde and hydroxylammonium chloride was chosen as a model reaction
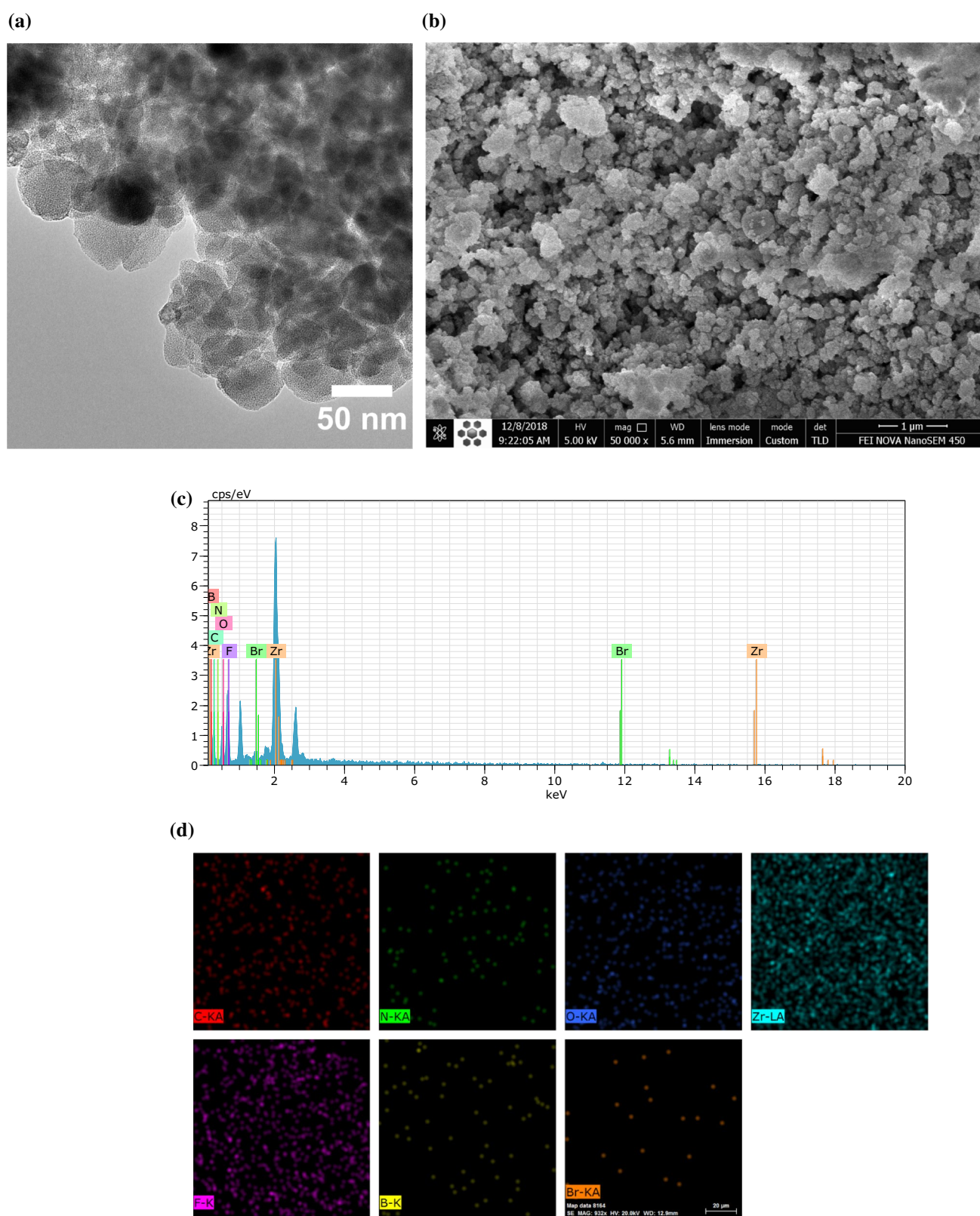

Fig. 3 Thermograms of (A) UiO-66-NH$_2$-ILBF$_4$$^-$, (B) UiO-66-NH$_2$-ILBF$_4$$^-$-urea, and (C)UiO-66-NH$_2$

(a)

(b)

(c)

(d)

Fig. 4 TEM (**a**) and SEM (**b**) images, EDS spectrum (**c**), and elemental mapping in selected area (**d**) of the UiO-66-NH$_2$-ILBF$_4^-$-urea

to examine the catalytic activity of UiO-66-NH$_2$-ILBF$_4^-$-urea as a heterogeneous catalyst. Urea acts as a basic site for catalyzing the reaction and also adjust the pH of the medium to neutral as HCl is generated from hydroxylamine hydrochloride [42]. With regards to the mechanism, the amine group of urea initially activates the oxygen of the carbonyl group (of benzaldehyde) via a hydrogen bonding and facilitates the nucleophilic addition of hydroxylamine to the carbon of the carbonyl [42]. Two hydrogen bonding donors have been proposed for urea on the carbonyl activation [57]. Oxime is finally formed by a dehydration reaction.

To optimize the reaction conditions, the effect of various reaction parameters such as type of solvent, temperature, and amount of catalyst were studied in the first stage (Table 3). The effect of common solvents such as ethanol, acetonitrile, mixture of water and ethanol, and toluene were investigated on the reaction (Table 3, entry 1–3 and 6). The results revealed that a solvent with medium polarity of is indispensable for the reaction to proceed. Ethanol was found to be the best choice for this reaction. The effect of various temperatures such as (25, 60 and 90 °C) were studied for the model reaction (Table 3, entry 4–6). In contrast to the reported results, the lower temperature (25 °C) showed a better result compared to the higher temperatures. When the temperature was increased from 25 to 90 °C, the yield was decreased from 86 to 51% (Table 3, entry 4). It is proposed that the local motions of the linear and long alkyl group (attached to urea) increase by increasing the temperature leading to unfavorable interaction between urea and the imidazolium ring (synergic effect, discuss later). Hence, the urea (in cooperation with the IL) is not able to activate the carbonyl group of aldehydes and ketones for nucleophilic addition reaction. The effect of the catalyst amount on the reaction was also studied by varying it from 0.05–0.1 g (Table 3, entry 6–9), while keeping the other parameters

Table 3 Optimization of the reaction conditions for the synthesis of oximes using UiO-66-NH$_2$-ILBF$_4^-$-urea as the catalyst

Entry	Solvents	Catalyst amount (g)	Temperature (°C)	Yield (%)[a]
1	Toluene	0.05	25	43
2	Acetonitrile	0.05	25	50
3	Ethanol + H$_2$O	0.05	25	68
4	Ethanol	0.05	90	51
5	Ethanol	0.05	60	70
6	Ethanol	0.05	25	86
7	Ethanol	0.04	25	80
8	Ethanol	0.03	25	70
9	Ethanol	0.1	25	86

Reaction conditions: benzaldehyde (1 mmol), hydroxylammonium chloride (1.5 mmol), solvent (1 mL), catalyst, reaction time (15 min)

[a]Isolated yield

constant. It was observed that 0.05 g of catalyst was sufficient for completion of the reaction. It was observed that by using a higher amount of catalyst, the yield of the reaction was not enhanced. The optimum condition was found to be 0.05 g of the catalyst, ethanol as a solvent, temperature at 25 °C with a reaction time of 15 min.

To extent the current approach, a variety of substrates were used for the synthesis of different oximes. As shown in Table 4 various types of aromatic aldehydes with electron donating and withdrawing groups were successfully reacted with hydroxylamine hydrochloride and afforded the corresponding oximes in good to excellent yields. The nature of the substituents did not show a significant effect on the reaction efficiency, which is in good agreement with the results reported in the literature [71]. According to the results, hydroxy as an electron-donating group improved the reaction yield (Table 4, entry 2), while the alkyl and halide groups in the *ortho* position made a steric hindrance for the reaction and reduce the yield (Table 4, entries 3 and 8). Moreover, cinnamaldehyde as a non-aromatic showed a reasonable yield in the reaction (Table 4, entry 5). The nitro group in the *para* position (Table 4, entry 6) exhibited more deactivating effect in the condensation reaction compared to that in the *meta* position (Table 4, entry 7) due to an effective electron delocalization of the carbonyl group towards the nitro group in the *para* position. Methoxy groups in the para and meta positions showed unexpected results, compared to electron-donating and -withdrawing groups, for unknown reasons (Table 4, entries 4 and 9). On the other hand, aromatic ketones are generally less reactive in the condensation reaction compared to aromatic aldehydes due to their steric hindrance [50]. Acetophenone (Table 4, entry 10) exhibited a good yield (75% in 25 min) in comparison with the reported result with (55% yield in 10 min) using nanostructured pyrophosphate catalyst [71]. An aliphatic cyclic ketone, cyclohexanone (Table 4, entry 1 l), showed better results compared to aromatic ketones and comparable result with aromatic aldehydes.

The effect of anion incorporated on the IL (BF$_4^-$ *vs.* Br$^-$) was also studied by keeping the other parameters such as amount of catalyst, solvent type and temperature (Table 5). By replacing Br$^-$ with BF$_4^-$, the reaction time is reduced, and the reaction efficiency enhanced, which was consistent with the reported results; the IL of bmiBF$_4$ has showed higher yields compared to bmiCl [54]. Moreover, Br$^-$ has a hydrophilic nature and is miscible in highly polar solvents, thus the ion solvation restricts the activity of the supported IL, in contrast BF$_4^-$ exhibit hydrophobicity and immiscibility in aqueous media [73]. The effect of the substrate (i.e. UiO-66-NH$_2$) was examined and the result showed a medium activity probably due to high surface area and available basic sites on the MOF. In addition, the activity of the ionic liquid (e.g. ILBr$^-$, IL-BF$_4^-$) and urea in homogenous

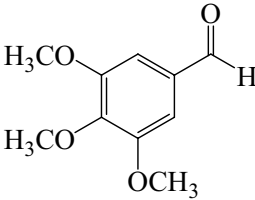**Table 4** Synthesis of oximes via reaction of aldehydes and/or ketones with hydroxylammonium chloride

Entry	Substrate	Time (min)	Yield (%)[a]	Melting point (°C) [Ref.]
1		15	86	31–33 (33–35) [56]
2		25	92	55–58 (57–59) [56]
3		25	82	57–59 (51–53) [72]
4		30	67	178–182
5		25	78	132–136 (136–138) [56]
6		30	77	126–128 (128–130) [56]
7		30	83	116–118 (116–118) [42]
8		30	61	63–65 (68–72) [42]

A Synergic Activity of Urea/Butyl Imidazolium Ionic Liquid Supported on UiO-66-NH$_2$ Metal–…

Table 4 (continued)

Entry	Substrate	Time (min)	Yield (%)[a]	Melting point (°C) [Ref.]
9	H$_3$CO–C$_6$H$_4$–CHO	35	65	131–133 (131–133) [56]
10	C$_6$H$_5$–CO–CH$_3$	25	75	56–57 (56–59) [42]
11	cyclohexanone	20	83	80–85 (84–85) [42]

Reaction conditions**:** aldehyde or ketone (1 mmol), hydroxylammonium chloride (1.5 mmol), ethanol (1 mL), UiO-66-NH$_2$-ILBF$_4^-$-urea (0.05 g) at 25 °C in 15–35 min

[a]Isolated yield

Table 5 The catalytic activity of the catalyst, the support and the IL in homogeneous phase

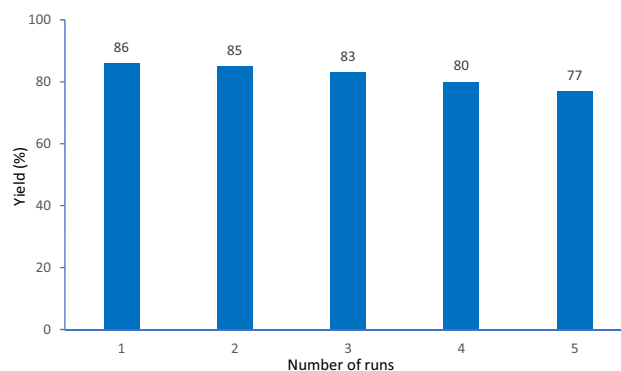| Catalyst	Time (min)	Yield (%)[a]
UiO-66-NH$_2$-ILBF$_4^-$-urea	15	86
UiO-66-NH$_2$-ILBr$^-$-urea	20	70
UiO-66-NH$_2$	30	43
ILBF$_4^-$	35	33
ILBr$^-$	35	20
Urea	35	Trace

Reaction conditions**:** benzaldehyde (1 mmol), hydroxylammonium chloride (1.5 mmol), ethanol (1 mL), temperature (25 °C), and catalyst or UiO-66-NH$_2$ or IL (0.05 g)

[a]Isolated yield

Fig. 5 Reusability of the catalyst for the synthesis of oxime

phase were investigated. ILs exhibited a limited effect on the activation of the carbonyl groups and deprotonation of hydroxyl amine by Br$^-$ and BF$_4^-$. Urea as a base was not effective in the homogeneous phase, while by grafting to the IL and the MOF, their synergic effects may promote the hydrogen-bonding donation of the urea in heterogeneous phase. A similar synergic activation has been found for (2-hydroxyethyl)trimethylammonium in choline chloride/urea system supported on molecular sieves for the CO$_2$ cyclization with epoxides [74].

3.2.1 Catalyst Recycling and Stability

The recyclability and reusability of the catalyst were studied for the condensation reaction using a model reaction between benzaldehyde with hydroxylammonium chloride

(Fig. 5). After each cycle, the catalyst was reactivated by centrifugation, washing with water and ethanol (to remove the residual starting materials on the catalyst surface and pores), and drying at 60 °C in an oven overnight. The catalyst was successfully recycled and reused 5 times without significant loss of the performance. The slight reduction in catalyst activity might be related to the partial blocking of the pores by trapped starting materials or product [75, 76]. The BET surface area and total pore volume of the reused catalyst were reduced (*cf.* the fresh catalyst) and found to be 427 m^2 g^{-1} and 0.34 cm^3 g^{-1}, respectively, although a slight increase in pore size (1.0 nm) was observed (Table 1). The N$_2$ adsorption–desorption isotherm and pore size distribution of the reused catalyst can be found in Fig. 1c, d.

The catalyst stability was investigated by XRD, FTIR, electron microscopy, and elemental analysis. XRD pattern

and the FT-IR spectrum of the reused UiO-66-NH$_2$-ILBF$_4^-$-urea show similar patterns (Fig. 1a, b) to those in fresh catalyst, indicating that the catalyst is almost stable under reaction conditions after five times of recycling and reusing. Furthermore, the morphology and the chemical composition of the UiO-66-NH$_2$-ILBF$_4^-$-urea (after five times of reusing) were studied by FE-SEM (Fig. 6) and elemental analysis/mapping (Figure S8 and S9, Supporting Information). The results showed a slight change in the morphology and similar
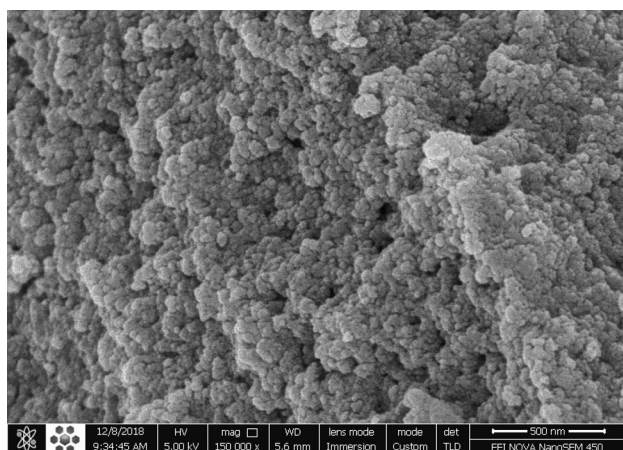

Fig. 6 FE-SEM image of the catalyst after five times reuse

composition for the recycled catalyst in comparison with those for the fresh catalyst. An atomic percentage for the corresponding elements in the recycled catalyst was found to be Zr (4.4%), O (18.6%), C (39.1%), N (5.2%), B (9.3%), and F (23.3%). A slight reduction in the content of B and F (corresponding to BF$_4^-$) caused negligible leaching for the reused catalyst after five successive recycling. Furthermore, the activity of the extracted catalyst after hot filtration (70 °C in EtOH for 2 h) was reduced to a yield of 80%, which could be related to leaching of BF$_4^-$ at an elevated temperature. Consequently, the catalyst can be easily recycled and reused several times with a reasonable stability.

Different types of acidic (Brønsted, Lewis, and solid acids, entries 1–11, Table 6) and basic (metal hydroxide and organic bases, entries 12–15) conditions were used for the synthesis of oximes. Organic and polar solvents and also solventless conditions were suitable media for the syntheses. Microwave (MW) and ultrasonic (US) irradiations, reflux, and grinding were applied to accelerate the reactions. Ionic liquids were also employed as a catalyst or reaction medium. Major environmental and economic concerns on the reported catalytic systems are catalyst recoverability and reusability, therefore, integration of catalysts to solid porous supports is encouraging. The current catalytic system, a heterogeneous basic catalyst, showed comparable results in terms of yield and reaction conditions (e.g. temperature and time), and

Table 6 Synthesis of oximes via reaction of benzaldehydes with hydroxylammonium chloride (NH$_2$OH.HCl) using different catalytic systems

Entry	Catalytic systems	Reaction conditions	Time (min)	Yield (%)	Ref
1	TiO$_2$/SO$_4^{2-}$ (0.05 g)	130 °C, solventless	1	100	[50]
2	Na$_2$SO$_4$ (0.1 mmol)	US (25–35 °C), EtOH	5	88	[42]
3	HCl (2 drops), K$_2$CO$_3$ (10%), pH 10	US, H$_2$O	Immediately	91	[77]
4	BF$_3$·Et$_2$O (10 mol%)	Reflux, CH$_3$OH	3.5 (h)	87[a]	[43]
5	BF$_3$·Et$_2$O (10 mol%)	MW, CH$_3$OH	6	95[a]	[43]
6	Silica gel 60, 230–400 mesh (1 g)	MW (800 W, 80–90 °C), solventless	3	100	[39]
7	Wet basic Al$_2$O$_3$ (1.5 equiv.)	MW, solventless	5	79	[52]
8	Molecular sieves 4 Å (2.5 g)	Grinding	30	60	[52]
9	Na$_2$CaP$_2$O$_7$ nanostructure (0.1 g)	MW (400 W, 80 °C), solventless	4	82	[71]
10	Na$_2$CaP$_2$O$_7$ nanostructure (0.1 g)	80 °C, solventless	10	83	[71]
11	Na$_{12}$[WZn$_3$(H$_2$O)$_2$(ZnW$_9$O$_{34}$)$_2$] (0.01 mmol)	H$_2$O$_2$ (27%), NH$_3$ (25%), H$_2$O, rt	6 (h)	95	[51]
12	NaOH (1.2 mol)	Grinding, CH$_3$OH (2–4 drops), rt	2	71[b]	[53]
13	DABCO[c] (1 mmol)	Grinding and MW (900 W), solventless	70 (s)	98	[56]
14	(PhCH$_2$)$_3$ N (1 mmol)	Grinding and MW (900 W), solventless	90	98	[56]
15	Glycine (0.5 mmol)	DMF, rt	5 (h)	96[d]	[58]
16	[bmIm]OH (2 mmol)	US, EtOH, rt	5	91	[55]
17	bmiBF$_4$ (2 mmol)	rt	30	95[d]	[54]
18	UiO-66-NH$_2$-ILBF$_4^-$-urea (0.05 g)	EtOH, rt	15	86	This work

[a]CH$_3$CONHOH was used instead of NH$_2$OH·HCl

[b]2-Hydroxybenzaldehyde as a precursor

[c]1,4-Diazabicyclo[2.2.2]octane

[d]Cyclohexane as a precursor

superior recyclability, reusability, and robustness compared to the reported systems.

4 Conclusion

A robust supported ionic liquid system is introduced for the organic synthesis of oximes. In the design strategy, the basic heterogeneous catalyst was successfully prepared by employing a chemical/thermal stable Zr-based MOF, UiO-66-NH$_2$ as a support. The MOF was initially modified with an ionic liquid to make a supported ionic liquid (SIL), followed by covalent anchoring of urea to the cation moiety of IL to form a TSIL. The as-prepared catalyst was examined for the synthesis of oximes. UiO-66-NH$_2$-ILBF$_4^-$-urea catalyst showed excellent performance in the reaction of various aldehydes and ketones with hydroxylammonium chloride in good yields. Ethanol was the best candidate as a solvent in the current method. The catalyst was successfully recycled and reused for several times without significant loss of activity. Due to high specific area and large porosity of the MOFs, they can be extensively employed in various catalytic reactions with efficient performance. Moreover, a large number of available pores in MOFs can be a suitable host for ionic liquids to produce a large variety of heterogeneous catalysts. More efforts can be helpful to design new task-specific ILs attached to MOF using basic groups (e.g. thiourea, polyamines, etc.) and/or acidic groups (e.g. –SO$_3$H).

References

1. Campisciano V, Giacalone F, Gruttadauria M (2017) Supported ionic liquids: a versatile and useful class of materials. Chem Rec 17:918–938
2. Romanovsky BV, Tarkhanova IG (2017) Supported ionic liquids in catalysis. Russ Chem Rev 86:444–458
3. Riisager A, Jørgensen B, Wasserscheid P, Fehrmann R (2006) First application of supported ionic liquid phase (SILP) catalysis for continuous methanol carbonylation. Chem Commun 9:994–996
4. Joni J, Haumann M, Wasserscheid P (2009) Development of a supported ionic liquid phase (SILP) catalyst for slurry-phase Friedel-Crafts alkylations of cumene. Adv Synth Catal 351:423–431
5. Lemus J, Palomar J, Gilarranz MA, Rodriguez JJ (2011) Characterization of supported ionic liquid phase (SILP) materials prepared from different supports. Adsorption 17:561–571
6. More S, Jadhav S, Salunkhe R, Kumbhar A (2017) Palladium supported ionic liquid phase catalyst (Pd@SILP-PS) for room temperature Suzuki-Miyaura cross-coupling reaction. Mol Catal 442:126–132
7. Xin B, Hao J (2014) Imidazolium-based ionic liquids grafted on solid surfaces. Chem Soc Rev 43:7171–7187
8. Riisager A, Fehrmann R, Haumann M, Wasserscheid P (2006) Supported ionic liquid phase (SILP) catalysis: An innovative concept for homogeneous catalysis in continuous fixed-bed reactors. Eur J Inorg Chem 2006:695–706
9. Zhang Q, Zhang S, Deng Y (2011) Recent advances in ionic liquid catalysis. Green Chem 13:2619–2637
10. Hagiwara H, Sekifuji M, Hoshi T, Qiao K, Yokoyama C (2007) Synthesis of bis(indolyl)methanes catalyzed by acidic ionic liquid immobilized on silica (ILIS). Synlett 2007:1320–1322
11. Gu Y, Li G (2009) Ionic liquids-based catalysis with solids: state of the art. Adv Synth Catal 351:817–847
12. Lee S-G (2006) Functionalized imidazolium salts for task-specific ionic liquids and their applications. Chem Commun 10:1049–1063
13. Olivier-Bourbigou H, Magna L, Morvan D (2010) Ionic liquids and catalysis: Recent progress from knowledge to applications. Appl Catal A 373:1–56
14. Sawant AD, Raut DG, Darvatkar NB, Salunkhe MM (2011) Recent developments of task-specific ionic liquids in organic synthesis. Green Chem Lett Rev 4:41–54
15. Izák P, Bobbink FD, Hulla M, Klepic M, Friess K, Hovorka S, Dyson PJ (2018) Catalytic ionic-liquid membranes: the convergence of ionic-liquid catalysis and ionic-liquid membrane separation technologies. ChemPlusChem 83:7–18
16. Mehnert CP (2005) Supported ionic liquid catalysis. Chem Eur J 11:50–56
17. Mehnert CP, Cook RA, Dispenziere NC, Afeworki M (2002) Supported ionic liquid catalysis—a new concept for homogeneous hydroformylation catalysis. J Am Chem Soc 124:12932–12933
18. Li H, Bhadury PS, Song B, Yang S (2012) Immobilized functional ionic liquids: efficient, green, and reusable catalysts. RSC Adv 2:12525–12551
19. Luo Q-X, An B-W, Ji M, Zhang J (2018) Hybridization of metal–organic frameworks and task-specific ionic liquids: fundamentals and challenges. Mater Chem Front 2:219–234
20. Takashima Y, Yokoyama M, Horikoshi A, Sato Y, Tsuruoka T, Akamatsu K (2017) Ionic liquid/metal–organic framework hybrid generated by ion-exchange reaction: synthesis and unique catalytic activity. New J Chem 41:14409–14413
21. Farrusseng D, Aguado S, Pinel C (2009) Metal–organic frameworks: Opportunities for catalysis. Angew Chem Int Ed 48:7502–7513
22. He H, Perman JA, Zhu G, Ma S (2016) Metal-organic frameworks for CO$_2$ chemical transformations. Small 12:6309–6324
23. Jiao L, Seow JYR, Skinner WS, Wang ZU, Jiang H-L (2019) Metal–organic frameworks: structures and functional applications. Mater Today 27:43–68
24. Luo Q-X, Ji M, Lu M-H, Hao C, Qiu J-S, Li Y-Q (2013) Organic electron-rich N-heterocyclic compound as a chemical bridge: building a Brönsted acidic ionic liquid confined in MIL-101 nanocages. J Mater Chem A 1:6530–6534
25. Luo Q-X, Ji M, Park S-E, Hao C, Li Y-Q (2016) PdCl$_2$ immobilized on metal–organic framework CuBTC with the aid of ionic liquids: enhanced catalytic performance in selective oxidation of cyclohexene. RSC Adv 6:33048–33054
26. Abednatanzi S, Leus K, Gohari Derakhshandeh P, Nahra F, De Keukeleere K, Van Hecke K, Van Driessche I, Abbasi A, Nolan SP, Van Der Voort P (2017) POM@IL-MOFs—inclusion of POMs in ionic liquid modified MOFs to produce recyclable oxidation catalysts. Catal Sci Technol 7:1478–1487
27. Abednatanzi S, Abbasi A, Masteri-Farahani M (2017) Immobilization of catalytically active polyoxotungstate into ionic liquid-modified MIL-100(Fe): a recyclable catalyst for selective oxidation of benzyl alcohol. Catal Commun 96:6–10
28. Khan NA, Hasan Z, Jhung SH (2014) Ionic liquids supported on metal-organic frameworks: remarkable adsorbents for adsorptive desulfurization. Chem Eur J 20:376–380

29. Wu J, Gao Y, Zhang W, Tan Y, Tang A, Men Y, Tang B (2015) Deep desulfurization by oxidation using an active ionic liquid-supported Zr metal–organic framework as catalyst. Appl Organometal Chem 29:96–100

30. Luo Q-X, Song X-D, Ji M, Park S-E, Hao C, Li Y-Q (2014) Molecular size- and shape-selective Knoevenagel condensation over microporous $Cu_3(BTC)_2$ immobilized amino-functionalized basic ionic liquid catalyst. Appl Catal A 478:81–90

31. Tharun J, Bhin K-M, Roshan R, Kim DW, Kathalikkattil AC, Babu R, Ahn HY, Won YS, Park D-W (2016) Ionic liquid tethered post functionalized ZIF-90 framework for the cycloaddition of propylene oxide and CO_2. Green Chem 18:2479–2487

32. Ding L-G, Yao B-J, Jiang W-L, Li J-T, Fu Q-J, Li Y-A, Liu Z-H, Ma J-P, Dong Y-B (2017) Bifunctional imidazolium-based ionic liquid decorated UiO-67 type MOF for selective CO_2 adsorption and catalytic property for CO_2 cycloaddition with epoxides. Inorg Chem 56:2337–2344

33. Ma D, Li B, Liu K, Zhang X, Zou W, Yang Y, Li G, Shi Z, Feng S (2015) Bifunctional MOF heterogeneous catalysts based on the synergy of dual functional sites for efficient conversion of CO_2 under mild and co-catalyst free conditions. J Mater Chem A 3:23136–23142

34. Wu Z, Chen C, Wan H, Wang L, Li Z, Li B, Guo Q, Guan G (2016) Fabrication of magnetic NH_2-MIL-88B (Fe) confined Brønsted ionic liquid as an efficient catalyst in biodiesel synthesis. Energy Fuels 30:10739–10746

35. Yang SH, Chang S (2001) Highly efficient and catalytic conversion of aldoximes to nitriles. Org Lett 3:4209–4211

36. Park S, Choi Y-A, Han H, Yang SH, Chang S (2003) Rh-Catalyzed one-pot and practical transformation of aldoximes to amides. Chem Commun 15:1936–1937

37. Peng H-G, Xu L, Wu H, Zhang K, Wu P (2013) One-pot synthesis of benzamide over a robust tandem catalyst based on center radially fibrous silica encapsulated TS-1. Chem Commun 49:2709–2711

38. Klitgaard SK, Egeblad K, Mentzel UV, Popov AG, Jensen T, Taarning E, Nielsen IS, Christensen CH (2008) Oxidations of amines with molecular oxygen using bifunctional gold–titania catalysts. Green Chem 10:419–423

39. Hajipour AR, Mallakpour SE, Imanzadeh G (1999) A rapid and convenient synthesis of oximes in dry media under microwave irradiation. J Chem Res (S) 3:228–229

40. Hajipour AR, Mallakpour SE, Khoee S (2002) An easy and fast method for conversion of oximes to the corresponding carbonyl compounds under microwave irradiation. Synth Commun 32:9–15

41. Kukushkin VY, Pombeiro AJL (1999) Oxime and oximate metal complexes: unconventional synthesis and reactivity. Coord Chem Rev 181:147–175

42. Li J-T, Li X-L, Li T-S (2006) Synthesis of oximes under ultrasound irradiation. Ultrason Sonochem 13:200–202

43. Sridhar M, Narsaiah C, Raveendra J, Reddy GK, Reddy MKK, Ramanaiah BC (2011) Efficient microwave-assisted synthesis of oximes from acetohydroxamic acid and carbonyl compounds using $BF_3 \cdot OEt_2$ as the catalyst. Tetrahedron Lett 52:4701–4704

44. Sha Q, Wei Y (2013) Base and solvent mediated decomposition of tosylhydrazones: highly selective synthesis of N-alkyl substituted hydrazones, dialkylidenehydrazines, and oximes. Tetrahedron 69:3829–3835

45. Yu J, Lu M (2015) Copper(II)-promoted direct conversion of methylarenes into aromatic oximes. Org Biomol Chem 13:7397–7401

46. Yu J, Jin Y, Lu M (2015) 3-Methyl-4-oxa-5-azahomoadamantane as an organocatalyst for the aerobic oxidation of primary amines to oximes in water. Adv Synth Catal 357:1175–1180

47. Xue X, Song F, Ma B, Yu Y, Li C, Ding Y (2013) Selective ammoximation of ketones and aldehydes catalyzed by a trivanadium-substituted polyoxometalate with H_2O_2 and ammonia. Catal Commun 33:61–65

48. Xing S, Han Q, Shi Z, Wang S, Yang PP, Wu Q, Li M (2017) A hydrophilic inorganic framework based on a sandwich polyoxometalate: unusual chemoselectivity for aldehydes/ketones with *in situ* generated hydroxylamine. Dalton Trans 46:11537–11541

49. Hyodo K, Togashi K, Oishi N, Hasegawa G, Uchida K (2016) Brønsted acid catalyzed transoximation reaction: synthesis of aldoximes and ketoximes without use of hydroxylamine salts. Green Chem 18:5788–5793

50. Guo J-J, Jin T-S, Zhang S-L, Li T-S (2001) TiO_2/SO_4^{2-}: an efficient and convenient catalyst for preparation of aromatic oximes. Green Chem 3:193–195

51. Sloboda-Rozner D, Neumann R (2006) Aqueous biphasic catalysis with polyoxometalates: oximation of ketones and aldehydes with aqueous ammonia and hydrogen peroxide. Green Chem 8:679–681

52. Kad GL, Bhandari M, Kaur J, Rathee R, Singh J (2001) Solventless preparation of oximes in the solid state and via microwave irradiation. Green Chem 3:275–277

53. Aakeröy CB, Sinha AS, Epa KN, Spartz CL, Desper J (2012) A versatile and green mechanochemical route for aldehyde–oxime conversions. Chem Commun 48:11289–11291

54. Ren RX, Ou W (2001) Preparation of cyclic ketoximes using aqueous hydroxylamine in ionic liquids. Tetrahedron Lett 42:8445–8446

55. Zang H, Wang M, Cheng B-W, Song J (2009) Ultrasound-promoted synthesis of oximes catalyzed by a basic ionic liquid [bmIm]OH. Ultrason Sonochem 16:301–303

56. Hajipour AR, Rafiee F, Ruoho AE (2010) A rapid and convenient method for the synthesis of aldoximes under microwave irradiation using in situ generated ionic liquids. J Iran Chem Soc 7:114–118

57. Taylor MS, Jacobsen EN (2006) Asymmetric catalysis by chiral hydrogen-bond donors. Angew Chem Int Ed 45:1520–1543

58. Maheswara M, Siddaiah V, Gopalaiah K, Rao VM, Rao CV (2006) A simple and effective glycine-catalysed procedure for the preparation of oximes. J Chem Res 2006:362–363

59. Vitz J, Mac DH, Legoupy S (2007) Ionic liquid supported tin reagents for Stille cross coupling reactions. Green Chem 9:431–433

60. Zhang Y, Zhen B, Li H, Feng Y (2018) Basic ionic liquid as catalyst and surfactant: green synthesis of quinazolinone in aqueous media. RSC Adv 8:36769–36774

61. Kandiah M, Nilsen MH, Usseglio S, Jakobsen S, Olsbye U, Tilset M, Larabi C, Quadrelli EA, Bonino F, Lillerud KP (2010) Synthesis and stability of tagged UiO-66 Zr-MOFs. Chem Mater 22:6632–6640

62. Katz MJ, Brown ZJ, Colón YJ, Siu PW, Scheidt KA, Snurr RQ, Hupp JT, Farha OK (2013) A facile synthesis of UiO-66, UiO-67 and their derivatives. Chem Commun 49:9449–9451

63. Zhang L, Chen H, Zha Z, Wang Z (2012) Electrochemical tandem synthesis of oximes from alcohols using KNO_3 as the nitrogen source, mediated by tin microspheres in aqueous medium. Chem Commun 28:6574–6576

64. Hinde CS, Webb WR, Chew BKJ, Tan HR, Zhang W-H, Hor TSA, Raja R (2016) Utilisation of gold nanoparticles on amine-functionalised UiO-66 (NH_2-UiO-66) nanocrystals for selective tandem catalytic reactions. Chem Commun 52:6557–6560

65. Thommes M, Kaneko K, Neimark AV, Olivier JP, Rodriguez-Reinoso F, Rouquerol J, Sing KSW (2015) Physisorption of gases, with special reference to the evaluation of surface area and pore size distribution (IUPAC technical report). Pure Appl Chem 87:1051–1069

66. Sui Z-Y, Cui Y, Zhu J-H, Han B-H (2013) Preparation of three-dimensional graphene oxide−polyethylenimine porous

materials as dye and gas adsorbents. ACS Appl Mater Interfaces 5:9172–9179

67. Beattie DA, Arcifa A, Delcheva I, Le Cerf BA, MacWilliams SV, Rossi A, Krasowska M (2018) Adsorption of ionic liquids onto silver studied by XPS. Colloids Surf A 544:78–85

68. Li X, Sui Z-Y, Sun Y-N, Xiao P-W, Wang X-Y, Han B-H (2018) Polyaniline-derived hierarchically porous nitrogen-doped carbons as gas adsorbents for carbon dioxide uptake. Microporous Mesoporous Mater 257:85–91

69. Xiao P-W, Zhao L, Sui Z-Y, Han B-H (2017) Synthesis of core−shell structured porous nitrogen-doped carbon@silica material via a sol−gel method. Langmuir 33:6038–6045

70. Gupta R, Yadav M, Gaur R, Arora G, Sharma RK (2017) A straightforward one-pot synthesis of bioactive *N*-aryl oxazolidin-2-ones via a highly efficient Fe_3O_4@SiO_2-supported acetate-based butylimidazolium ionic liquid nanocatalyst under metal- and solvent-free conditions. Green Chem 19:3801–3812

71. Elmakssoudi A, Abdelouahdi K, Zahouily M, Clark J, Solhy A (2012) Efficient conversion of aldehydes and ketones into oximes using a nanostructured pyrophosphate catalyst in a solvent-free process. Catal Commun 29:53–57

72. Ribeiro TS, Prates A, Alves SR, Oliveira-Silva JJ, Riehl CAS, Figueroa-Villar JD (2012) The effect of neutral oximes on the reactivation of human acetylcholinesterase inhibited with par-aoxon. J Braz Chem Soc 23:1216–1225

73. Van Doorslaer C, Wahlen J, Mertens P, Binnemans K, De Vos D (2010) Immobilization of molecular catalysts in supported ionic liquid phases. Dalton Trans 39:8377–8390

74. Zhu A, Jiang T, Han B, Zhang J, Xie Y, Ma X (2007) Supported choline chloride/urea as a heterogeneous catalyst for chemical fixation of carbon dioxide to cyclic carbonates. Green Chem 9:169–172

75. Corma A, García H, Llabrés i Xamena FX (2010) Engineering metal organic frameworks for heterogeneous catalysis. Chem Rev 110:4606–4655

76. Chen J, Shen K, Li Y (2017) Greening the processes of metal–organic framework synthesis and their use in sustainable catalysis. Chemsuschem 10:3165–3187

77. Khoramabadi-Zad A, Azadmanesh M, Rezaee A (2010) Simple, Efficient and green synthesis of oximes under ultrasound irradiation. S Afr J Chem 63:192–194

Affiliations

Saeed Askari[1] · Mohammad Jafarzadeh[1] · David Benjamin Christensen[2] · Søren Kegnæs[2]

[1] Faculty of Chemistry, Razi University, 67144-14971 Kermanshah, Iran

[2] Department of Chemistry, Technical University of Denmark, 2800 Kgs. Lyngby, Denmark